UNIVERSITÀ
DEGLI STUDI
DI PADOVA

Università degli Studi di Padova

Department of Chemical Science

Ph.D. Course in Material Science and Engineering

OPTICAL NANOSTRUCTURES for EXCITONIC DEVICES

Coordinator: Ch.mo Prof. Giovanni Mattei

Supervisor: Ch.mo Prof. Renato Bozio

Ph.D. Student: Marcello Righetto

XXX Cycle

Per quanto piccola una cosa
può fornire un esempio di grandi cose
ed una pallida idea della loro conoscenza

Tito Lucrezio Caro- De rerum natura
(I sec. B.C.)

Abstract

Unrelenting advances in the field of nanoscience are fostering the progress in diverse research fields, ranging from light-emitting to medicine and diagnostics, from energy conversion to communication technologies. Besides representing the most paradigmatic example of nanoscience, semiconductor quantum dots (QDs) avowedly brought revolutions in many of the research fields mentioned above. Nowadays, some QDs-based devices and applications reported efficiencies almost as good as current state-of-the-art technologies. The founding concept of QDs is the application of quantum confinement effects on excitons, i.e., the main players of optical properties in bulk semiconductors. Among the wealth of ensuing properties, the size- and shape- tunability of the electronic excitations and increased coupling with light field aroused much interest. Also, the colloidal approach endows QDs with high processability and low cost, thereby encouraging their implementation in existing technologies and extending their impact to other fields. Howbeit, despite three decades of investigations, the bottom line has not been reached yet, and researchers are still delving deeper into the photophysics of these nanosystems. Though many of the low hanging fruit of QDs have been harvested, higher-lying ones seem to be even more succulent.

This thesis deals with the quest for highly performing nanostructures, as a prerequisite for some high impact optoelectronic applications, e.g., QD-Lasers and QD-Solar Cells. Within this framework, the struggle against fast Auger recombinations and trapping of either hot carriers or cold excitons was addressed mainly by sophisticated core/shell technologies. Thus, the first part of the thesis reports how tuning different shell parameters (e.g., the smoothness of the interface potential, the height of the confining potential, and the interfacial strain) it is possible to exert control on these detrimental recombination processes. Though often disregarded, even the role of organic capping ligand is reconsidered in promoting the outcoupling of QDs excited states and addressing their interaction. Besides the useful and technologically relevant advice gathered within these studies, the primary inheritance of the first part is the comprehensive photophysical scenario, portrayed by a phenomenological model that successfully describes many aspects of the exciton dynamics in QDs. This amount of knowledge was capitalized in the second part of this thesis, dealing with the quest for novel materials, potentially outpacing conventional CdSe-based QDs. Perovskite-based QDs reported promising results, whereas some pitfall in the conventional characterization of carbon-based QDs were discovered. The rationalization of both nature and dynamics of this materials is expected to expedite their development as alternative (and potentially superior) technologies concerning those studied in the first part.

Contents

List of Acronyms and Abbreviations

AR: Auger Recombination
Arg-CDs: Arginine based CDs
BBO: Beta Barium Borate (β-BaB_2O_4)
CB: Conduction Band
Arg-CDs: Arginine based CDs
Cit-CDs: Citric Acid based CDs
CM: Carrier Multiplication
DOS: Density Of States
EMA: Effective Mass Approximation
EPR: Electron Paramagnetic Resonance
ESA: Excited State Absorption
FCS: Fluorescence Correlation Spectroscopy
fs: Femtosecond
GSB: Ground State Bleaching
HP: Hybrid Perovskite
HH: Heavy-Hole
HT: Higher lying traps
IRF: Internal Response Function
IPCA :imidazo[1,2-a]pyridine-7-carboxylic acid, 1,2,3,5-tetrahydro-5-oxo
LARP: Ligand Assisted Reprecipitation
LED: Light Emitting Diode
LEPR: Light-Induced EPR
LH: Light-Hole
LO: Longitudinal Optical (phonon)
MEG: Multi-Exciton Generation
MER: Multi-Exciton Recombination
ML: Monolayer
NC: Nanocrystal
NIR: Near Infrared
NL: Nonlinear
N-18: Oleylamine capped QDs
ODE: 1-Octadecene
OLA: 1-Oleylamine
PIA: Photoinduced Absorption
PD: Perovskite Dot
P&P: Pump and Probe
PL: Photoluminescence
PLQY: Photoluminescence Quantum Yield
PV: Photovoltaics
QD: Quantum Dot
QD-LED: Quantum Dot Light emitting diode
QDSC: Quantum Dot Solar Cell
RT: Room Temperature
S-3: propanethiol capped QDs
S-18: octadecanethiol capped QDs
SE: Stimulated Emission
SILAR: Successive Ionic Layer Adsorption and Reaction
SPAD: Single Photon Avalanche Diode
TA: Transient Absorption
TCSPC: Time-Correlated Single Photon Counting
TO: Transverse Optical (phonon)
TOP: Trioctylphosphine
TOPO: Trioctylphosphine Oxide
TEM: Transmission Electron Microscopy
TRPL: Transient Photoluminescence
TREPR: Time-Resolved EPR
VB: Valence Band

INTRODUCTION

ABSTRACT-The burgeoning of modern societies relied heavily on some technological revolutions, bringing food, energy, health services and connectivity in everyday life of an increasing number of human beings. Albeit these developments dragged billions of people out of poverty and famine, there is another side of the coin. The sustainability of this global growth is one of the toughest hurdles to overcome for our societies. One of the promises of nanoscience is to provide us with innovative materials, potentially reducing the environmental cost of many technologies. Within this framework, the emphatic pursuit of outstandingly performing nanostructures is not a whim, but rather an urgent need. Specifically, this thesis deals with energetic issues, i.e., the search for highly efficient nanomaterials to emit artificial light, or to harvest the sunlight. Excitonic nanostructures are among the most promising materials, thanks to their enhanced interaction with the electromagnetic field. Yet many different processes hamper their efficiencies, either in converting photons or in generating free carriers. Different chapters will try to contribute in facing these issues by following a distinct path: starting from well-known materials and ending up with the exploration of novel and disruptive nanostructures.

The prospects of engineering, controlling and ultimately tailoring materials' properties, to fulfill specific demands dictated by applications, lie at heart of current research in nanoscience and nanotechnology. Shrinking the physical size of materials, down to nanometer scale, allows entering the quantum confinement regime, where the size is comparable with a characteristic length of the material. According to the functional property of interest, this characteristic length can be either the Bloch domain size (magnetic properties), or the Bohr exciton radius (optical properties), or the electron mean free path (plasmonic properties). Thence, quantum confinement regime offers the revolutionary possibility to control and tailor the materials' properties by acting on their size and shape.

Conventionally, Quantum Dots (QDs) are defined as semiconductor nanocrystals, in which the photo-generated electron-hole wavefunctions experience a three-dimensional quantum confinement effect. These bound electron-hole pairs, or excitons, stem as the leading actors of optical properties in semiconductor materials and their pivotal role is further emphasized in QDs. Indeed, the spatial localization of excitons results in size-dependent optical transitions and enhanced carrier-carrier interactions.

Albeit their size bridges the gap between molecules and solids, it is largely misleading to consider QDs as mere halfway between molecular and solid state worlds. Indeed, they display entirely unique photophysical properties, such as strong coupling with electromagnetic radiation and completely different energy relaxation mechanisms.

These properties fueled a burgeoning research field, puzzling material scientists, chemists and physicists for up to 25 years. The unceasing interplay between synthesis, characterization and device implementation contributed in uncovering much of the physics behind QDs properties. A crucial difference between QDs and conventional materials emerges when considering their sensitivity to surface defects. Albeit thermodynamics favors the absence of volume defects, QDs' photophysics appears to be primarily driven by dangling bonds at surfaces that may act as trap sites (i.e., surface traps) for excited charge carriers. Exciton-trap interactions are detrimental for optical properties of QDs and hamper their implementation in operating devices.

The introduction of core-shell heterostructures is a landmark in the struggle against exciton and carrier traps. Epitaxial growth of an inorganic shell proved to be an efficient way to enhance emission efficiency and stability of QDs. One of the most significant challenges in this field was to achieve complete trap passivation to attain near-unity emission efficiencies. Up to 95% quantum yield (PLQY) was obtained using sophisticated heterostructures (Giant Shell and Multi Shell QDs).

Unfortunately, this increase in heterostructures variety and complexity left many open questions about the underlying photophysics. The interaction of surface traps with unrelaxed excitons (hot excitons or hot carriers, in case that excess energy overtakes exciton binding energy), the effect of long-lived charged states (trions) on PLQY, and the relaxation dynamics of trions in different core-shell heterostructures are among most important open questions. In Chapters 3 and 4 these questions are tackled from a spectroscopic and modeling point of view. Specifically, the measurement of PLQY excitation profiles allows delving deeper into the energetics of carrier trapping. The resulting picture reveals an essential connection, which bridges the energetics and the dynamics of this detrimental process. Also, the introduction of global analysis techniques, in deciphering transient absorption spectroscopy results, allowed overcoming spectral crowding issues and directly visualizing fast recombination processes, which were only hypothesized by PLQY analysis.

Nevertheless, the other side of the coin for inorganic shelling is the contextual isolation of excitons not only from surface traps but also from other dots, when QDs are cast into films. This aspect is fundamental when dealing with applications that may require either charge transport, or exciton dissociation, or exciton migration. A quest for the best compromise between passivation and accessibility of electronic states is thereby animating current research in QDs science.

As mentioned above, the core-shell technology can overcome main issues hampering the application of QDs in devices.

Namely, thwarting exciton trapping processes to achieve higher emission efficiencies and slowing down exciton recombinations to achieve gain and inversion in QDs media. These advances are crucial for applications concerning light-emission such as QDs-based light-emitting devices (QD-LEDs). Nonetheless, many other promising applications require interactions between QDs' excitons and other materials. For instance, QDs-based Solar Cells (QDSCs) and photo-catalytic applications are based on charge transfer processes, thereby requiring an overlap between wavefunctions, hindered by inorganic shells. QDs-based lasers (QDs-Lasers) would profit of collective sharing of excitation between QDs in hierarchical QDs superlattices, as well. Therefore, developing new strategies to engineer QDs interaction is of utter importance. In Chapter 5, a surface chemistry-based solution is proposed for CdSe/CdS QDs-PCBM systems. Specifically, the interaction between QDs charge donors and acceptors is tailored and strengthened by taking advantage of a simple ligand exchange procedure.

Whilst conventional semiconducting materials such as Si, Ge, GaAs, were studied in QDs form, a substantial part of this thesis (i.e., Part I) is focused on CdSe QDs and related heterostructures. Indeed, owing to both historical and practical reasons CdSe QDs stemmed as archetypal systems in the QDs community. The historical reason traces back to the inception and discovery of QDs, by Aleksei Ekimov, Sasha Efros, and Louis Brus, who pioneered this field studying experimentally and theoretically CdSe-doped glasses. On the other hand, the practical reasons foster the eventual application of QDs. Indeed, the valuable combination of CdSe bulk band gap (1.75 eV) and exciton Bohr radius (~ 6 nm) allows obtaining sharp and bright emission peaks throughout the entire visible range, by directly acting on nanocrystals' size. Also, the facile colloidal synthesis endows QDs with solution processability, low size-dispersion (down to 5%) and a high crystallinity. Despite being studied for more than 25 years, CdSe still draws much attention within the scientific community. This interest can be explained considering its archetypal role as a photophysical playground. Indeed, most of the strategies developed for boosting CdSe QDs optical performances can also be extended to other materials. Nonetheless, this necessarily implies a parallel research on different materials, possibly overcoming issues affecting CdSe (e.g., toxicity and restriction to the visible range). Thus, an equally considerable part of this thesis (i.e., Part II) focuses on the application of theories developed and concepts discovered in Part I.

The employment of different metal cations, within II-VI chalcogenides family, gives access to different regions of the electromagnetic spectrum: from mid-infrared (Hg) to near-infrared (Pb), to UV (Zn). Nevertheless, the quest for heavy-metal free QDs shifted attention towards other materials and phases, such as III-V (e.g., InP) and ternary (e.g., CuInS2).

In recent years, the concepts underlying QDs physics have been extended towards non-conventional materials, such as Nowotny-Juza phases, two-dimensional transition metal dichalcogenides (TMDC), graphene, carbon and hybrid organic-inorganic perovskites. This resulted in the emergence of a wide variety of novel nanostructures. Consequently, many efforts are focused on providing the necessary photo-physical characterization of these novel materials and follow the lucrative synergy between synthesis and characterization established by CdSe QDs. In Chapters 6, some aspects of the optical properties of carbon dots (CDs) and lead-bromide perovskites dots (PDs) are discussed.
CDs are an emerging class of carbon nanomaterial, currently drawing increasing attention, as witnessed by the growing number of publications. These carbon nanoparticles display a long track record of desirable properties, thereby ensuing a burgeoning interest aimed to replace inorganic semiconductor-based QDs. CDs are cheap and made up of earth-abundant materials. Moreover, they display peculiar and intriguing photophysical properties, such as excitation- and size-dependent emission spectra. Lastly, they are biocompatible and exhibit low cytotoxicity, hence are widely investigated for in vivo applications. Specifically, in Chapter 8, the hidden face of CDs optical properties is discussed, with a focus the role of fluorescence by small molecules. There reported discoveries pose some serious questions on the very nature of CDs, which is mandatory to consider whenever original CDs synthesis are proposed.
Since the early 2010s, hybrid organic-inorganic perovskites (HPs) took the scientific community by storm. The interest sparked by unprecedented high power conversion efficiencies based on HPs encouraged scientists to delve deeper into their photophysics. HPs revealed to be a wonderland for physicists and materials scientists, thanks to the wealth of uncommon and intriguing photophysical effects, such as Rashba splitting, strong polaronic effects, and band-gap renormalization effects. As the natural course of new material, current research is taking them to the nanoscale. In analogy with conventional semiconductors, exciting physical facets emerge when miniaturization of hybrid perovskites reaches the nanometer scale. First reports of PDs revealed superior optical emission properties, as well. In Chapter 9, the photophysics of a series of PDs is investigated, and central questions are tackled by a spectroscopic approach. Specifically, these materials were studied by applying concepts developed for CdSe QDs. With a twofold aim, this investigation both unveiled some unknown aspects of PDs photophysics (e.g., the presence of trapping/de-trapping equilibrium) and posed new questions for further work on trapping mechanisms and hot-carrier relaxations.

OUTLINE OF THE THESIS

This thesis is divided into two main parts :

Part I deals with an in-depth investigation of fine details of the photophysics of archetypal CdSe-based core-shell QDs. This part comprises five chapters. After introducing the theoretical background (**Chapter 1**), the materials and methodologies (**Chapter 2**), the question of hot carrier trapping is addressed in **Chapter 3**. Experimentally, this critical process is studied using PLQY excitation profile measurements. These measurements provide a "photoaction" spectrum, in which is possible to mine information on the energetics of trapping process. Previous work by Bozio et al. provided the theoretical basis for interpreting the results, which are here adapted and extended to bridge dynamics and energetics of trapping. The portrayal of a comprehensive picture for trapping processes requested the postulation of photophysical processes, such as fast trion Auger recombinations. In **Chapter 4**, these processes are investigated by transient absorption spectroscopy. The untangling of these data, using global analysis procedures, allowed obtaining values for the non-radiative time constant that nicely fit into the developed model. Accordingly, in these first chapters, a complete photophysical scenario for CdSe-based core/shell QDs is depicted.

In **Chapter 5**, the issue of the interaction between QDs excited states and other material is tackled by a surface chemistry perspective. The interaction between the most promising systems studied in previous Chapters (from a photovoltaics perspective), and charge acceptors are tailored by ligand exchange reactions. Using a combination of different spectroscopic techniques (in collaboration with other groups) the complex interaction between QDs and charge acceptors is investigated on a broad timescale.

Part II deals with the photophysics of novel quantum confined materials, i.e., CDs and PDs. In **Chapter 6**, the development of these nanostructures is traced back from a historical perspective. This approach allowed emphasizing the underlying ideas and possible pitfalls in their development. Also, **Chapter 7** introduces materials and methodologies used. The characterization of CDs photophysics is provided in **Chapter 8**. Beyond conventional characterization, the compelling evidence for inhomogeneity driven optical properties is tackled using fluorescence correlation spectroscopy. This uncommon spectroscopic technique reveals the molecular nature of CDs emission, thereby posing the urgency for ratiocinations of the development of these nanostructures.

In **Chapter 9**, the characterization of PDs is carried on by employing concepts developed in the previous Part. The analysis of the photoluminescence uncovers the persisting trapping/de-trapping equilibrium, influenced by band edge energy of PDs. Furthermore, hot carriers trapping is revealed, and its importance is further emphasized by preliminary results reporting slow carrier cooling rates.

PART I:

The $CdSe/Cd_xZn_{1-x}S$ QDs series

CHAPTER 1

The Physics and Chemistry of Quantum Dots

ABSTRACT- Semiconductor quantum dots (QDs) owe their central role in nanoscience both to a peculiar electronic structure and to a flexible surface chemistry. The synthesis of these nanostructures requires ad-hoc synthetic strategies, borrowed from colloidal chemistry methodologies. Colloidal synthesis techniques exploit coordinating ligands to address the reaction towards desired shape, dimension, and dimensionalities. Thus, also considering the high surface-to-volume ration, their chemistry is driven by surface sites: the passivation of these sites through capping ligands determines the quality of QDs optical properties, their stability, and addresses their excited state interactions. The interactions between surface sites and ligands are analogous to that of metal coordination compounds, and their description relies on Lewis acid-base theory.
By their intermediate size regime, between molecules and solids, novel theoretical physical constructs are needed bridging these two worlds. Much of the new physics underlying QDs intriguing performances stems from the confinement effect, i.e., electronic wavefunctions are enclosed in a volume smaller than they occupy in bulk material. The spatial confinement endows QDs with strong coupling to the electromagnetic field, thereby enhancing and fostering their optical properties. Thence, *excitons* i.e., bound electron-hole pairs to become leading players of the optical properties and their interaction with the surfaces becomes of paramount importance.
In the following, a comprehensive explanation of QDs surface chemistry and electronic structure is provided. These concepts give access to the description of some well-established aspects of the excitation dynamics in both isolate and interacting environment. Specifically, the case of CdSe QDs is discussed, however much of the physics and chemistry described here has been successfully translated to other materials.

1.1 Synthesis and Surface Chemistry of QDs

This part of the thesis focuses on colloidal semiconductor QDs, synthesized by colloidal chemical routes. These nanostructures consist of an inorganic nano-crystalline core, surrounded by a layer of organic ligands. Ligands increase the stability of the colloidal solution, avoiding aggregation of the nanocrystals, and contribute to the electronic passivation of surface dangling bonds.

The typical semiconductor QDs systems present sub-10nm diameter, with very narrow size distributions (<5%). These strict requirements can be satisfied by precise colloidal synthetic techniques. The QDs studied in this thesis, i.e., all the QDs presented as $CdSe/Cd_xZn_{1-x}S$ series were synthesized and characterized from a structural point of view by Prof. Jaiseniak at CSIRO (Solution-Processed Inorganic Optoelectronics group, Ian Wark Laboratory, Clayton, Australia) using hot-injection method and SILAR techniques. For the sake of completeness, the synthetic approaches used by Prof. Jasieniak are briefly reviewed in the following pages.

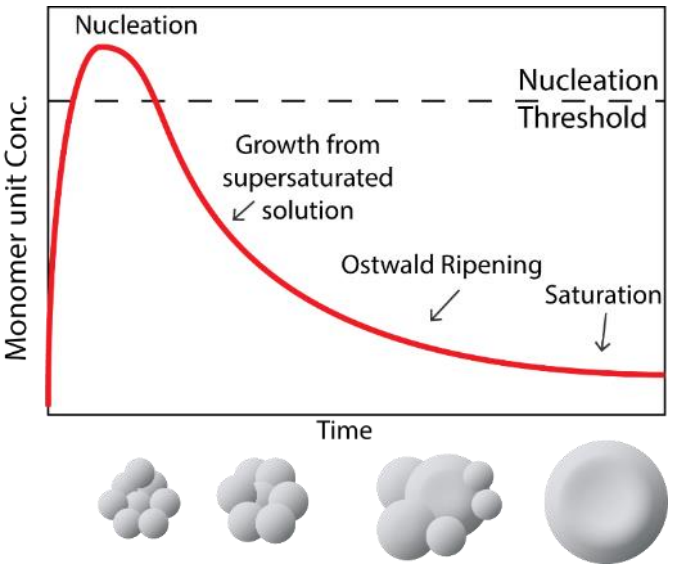

Figure 1.1 - Schematic illustration of colloidal nanoparticles growth according to the LaMer-Dinegar model. The starting point is the injection of precursors, which generate monomer units. During the nucleation phase, the supersaturated solution reaches the nucleation threshold, and first nuclei become stable. The progressive nucleation lowers the monomer concentration below the critical threshold. This marks off the nucleation from growth phases. When monomer concentration is relatively high, the small nuclei grow in a diffusion-limited aggregation process. Nevertheless, upon depletion of monomers, a competitive growth regime gains importance. This is known as Lifshitz-Slyozov-Wagner growth or Ostwald ripening and contributes to obtaining narrow size dispersion at the cost of having coarser nanoparticles. The production of the sharpest supersaturation profile, as well as the temporal separation of nucleation and growth phases, are fundamental in achieving extremely small-sized nanoparticles with narrow size dispersions.

Albeit the pioneering work by Brus and Henglein paved the way to the research on QDs, first proposed synthesis could not achieve sufficient crystallinity, monodispersity and emission efficiency.[1-3] The history of colloidal QDs synthesis is hinged on three significant revolutions.

The *hot-injection* method, introduced by Bawendi's group in 1993, was the first ground-breaking advance in this field, yielding unprecedented high-quality nanostructures.[4] This method is based on the pyrolysis of metalorganic precursors in high boiling point solvents with organic coordinating molecules. LaMer-Dinegar model of nanoparticles growth (Figure 1.1) readily explains the fundamental concept underlying this synthetic approach.[5-7] During this synthesis, a sharp supersaturation profile is produced by a quasi-instantaneous pyrolysis of the precursors in hot solvent. Following this, the coordination equilibrium of organic molecules drives the growth of small nanocluster into nanocrystalline cores. Bawendi's work proposed the synthesis of *cadmium chalcogenide* QDs (CdX; X = S, Se, Te) using dimethyl cadmium as a metal precursor; and phosphine selenide/Telluride, or bistrimethylsilyl sulfide as the chalcogenide source. Trioctylphosphine (TOP) and trioctylphosphine oxide (TOPO) served both as the solvent and coordinating molecules.[4] Very high synthesis temperatures (~ 300 °C) allowed obtaining both high crystallinity and narrow size dispersion. Thus, by controlling the reaction temperature, the particle size could be tuned in the range 12–115 Å.

Unfortunately, the organometallic precursors used in Bawendi's synthesis were extraordinarily toxic and pyrophoric. Therefore, the second revolution was the introduction of less hazardous precursors, such as cadmium salts. In 2001, Peng introduced air-stable CdO as the Cd precursor.

Compared to dimethyl-cadmium compounds, CdO is less toxic and more stable in ambient conditions.[8] Noteworthy, this precursor yielded CdX nanocrystals (NCs) of high quality, comparable to that of the best results reported by the organometallic method. The exclusion of organometallic cadmium has the advantage of avoiding strongly air-sensitive chemicals from the synthesis, enabling NCs to be prepared without using a glovebox, representing an essential step toward green-chemistry synthesis of CdX NCs.[9]

Despite their high crystallinity, the intrinsic defectivity of NCs surfaces hampered their performances.[10-11] The inherent undercoordination surface atoms leads to unsaturated dangling bonds and substantial reconstructions of atomic positions. The energy levels corresponding to dangling bond orbitals lie within or in the proximity to the forbidden region between the electronic band gaps of bulk solids. These states are commonly referred as *trap-states* and have a profound influence on excited states dynamics of either negative (electron trap) or positive (hole trap) carriers.

Surface passivation, i.e., raising the coordination number of surface atoms, is a necessary step given each potential application of QDs. The standard strategy was based on the above-mentioned organic ligands. Indeed, the Lewis acid-base equilibrium with surface sites saturates the coordination of surface atoms. Nevertheless, some issues affect this approach: due to steric hindrance between ligands a non-negligible amount of traps is not passivated and organically passivated QDs exhibited limited photo-stability.[12]

The third revolution in QDs history was the introduction of core-shell (CS) heterostructures. Within this approach, the epitaxial growth of a wider-gap material shell is used as surface passivation strategy. [13] The inorganic shell passivates both anionic and cationic trap sites and provides increased photo-stability. To achieve a complete passivation of the surface, many critical parameters need to be balanced in the choice of shell material, i.e., the lattice mismatch between core and shell and the potential barrier for photoexcited carriers. [14]

The lattice mismatch between core and shell material critically determines the improvement of optical properties by shelling. Indeed, different crystallographic parameters between the core and the shell can lead to unintended strain at the interface. The accumulation of elastic energy at the interface can affect the degree of epitaxial growth and results in the nucleation of interface defects. The effect of interface defects on the optical properties will be widely discussed in Chapter 4.[15]

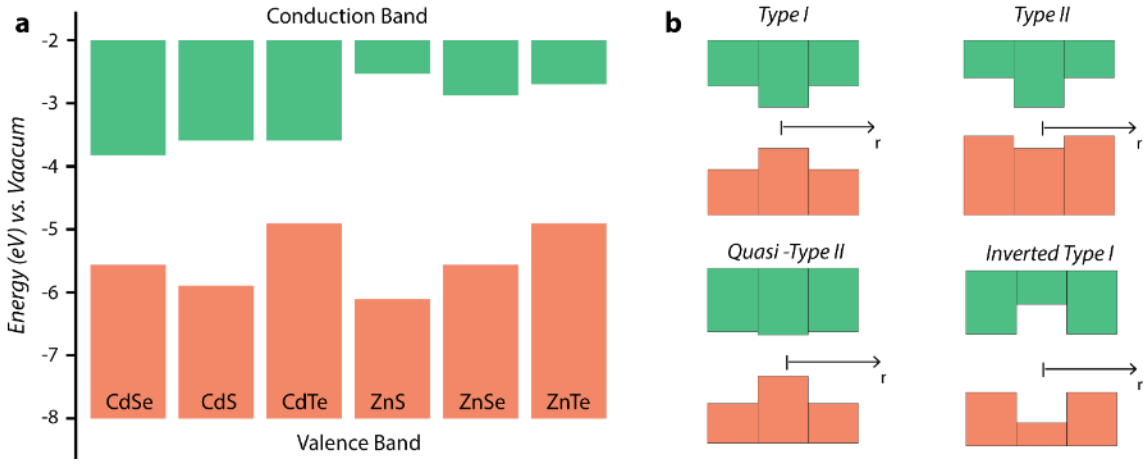

Figure 1.2- (**a**) Band edge electronic energy levels for most widely employed semiconducting materials in colloidal QDs field. Green rectangles indicate the conduction band (CB), orange rectangles indicate the valence band (VB). (**b**) Band alignment in different heterostructure type. In Type I heterostructures the minimum of CB and maximum of VB are located in the core. In Type II heterostructures, the minimum of CB and maximum of VB are not located in the same spatial region. In quasi-Type II heterostructures, the offset of CB minima is smaller than thermal energy, or vice-versa. In inverted Type I heterostructures, the minimum of CB and maximum of VB are located in the shell.

CS heterostructures offer additional electronic tunability due to band-edge alignment at the hetero-interface. In Figure 1.2**a** are reported the band-edge levels of most widely employed semiconductor materials. Conventionally, considering the band-edge alignment, we can classify CS-QDs either as *Type-I* or *Type-II heterostructures* (Figure 1.2**b**).[13-14, 16]

In Type-I heterostructures, the CB and VB of the shell material wrap those of the core. CdSe/ZnS is the most famous example of Type-I CS-QDs. In this configuration, photo-excited carriers experience an additional confining potential that localizes them inside the core, thereby diminishing the probability of interaction with surface sites and enhancing the emission efficiency.

Type-II heterostructures present a staggered band alignment (Figure 1.2**b**). The asymmetry of the potential felt by photo-excited carriers (i.e., the lowest energy states for electrons and holes are in different semiconductors) induces the formation charge-transfer excitons. This configuration is particularly interesting for photodetection and photovoltaic applications.

The synthetic strategies for growing CS-QDs profoundly evolved and refined since first experimental reports by Guyot-Sionnest and others.[17-18] Two fundamental prerequisites for obtaining high-quality CS-QDs are the narrowing of size distribution and minimization of shell material self-nucleation. These are usually achieved using different synthesis, such as SILAR or cation exchange procedures. In the following, only SILAR procedure is discussed, for reviewing other synthetic approaches the reader is referred to review articles (Refs. 12,17).

Successive Ion Layer Adsorption and Reaction (SILAR) was a synthetic procedure initially developed for thin films. In 2003, Peng successfully applied this approach to CdSe/CdS QDs. Peng's procedure starting point are crystalline core QDs.[19] This synthesis is based on the growth of one monolayer in turn, via the alternate introduction of cationic and anionic precursors into the solution of core QDs. The combination of SILAR technique and many different post-synthesis treatments allowed obtaining near-unitary emission efficiencies CS-QDs, for instance in CdSe/CdS QDs.[20-21]

Significant drawbacks of the core-shell approach in solving trap-related issues are: (i) the alteration of the carrier density of individual core NCs and (ii) the barrier to electron transport dynamics between NCs. These aspects are critically important when the possible application of QDs are envisioned. Indeed, many of the possible application of QDs, ranging from light emitting to lasing to photo-catalysis, rely on assembled and interacting QDs systems. [22-23] Given these applications, the surface passivation with capping ligands gained much attention over last years.

Albeit the colloidal synthetic procedures inherently endows as-synthesized QDs with capping ligands such as carboxylic acids, amines, and phosphines, an entire library of ligands can be introduced by ligand exchange reaction.[24-25] A variety of capping ligands was explored for the surface passivation of QDs, generally pursuing the achievement of both obtaining complete surface passivation and preserving the possibility of coupling QDs carriers with the outside environment. To this extent, the surface chemistry of QDs plays a pivotal role in enhancing some specific features of QDs.[17] Recently, Owen adapted previous theories developed for metal coordination complexes [26] to categorize capping ligands according to their interaction with surface atoms. Within this model, three classes of metal-ligand interactions are characterized based on the number of electrons involved, and the identity of the electron donor and acceptor groups. According to this, we can distinguish between *L-type*, *Z-type* and *X-type* ligands. [24]

L-type ligands are neutral two-electron donors with an electron lone pair, which is datively coordinated to surface metal centers (e.g., alkylamines ($R-NH_2$), organo-phosphines (PR_3), and organo phosphine oxides ($O=PR_3$)).

X-type ligands are one electron donor, having an odd number of valence-shell electrons. Therefore, they require borrowing an additional electron from the QD surface site to form a covalent bond. This surface chemistry often results in heterolytic cleavage, yielding closed shell ionic species formation. From a chemical point of view, X-type ligands can be either neutral radicals species or monovalent ions binding oppositely charged sites at the surface (e.g., carboxylates ($R-COO^-$), thiolates ($R-S^-$), and inorganic ions (Cl^-, S_2^-, SnS_4^{4-}). Inorganic ions emerged as particularly important ligands in view of photovoltaic and optoelectronic application, owing to the enhanced interaction between QDs in superlattices favored by their atomic size.

According to Lewis acid-base theory, both L- and X-type ligands are basic. These nucleophilic (electron-rich) ligands bind to electrophilic (electron-deficient) sites at QDs surface, typically undercoordinated metal sites exhibiting pronounced Lewis acidity. On the other hand, electron-deficient ligands are commonly referred as Z-type ligands. This category encompasses metal salts and complexes (e.g., $M(COOR)_2, MCl_2$) which bind to surface chalcogenides atoms as electron lone pair acceptors. [14, 24]

By this theoretical framework, ligand exchange reactions are described in a way reminiscent of substitution reactions in coordination complexes. Both kinetics and mechanism of ligand exchange reactions are mainly driven by solvent polarity and coordinating ability. Moreover, the steric crowding at surfaces implies the necessity for ligands to unbind from surfaces, before new ligands can bind.

In nonpolar solvents, electrical neutrality is strictly required for all species involved.[24] Hence, L-type ligands can rapidly absorb and desorb at room temperature. Conversely, X-type ligands remain tightly bound to the surface, because of the electrostatic charging induced by their self-desorption. Therefore, a direct ligand X to L ligand exchange is highly unfavorable due to charge neutrality related issues. All these aspects need to be kept in consideration when attempting to exchange ligands at surfaces. Moreover, ligand exchange procedures comprise also solid-state ligand exchange procedures; Owen and Talapin developed complete theories for these ligand exchange reactions.[24-25]

1.2 The electronic structure of QDs

The simplest way to describe the electron energy states of QDs is based on the particle-in-a-sphere (PIS) model. Through this model, introduced by Efros and Brus in early 1980s, the electronic structure of QDs is described qualitatively, and interband absorption properties are successfully explained.[1, 27-29]

Nevertheless, many relevant effects are ignored in this model, e.g., valence band mixing, surface states and real shape of QDs. Although completely accurate atomistic approaches such as empirical pseudopotential method (EPM)[30] and ab initio methods have been elaborated throughout years, their discussion is beyond the scope of this thesis. Here, we review PIS and effective mass approach (EMA).[31-32] The EMA approach was proposed by Bawendi and can be considered as a hierarchically superordinate of PIS approach, as it keeps into account the real band structure of CdSe.

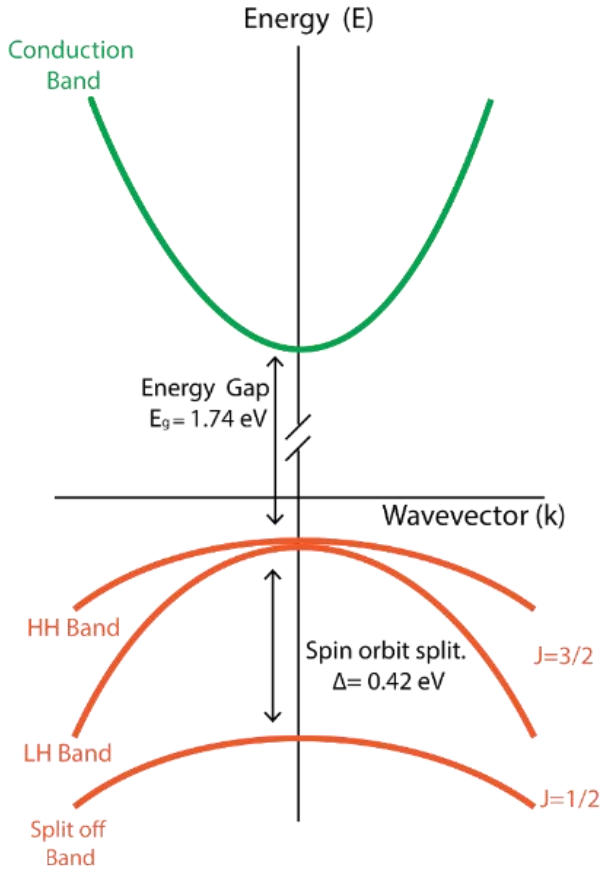

Figure 1.3- Band structure of bulk CdSe near the center of Brillouin zone. This material is a direct-gap semiconductor with both CB minimum and VB maximum at Γ point. The conduction band (green line) mainly arises from Cd 5s empty orbitals, resulting in conduction electrons with effective mass $m_e^*=0.11m_0$. The valence band presents main contributions from Se 4p orbitals and displays higher complexity due to 6-fold degeneracy. Spin-orbit coupling splits these bands, by their total angular momentum J. Heavy hole (HH) band (effective mass $m_h^*= 1.14m_0$) lies at higher energies, with angular momentum (J=3/2, J_z=±3/2). Light hole (LH) band (effective mass $m_h^*= 0.31m_0$) has angular momentum (J=3/2, J_z=±3/2). These two bands are nearly degenerate at Γ point, leading to band-mixing effects. Split-Off (SO) band (effective mass $m_h^*= 0.48m_0$) is shifted to higher hole energies by Δ=0.42eV and has angular momentum (J=3/2, J_z=±3/2). Further details on the band structure are reported in Ref. 31

The starting point is the near-edge electronic band structure of CdSe, reported in Figure 1.3. This comprises a conduction band and three valence bands, arising from Cd 5s and Se 4p orbitals respectively. These bands describe the possible combinations of energies and wavevectors values, which can be assumed by a single electron in the crystal, thereby identifying single-particle states. These single particle states infinitely extend over the crystal, according to Bloch theory. Nevertheless, the limited spatial extent of the nanocrystal prevents this and imposes the consideration of a confining potential.

Quantum confinement effects are applied in the envelope function formalism to every single band. Band mixing effect, induced by spatial confinement, are neglected at this level.[33] Other more sophisticated theories keep them into account.

The single particle states in a semiconductor crystal are obtained by solving Schrödinger equation with a periodic potential $U(\boldsymbol{r}) = U(\boldsymbol{r} + \boldsymbol{R})$. The equation reads

$$\left(\frac{-\hbar^2 \nabla^2}{2m} + U(r)\right)\psi(r) = E\,\psi(r) \qquad \textbf{(Eq. 1.1)}$$

where $\psi(\mathbf{r})$ is the single electron wavefunction. According to Bloch theorem, for an infinite crystal, this can be written as a plane wave modulated by a function with the periodicity of the crystal lattice.[34] Therefore, we can write solutions to Equation 1.1 as

$$\psi(r) = \phi(r)\,u(r) \qquad \textbf{(Eq. 1.2)}$$

where $u(\mathbf{r})$ is the above mentioned periodical function, which will resemble that of atomic orbitals in a semiconductor crystal. The most important part of the function in Eq. 1.2, when aiming to describe the electronic structure of QDs, is $\phi(\mathbf{r})$.[35] This function describes the contribution of each atomic orbital centered in different lattice sites and is called envelope function.

For an infinite crystal, as stated by Bloch theorem, the envelope function is a plane wave $\phi(\mathbf{r}) = e^{i\boldsymbol{k}\cdot\boldsymbol{r}}$. In the case of a QD, it encodes the information on finite extension of the nanocrystals, as well as on the symmetry of the electronic states. Therefore, the confining potential is considered to act on the sole envelope function, because the potential variation is so slow that it "feels" just a macroscopic average of the crystalline lattice.

As suggested by the name, EMA approach assumes isotropic and parabolic bands. The information on the complete band structure is contained in a single parameter, i.e., the effective mass m^*.[36]

These assumptions reduce the problem of solving an ordinary particle-in-a-sphere equation, written for the envelope function as

$$\left(\frac{-\hbar^2 \nabla^2}{2m^*} + V(r)\right)\phi(r) = E\,\phi(r) \qquad \textbf{(Eq. 1.3)}$$

where the potential term $V(\boldsymbol{r})$, in the simplest case of nanocrystals with radius a, is defined as

$$V(r) = \begin{cases} 0, & r \leq a \\ \infty, & r \geq a \end{cases} \quad \textbf{(Eq. 1.4)}$$

Nevertheless, this approach can be generalized to different shapes, e.g., nanorods, nano-tetrapods and to account for more complex systems, e.g., core-shell heterostructures (with shell thickness t) can be described by a potential

$$V_{CS}(r) = \begin{cases} 0, & r \leq a \\ \Delta V, & a < r \leq a + t \\ \infty, & r > a + t \end{cases} \quad \textbf{(Eq. 1.5)}$$

The solution to Eq. 1.4 for spherical QDs resemble hydrogenoid atoms wavefunctions. Yet the finite extension yields discrete eigenvalues and the spherical shape yields s, p, d,.. symmetries of the eigenfunctions. Mathematically, eigenfunctions can be factorized as product of a radial and an angular part,

$$\phi_{n,l,m}(r, \theta, \varphi) = R_{nl}(r) Y_l^m(\theta, \varphi) \quad \textbf{(Eq. 1.6)}$$

where the overall symmetry is determined by spherical harmonics $Y_l^m(\theta, \varphi)$ as for atomic wavefunctions, e.g. S-symmetry for l=0, P-symmetry for l=1 and so forth. l is the azimuthal quantum number and it is not restricted, resulting, for instance, in the existence of 1P and 1D states.[36]

The radial part of the envelope function (Eq. 1.6) can be expressed as $R_{nl}(r) = \frac{C}{r} j_l(k_{n,l}, r)$, where j_l are Bessel functions, different from that of atomic orbitals. The difference stems from the sources of the confining potential, i.e. a point charge in the origin for atomic orbitals, while an abrupt potential variation at r=a for QDs.

The corresponding eigenvalues, constituting the energy levels of electrons in QDs, are

$$E_{n,l} = \frac{\hbar^2 \alpha_{n,l}^2}{2Ma^2} \quad \textbf{(Eq. 1.7)}$$

where n is the principal quantum number and $\alpha_{n,l}^2$ are Bessel function roots. Noteworthy, this discrete energy spectrum depends on the dot size $E_{n,l} \propto a^{-2}$.

These discrete energy levels result in a different density of electronic states (DOS), depicted in Figure 1.4. The quantization of electronic motion, as result of the confinement, yields a squeezing of the conventional bulk DOS.

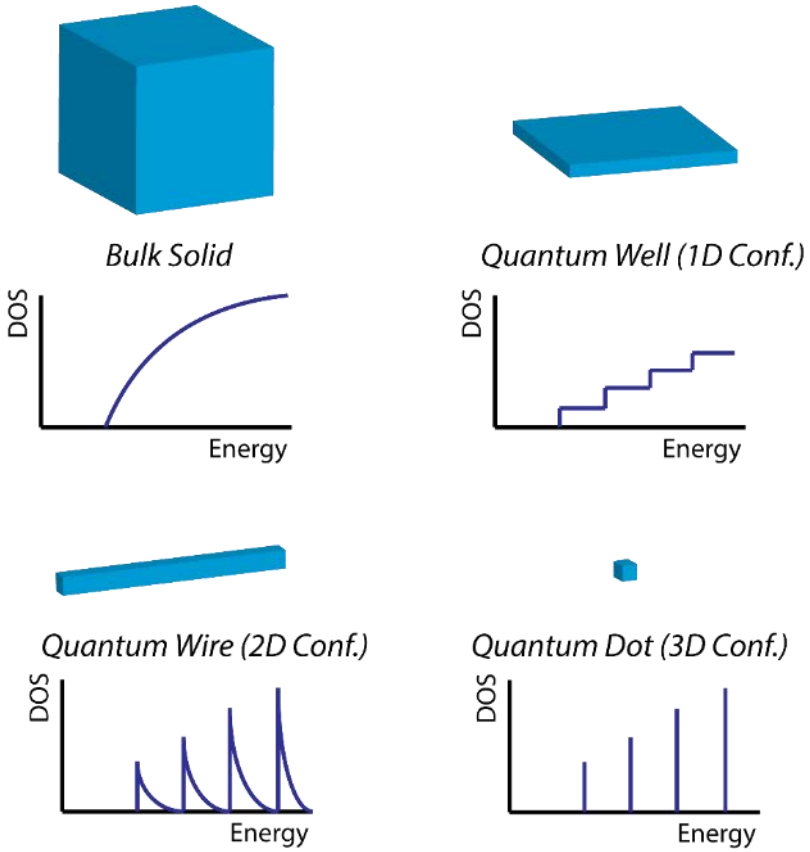

Figure 1.4 - Evolution of electronic density of states (DOS) upon reduction of dimensionality. In bulk solids, the DOS is a continuum and display a square-root growth on the energy. Quantum wells are two-dimensional systems, and their DOS is independent of energy within a given state. Once the upper state is reached, the DOS display a step-like growth. Quantum wires are monodimensional systems in which the DOS displays a singular reciprocal square-root behavior. Lastly, the DOS of quantum dots assumes non-negligible values at defined energy values.

Electrons in QDs experience three-dimensional confinement, which results in a discretized DOS, comprising Dirac's delta function peaked at discrete electron energy levels of Eq. 1.7

$$DOS(E)_{Bulk} \propto (E - E_{CB})^{1/2} \xrightarrow{3D\ Confinement} DOS(E)_{QD} \propto \delta(E - E_{n,l})$$

As reported in Figure 1.4, this theory is readily generalized to nanostructures with different dimensionalities: in quantum wires, two-dimensional confinement, i.e., $V(\boldsymbol{r}) = V(x, y)$, results in an inverse dependence on energy $DOS(E)_{QWire} \propto (E - E_c)^{-1/2}$. On the other hand, in quantum wells electrons experience one dimensional confinement potential, i.e. $V(\boldsymbol{r}) = V(x)$. The resulting 2D DOS is independent of energy of the states. The energetic distribution of the DOS dramatically affects the response of the electronic subsystem to external stimuli (electronic, magnetic, and optical). Indeed, the progressive reduction of dimensionality modifies the number of available states immediately above

the energy gap. Thence, this condensation of electrons in discrete states produces highly polarizable systems and is key to explaining the superior optical properties of QDs. [37]

The optical properties of QDs stem form transition between discrete electron energy levels, induced by the electromagnetic field. This interaction is mediated by two-particle bound states, i.e., electron-hole bound states commonly referred to as *excitons*.

Quantum confinement acts on excitons as well and profoundly modifies their energies. The consideration of the qualitative picture of the confinement strength is obtained comparing the intrinsic exciton Bohr radius a_{exc} and the size of the nanocrystals. The exciton Bohr radius quantifies the spatial extent of an exciton in the bulk material and is determined by the dielectric screening between the two particle and their relative velocities. Therefore, the exciton Bohr radius is given by

$$a_{exc} = \epsilon \frac{m}{m_e} a_B \qquad \textbf{(Eq. 1.7)}$$

where ϵ is the dielectric constant, m and m_e are electron rest and effective masses, and a_B is the Bohr radius. Almost all materials of interest present a_B of the order of tens of nanometers. Therefore, QDs are generally few-nanometer sized nanocrystals.

Excitons found themselves squeezed into nanocrystals to different extents. Aiming to quantify the magnitude of this squeezing, three quantum confinement regimes [36] were defined as:

1. Weak Confinement Regime $a_{exc} > a > a_e, a_h$
2. Intermediate Confinement Regime $a_e, a_{exc} > a > a_h$
3. Strong Confinement Regime $a_e, a_{exc}, a_h > a$

where a_e, a_h are single particle Bohr radii.

From a historical perspective, the weak confinement regime was the first quantum size effect studied in large nanocrystals. This is described by considering the quantum-size effect on the center-of-mass motion of the Wannier excitons for the bulk material, without considering any effect on electron and holes. Conversely, in the strong confinement limit excitons are squeezed in a smaller volume where confinement effects influence electron wavefunctions as well. Archetypal CdSe ($a_{exc} = 5.6nm$) nanocrystals fall in this regime.

In this case, the confinement energy ($\propto a^{-2}$) dominates over electron-hole Coulomb interaction energy ($\propto a^{-1}$). Accordingly, we can treat Coulombic term as a small perturbation to the quantum confined electron and hole energies.

The complete two-particle Schrödinger equation is

$$\left(-\frac{\hbar^2\nabla_e^2}{2m_e^*}-\frac{\hbar^2\nabla_h^2}{2m_h^*}+V(r_e)+V(r_h)-\frac{e^2}{\epsilon|r_e-r_h|}\right)\Psi_X(r_e,r_h)=E\Psi_X(r_e,r_h) \qquad \textbf{(Eq. 1.8)}$$

Using perturbation theory, the Coulomb interaction term can be treated as the first-order correction to excitonic energies. Therefore, the exciton wavefunction is given by the product of electron and hole single-particle wavefunctions:

$$\Psi_X(r_e,r_h)=\psi_e(r_e)\psi_h(r_h) \qquad \textbf{(Eq. 1.9)}$$

The resulting expression for the exciton energy is the sum of the band gap energy, the single-particle confinement energies, and the Coulomb interaction correction. The general expression is

$$E_{n_e,l_e,n_h,l_h}=\frac{\hbar^2}{2a^2}\left(\frac{\alpha_{n_e,l_e}^2}{m_e^*}+\frac{\alpha_{n_h,l_h}^2}{m_h^*}\right)-C\frac{e^2}{a\epsilon} \qquad \textbf{(Eq. 1.10)}$$

where eigenstates are labeled by the quantum numbers $n_h l_h$-$n_e l_e$. Each level is shifted in energy by a factor $\propto 1/a$, due to the Coulomb interaction. The C constant results from an integration of the Coulomb interaction over the position of electron and hole, as given by the single-particle envelope functions.

Using the simple EMA we can obtain a qualitative picture of quantum confinement, however quantum confinement energy is overestimated.[38] The size dependence of the band edge absorption strength will be quantitatively different for different semiconductor materials and different size ranges (even for the same material), because it is driven by a subtle balance between two relative contributions to the total exciton energy: quantum confinement energy and electron-hole Coulomb interactions. As mentioned above, more sophisticated models were developed to account for experimentally observed trends. According to the desired accuracy, different models can be used.[39]

Besides the size dependence of the energy gap, quantum confinement profoundly affects optical properties of nanocrystals. As discussed above, the bulk electronic DOS is redistributed and squeezed at discrete energies. The oscillator strength quantifies the magnitude of the interaction between the electronic system and the electromagnetic field.[40] The total interband oscillator strength f_{tot}, obtained by integrating over all the exciton states, depends on the interband matrix element per CdSe unit, $|\langle\psi_e|\boldsymbol{\varepsilon}\cdot\hat{\mathbf{p}}|\psi_h\rangle|$, and the number of units per QD.

Being this global matrix element determined by the chemical composition and the crystal lattice, it can be expected that f_{tot} per QD scales linearly with the QD volume. On the other hand, the quantum size effect modifies its distribution among different exciton states, according to the different DOS. Therefore, the increase in the electron-hole overlap and the peculiar DOS augment significantly the fraction of oscillator strength assigned to the lower lying exciton states.[37] The resulting strong coupling with light and constitute the basis for much of the interest sparked by QDs over the last years.

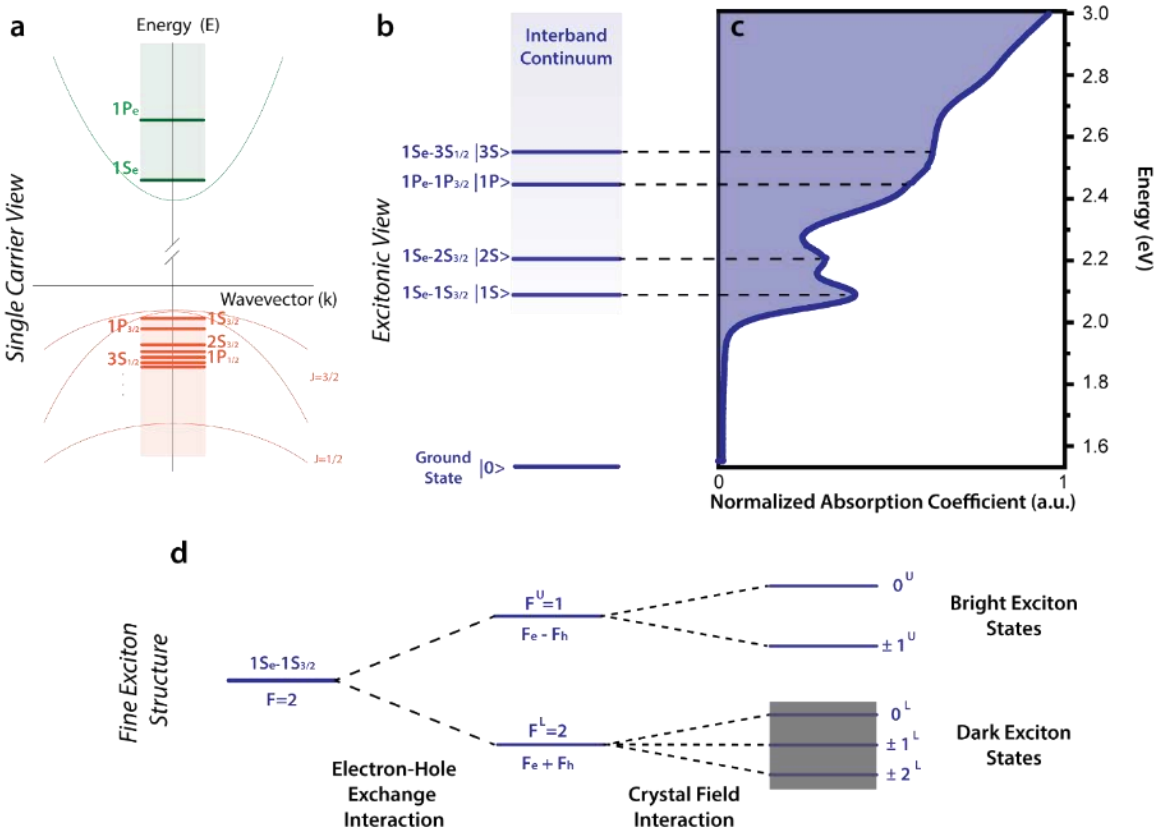

Figure 1.5- (**a**) Quantized electron (green) and hole (orange) states in a spherical CdSe quantum dot. Conduction band quantized states are classical particle-in-a-sphere states, with different symmetries (s,p,d,..). On the other hand, due to band mixing effects triggered by quantum confinement, the valence band produces a complicated and dense structure of hole quantized states. Electron levels are sparser than hole level mainly due to different effective masses (Eq. 1.3). (**b**) Single exciton states in a spherical CdSe QD, obtained by applying optical transition selection rules to ($\Delta n = 0$, $\Delta l = 0$) states described in **a** panel. (**c**) Interpretation of a real absorption spectrum for a CdSe QD with r=2.1nm, based on Refs. 4,33,41. (**d**) The lifting of degeneracies in the lower exciton manifold of CdSe QDs. The 8-fold degenerate |1S> exciton is split by exchange interactions into a 5-fold degenerate $F^L = 2$ state and a 3-fold $F^U=1$ state. (U and L superscripts distinguish between states with the same magnitude of the projection of angular momentum. Only the upper manifold is optically active., whereas the lower one is dark. Crystal field interactions further split these states, depending on the projection of angular momentum.

Also, the exciton binding energies E_X become size dependent and higher concerning those of Wannier-Mott excitons in bulk solids. Owing to this, excitons in QDs become stable at room temperature and gain a central role in the photophysics of these materials.

The probability of optical transition is quantified by the transition dipole moment, in excitonic view (Figure 1.5) $|\langle\Psi_{\mathbf{X}}|\boldsymbol{\varepsilon}\cdot\hat{\mathbf{p}}|0\rangle|^2$, evaluated between an exciton state and the ground state. The analysis of this matrix element yields selection rules ($\Delta n = 0$, $\Delta l = 0$) for transitions from the ground state. However, in order to explain many other aspects of QD photo-physics, such as Stokes shift and the exciton fine structure a more detailed description of the band structure need to be considered.[41]

The richness of CdSe band structure was the starting point for the pioneering work by Bawendi et al., who was first to successfully assign the optical spectrum of CdSe QDs.[33] As mentioned above, Bawendi relaxed one of the assumptions underlying PIS/EMA model. Although the starting point was the separate calculation of electron and hole energy levels, they introduced *valence band mixing* effects. As mentioned above, in this material, the VB arises from Se 4p orbitals and has a 6-fold degeneracy. The strong spin-orbit coupling $\Delta = 0.42$ eV splits the VB degeneracy in $p_{3/2}$ and $p_{1/2}$ at $\mathbf{k} = 0$. Moreover, away from this point, the $p_{3/2}$ is further split into light-hole (LH) and heavy-hole (HH) bands.

The consideration of mixing effects yielded complicated hole states, enclosing contributions from all three VBs. These states were referred as nL_M, where M is the total angular momentum, L the lowest envelope angular momentum contained, and n the band symmetry index. Applying selection rules to transitions between these states, the excitonic structure of CdSe was assigned as shown in Figure 1.5**b**.

The total quantum number for an excitonic state will have contributions from the atomic basis as well as the envelope function.[33, 41] The atomic basis is constituted by Cd 5s orbitals in CB and Se 4p orbitals in VB, therefore the azimuthal quantum numbers are $l_e = 0$ and $l_h = 1$. For the lowest energy exciton (*1S* exciton), the envelope function contribution is $L_e = L_h = 0$. Therefore, we can write the total quantum number for 1S exciton as, $F = F_e + F_h = (l_h + s + L_h) + (l_e + s + L_e) = 2$. The label notation used in Figure 1.5 is $1S_{1/2}\ 1S_{3/2}$, where the first part corresponds to the electron $n_e L_{eF_e}$ and the second to the hole $n_h L_{hF_h}$.

Delving deeper into the excitonic structure of CdSe QDs, the relaxation of spherical shape and cubic lattice approximations leads to the so-called *exciton fine structure*. The lifting of the eightfold degeneracy of the *1S* exciton state, due to crystal field and exchange interactions, results in six different manifolds, as shown in Figure 1.5**d**.

1.3 Energy Relaxation Pathways

Many different energy relaxation processes concur in limiting the lifespan of photo-generated excited states. Such processes become utterly important when envisioning possible applications, e.g., light-emitting devices, lasers, sensors and photo-catalytic reactions. Indeed, depending on the application purpose, energy relaxation processes can be either detrimental or fundamental.

In QDs at least three primary energy relaxation pathways need to be considered: *radiative recombination*, *trap-mediated recombinations,* and *Auger recombinations.*

In *Radiative recombination* process, an electron-hole pair is annihilated to generate the emission of one photon. Albeit lasers are based on stimulated emission, in which this recombination is promoted by a high-intensity photon field, spontaneous emission is more common. Fermi Golden Rule, applied to light-matter interaction, determines the radiative rate. Quantitatively,

$$k_r = \frac{2\pi}{\hbar}|V|^2\,\rho \qquad \textbf{(Eq. 1.11)}$$

where V is the transition dipole moment operator, $|V|^2 = |\langle \Psi_{\mathbf{X}}|\boldsymbol{\varepsilon}\cdot\hat{\mathbf{p}}|0\rangle|^2$ and ρ is the exciton density of states.

Emission process is tightly related to light absorption, as described by Einstein A and B coefficients. According to this, the radiative rate (k_r) is related to oscillator strength (f) as

$$k_r \propto |f_{LF}|^2 f \qquad \textbf{(Eq. 1.12)}$$

where f_{LF} is the local field factor. Nevertheless, this relation applies to single oscillators Therefore; its practical use is hindered by inherent complexity of QDs systems.

Fine exciton structure splitting results into excited states described as a thermal population of different exciton levels, some of which have allowed (bright state) and some of which have forbidden (dark state) transitions to the ground state (Figure 1.5**d**). The resulting emission is therefore originated by a temperature-dependent distribution of states, each having its own oscillator strength and radiative rate. Thence, a comprehensive description of QDs emission (luminescence) requires the consideration of the exciton manifold inner dynamics.

When dealing with QDs, *trap-mediated recombinations* are one of the most crucial recombination processes. Traps owe their central role mostly to the high surface-to-

volume ratio in QDs. As discussed above, dangling bonds at surfaces results in a plethora of mid-gap states. Although different passivation techniques have been developed through the years, none of them allows achieving a complete elimination of trap-states. Passivation through capping ligands can be achieved through both electrophilic or nucleophilic ligands. As shown in Figure 1.6, the chemical bonding between the ligand and the surface site produces two new orbitals shifted from the gap. Generally, the use of a single molecule as ligand does not allow the complete passivation of both anionic and cationic sites. Moreover, steric crowding at surface prevents a complete surface coverage.

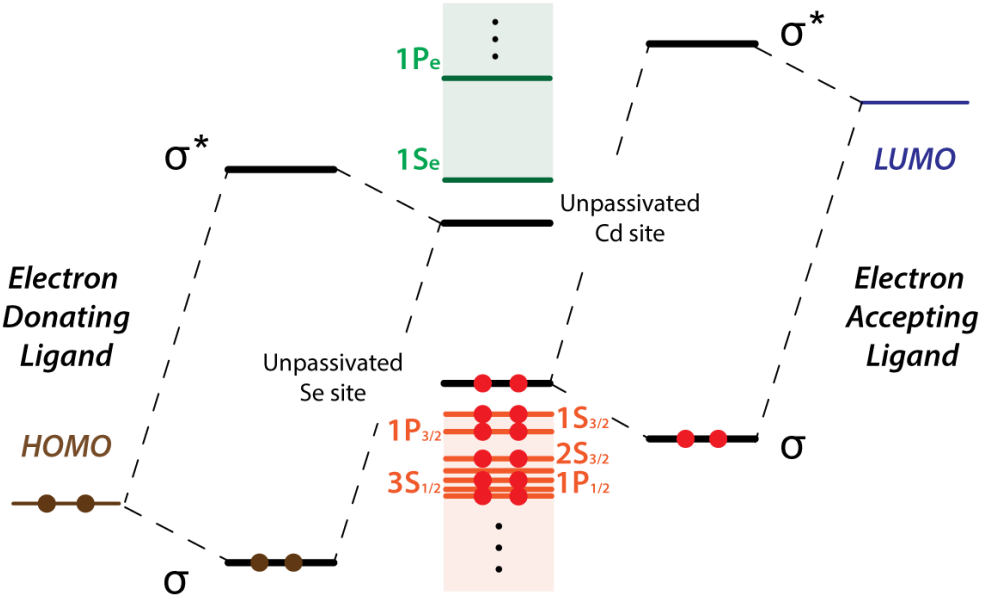

Figure 1.6 - Simplified view of electronic passivation of surface states by means of capping ligands. Due to the coordination number, surface Cd and Se sites generate energy levels that lay in the midgap. The interaction either with the highest occupied molecular orbital (HOMO) of a nucleophilic ligand or with the lowest unoccupied molecular orbital (LUMO) of an electrophilic ligand results in electronic passivation. Upon chemical bonding formation, two newly resulting orbitals are pushed back into the state manifold.

Yet, passivation through inorganic shell present some drawbacks as well. Due to the nucleation of interface defects and low barrier potentials issues, trap-mediated recombinations need to be also considered in CS QDs. This will be widely discussed in Chapters 3 and 4.

First experimental observations of trap-mediated recombination were based on low-temperature photoluminescence (PL) measurements. In early studies, the presence of a broad and red-shifted emission band was associated with a distribution of mid-gap trap states. Accordingly, trap-mediated recombinations could be either Read-Hall-Shockley processes, assisted by ligands vibrational coupling, or trap-states radiative recombinations. In recent years, Kambhampati and Scholes groups challenged this view, redefining trap states as strongly coupled surface states.

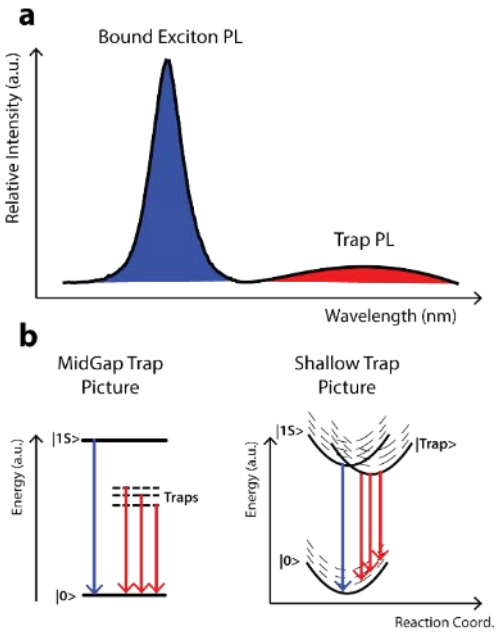

Figure 1.7 - (**a**) Typical emission profile from highly defective QDs. PL lineshape comprises a sharp and intense peak (blue area) assigned to emission from core |1S> excitons. Moreover, the broad and red-shifted peak is assigned to radiative recombination from trap states, e.g., recombination from charge-transfer excitons. (**b**) Comparison between two different models adopted for describing trap energetics and dynamics in QDs. The "midgap trap" picture invokes a broad distribution of deep trap states, located in the midgap. The "shallow trap" picture is based on a semiclassical electron-transfer model (Marcus-Jortner model). Within this model, traps are located nearby the band edge, and the red-shift is caused by strong vibrational coupling. Many experimental pieces of evidence confirmed the validity of this latter model, which is therefore adopted in this thesis.

The resulting model, referred to as *trapping model*, was based on shallow trap-levels interacting with bound excitons through charge-transfer processes. As depicted in Figure 1.7, this model allows explaining essential features of trap-mediated recombination without invoking mid-gap trap states. Within this model, trap-states are dynamical in nature, owing to the microscopic reversibility of trapping process. This is the main peculiarity of trap-mediated recombination dynamics: traps do not behave as infinitely long-living charge accumulators, but rather de-trapping is energetically favored at room temperature. De-trapped charges can radiatively recombine, with a delay that is coherent with the long stretched PL decays observed. Long living charged states, mainly localized on the surface, are the principal source for single QD PL blinking and Auger non-radiative recombination. This consideration justifies why so much effort is spent to improve localization of excitons far from the dot surface defects.

In QDs, phonon-based energy relaxation mechanisms are hindered by energy levels modification: larger energy levels spacing would require multi-phonon relaxation mechanisms, whose probability is low. This effect is known as "phonon bottleneck". Albeit this relaxation channel loses its efficiency, Auger recombination gains importance in zero-dimensional systems. Auger processes are defined as inelastic scattering involving

excited carriers. As depicted in Figure 1.8**a**, in bulk semiconductors momentum conservation requires the emission of phonons, thereby resulting in low probabilities for this process. The breaking of translational invariance (see Eq. 1.3) relaxes this constraint, further introducing a size-dependent scaling for its efficiency. Therefore, Auger recombination (AR) stems from main intraband exciton relaxation process in QDs. Namely, all excited states but the lowest lying suffer from fast AR. During intraband AR process Figure 1.8**d**, the scattering of a hole by an excited electron results in the non-radiative transfer of excess energy to the hole. Indeed, due to the high density of the valence band states, many hole transitions are in resonance with the electron intraband transitions. The resulting excited hole state relaxes through coupling with phonons, thanks to the smaller spacing between energy levels. This process is referred to the cooling of *hot-excitons* (i.e., excitons with excess energy).

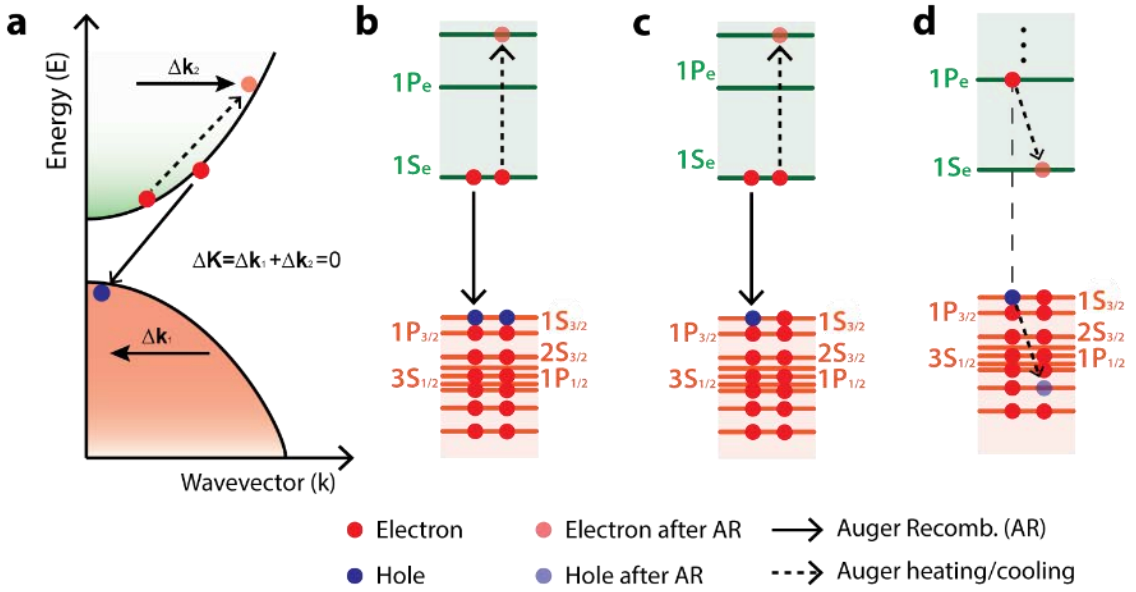

Figure 1.8- (**a**) Auger recombination process in bulk semiconductors. This is a three particle process, which dominates recombinations in high injection regime. The recombination energy of the first electron-hole pair is transferred to a third carrier. The periodicity of the crystal potential requires the entire process to satisfy crystal quasi-momentum (k) conservation. Therefore, this process results in phonon emission. (**b**) Multi-exciton Auger recombination in QDs. Carrier-carrier scattering results in the transfer of energy from an excited electron-hole pair to a third carrier involved in an exciton state. During this process, a biexciton state is transformed into a single hot-exciton state (i.e., exciton with excess energy). (**c**)Trion Auger recombination in QDs. Analogously to multi-exciton recombination, the electron-hole pair energy is transferred to a third free-carrier. (**d**) Intraband Auger recombination in QDs. An excited electron transfers its energy to a hole. The electron cooling results in a hole heating.

AR processes are critical when dealing with multi-excitons and trions as well. Physically, in this process, the electron-hole recombination energy is transformed into kinetic energy for a third photoexcited carrier.

Multi-excitons are bound states between two excitons, generated by the sequential absorption of two photons. Multi-exciton AR is the dominant relaxation mechanism whereby a bi-exciton relaxes to a single-exciton state. This scales with the average exciton

concentration per dot <*N*>. Thence, AR is generally much faster than the multi-exciton radiative recombination rate. Limiting Auger recombination and consequently achieving efficient multi-exciton light emission is the grail in QDs-lasing field.

Trions are charged excitons, i.e., a three particle bound excited state comprising an exciton, which interacts with a free carrier. Their recombination follows an analogous scheme as that of multi-excitons. As a result, trion lifetimes are limited to hundredth of picoseconds.

Summarizing, the unusual aspects of both QDs physics and chemistry profoundly alter the dynamics of excitations in these nanostructures. Driven by interests arose by QDs applications, much of the recent research in this field is pursuing the circumvention of trap- and Auger related issues. The struggle against efficient non-radiative recombinations is taken by a careful design and engineering of the nanostructures.

References

1. Brus, L. E., Electron-Electron and Electron-Hole Interactions in Small Semiconductor Crystallites: The Size Dependence of the Lowest Excited Electronic State. *The Journal of Chemical Physics* **1984**, *80*, 4403-4409.

2. Henglein, A., Photo-Degradation and Fluorescence of Colloidal-Cadmium Sulfide in Aqueous Solution. *Berichte der Bunsengesellschaft für physikalische Chemie* **1982**, *86*, 301-305.

3. The Many Aspects of Quantum Dots. *Nat Nano* **2010**, *5*, 381-381.

4. Murray, C. B.; Norris, D. J.Bawendi, M. G., Synthesis and Characterization of Nearly Monodisperse CdE (E = Sulfur, Selenium, Tellurium) Semiconductor Nanocrystallites. *Journal of the American Chemical Society* **1993**, *115*, 8706-8715.

5. LaMer, V. K.Dinegar, R. H., Theory, Production and Mechanism of Formation of Monodispersed Hydrosols. *Journal of the American Chemical Society* **1950**, *72*, 4847-4854.

6. Mer, V. K. L., Nucleation in Phase Transitions. *Industrial & Engineering Chemistry* **1952**, *44*, 1270-1277.

7. Baronov, A.; Bufkin, K.; Shaw, D. W.; Johnson, B. L.Patrick, D. L., A Simple Model of Burst Nucleation. *Physical Chemistry Chemical Physics* **2015**, *17*, 20846-20852.

8. Peng, X.; Manna, L.; Yang, W.; Wickham, J.; Scher, E.; Kadavanich, A.Alivisatos, A. P., Shape Control of CdSe Nanocrystals. *Nature* **2000**, *404*, 59-61.

9. Peng, Z. A.Peng, X., Formation of High-Quality CdTe, CdSe, and CdS Nanocrystals Using Cdo as Precursor. *Journal of the American Chemical Society* **2001**, *123*, 183-184.

10. Kalyuzhny, G.Murray, R. W., Ligand Effects on Optical Properties of CdSe Nanocrystals. *The Journal of Physical Chemistry B* **2005**, *109*, 7012-7021.

11. Kern, S. J.; Sahu, K.Berg, M. A., Heterogeneity of the Electron-Trapping Kinetics in CdSe Nanoparticles. *Nano Letters* **2011**, *11*, 3493-3498.

12. Smith, A. M.Nie, S., Semiconductor Nanocrystals: Structure, Properties, and Band Gap Engineering. *Accounts of Chemical Research* **2010**, *43*, 190-200.

13. Reiss, P.; Protière, M.Li, L., Core/Shell Semiconductor Nanocrystals. *Small* **2009**, *5*, 154-168.

14. Jang, Y., et al., Interface Control of Electronic and Optical Properties in Iv-Vi and Ii-Vi Core/Shell Colloidal Quantum Dots: A Review. *Chemical Communications* **2017**, *53*, 1002-1024.

15. Todescato, F.; Minotto, A.; Signorini, R.; Jasieniak, J. J.Bozio, R., Investigation into the Heterostructure Interface of CdSe-Based Core-Shell Quantum Dots Using Surface-Enhanced Raman Spectroscopy. *ACS Nano* **2013**, *7*, 6649-6657.

16. Todescato, F.; Fortunati, I.; Minotto, A.; Signorini, R.; Jasieniak, J.Bozio, R., Engineering of Semiconductor Nanocrystals for Light Emitting Applications. *Materials* **2016**, *9*, 672.

17. Peng, X.; Wickham, J.; Alivisatos, A. P. Kinetics of II-VI and III-V Colloidal Semiconductor Nanocrystal Growth: "Focusing" of Size Distributions *J. Am. Chem. Soc.* **1998**, 120, 5343– 5344

18. Hines, M. A. ,Guyot-Sionnest, P., Synthesis and Characterization of Strongly Luminescing ZnS-Capped CdSe Nanocrystals. *The Journal of Physical Chemistry* **1996**, *100*, 468-471.

19. Li, J. J.; Wang, Y. A.; Guo, W.; Keay, J. C.; Mishima, T. D.; Johnson, M. B.Peng, X., Large-Scale Synthesis of Nearly Monodisperse CdSe/CdS Core/Shell Nanocrystals Using Air-Stable Reagents Via Successive Ion Layer Adsorption and Reaction. *Journal of the American Chemical Society* **2003**, *125*, 12567-12575.

20. Saha, A.; Chellappan, K. V.; Narayan, K. S.; Ghatak, J.; Datta, R.Viswanatha, R., Near-Unity Quantum Yield in Semiconducting Nanostructures: Structural Understanding Leading to Energy Efficient Applications. *The Journal of Physical Chemistry Letters* **2013**, *4*, 3544-3549.

21. Greytak, A. B.; Allen, P. M.; Liu, W.; Zhao, J.; Young, E. R.; Popovic, Z.; Walker, B. J.; Nocera, D. G.Bawendi, M. G., Alternating Layer Addition Approach to CdSe/CdS Core/Shell Quantum Dots with near-Unity Quantum Yield and High on-Time Fractions. *Chemical Science* **2012**, *3*, 2028-2034.

22. Ustinov, V. M., *Quantum Dot Lasers*; Oxford University Press, 2003.

23. Robel, I.; Kuno, M.Kamat, P. V., Size-Dependent Electron Injection from Excited CdSe Quantum Dots into TiO2 Nanoparticles. *Journal of the American Chemical Society* **2007**, *129*, 4136-4137.

24. Boles, M. A.; Ling, D.; Hyeon, T.Talapin, D. V., The Surface Science of Nanocrystals. *Nat Mater* **2016**, *15*, 141-153.

25. Anderson, N. C.; Hendricks, M. P.; Choi, J. J.Owen, J. S., Ligand Exchange and the Stoichiometry of Metal Chalcogenide Nanocrystals: Spectroscopic Observation of Facile Metal-Carboxylate Displacement and Binding. *Journal of the American Chemical Society* **2013**, *135*, 18536-18548.

26. Owen, J., The Coordination Chemistry of Nanocrystal Surfaces. *Science* **2015**, *347*, 615-616.

27. Ekimov, A. I.; Efros, A. L.Onushchenko, A. A., Quantum Size Effect in Semiconductor Microcrystals. *Solid State Communications* **1993**, *88*, 947-950.

28. Efros, A. L.; Rosen, M.; Kuno, M.; Nirmal, M.; Norris, D. J.Bawendi, M., Band-Edge Exciton in Quantum Dots of Semiconductors with a Degenerate Valence Band: Dark and Bright Exciton States. *Physical Review B* **1996**, *54*, 4843-4856.

29. Ekimov, A. I.; Hache, F.; Schanne-Klein, M. C.; Ricard, D.; Flytzanis, C.; Kudryavtsev, I. A.; Yazeva, T. V.; Rodina, A. V.Efros, A. L., Absorption and Intensity-Dependent Photoluminescence Measurements on CdSe Quantum Dots: Assignment of the First Electronic Transitions. *J. Opt. Soc. Am. B* **1993**, *10*, 100-107.

30. Wang, L.-W.Zunger, A., Pseudopotential Calculations of Nanoscale CdSe Quantum Dots. *Physical Review B* **1996**, *53*, 9579-9582.

31. Norris, D. J.Bawendi, M. G., Measurement and Assignment of the Size-Dependent Optical Spectrum in CdSe Quantum Dots. *Physical Review B* **1996**, *53*, 16338-16346.

32. Kambhampati, P., Unraveling the Structure and Dynamics of Excitons in Semiconductor Quantum Dots. *Accounts of Chemical Research* **2011**, *44*, 1-13.

33. Norris, D. J.; Efros, A. L.; Rosen, M.Bawendi, M. G., Size Dependence of Exciton Fine Structure in CdSe Quantum Dots. *Physical Review B* **1996**, *53*, 16347-16354.

34. Ashcroft, N. W.Mermin, N. D., *Solid State Physics*; Holt, Rinehart and Winston, 1976.

35. Klimov, V. I., *Nanocrystal Quantum Dots, Second Edition*; Taylor & Francis, 2010.

36. Delerue, C. J.Lannoo, M., *Nanostructures: Theory and Modeling*; Springer Berlin Heidelberg, 2013.

37. Prasad, P. N., *Nanophotonics*; Wiley, 2004.

38. de Mello Donegá, C.Koole, R., Size Dependence of the Spontaneous Emission Rate and Absorption Cross Section of CdSe and CdTe Quantum Dots. *The Journal of Physical Chemistry C* **2009**, *113*, 6511-6520.

39. A.A. Efros and, A. L. E.Rosen, M., The Electronic Structure of Semiconductor Nanocrystals. *Annual Review of Materials Science* **2000**, *30*, 475-521.

40. Gong, K.; Zeng, Y.Kelley, D. F., Extinction Coefficients, Oscillator Strengths, and Radiative Lifetimes of CdSe, CdTe, and CdTe/CdSe Nanocrystals. *The Journal of Physical Chemistry C* **2013**, *117*, 20268-20279.

41. Klimov, V. I., Spectral and Dynamical Properties of Multiexcitons in Semiconductor Nanocrystals. *Annual Review of Physical Chemistry* **2007**, *58*, 635-673.

CHAPTER 2

Materials and Methods.1

ABSTRACT- In this chapter, both the material studied and the main optical spectroscopy techniques employed throughout this part of the work are presented. Specifically, here are provided both the theoretical basis and the experimental setups for each technique and methodology. The discussion for each technique is marked out specifically for quantum dots (QDs). Thus, peculiarities for the study of QDs by means of these techniques are highlighted. In particular, steady-state absorption and PL quantum yield determination methods were employed to study the hot exciton dynamics (Chapter 3). Transient absorption spectroscopy has been employed in determining fast recombinations (Chapter 4) and studying excited state interaction process of QDs (Chapter 5). In addition, the synthesis and the optical properties of the bare core and CS QDs, belonging to the CdSe/$Cd_xZn_{1-x}S$ series are briefly summarized, being these samples the focus of following Chapters.

2.1 Steady State Absorption Spectroscopy

Linear absorption measurements were performed in the Uv-Visible (200-800nm) range, using a Varian Cary-5000 spectrometer. All spectra were recorded from diluted QDs colloidal solutions in organic solvents (chloroform, toluene), using 1 cm square quartz cuvettes. The nature and the assignment of each absorption feature observed for CS QDs are discussed in the previous Chapter and further described in Section 2.4. Steady-state absorption spectroscopy probes efficiently the excitonic response in quantum-confined systems. Furthermore, absorption spectra give access to quantitative information about average sizes, as well as size dispersion, and absorption cross sections.[1]

2.2 Photoluminescence Quantum Yield

Photoluminescence quantum yield (PLQY) measurements allow quantifying the photon conversion efficiency for a fluorophore. Albeit absolute PLQY determination methods are becoming more common, the relative determination is indubitably the most reliable approach in determining PLQY with high accuracy.[2]

This method is based on steady-state PL spectroscopy. Accordingly, PL spectra were recorded using a FluoroMax-P (Jobin-Yvon) fluorimeter. Samples were highly diluted QDs colloidal solutions in organic solvents (chloroform, toluene) in 1 cm square quartz cuvettes. Recorded spectra were corrected for scattering. Typical PL spectra of QDs consist of a sharp peak, shifted by few tenths of meVs from the absorption edge.[3] As discussed in Chapter 1, highly defective samples could present a broad and red-shifted emission band due to trap-state radiative recombination.[4]

PLQY is defined as the ratio between the number of photons emitted (ϕ_{em}) and the number of photons absorbed (ϕ_{abs}). Furthermore, in two-level system approximation, it is related to radiative (k_r) and non-radiative constants (k_{nr}).

Thence, the standard definition of PLQY is

$$PLQY = \frac{\phi_{em}}{\phi_{abs}} \approx \frac{k_r}{k_r + k_{nr}}. \qquad \textbf{(Eq. 2.1)}$$

Consequently, Eq. 2.1 states that non-unitary PLQY values are associated with the presence of non-radiative recombination mechanisms for the excited state. Although recombination of QDs excited states is generally dominated by trapping processes,[5] as discussed in the previous chapter, the role of different photophysical species will be discussed in Chapter 3. Indeed, different dots in a QDs ensemble happen to exhibit different emission efficiencies, reducing PLQY to an averaged parameter.[6] Further complications arise from the PL blinking effect, which makes the single dot QY randomly intermittent.[7] Moreover, the dynamical nature of trap-states will demand a redefinition of PLQY for QDs (see Chapter 4).

PLQY was determined using the relative methodology introduced by Vavilov [8] and readapted by Crosby and others [2, 9] In this experiment, PLQY of the studied sample is determined with respect to that of a reference standard with known PLQY. Experimentally, the steady-state absorption and PL spectra of sample and reference samples were recorded from very diluted QDs solutions in organic solvents.

Thence, the PLQY of the sample ($PLQY_x$) is defined as

$$PLQY_x = PLQY_{ref}\left(\frac{A_{ref}(\lambda_{ref})}{A_x(\lambda_x)}\right)\left(\frac{I(\lambda_{ref})}{I(\lambda_x)}\right)\left(\frac{E_x}{E_{ref}}\right)\left(\frac{n_x}{n_{ref}}\right)^2 \qquad \textbf{(Eq. 2.2)}$$

where $PLQY_{ref}$ indicates the PLQY of the reference standard. The number of absorbed photons is quantified by $A(\lambda)$ and $I(\lambda)$ parameters, which are absorbance of the solution and the relative intensity of the exciting light at wavelength λ, respectively. The E parameter quantifies the number of emitted photons and can be estimated by the integrated area under the scattering-corrected PL spectrum. Lastly, dielectric effects are considered by means of average refractive index of the solution n.

Many assumptions underlie the Vavilov model: (i) direct proportionality between the integrated PL intensity and to the fraction of absorbed light, (ii) identical reflection effects and geometrical factors in the two measurements (iii) monochromatic excitation beams (iv) minimal reabsorption and reemission effects.[9] A careful minimization of errors was undertaken through some experimental expedients.

Accordingly, the sample and reference solutions were prepared with identical and low (<0.15) absorbance, in order to both minimize the reabsorption effects and excite an

analogous number of molecules. Moreover, reabsorption and reemission were applied to measured parameters. The number of absorbed photons was considered proportional to $(1\text{-}10^{-AL/2})$ instead of merely AL, where L is the optical path of the cuvette and $L/2$ is the thickness of the excited sample. The reabsorption of the emitted photons was corrected through Lambert-Beer. This was done by dividing the measured PL spectrum for the same attenuation factor $10^{-AL/2}$. The magnitude of these corrections can be estimated as high as 10% for samples with low absorbances.

In this thesis, most common fluorescence reference standard were employed:

- Fluorescein in basic (pH=11) in H_2O (PLQY=96%) [10]
- Quinine sulphate (pH=2) in H_2O (PLQY=56%) [11]
- Rhodamine B in MeOH (PLQY=80%) [12]
- Rhodamine 6G in EtOH (PLQY=95%) [13]
- Coumarin 540A in H_2O (PLQY=44%) [14]

Errors and error bars of Fig. 3.7 and Table 3-I on PLQY values were estimated by repeated measurements and by application of the error propagation theory, respectively. An 10% error is consistent with literature reports on this method. Most important contribution to uncertainties stemmed from the determination of emitted photons.

2.3 Transient Absorption Spectroscopy

Transient Absorption (TA) spectroscopy, also known as pump and probe (P&P) spectroscopy, was employed both to monitor the intrinsic excited state dynamics of CS QDs (Chapter 4) and the interaction dynamics between quantum dots and PCBM (Chapter 5). In addition, some preliminary results on novel materials (perovskite dots) are reported at the end of Chapter 9.

TA technique allows investigating the photophysics of the condensed matter systems, ranging from molecular to bulk solid systems.[15-17] This is done by introducing a perturbation, in a controlled and reproducible way, and monitoring the response of the systems.

By definition, TA spectroscopy is a third-order non-linear (NL) spectroscopy technique, in which two laser pulses, called “pump” and “probe” hit the sample, thereby generating a non-linear response. The pump pulse generates an excited state in the sample, which is monitored at different time delays by the probe pulse. This experiment allows measuring ultrafast dynamics by using a femtosecond laser as light source. Indeed, the time resolution is not dictated by the detector nor by electronics but rather depends on the pulse duration.

The theoretical background for a rigorous description of TA experiments relies on time-dependent perturbative theory to light-matter interaction, within the density matrix

formalism. Accordingly, TA is a *four-wave mixing* experiment, involving the generation and detection of a third-order NL polarization $\mathbf{P}^{(3)}(t) = \chi^{(3)}\,\mathbf{E}^{3}(t)$, where the superscript (3) indicates the perturbative third order.[18]

Nevertheless, as far as concerns this thesis the interpretation of TA experiments and datasets does not require invoking the fully detailed theoretical treatment, based on non-linear optics description. Albeit $\mathbf{P}^{(3)}$ can, in principle, contain contributions from many NL photophysical processes. Yet most of these processes take place during pump and probe pulse overlap in time. Hence, in our experiment these processes are observed in a sharp signal, at zero time delay, called *coherent spike*. Among them, main processes are stimulated Raman scattering, self-phase modulation, two-photon absorption, pump-perturbed free induction decay. [18]

Yet when the two pulses are well-separated in time, i.e., in the so-called *incoherent regime*, only one term survives. This so-called *population* term and is a direct manifestation of third-order NL processes. Nonetheless, it is possible to embody the entire third-order susceptibility formalism in *time-dependent population* terms, thereby treating the NL response term into an effective linear one.[18,19]

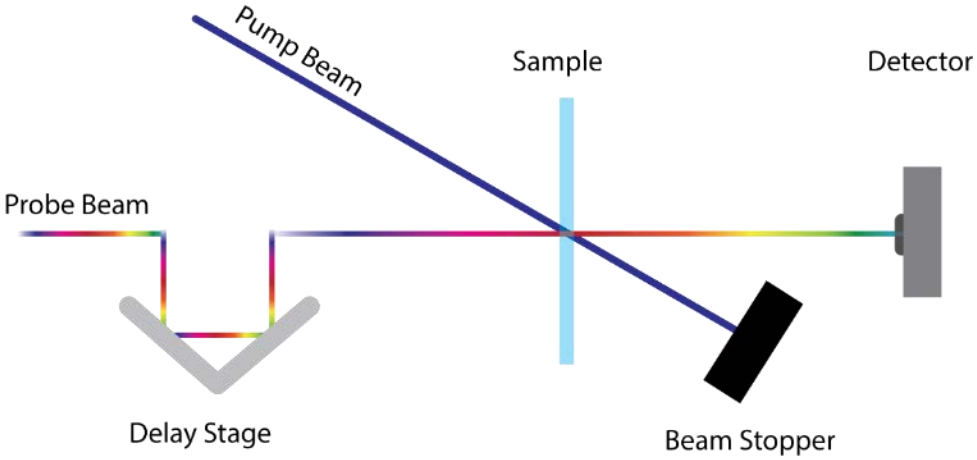

Figure 2.1 - The heart of transient absorption spectroscopy. The pump beam (in this case, a frequency doubled Ti:Sapphire laser output) impinges on the sample, generating an excited state. The probe beam (supercontinuum white light pulse) follows a longer optical path and therefore is time-delayed. The probe beam hit the sample, spatially overlapping with the probe beam. Thus the excited region of the sample is probed.

A scheme reporting the basic TA experiment is reported in Figure 2.1. Pump and probe pulses spatially overlap in the sample, whereas the time delay is controlled by a delay stage. Hence, variations in probe transmittance are measured as a function of the time delay.

The detected signal is represented as: [18]

$$\Delta A = A^{*} - A \qquad \textbf{(Eq. 2.3)}$$

where A^* and A are absorbance of the sample measured with and without the pump interaction, respectively. Absorbance is related to measured transmittance (T), through the relation $A = -log_{10}\, T$, where the transmittance is related to the absorption coefficient (α) and sample length L via relation $T = e^{-\alpha L}$.

The absorption coefficient encloses the whole information on the sample, is defined as:

$$\alpha = \sum_{k,l} \sigma_{k,l}(\lambda)\,(N_k - N_l) \qquad \textbf{(Eq. 2.4)}$$

where N_k and N_l are populations of *m- and l-* state, respectively.[19] $\sigma_{k,l}$ is the absorption cross section, which quantifies the strength of light-matter interaction for a transition between these two states (e.g., either an electron and a hole state in *single particle view* or the ground state and one exciton state in *excitonic view*, details in Chapter 2). It is worth to note that in TA experiments, the cross section is defined as an effective one, enclosing a negative sign for downward transitions is.[18,19] Microscopically, this quantity is tightly bound to oscillator strength and transition dipole moment quantities, described in previous chapter.

The pump pulse interaction generates a non-equilibrium excited state in the sample, thereby yielding a redistribution among the populations of different states inside the sample. Considering an *m-th* state (e.g., an exciton state in a QD): the pump interaction drags the population N_m out of equilibrium

$$N_m^*(t) = N_m + \Delta N(t). \qquad \textbf{(Eq. 2.5)}$$

The probe pulse hit the excited sample after a time delay τ and detects an absorbance variation defined as [19]

$$\Delta A(\lambda,\tau) = -log\left(\frac{\int I_{probe}(\lambda, t-\tau)\, exp(-\sum_{m,l}\sigma_{m,l}(\lambda)\,\Delta N_m(t)L)\; dt}{\int I_{probe}(\lambda,t)\, dt}\right) \qquad \textbf{(Eq. 2.6)}$$

In Eq.2.6 the detected signal is intertwined with intensity and temporal profile of the probe beam $I_{probe}(t)$. Fortunately, in the limit of low intensities and very short pulses it is possible to de-convolve this contribution.

Therefore, the resulting expression for the detected signal is

$$\Delta A(\lambda,\tau) = \frac{1}{2.3}\sum_{m,l}\sigma_{m,l}(\lambda)\,\Delta N_m(t) L \otimes f_{probe} \qquad \textbf{(Eq. 2.7)}$$

where f_{probe} is the temporal profile of the probe beam. Eq. 2.7 exemplifies the full potential of TA spectroscopy in studying excited state dynamics of nanomaterials. Given the probe temporal profile and the knowledge of the absorption cross section, a TA measurements is directly related to the relaxation of excited state populations $\Delta N_m(t)$. Notably, such knowledge is of paramount importance for every possible application of QDs in optics and optoelectronics field.

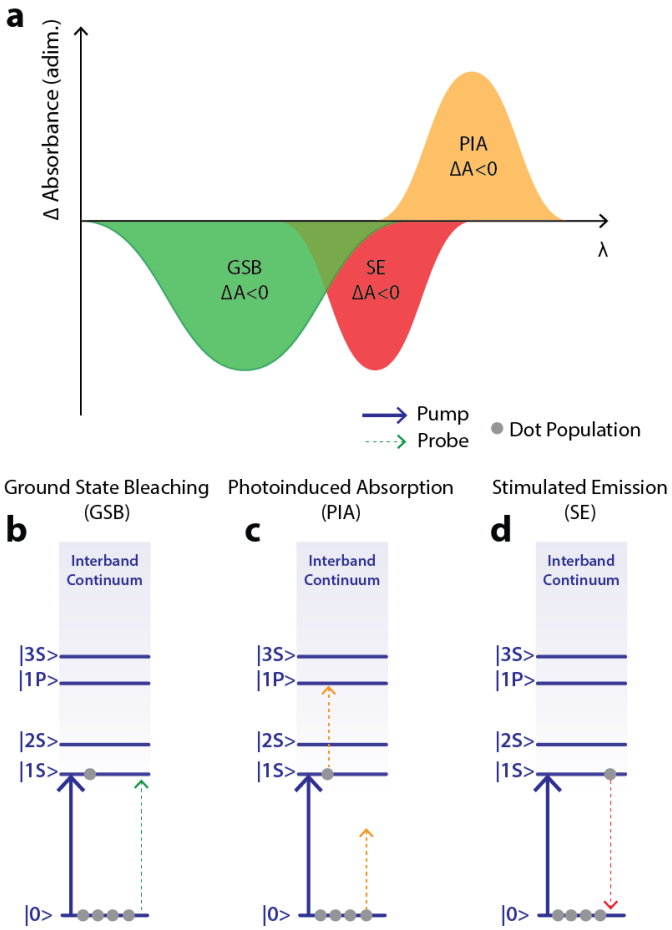

Figure 2.2 - (**a**) Spectral distribution of transient absorption signals generated by processes described in Panel **b**,**c**,**d**. (**b**) Ground state bleaching signal generated by optical pumping of the |1S> exciton state. The decrease of the number of dots in the ground state result diminishes the absorbance. This results in a negative Δ*A* signal peaked at the |1S> absorption wavelength, as reported in Panel **a** (**c**) Description of the photoinduced absorption process. Excited states can access new transitions, therefore the absorbance of the probe is augmented in certain spectral regions (Panel **a**) (**d**) Description of the stimulated emission process induced by optical pumping of |1S> state. The emitted photon contributes in reducing detected absorbance. Being a emission process, the negative Δ*A* signal is slightly redshifted with respect to the bleaching.

$\Delta A(\tau)$ curves are commonly referred as pump&probe transients, whereas the simultaneous measurement of these transients at different wavelength constitute a transient absorption spectrum $\Delta A(\lambda, \tau)$. As shown in Figure 2.2, three different physical processes results in a $\Delta A(\lambda)$ signal: *ground state bleaching* (GSB), *excited state/photoinduced absorption* (ESA/PIA) and *stimulated emission* (SE). [20]

Considering a quantum dot ensemble (e.g., a solution of QDs), the pump pulse interaction promotes fraction of the dots from the ground state to an excited state. In Figure 2.2, the $|0\rangle \Rightarrow |1S\rangle$ transition is considered as pump transition.

The GSB signal originates from the contextual depletion of the ground state dot population and the increasing of the excited state population. Hence, the ground-state absorption in the excited sample is diminished with respect to that of the non-excited sample. Consequently, a negative $\Delta A(\lambda)$ signal is observed in the wavelength region corresponding to the ground state absorption.

The ESA signal reflects the possibility that optically allowed transitions from the excited (populated) states of a dot to higher excited states may exist in specific wavelength regions, and absorption of the probe pulse at these wavelengths will occur. Consequently, a positive $\Delta A(\lambda)$ signal in the wavelength region of excited-state absorption. As discussed in the previous chapter, differently from molecular chromophores, QDs do support multiple excitation in the same dot, e.g. *multi-excitons*. Therefore, the final state of this process can be either a hot exciton state or a multi-exciton state. [21-22]

The SE signal originates the emission of one photon from an excited dot, induced by the probe beam light field. The SE photon is emitted in the same direction of the probe, hence is detected with it. Stimulated emission occurs only for optically allowed transitions and has a spectral profile resembling that of the PL spectrum, i.e., Stokes shifted with respect to the ground-state bleach.

TA experiments were conducted on a home-built setup wisely realized by Prof. Camilla Ferrante and Dr. Luca Bolzonello in the Laser Spectroscopy and Nanophotonics group at the University of Padova. The experimental setup is shown in Figure 2.3. The laser pulse generation is omitted in this scheme.

An amplified Ti:Sapphire femtosecond (fs) laser system is used as excitation source. This system comprises two central units: the seed laser system and an oscillator cavity.

A Spectra Physics Mai-Tai system is used as seed. This mode-locked Ti:Sapphire fs laser system embodies a Nd:YVO_4 laser (Millennia), used as pump system. The output beam is composed of ~120 fs pulses peaked at 806nm with 84 MHz repetition rate. The energy per pulse is quite low $\approx 5 - 10$nJ and would not result in detectable TA signals.

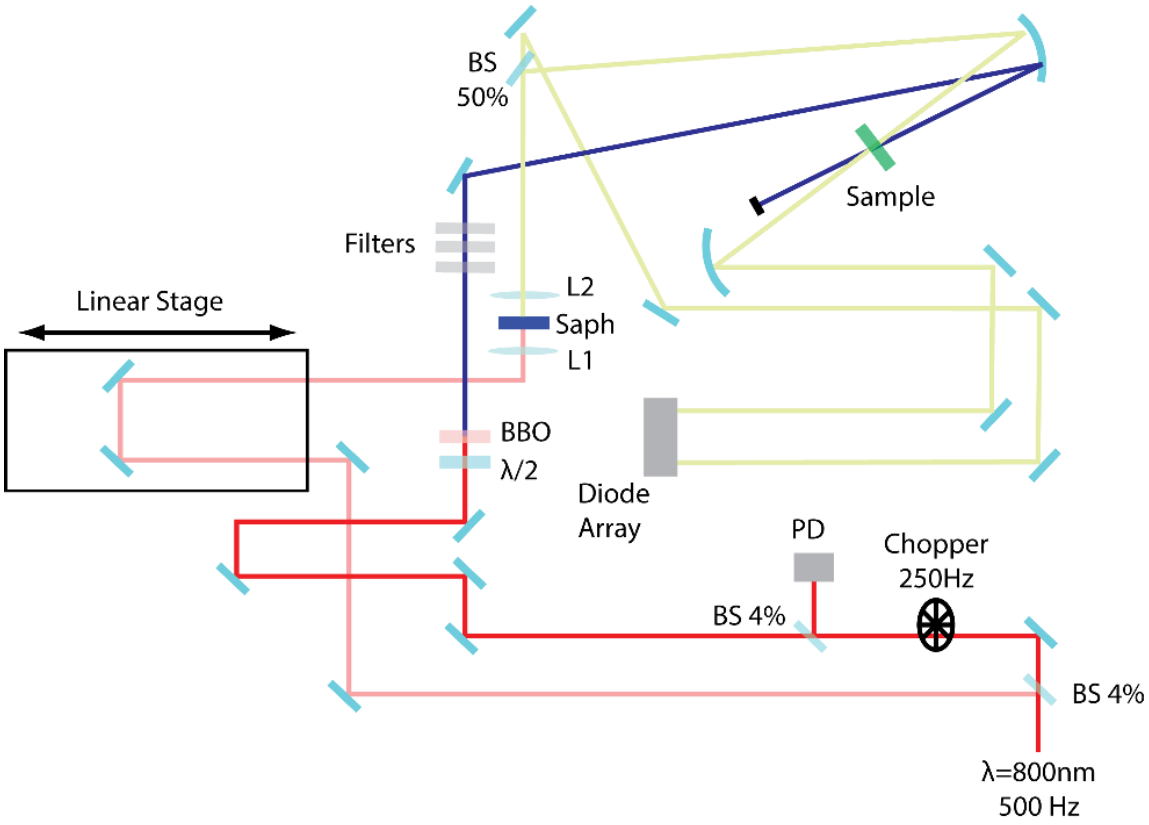

Figure 2.3 - Experimental set-up used for transient absorption measurements, realized by Dr. Bolzonello and Prof. Ferrante. The Spitfire output beam is used as pump beam. This repetition rate of this beam is halved by a chopper, and a fraction of scattered light is sent to a photodiode (PD) to obtain a trigger signal. The beam is sent into a BBO NL crystal to achieve second harmonic generation. The resulting beam is sent to the sample through the spherical mirror. A low-intensity replica of the Spitfire output beam is generated by a beam splitter, to serve as the probe beam. This beam is sent into a motorized linear stage, which controls its optical path length. Then, probe pulse is focused into a thin sapphire crystal to be converted into white light pulses. This beam is split into two beams, hitting the sample (see Fig 2.2) and the other serving as a reference.

Hence, the seed output is sent into an oscillator cavity to amplify these pulses up to one order of magnitude. A Spectra Physics Spitfire regenerative amplifier, within chirped pulse amplification scheme, is used to achieve the amplification stage. Briefly, the input beam is temporally stretched and sent into a Ti:Sapphire rod, synchronously pumped by a frequency doubled Nd:YLF nanosecond laser (Spectra Physics Empower). After multiple passes through the pumped rod, the stretched seed is highly amplified. Lastly, through a pulse peaker, the beam is extracted from the oscillator cavity and then recompressed.

The resulting beam is composed of highly energetic (up to 1mJ) pulses, peaked at 800nm and with temporal duration of ~130fs. The repetition rate, tunable between 10Hz and 1kHz, is set at 500Hz for TA experiment.

As shown in Figure 2.3, the output beam passes through the first beam splitter (96-4%), thereby generating a replica. From now on, the transmitted beam will be referred as the pump, while the reflected beam will be referred as the probe.

With the aim of recording both pumped and unpumped spectra, the repetition rate of the pump beam is halved by means of a chopper. Before hitting the sample, the pump beam is frequency doubled into a beta-barium borate (BBO) crystal, taking advantage of the *second harmonic generation* phenomenon.

The probe beam follows a parallel path. The linear stage controls the time delay between pump and probe pulses, by changing the probe beam optical path. Before hitting the sample, the probe beam is converted into white light exploiting super-continuum white light generation in a thin sapphire crystal. Through a spherical mirror, pump and probe beams are directed toward the sample, where they spatially overlap. The transmitted probe beam is recorded and analyzed in wavelength. The detecting unit comprises a diffraction grating and a calibrated diode array.

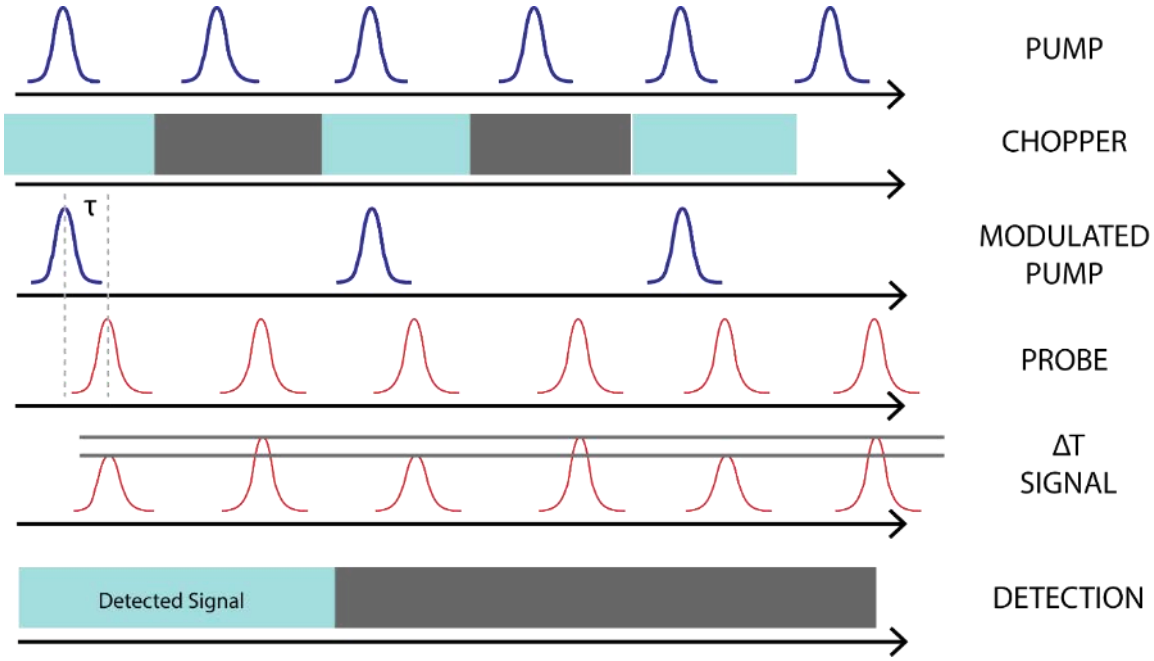

Figure 2.4 -Scheme representing the detection scheme used in TA experiments. The 500Hz repetition rate of the pump is halved by means of a chopper. Probe pulses impinge on the sample at a repetition rate which is nearly doubled, with respect to that of the pump. Hence, the transmitted probe signals will be a sequence of pumped and unpumped probe pulses. Lastly, the detection unit cannot operate pulse by pulse detection. Then, only the first couple of pulses (pumped/unpumped) is recorded. Accumulation is used to obtain higher signal-to-noise ratios.

A Labview software controls the linear stage in order to scan the pump-probe delay time. The detection scheme is reported in Figure 2.4. The use of a chopped pump allows recording both pumped and unpumped probe transmittance. Unfortunately, the repetition rate of the diode array detection unit does not allow pulse by pulse detection. Therefore, only the first couple of pumped/unpumped signals are recorded within a detector cycle. Signal to noise ratio is increased by means of accumulation.

During a typical acquisition, transient spectra are recorded at different pump-probe delays, spanning an 800ps range with 1ps time resolution. This allows building bi-

dimensional (wavelength versus delay time) TA maps. Pump pulse energy E_p is tuned using a set of OD filters and is monitored using a pyroelectric detector (Molectron J3-05). Combining this parameter with the pump beam waist *w*, and the energy of pump photons ($\varepsilon = 3.1eV$), the fluence as $j = \frac{E_p/\varepsilon}{\pi(w/2)^2}$ is obtained.

Fluence parameter is of utter importance when the excited state dynamics of QDs is investigated. Assuming that, the probability of photon absorption by QDs is independent of the number of photons absorbed hitherto, the optical excitation of QDs is described by a Poissonian statistics. [21, 23] The average exciton occupancy <*N*> after a short laser pulse is calculated as

$$\langle N \rangle = j\,[\frac{ph}{cm^2}] \cdot \sigma[cm^2] \qquad \textbf{(Eq. 2.8)}$$

where σ is the absorption cross section at the wavelegth of the laser pulse. According to Poisson statistics, the probability of having an exciton in a definite QDs is then

$$P(N) = \langle N \rangle^N \frac{e^{-\langle N \rangle}}{N!} \qquad \textbf{(Eq. 2.9)}$$

According to this equation, when average exciton occupancy is set to $\langle N \rangle = 1$, statistically one third of the QDs in the ensemble will carry a bi-exciton. Therefore, signals in TA spectra of QDs arise from a complicated mixture of different photophysical species. This problem requires accurate data analysis procedure, which will be discussed in Chapter 4.

2.4 The CdSe/$Cd_xZn_{1-x}S$ CS QDs series

In this thesis were investigated the optical properties of different CS QDs samples, with variable shell thickness and composition. Henceforward, this variety of QDs will be referred as the CdSe/$Cd_xZn_{1-x}S$ CS QDs series. This series is made up of 18 different batches, comprising:

- CdSe core QDs
- CdSe-CdS core-shell QDs (with 1 to 6 shell ML);
- CdSe-$Cd_{0.5}Zn_{0.5}S$ core-shell QDs (with 1 to 6 shell ML);
- CdSe-ZnS core-shell QDs (with 1 to 5 shell ML);

Dr. J.J. Jasieniak and Dr. F. Todescato synthesized all these QDs at CSIRO Ian Wark Laboratory, in Clayton, Australia.

Core CdSe QDs were synthesized by means of the salt-based hot-injection method, whose chemistry was discussed in Chapter 1.[24] 1-octadecene was used as a non-coordinating solvent, whereas a mixture of TMPPA (Bis-(2,2,4-trimethylpentyl)phosphinic acid) and oleic acid was used as nucleophilic capping ligands. Purification was achieved through anti-solvent precipitation and extraction in different organic solvents (cyclohexane, toluene). Lastly, QDs were dispersed in toluene, and native ligands are exchanged with 1-oleylamine.

Two slightly different batches of CdSe cores were synthesized. Hence, slightly different cores were used in different core-shell series. The basic linear optical properties of the two samples are shown in Figure 2.5.

The excitonic structure is well resolved in absorption spectra of both small (Fig. 2.5**a**) and large (Fig. 2.5**b**) CdSe core QDs. Exciton peaks can be assigned, as discussed in Chapter 1, Figure 1.5. Differences in the absorption features stem from the size dependence of exciton levels. Notably, the energy splitting between the first two transitions ($|1S\rangle$ and $|2S\rangle$ exciton state, respectively) is increased with increasing size. Moreover, the larger dot display a stronger absorption contribution from interband transitions, resulting in the less resolved excitonic structure at higher energies. The emission spectrum is Stokes-shifted from the band-edge ($|1S\rangle$) exciton absorption. Furthermore, emission spectrum for larger dots is narrower. Considering the wavelength scale (reciprocal with respect to energy), this effect stems from differences in size dispersion parameter.

The CdSe/CdxZn1-xS CS QDs series

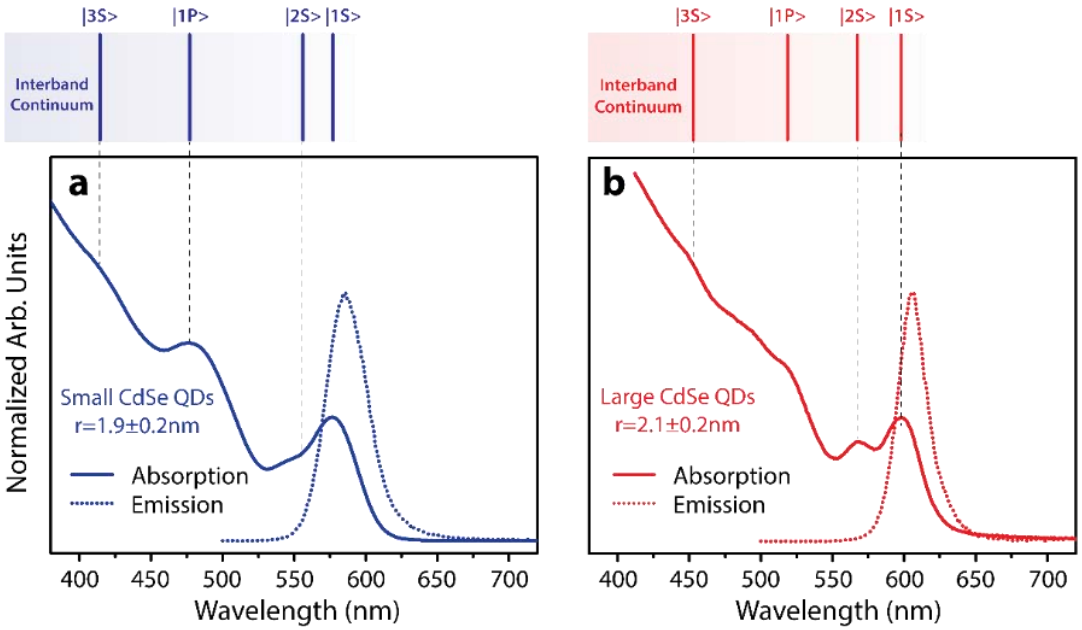

Figure 2.5 -(**a**/**b**) Absorption (solid line) and emission (dashed line) spectra of the small/large CdSe QDs studied. As discussed in Chapter 1. Each absorption peak is assigned to an exciton transition, according to Ref 21. The broad interband absorption band, underlying the exciton absorption peaks is increased in the large QDs.

According to the empirical model, developed by Dr. Jaiseniak for CdSe QDs,[25] the average size (diameter) of core QDs is estimated as:

$$D(nm) = 59.608 - 0.5473\lambda + 1.887 \cdot 10^{-3}\lambda^2 - 2.857 \cdot 10^{-6}\lambda^3 + 1.629 \cdot 10^{-9}\lambda^4 \qquad \textbf{(Eq. 2.9)}$$

where λ is the band-edge exciton absorption wavelength. Resulting size were D_S=3.8 nm and D_L=4.3nm for small and large CdSe QDs, respectively. Previously published statistical TEM analysis, performed by Prof. G. Mattei shown complete agreement with empirical model results (from TEM, D_S=3.9±0.5nm and D_L=4.2±0.5nm). [26]

Small CdSe QDs were employed as seeds for CdS and $Cd_{0.5}Zn_{0.5}S$ shell growth. On the other hand, large CdSe QDs were used as seeds for ZnS shell growth. Shell growth followed the SILAR method, described in Chapter 1. [27] Briefly, washed CdSe cores were dispersed in a 1:1 mixture of 1-oleylamine/1-octadecene at a concentration of 40 μM. The solution was degassed for 30min and then heated under nitrogen atmosphere up to 235 °C. The first step was the addition of a Cd enriching layer, equivalent to a half stoichiometric ML of CdSe. After 5 min, an equivalent quantity of ODE-Sulfur solution was added to form 1 ML of shell material. After 10 min growth, the solution temperature was reduced to 120 °C to take aliquots of the samples after each ML.

Following, the temperature was increased to 235-250 °C. The exact final temperature was increased by 5 °C every 2 MLs up to a maximum of 250 °C. As-synthesized core–shell QDs were purified through multiple antisolvent precipitations and extractions using MeOH, EtOH, and acetone, prior to being dispersed in toluene and capped with 1-oleylamine.

Unfortunately, no empirical model can be used to calculate core-shell QDs size on the basis of the absorption spectra. Simple geometrical considerations allow estimating their dimension, at least qualitatively. Considering half of the *c*-lattice parameter of the bulk shell semiconductor as the equivalent thickness of one monolayer, dimensions of the core-shell nanocrystals can be roughly estimated. Accordingly, 1ML of CdS corresponds to 0.34 nm, 1ML of ZnS 0.31 nm and through lever rule 1ML of $Cd_{0.5}Zn_{0.5}S$ corresponds to 0.33 nm.[28] These results were further confirmed by TEM analysis, previously published.[26]

2.4.1 Linear Optical properties

The absorption spectra of the core-shell series are shown in Figure 2.6. The optical properties of core-shell QDs, the nature of excitonic transitions and differences among the core-shell series will be extensively discussed in the next Chapter.

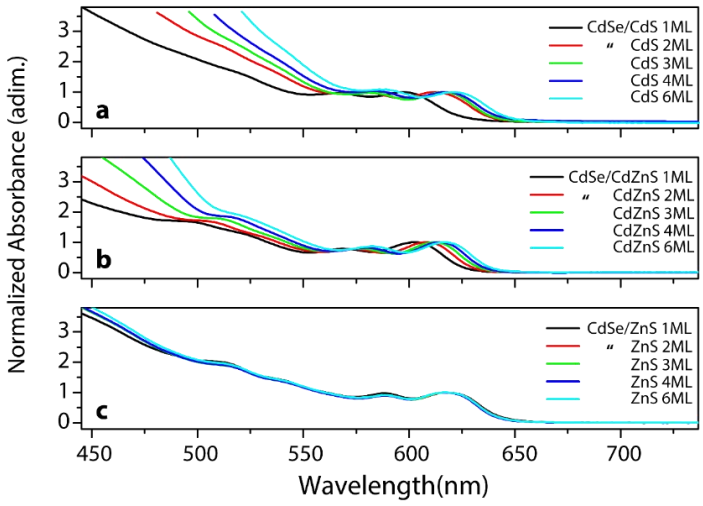

Figure 2.6- (**a**,**b**,**c**) Comparison of the absorption spectra for each of the three CdSe/$Cd_xZn_{1-x}S$ series. The red-shift of the absorption spectra with increasing shell thickness is evident for CdS and CdZnS, whereas it is not observed for ZnS. This effect is associated with a reduced confinement effect caused by the lower confining potential of the shell, with respect to vacuum. The increased interband continuum band (**a**,**b**) in low wavelength region originates from interband absorption of shell material (CdS and CdZnS). On the other hand, the onset of ZnS bulk interband absorption is found at lower wavelengths and is not observed in (**c**).

Briefly, all CS QDs display similar excitonic structure, which is preserved from CdSe core QDs. Hence, the optical properties of core-shell QDs are mainly dictated by core QDs. Nevertheless, the shell influence is noticeable: the entire excitonic structure is red-shifted for each QDs to different extents, and absorbance dramatically increases at lower wavelengths. The redshift is caused by wavefunction modification induced when a shell material is grown, in particular to the reduced confinement effect (i.e., the confining potential of the shell is lower than vacuum level, causing a non-negligible wavefunction spill out in shell material).[27] The dramatic absorbance increase in the low wavelength region is explained by augmented interband transitions, i.e., those of shell materials (CdS, $E_{g,0}$ =2.49 eV) and ZnS (E_g^{Bulk} = 3.61 eV).

The series of CdSe/CdS QDs with increasing shell thickness from 1 to 6 ML belongs to the quasi type-II heterostructures category (Chapter 1), in which holes are confined in the core whereas electrons spread over the entire nanostructure. At the temperature reached during the CdS shell growth, anionic inter-diffusion is allowed and results in the formation of a $CdSe_xS_{1-x}$ alloy. Alloying was discovered on CdSe/CdS by Klimov and confirmed on these QDs by surface-enhanced Raman scattering experiments (see Ref . 26 by Todescato et al.). This alloy has a twofold effect: (i) a reduction of interfacial defects (e.g., dislocations) caused by the lattice mismatch driven elastic energy accumulation; (ii) the smoothing of the potential barrier between core and shell, contributing in the reduction of the non-radiative Auger mechanism for exciton relaxation. These features, together with the reduced Coulomb interactions between electrons and holes due to reduced wavefunction overlap, contribute to making CdSe/CdS QDs exhibiting record high PLQY.

However, the full achievement of this result requires growing thick CdS shells up to CdSe/CdS QDs known as *giant-QDs*. As mentioned in the previous chapter, thick shell are detrimental for applications requiring inter-dot coupling.

CdSe/CdZnS and CdSe/ZnS QDs are classified as type-I heterostructures. Owing to the band alignment, in which the band edges of the shell wrap those of the core, photoexcited carriers are confined inside core volume. Although this energy level configuration increases the surface passivation, with respect to CdSe/CdS QDs, some drawbacks come into play. The presence of sharp interfaces causes the formation of defects, due to lattice mismatch, hampering their optical properties. Moreover, this shape of the interface potential favors Auger recombinations.

References

1. Leatherdale, C. A.; Woo, W. K.; Mikulec, F. V.Bawendi, M. G., On the Absorption Cross Section of CdSe Nanocrystal Quantum Dots. *The Journal of Physical Chemistry B* **2002**, *106*, 7619-7622.

2. Würth, C.; Grabolle, M.; Pauli, J.; Spieles, M.Resch-Genger, U., Relative and Absolute Determination of Fluorescence Quantum Yields of Transparent Samples. *Nat. Protocols* **2013**, *8*, 1535-1550.

3. An, J. M.; Franceschetti, A.Zunger, A., The Excitonic Exchange Splitting and Radiative Lifetime in Pbse Quantum Dots. *Nano Letters* **2007**, *7*, 2129-2135.

4. Krause, M. M.; Mooney, J.Kambhampati, P., Chemical and Thermodynamic Control of the Surface of Semiconductor Nanocrystals for Designer White Light Emitters. *ACS Nano* **2013**, *7*, 5922-5929.

5. Saha, A.; Chellappan, K. V.; Narayan, K. S.; Ghatak, J.; Datta, R.Viswanatha, R., Near-Unity Quantum Yield in Semiconducting Nanostructures: Structural Understanding Leading to Energy Efficient Applications. *The Journal of Physical Chemistry Letters* **2013**, *4*, 3544-3549.

6. Orfield, N. J.; McBride, J. R.; Wang, F.; Buck, M. R.; Keene, J. D.; Reid, K. R.; Htoon, H.; Hollingsworth, J. A.Rosenthal, S. J., Quantum Yield Heterogeneity among Single Nonblinking Quantum Dots Revealed by Atomic Structure-Quantum Optics Correlation. *ACS Nano* **2016**, *10*, 1960-1968.

7. Zhang, A.; Dong, C.; Liu, H.Ren, J., Blinking Behavior of CdSe/CdS Quantum Dots Controlled by Alkylthiols as Surface Trap Modifiers. *The Journal of Physical Chemistry C* **2013**, *117*, 24592-24600.

8. Wawilow, S. J., Die Fluoreszenzausbeute Von Farbstofflösungen. *Zeitschrift für Physik* **1924**, *22*, 266-272.

9. Crosby, G. A.Demas, J. N., Measurement of Photoluminescence Quantum Yields. Review. *The Journal of Physical Chemistry* **1971**, *75*, 991-1024.

10. Klonis, N.Sawyer, W. H., Spectral Properties of the Prototropic Forms of Fluorescein in Aqueous Solution. *J Fluoresc* **1996**, *6*, 147-157.

11. Fletcher, A. N., Quinine Sulfate as a Fluorescence Quantum Yield Standard. *Photochemistry and Photobiology* **1969**, *9*, 439-444.

12. Bindhu, C. V.; Harilal, S. S.; Geetha, K. V.; Riju, C. I.; Nampoori, V. P. N.Vallabhan, C. P. G., Measurement of the Absolute Fluorescence Quantum Yield of Rhodamine B Solution Using a Dual-Beam Thermal Lens Technique. *Journal of Physics D: Applied Physics* **1996**, *29*, 1074

13. Kubin, R. F.Fletcher, A. N., Fluorescence Quantum Yields of Some Rhodamine Dyes. *Journal of Luminescence* **1982**, *27*, 455-462.

14. Drexhage, K. H., *Fluorescence Efficiency of Laser Dyes*, 1976; Vol. 80A, p 421.

15. Tauc, J., Photoinduced Absorption in Amorphous Silicon. In Festkörperprobleme 22: Plenary Lectures of the 46th Annual Meeting of the German Physical Society (Dpg) and of the Divisions "Semiconductor Physics" "Metal Physics" "Low Temperature Physics" "Thermodynamics and Statistical Physics" "Thin Films" "Surface Physics" "Magnetism" Münster, March 29–April 2, 1982, Grosse Aachen, P., Ed. Springer Berlin Heidelberg: Berlin, Heidelberg, 1982; pp 85-113.

16. Linnros, J., Carrier Lifetime Measurements Using Free Carrier Absorption Transients. I. Principle and Injection Dependence. *Journal of Applied Physics* **1998**, *84*, 275-283.

17. Ruckebusch, C.; Sliwa, M.; Pernot, P.; de Juan, A.Tauler, R., Comprehensive Data Analysis of Femtosecond Transient Absorption Spectra: A Review. *Journal of Photochemistry and Photobiology C: Photochemistry Reviews* **2012**, *13*, 1-27.

18. Mukamel, S., *Principles of Nonlinear Optical Spectroscopy*; Oxford University Press, 1995.

19. Lanzani, G., The Photophysics Behind Photovoltaics and Photonics; Wiley, 2012.

20. Berera, R.; van Grondelle, R.Kennis, J. T. M., Ultrafast Transient Absorption Spectroscopy: Principles and Application to Photosynthetic Systems. *Photosynthesis Research* **2009**, *101*, 105-118.

21. Klimov, V. I., Spectral and Dynamical Properties of Multiexcitons in Semiconductor Nanocrystals. *Annual Review of Physical Chemistry* **2007**, *58*, 635-673.

22. Tyagi, P.Kambhampati, P., False Multiple Exciton Recombination and Multiple Exciton Generation Signals in Semiconductor Quantum Dots Arise from Surface Charge Trapping. *The Journal of Chemical Physics* **2011**, *134*, 094706.

23. Makarov, N. S.; McDaniel, H.; Fuke, N.; Robel, I.Klimov, V. I., Photocharging Artifacts in Measurements of Electron Transfer in Quantum-Dot-Sensitized Mesoporous Titania Films. *The Journal of Physical Chemistry Letters* **2014**, *5*, 111-118.

24. van Embden, J.Mulvaney, P., Nucleation and Growth of CdSe Nanocrystals in a Binary Ligand System. *Langmuir* **2005**, *21*, 10226-10233.

25. Jasieniak, J.; Smith, L.; van Embden, J.; Mulvaney, P.Califano, M., Re-Examination of the Size-Dependent Absorption Properties of CdSe Quantum Dots. *The Journal of Physical Chemistry C* **2009**, *113*, 19468-19474.

26. Todescato, F.; Minotto, A.; Signorini, R.; Jasieniak, J. J.Bozio, R., Investigation into the Heterostructure Interface of CdSe-Based Core-Shell Quantum Dots Using Surface-Enhanced Raman Spectroscopy. *ACS Nano* **2013**, *7*, 6649-6657.

27. van Embden, J.; Jasieniak, J.Mulvaney, P., Mapping the Optical Properties of CdSe/CdS Heterostructure Nanocrystals: The Effects of Core Size and Shell Thickness. *Journal of the American Chemical Society* **2009**, *131*, 14299-14309.

28. Rogach, A., Semiconductor Nanocrystal Quantum Dots: Synthesis, Assembly, Spectroscopy and Applications; Springer Vienna, 2008.

CHAPTER 3

Bridging the Energetics and Dynamics of Exciton Trapping

Part of this Chapter is based on:

Righetto et al. The Journal of Physical Chemistry C **2017**, 121, 896-902.

ABSTRACT- The widespread application of quantum dots dramatically profits from their broad absorption band. However, the nature of excitations within these bands is variable. As discussed in Chapter 1, the absorption spectrum of QDs comprises both a variety of exciton states and an underlying interband continuum absorption. Different photoexcited states are associated with different wavefunction of photoexcited carriers. Thence, it is legitimate to assume various interactions with trap states inasmuch as the wavefunction distribution drives the electronic coupling between carrier and traps.

In this chapter, the different role played by hot and cold carrier trapping is discussed by determining photoluminescence quantum yields (PLQY). The contrast between the dynamics of hot and cold carrier trapping results in a peculiar energetics of carrier trapping, i.e., an undesired excitation energy dependence of steady-state emission properties. The following analysis relates the energetic parameters with the state-of-the-art knowledge on the dynamics of charge trapping. The primary outcome of this work is that delicate balance between trapping and de-trapping processes controls the charge accumulation at surfaces. This has a profound effect on steady-state emission properties of QDs. The excitation dependent photoluminescence quantum yields (PLQY) in different CdSe/$Cd_xZn_{1-x}S$ (x = 0, 0.5, 1) quantum dots were investigated with the aim of identifying best-performing heterostructures, in terms of shell thickness and composition. Our rationalization of the observed behavior is focused on the modulation of trapping and de-trapping rates. The combination of experimental results and PLQY kinetics modeling reveals the need to consider hot-carrier trapping, supporting recent observations of dynamical properties. Thus, the present chapter provides a deeper insight into trapping processes in quantum dots, relating their energetics and dynamics.

3.1 Introduction & State-of-the-art

3.1.1 Phenomenological Kinetic Modeling of PL dynamics

This work concerns hot carrier trapping and aims to extend and deepen the work carried on by prof. Bozio and Dr. Minotto on cold exciton trapping dynamics in the CdSe/$Cd_xZn_{1-x}S$ series.[1] In this section, their discoveries, representing the state-of-the-art on this topic, are briefly reviewed to provide a sound basis for further discussion on hot carrier trapping. Moreover, a refinement of the model developed by Dr. Minotto, which will be used in the following section is presented.

In the paper "*Role of Core-Shell Interfaces on Exciton Recombination in CdSe–$Cd_xZn_{1-x}S$ Quantum Dots*", published on Journal of Physical Chemistry C in 2014, systematic measurements and analyses of the photoluminescence decay curves were carried out for the three series of QDs, CdSe/CdS, CdSe/CdZnS, and CdSe/ZnS, with increasing number of monolayers (ML) composing the shell. These experiments aimed to clarify the effect of different core/shell interfaces on cold exciton trapping dynamics. Indeed, trapping processes are intertwined with radiative recombination of excitons in QDs. Kambhampati and Scholes groups showed in seminal papers[2-3] that trap sites do not behave as static charge accumulators. The de-trapping process, i.e., the inverse process with respect to trapping, is not only possible but also energetically favored at room temperature.

This process results in the regeneration of bound excitons, contributing to PL in a delayed fashion, coherently with microsecond lasting PL observed for CdSe QDs.[4] This intricate balance of processes, underlying QDs emission, has profound effects on PL dynamics. Hence, radiative rate combines with trapping processes, resulting in multi-exponential PL decays. Due to overlapping timescales, the conventional multi-exponential fitting analysis is not reliable in separating these contributions. Thence, in the above-mentioned paper Minotto et al. demonstrated that an accurate untangling of these processes is possible by formulating a kinetic model for the description of PL dynamics.

The presented model reduces that initially proposed by Scholes to a phenomenological formulation, i.e., the rate constant introduced can be modified to suitably fit other systems. According to Scholes model [3], different distributions of radially distributed traps interact with bound excitons, resulting in a delicate balance between trapping and de-trapping processes. Therefore, a set of differential equations accounts for the time evolution of bound exciton population (ρ_X) and trap states (ρ_i), where the *i* index indicates the i-th trap distribution.

Equation reads:

$$\begin{cases} \dfrac{d\rho_X(t)}{dt} = \sum_i \left(v_{dt,i}\rho_i(t) - (v_{t,i} + k_{NR} + k_R)\rho_X(t) \right) \\ \dfrac{d\rho_i(t)}{dt} = v_{t,i}\rho_X(t) - v_{dt,i}\rho_i(t) \end{cases} \qquad \textbf{(Eq. 3.1)}$$

where $v_{t,i}(v_{dt,i})$ represents trapping (de-trapping) constant for the i-th trap distribution. Accordingly, radiative and non-radiative processes, described by k_R and k_{NR} respectively, and trapping deplete bound exciton population, whereas de-trapping augment it.

The PL decay curve I(t) was then correlated with this population, through the radiative rate. Therefore, Minotto demonstrated the possibility of extracting the whole set of relevant parameter, by performing a least square fitting procedure, through minimization of the function:

$$\chi = \int_0^t \left(I(t) - C * k_R \rho_X\left([k_R, v_{t,i}, v_{dt,i}], t\right) \right)^2 dt, \qquad \textbf{(Eq. 3.2)}$$

In Figure 3.1, a panel of representative results for the CdSe/CdS series is reported (Adapted from Ref.1). Notably, two trap distributions were found necessary to fit the exciton population, and according to Jones calculations, faster (slower) traps are ascribed to the surface (interface) trapping.[3]

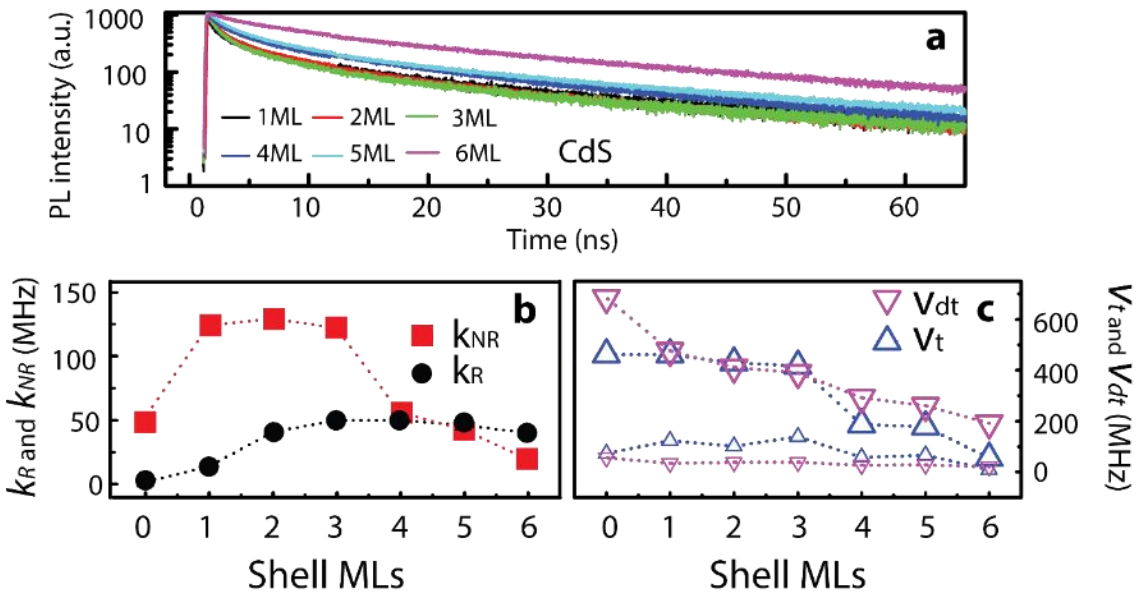

Figure 3.1- (**a**) Time-resolved PL measurements for the CdSe/CdS series. (**b**) Non-Radiative (red squares) and radiative (black circles) rates obtained by model fitting of PL decay curve for CdSe/CdS series, lines are a guide for the eye (**c**) Trapping (blue triangle) and de-trapping (purple inverted triangle) rates obtained by model fitting of PL decay curve for CdSe/CdSe series, big triangle and small triangle indicate two different traps distributions. Adapted from Ref.1

The presence of de-trapping accurately accounts for PL dynamics at long time delays. The behavior of trapping/detrapping rates reveals deep insights into the photophysics of shelling. Surface trapping rates display a decreasing trend with increasing shell thickness, due to reduced electronic coupling between bound exciton and trap states, as suggested by absorption spectra.

This behavior can be observed for each of the three series, confirming the excellent passivation of surfaces. In particular, the CdZnS shell seems to provide the best passivation among the series, with $k_{t,1}$ decreasing from 462 to 50 MHz, from bare core to 6ML thick shell. On the contrary, interfacial trapping rates gain more importance in thick shell samples, due to the physical origin of interface traps, associated with lattice mismatch. Comparing different series, interface trapping is higher in CdSe/ZnS with respect to CdSe/CdZnS and CdSe/CdS, thereby confirming the detrimental formation of defects at the CdSe/ZnS interface. Lastly, model fitting provided information on radiative constant, as well. The observed non-monotonous trend for the radiative constant in the CdSe/CdS is explained by the concurrence of two counteracting effects. The formation of $CdSe_xS_{1-x}$ alloy induces an increase in effective volume, increasing k_R. [5-6] On the other hand, the quasi-Type II nature of CdSe/CdS interface reduces electron-hole overlap, thereby reducing k_R. Therefore, the alloy formation up to the third ML induces an increase in the radiative constant. The saturation of the alloy, results in the expected attenuation of k_R.

One fundamental inconsistency in the presented model is the possibility of having de-trapping from empty trap sites. Albeit this is mathematically possible in model Eq. 3.1, this would violate charge conservation, and therefore it is physically unreasonable.
Hence, the phenomenological model can be refined by introducing the distinction between trap velocities and trapping rates. Here, the refined version of the phenomenological model, where exciton trapping is described as a chemical process:

$$X + N \underset{k_{dt}}{\overset{k_t}{\rightleftarrows}} c. \qquad \textbf{(Eq. 3.3)}$$

The reaction between a bound exciton (X) and a neutral trap site (N) produces a charged trap species (c) with a rate constant (k_t). In turn, the charged trap can regenerate the bound exciton with de-trapping constant (k_{dt}). It is worth to note that the formation of an isolated charge in the core region is not considered, but is granted by charge conservation.
The resulting rate equation system reads:

$$\begin{cases} \frac{d\rho_X}{dt} = \sum_i (-k_{t,i}\rho_X\rho_{N,i} + k_{dt,i}\rho_C) - (k_R + k_{NR})\rho_X \\ \frac{d\rho_{N,i}}{dt} = -k_{t,i}\rho_X\rho_{N,i} + k_{dt,i}\rho_{C,i} \\ \frac{d\rho_{c,i}}{dt} = k_{t,i}\rho_X\rho_{N,i} - k_{dt,i}\rho_{C,i} \end{cases} \qquad \textbf{(Eq. 3.4)}$$

where the first equation describes the bound exciton population ρ_X, depleted by trapping (first term on RHS), radiative and other non-radiative recombinations while augmented by de-trapping. The second and third equations describe respectively neutral (ρ_N) and charged (ρ_c) trap sites population. Their evolution is symmetrical, with trapping depleting neutral trap population while de-trapping increasing it and vice versa for charged trap population.

3.1.2 Excitation Energy Dependence of PLQY

Albeit the dynamics of trapping processes is now understood, their energetics remains widely unexplored. During past years, some groups reported the dispersion of PLQY values for QDs, measured under different excitation energies. The broadband absorber nature of QDs allows excitation over the entire visible spectrum. However, the emission efficiency of these materials depends on excitation conditions and decreases at increasing excitation energy. Such peculiarity cannot be disregarded as, for instance, both electrically and optically pumped QD-LED work under high-energy excitation.

Recently, Kambhampati investigated the existence of PLQY excitation spectra[7], i.e., the dependence of PLQY on the photon energy used for excitation, by microscopic modeling of QDs temperature-dependent PL spectra.[8-9]

A previously reported work on the competition between relaxation of band edge excitons and trapping at surface defects of small CdSe dots was extended to account for the dynamics of "hot excitons" generated by high energy photons.[10] By means of a semi-classical electron transfer model, Kambhampati related the excitation energy dependence (EED) of PLQY with energy-dependent trapping rates in core CdSe QDs.[2] The outcome of that analysis led to the prediction that the PLQY may exhibit a dependence on the excitation energy that markedly increases on lowering the temperature. Kambhampati's analysis was based on data from ultrafast time-resolved measurements. Direct experimental measurements of the excitation dependence of steady-state PL were carried out either by observing deviations of PL excitation spectra from absorption spectra or by directly measuring the PLQY. Nevertheless, the variable and conflicting nature of experimental reports on PLQY excitation spectra suffered from variance in synthesis and passivation quality.[11-14]

The aim of this work is to extend the investigation of the EED of PLQY and of the underlying trapping and de-trapping mechanisms to core/shell CdSe QDs with different composition and structure of the shell. This will offer the opportunity to analyze how surface/interface trapping changes when structure and energy gap of the shell are changed while keeping constant the core properties. A study on well-defined systems, such as core/shell QDs, offers the possibility to get physical insights of broad significance. In addition to this, we also discuss why steady-state measurements are likely to yield results different from those inferred from ultrafast time-resolved measurements. The key factor here is the effect of long-lived trapped charges on further photoexcitation and enhanced Auger recombination.

3.2 Linear Optical Properties

Three different series of CdSe/$Cd_xZn_{1-x}S$ QDs were investigated in this work, CdS and $Cd_{0.5}Zn_{0.5}S$ (henceforth CdZnS) shells were epitaxially grown on 3.8 nm CdSe core QDs, with shell thicknesses ranging from 1 to 6 monolayers (ML). Homogeneous ZnS shells, with a thickness ranging from 1 to 5 ML were grown on 4.2 nm CdSe core QDs. We aided the challenging epitaxial growth of ZnS on CdSe, due to a 12% lattice mismatch,[15] by interposing an enriching layer of CdS, whose lattice mismatch is about three times lower.[16] More details on the synthesis procedure of CdSe cores and shell growth by successive ionic layer adsorption and reaction (SILAR) technique are reported in previous papers.[17-19] For characterization by high-resolution electron microscopy, we refer to our previous work.[20]

In Figure 2**a-c** we report the evolution of the linear absorption spectrum of the three series (1 to 6 ML, 1 to 5 ML for CdSe/ZnS) in solution. Absorption spectra of CdSe are described in terms of their excitonic structure.[21-22] The band edge exciton (|1S> exciton), is related to $1S_e$-$1S_{3/2}$ electron-hole pair creation. Transitions to higher energy (|1P>, |2S>,…) are related to the excitation of more energetic electron-hole pairs.[23] Above 2.75 eV, the high joint density of states results in a broadened band, which is related to the excitation of so-called "hot carriers" (i.e., unbound electron-hole pairs).

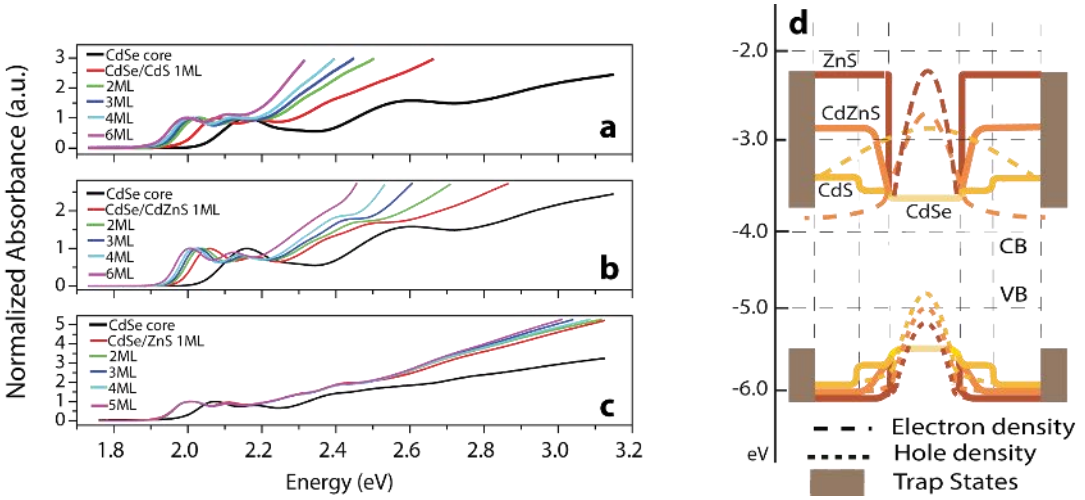

Figure 3.2 - Normalized (at the |1S> exciton peak absorption) linear absorption spectra of (**a**) CdSe/CdS series (1-6 ML), (**b**) CdSe/CdZnS series (1-6 ML), (**c**) CdSe/ZnS series (1-5 ML) in solution. (**d**) Scheme of energy levels and electron/hole wavefunctions in different core/shell heterostructures. The dashed curves symbolize the wavefunction distribution and do not refer to the energy scale on the left. The spill out of the exciton wavefunction gradually decreases with increasing Zn concentration.

For the CdSe/CdS series (Fig. 3.2**a**) the increase in shell thickness results in a redshift of the excitonic bands (≈150 meV for 6 ML). A similar behavior, though less pronounced, is observed for CdSe/CdZnS series, where the redshift for the thickest shell is up to 120 meV (Fig. 3.2**b**). As already pointed out before, this phenomenon is related to the spill out of the exciton wavefunction into the surrounding shell.[24-25] The delocalization of the exciton wavefunction over the shell volume results in a reduced confinement effect and a consequent redshift due to a reduced quantum size effect. Consistently, CdSe/CdS is a "quasi-Type II" hetero-structure,[26] where the electron wavefunction is completely delocalized in the QD volume whereas the hole is confined in the core. The increase in Zn anion concentration progressively creates a steeper potential barrier for the electronic motion and increase the "type-I" [16] nature of the core-shell heterostructure. For this reason, the CdSe/ZnS series reveals a substantial independence of exciton energies from shell thickness. A scheme representing energy levels and wave functions in different core-shell heterostructures is reported in Figure 3.2**d**. Notably, in an ideal "type-I" hetero-structure the shell confinement should restrain the band edge exciton wavefunction away from the outer surface trap sites, thereby reducing the trapping probability. However, the epitaxial growth of the shell can result in the formation of lattice defects at the core/shell interface.[15] The outer surface uncoordinated atoms, as well as the under-coordinated sites and dislocations at core/shell interfaces, can act as traps for excitons. In 2005 Mews identified the effect of interface defects on the optical properties of core/shell QDs.[16] He used PLQY as a suitable parameter to quantify non-radiative relaxation pathways and evaluate their relative importance. Both interface and surface defects (i.e., dislocation and dangling bonds, respectively) are expected to affect PLQY.

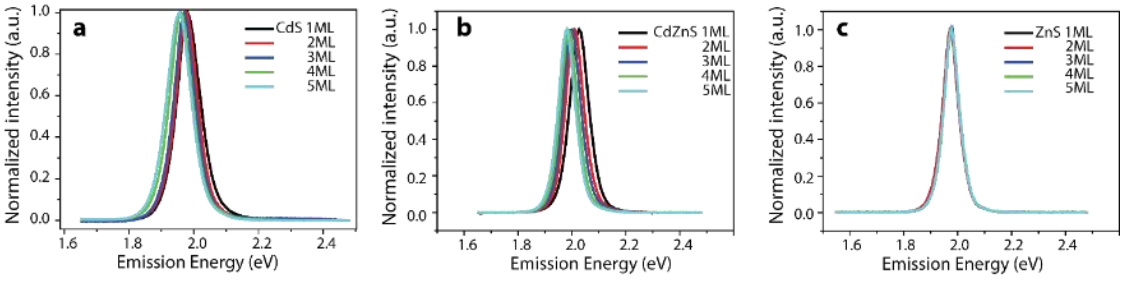

Figure 3.3 - Steady-state PL spectra recorded under 2.25eV excitation for CdSe/CdS (**a**), CdSe/CdZnS (**b**), and CdSe/ZnS (**c**) core/shell QDs in solution. PL peak energy shifts, according to absorption spectra, due to reduced confinement. This effect is even more pronounced for CdS and CdZnS shell. Any appreciable shift is not observed for ZnS shell.

In Figure 3.3**a-c** narrow PL bands are reported for the three QD series: the FWHM of PL band is ≈ 70 meV for the CdSe/CdS and CdSe/CdZnS series and drops to ≈ 60 meV for the CdSe/ZnS series. The observed Stokes shift (≈10 meV) is consistent with commonly reported values. This PL band originates from the radiative relaxation of the |1S> exciton.

In all cases, any trapped exciton emission [2] bands were observed under 2.25eV excitation. However, despite the absence of a surface defect emission band, trapping processes cannot be neglected when describing the PL properties of QDs.[27] In addition, effects such as interface defects must be considered, albeit the increasing confinement exerted by the shell should lead to higher PLQY.

3.3 Interpreting PLQY in QDs systems

The PLQY is a phenomenological parameter directly quantifying the conversion of absorbed photons into emitted photons. The measurement of this parameter usually relies on the spectrally integrated emission intensity in a steady-state experiment. During these measurements, QDs are repeatedly excited, and the emission is detected on time-scales considerably longer than the exciton lifetime. The main processes that can occur during the photo-excitation of QDs are depicted in Figure 3.4**a** and 3.4**b**.

According to the literature,[2-3, 28] carrier trapping is described as a charge-transfer process, resulting in localized charges whose excess energy is slowly and non-radiatively released via coupling to ligand vibrations. Nevertheless, the effect of carrier trapping on PLQY is twofold. Beside the first loss of photon conversion due to trapping, the long-living localized charges give also rise to photo-charged QDs.[29] Photo-charged species strongly affect the recombination mechanism of subsequent excitations during the experiment, promoting non-radiative Auger recombination (recently also defined as "trion Auger recombination"[30-31]). This second aspect, given the microseconds to milliseconds reported charge lifetimes, is potentially the most detrimental to the PL efficiency.

An estimate of the likelihood that a charged QD absorbs a second photon during the PLQY measurements and follows the path of Fig. 3.4**b** can be obtained by estimating the rate of photon absorption and the diffusivity of QDs in static solutions. The average rate of photon absorption was obtained by multiplying the measured photon flux $\phi \sim 1 - 2 \cdot 10^{16} \left[\frac{\text{ph}}{\text{s}\cdot\text{cm}^2}\right]$ and the absorption cross section of QDs $\sigma \sim 2 - 11 \cdot 10^{-15}$ [cm^2]. The average rate of absorption is on the order of ~100 absorbed photons per second per QDs. The diffusion coefficient for a QD can be calculated via Einstein-Stokes equation $D = \frac{k_B T}{6\pi\eta R_h} = 1.8 \times 10^{-6} \frac{\text{cm}^2}{\text{s}}$ (cores). To provide a conservative esteem, the hydrodynamic radius was underestimated by neglecting the presence of ligand shell, thereby overestimating the diffusion coefficient. The resulting diffusion coefficient is in agreement with literature data.[32]

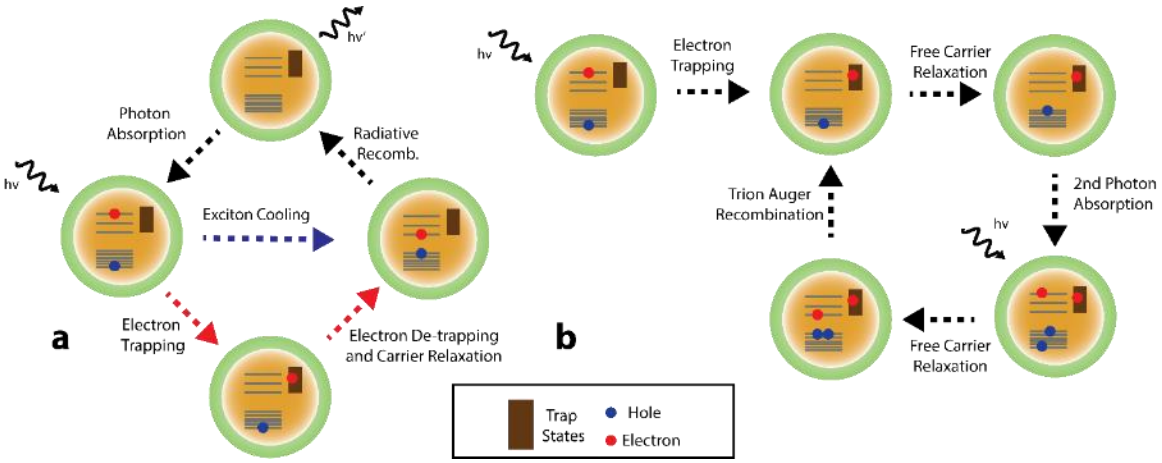

Figure 3.4 - Scheme representing the evolution of excited states in core/shell QDs in the presence of carrier trapping, during a steady-state spectroscopy experiment. Two photo-physical scenarios can be envisaged, depending on the presence of carrier de-trapping. (**a**) After the first photo-excitation, exciton cooling process competes with fast carrier trapping. Exciton cooling results in cold exciton species, able to undergo radiative relaxation. Carrier trapping, on the other hand, localizes a charge carrier at surface/core-shell interface. The restoring of bound exciton species, via carrier de-trapping process, allows radiative recombination to take place. (**b**) A different scenario comprising carrier trapping, after the first photo-excitation. A free charge can also undergo cooling (through ligand vibration coupling), and a long-living charge-separated state is formed. The subsequent photo-excitation generates trion species, which rapidly recombine via Auger recombination. This second pathway, due to the presence of long-living localized charges, gives a negligible contribution to steady-state PL. Accumulation of charges at surfaces generates a subset of dark QDs within the ensemble. Therefore, it is detrimental to PLQY.

Therefore, considering the smaller axis of the excitation beam profile $l_1 = 0.12\text{cm}$, the average diffusion time is estimated to be $\tau_D = 5 \times 10^2\text{s}$. Namely, it is possible to consider a single QD to dwell into excitation volume for the entire duration of the steady-state measurement. Concerning the lifetime of charged states, recent papers [4, 33] reported an investigation of the delayed emission and PL QY of single-QDs with a core/shell structure quite similar to one of the series of QDs reported in our paper. The percentage of intensity emitted at delay times longer than one microsecond is estimated to be a few percent. However, long-lived charged QDs are likely in higher amounts because, on steady-state excitation, absorption of a second photon would produce a dark state owing to Auger recombination in a trion.

PLQY measurement is an experiment based on steady-state PL spectroscopy. Hence, the starting point for the description of PLQY by means of this model is the application of steady-state conditions, i.e., derivative with respect to time of population terms are set equal to zero,

$$\begin{cases} \dfrac{d\rho_X}{dt} = \displaystyle\sum_i (-k_{t,i}\rho_X\rho_{N,i} + k_{dt,i}\rho_C) - (k_R + k_{NR})\rho_X \\ \dfrac{d\rho_{N,i}}{dt} = -k_{t,i}\rho_X\rho_{N,i} + k_{dt,i}\rho_{C,i} \\ \dfrac{d\rho_{c,i}}{dt} = k_{t,i}\rho_X\rho_{N,i} - k_{dt,i}\rho_{C,i} \end{cases} \qquad \textbf{(Eq. 3.5)}$$

Noteworthy, manipulating Equation 3.5 it is possible to extract an expression for the ratio between charged and neutral traps. When steady state conditions are imposed to the above rate equations, one obtains the apparent conditions that the trapping and de-trapping velocities equal each other, namely:

$$v_t = k_t \rho_x \rho_N = v_{dt} = k_{dt} \rho_c. \qquad \textbf{(Eq. 3.6)}$$

Since ρ_X is also constant, we get:

$$\frac{v_{dt}}{v_t} \propto \frac{k_{dt}}{k_t} = R_{DT}. \qquad \textbf{(Eq. 3.7)}$$

From a physical point of view, a correlation between PLQY and the ratio between de-trapping and trapping rate constants expressed merely by $R_{DT,}$ is expected. The outcome of this comparison is reported in Figure 3.5 where the trends of PLQY for core/shell QDs with increasing number of shell monolayers are compared with R_{DT} values. An inherent limitation of this comparison derives from the fact that, while the density of trapping and de-trapping centers is constant at steady-state, it is prone to possible changes as the number of shell monolayers increases.

As shown in Figure 3.5, PLQY and R_{DT} exhibit a similar trend with respect to shell thickness, i.e., for all the QDs series an increase of R_{DT} corresponds to an increase of the PLQY. Keep in mind, however, that the two parameters, R_{DT} and the PLQY, are plotted on different scales, and the comparison of the two indicates that R_{DT} acts to modulate the PLQY, not to determine its absolute value. This suggests that whenever the de-trapping rate decreases with respect to the trapping rate the non-radiative rate increases. Although this result might seem trivial, it is important to emphasize that we measured the PLQY values from steady-state PL experiments and thereby independently from R_{DT}, which we extracted by fitting the PL decays with the phenomenological model.

The direct relation between these two independently obtained parameters is a proof of the detrimental effect of accumulated charges on the photon conversion efficiency. The importance of the exciton de-trapping processes in influencing steady-state properties is dependent on the energy distribution of the trap states. Excitations at energies higher than the band-gap generate “hot” excitons with different carrier distribution, that are subject to charge transfer with fast rates to high-lying trap levels (HTs). Such HTs contain several quanta of ligand vibrations, and the trapped charges are formed under non-equilibrium conditions from which they relax and become long-lived.

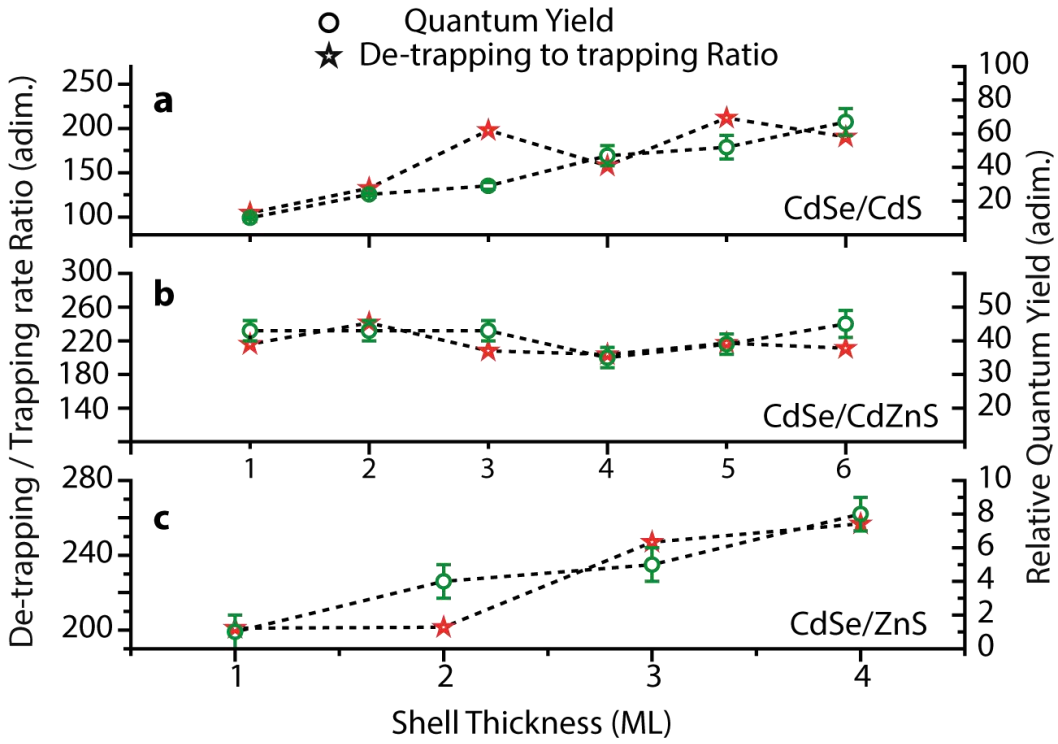

Figure 3.5 - Direct comparison between the de-trapping/trapping rate constants ratio (obtained from phenomenological model fitting of TRPL data using a 3.1eV excitation) and measured PLQY (by steady-state PL experiments using a 2.53eV excitation). The comparison is extended to each sample of the three series (**a**) CdSe/ZnS, (**b**) CdSe/CdZnS, (**c**) CdSe/CdS. Data on the rate coefficients and R_{DT} values are given in the main text.

3.4 EED of PLQY in Core/Shell QDs

To investigate hot carrier trapping in core/shell QDs systems, excitation energy resolved PLQY measurements were performed on the three CdSe/$Cd_xZn_{1-x}S$ QDs series by exciting them at three different energies: 2.25, 2.53 and 3.10 eV. As reported in Table 3-I and Figure 3.7, PLQY values are strongly dependent on the excitation energy. We observe up to an eight-fold increased PLQY by lowering the excitation energy from 3.1 eV to 2.25 eV. Loomis [13] reported similar observations, by considering the mismatch between absorption and excitation profiles in core and core/shell quantum dots. A complementary explanation of the observed phenomena should consider, besides the energy distribution of exciton traps, also the relation between trapping and de-trapping rates and PLQY.

In here reported experiments, excitation energy is spanned across a 1eV interval above the bandgap, and the highest excitation energy used lies about 1.2 eV above the CdSe band-gap. Highly energetic photons generate "hot-carriers", whose wavefunction distribution is different from and carries higher energy than bound excitons' one. Hot-carriers were recently observed to undergo ultrafast trapping at HT levels.[10] Under continuous irradiation, charges accumulate at HT levels, increasing the non-radiative Auger recombination (Figure 3.4**b**) and reducing the beneficial recovery of bound

excitons via de-trapping. Therefore, the HT harmfulness stems from their higher trapping rate compared to the de-trapping rate, thus generating long-lived trapped charges. The accumulation of charges at HT levels explains, according to the scheme in Figure 3.4, the drastic changes in PLQY values that cannot be justified starting from the trapping and de-trapping rates extracted from TRPL measurements.[1] Microscopically, this is consistent with theoretical predictions relating the excitation energy dependence of PLQY to energy dependent carrier trapping rates.[7-8]

Table3-I- Results of PLQY excitation energy dependent measurements for the three series of core/shell QDs. Red values are those used for normalization in Figure 3.6.

			CdS			
Excitation (eV)	1ML	2ML	3ML	4ML	5ML	6ML
3.14	2.9±0.4	6.3±0.6	4±0.4	2±0.2	14±1	6.7±0.7
3.1	2.7±0.4	6.6±0.6	4.1±0.4	2.2±0.2	15±1	7.6±0.7
3.06	3.3±0.5	7±0.6	4.3±0.4	2.5±0.2	15±1	8.2±0.8
2.56	4.4±0.5	10±1	7.1±0.7	5.4±0.5	22±1	21±2
2.53	4.3±0.5	11±1	7.3±0.7	5.4±0.5	23±1	22±2
2.51	4.5±0.5	12±1	7.8±0.8	6.2±0.6	22±1	26±2
2.28	3.9±0.5	12±1	8.2±0.8	8±0.8	25±1	36±3
2.25	3.1±0.4	12±1	8.2±0.8	7.8±0.8	25±1	38±4
2.23	3.7±0.5	12±1	8.5±0.8	8.5±0.8	26±1	38±4
			CdZnS			
Excitation (eV)	1ML	2ML	3ML	4ML	5ML	6ML
3.14	19±2	30±3	31±3	17±1	12±1	44±4
3.1	20±2	31±3	32±3	18±2	13±1	44±4
3.06	21±2	32±3	33±3	19±2	14±1	45±4
2.56	17±2	26±2	30±3	22±2	21±2	30±3
2.53	17±2	27±2	31±3	23±2	23±2	30±3
2.51	19±2	28±2	31±3	24±2	24±2	31±3
2.28	24±2	40±4	44±4	37±3	40±4	48±4
2.25	24±2	40±4	42±4	37±3	39±4	46±4
2.23	26±2	40±4	43±4	38±3	39±4	46±4

ZnS

Excitation (eV)	1ML	2ML	3ML	4ML	5ML
3.1	12±1	3±0.5	8±1	14±1	4±0.5
2.53	26±2	17±1	17±1	17±1	16±1
2.48	28±2	18±1	19±2	17±1	16±1
2.43	30±3	19±1	20±2	19±1	18±1
2.38	30±3	20±1	20±2	19±2	18±1
2.34	31±3	21±2	21±2	20±2	19±1
2.3	33±3	22±2	21±2	21±2	20±2
2.25	31±3	22±2	22±2	20±2	19±2
2.21	31±3	21±2	22±2	21±2	20±2
2.18	32±3	23±1	22±2	21±2	19±2

As shown in Figure 3.6, both hot carriers and cold excitons can interact with surface traps. Nevertheless, as discussed in Chapter 1, these states are strongly coupled with vibrations. Hence, hot carriers interact with vibrationally excited trap states. Due to the higher density of states, the resonant charge transfer process is faster and followed by vibrational relaxation. The consequent absence of the beneficial trapping/de-trapping equilibrium leads to an unbalance in R_{DT}, underlying charge accumulation at surfaces and resulting in lower PLQY.

In addition to this, the dependence of PLQY on excitation energy and shell thickness provides further information on the nature of these traps. All reported measurements were performed at room temperature and only changing the shell thickness within a core/shell series while maintaining the same CdSe core dimension. Therefore, within a Marcus-Jortner scheme for transfer of charges to traps, the relevant changes concern the electronic coupling[34]. In turn, this coupling is affected by the changes in the shape and amplitude of the confining potential and by the correlated changes in the carrier wavefunctions.

In the CdSe/CdS and CdSe/CdZnS series, we observe a marked dependence on excitation wavelength, especially for thicker shells. On the other hand, for less than 3ML thick shells we report only a slight excitation wavelength dependence of PLQY. Incidentally, the Raman characterization of analogous series evidenced a peculiar behavior above a 3ML shell thickness.[20]

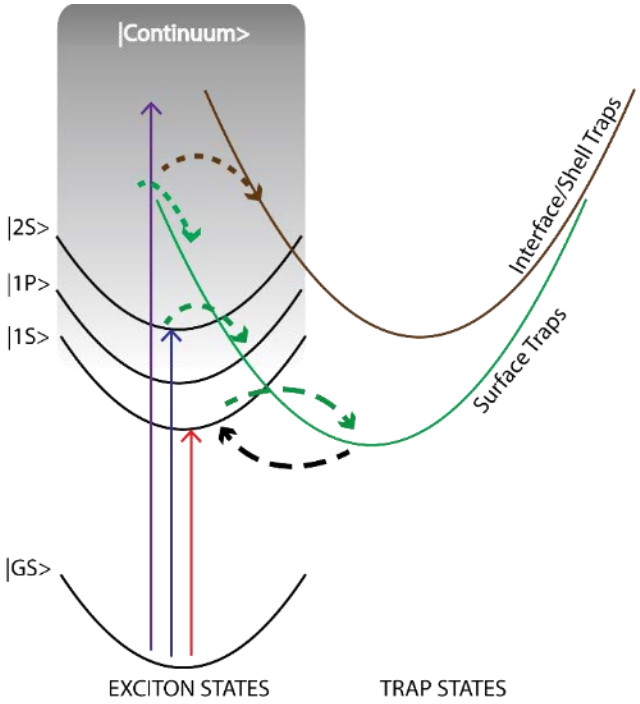

Figure 3.6-Schematic representation of the carrier trapping process for different excitations in QDs. Trap states are strongly coupled with ligands vibrations. Hot carriers are likely to interact with vibrationally excited trap states, leading to ultrafast carrier trapping. Together with the absence of the trapping/detrapping equilibrium, this leads to charge accumulation at surfaces and accounts for the measured lower PLQY values.

For the CdSe/CdS, this was ascribed to the formation of a 3ML thick CdSeS alloy at the core/shell interface, whereas for the CdSe/CdZnS any alloy formation was observed. Accordingly, it was possible to infer that an abrupt interface is formed when CdZnS is grown onto CdSe QDs. As shown in Figure 3.7, the smoother interface due to the alloy between the CdSe core and CdS shell allows a more efficient improvement of the PLQY as the excitation energy is lowered compared to the CdZnS series. The achievement of higher PLQYs in the presence of an alloyed core/shell interface, resulting in a smooth variation of the confinement potential, is in complete agreement with previous theoretical and experimental works by Efros and Klimov groups on the suppression of Auger recombination.[26, 35] Some groups, including that of Prof. Bozio, already reported this result in previous papers.

By exciting at 3.1 eV "hot-excitons" are generated both in the CdSe and in the CdS (energy gap is 2.42 eV) or CdZnS (energy gap 3 eV from Vegard's law) shell, thereby the PLQY is lowered by the strong interaction with the outer surface HT states. At lower excitation energies, well below the gap of the shell material, hot-excitons are generated inside the CdSe core, leading to an increase of the PLQY for both CdS and CdZnS series (Figure 3.7**a** and 3.7**b**). Although the higher confining potential of CdZnS should minimize the interaction with surface HT sites, the increase of PLQY is more pronounced for CdSe/CdS QDs, especially for thick shell samples.

At 6ML the increase of PLQY from 3.1 eV to 2.25eV is only threefold for CdZnS, whereas it is sixfold for CdS. This confirms that, in the case of CdZnS, part of the HT sites are located at the core/shell abrupt interface, from which they interact more efficiently with the core confined bound excitons. This result also suggests that interface HTs are distributed at a lower average energy compared to the outer surface HTs. On the other hand, for CdS, the majority of the HT states resides in the outer shell, thanks to the smoother lattice parameter variation induced by the CdSeS alloy, which limits the formation of defects at the core-shell interface.

The relation between interfacial effects and PLQY excitation wavelength dependence is made even more explicit by the CdSe/ZnS series. None of the excitation energies used in this work exceeds the >3.5 eV band-gap of ZnS, which means that excitons, in this case, are generated only in the CdSe core. For samples with one and two MLs of ZnS shell, the PLQY increases when the excitation energy is reduced. In particular, for the ZnS 2ML sample, we observe the steepest (eight-fold) PLQY recovery reducing from 3.1 eV to 2.25 eV excitation energy, mainly due to the efficient screening from the outer surface HT sites provided by the ZnS confinement potential. Furthermore, the CdS "enriching" layer deposited on top of the CdSe core prior to ZnS shell deposition limits the formation of traps at the core/shell interface.

At shell thickness above 3ML, the beneficial effect of the ZnS confinement potential is counteracted by the breakdown of the ZnS epitaxial growth and the formation of lattice dislocations. This increases the probability of interaction between "hot-excitons" and HTs, eventually leading to lower PLQYs absolute values (Table 3-1) and reduces the PLQY recovery at lower excitation energy compared to samples with thinner shells.

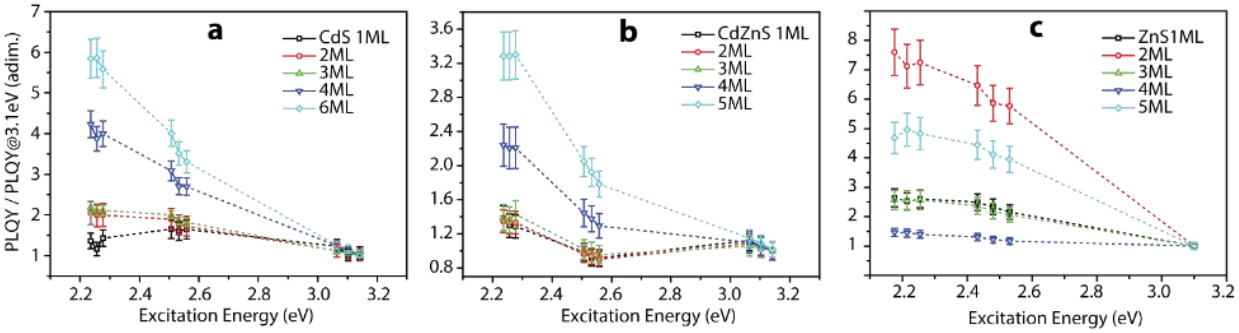

Figure 3.7 - Behavior of PLQY with respect to the excitation wavelength. Data are reported for each sample of the three series CdSe/CdS (**a**), CdSe/CdZnS (**b**), CdSe/ZnS (**c**). Normalized PLQY values, with respect to PLQY measured under 3.1eV excitation, are reported. Each point indicates the relative increase of PLQY with decreasing excitation energy from 3.1eV to 2.25eV. Normalization values and the entire set of PLQY is reported in SI. Error bars are obtained propagating PLQY errors in Table 3-I. Further details in Section 2.2.

3.5 Conclusions

To summarize, in this Chapter are analyzed the drastic changes of steady-state PL properties at different excitation wavelengths. Decreasing PLQY values with increasing excitation energy, by factors reaching eight for the CdSe/ZnS series, and distinct behavior with the different chemical composition of the shell were observed. The explanation of these findings relies on the charge trapping dynamics. By using the information obtained by applying a kinetic model to the analysis of TRPL data,[1] we identified a correlation between the trapping and de-trapping rates and the PL efficiency. We then related the PLQY decrease at higher excitation energies to the fast trapping of hot carriers into vibrationally excited traps. The increased trapping/de-trapping ratio is unfavorable to the regeneration of emissive excitons. Instead, accumulation of trapped charges leads to loss of PLQY due to Auger trion recombination.

The different behavior of the EED of PLQY in the three series of core/shell QDs is explained as the result of differences in the confining potential and in the nature of the traps. A thorough characterization of the photophysical dynamics in the series of QDs investigated here via time-resolved measurements is presently underway in our lab.

In the last few years, there has been a fast-growing interest in applications of semiconductor nanocrystals in lighting and display technologies, where QDs operate in steady-state conditions under highly energetic excitation or charge injection. The results presented here provide hints as to the choice of most appropriate shell structures for high-efficiency emission.

References

1. Minotto, A.; Todescato, F.; Fortunati, I.; Signorini, R.; Jasieniak, J. J.Bozio, R., Role of Core-Shell Interfaces on Exciton Recombination in CdSe–Cdxzn1–Xs Quantum Dots. *The Journal of Physical Chemistry C* **2014**, *118*, 24117-24126.

2. Mooney, J.; Krause, M. M.; Saari, J. I.Kambhampati, P., Challenge to the Deep-Trap Model of the Surface in Semiconductor Nanocrystals. *Physical Review B* **2013**, *87*, 081201.

3. Jones, M.; Lo, S. S.Scholes, G. D., Quantitative Modeling of the Role of Surface Traps in CdSe/CdS/ZnS Nanocrystal Photoluminescence Decay Dynamics. *Proceedings of the National Academy of Sciences* **2009**, *106*, 3011-3016.

4. Abdellah, M.; Karki, K. J.; Lenngren, N.; Zheng, K.; Pascher, T.; Yartsev, A.Pullerits, T., Ultra Long-Lived Radiative Trap States in CdSe Quantum Dots. *The Journal of Physical Chemistry C* **2014**, *118*, 21682-21686.

5. García-Santamaría, F.; Brovelli, S.; Viswanatha, R.; Hollingsworth, J. A.; Htoon, H.; Crooker, S. A.Klimov, V. I., Breakdown of Volume Scaling in Auger Recombination in CdSe/CdS Heteronanocrystals: The Role of the Core–Shell Interface. *Nano Letters* **2011**, *11*, 687-693.

6. Gong, K.; Zeng, Y.Kelley, D. F., Extinction Coefficients, Oscillator Strengths, and Radiative Lifetimes of CdSe, CdTe, and CdTe/CdSe Nanocrystals. *The Journal of Physical Chemistry C* **2013**, *117*, 20268-20279.

7. Mooney, J.; Krause, M. M.Kambhampati, P., Connecting the Dots: The Kinetics and Thermodynamics of Hot, Cold, and Surface-Trapped Excitons in Semiconductor Nanocrystals. *The Journal of Physical Chemistry C* **2014**, *118*, 7730-7739.

8. Kambhampati, P., On the Kinetics and Thermodynamics of Excitons at the Surface of Semiconductor Nanocrystals: Are There Surface Excitons? *Chemical Physics* **2015**, *446*, 92-107.

9. Krause, M. M.Kambhampati, P., Linking Surface Chemistry to Optical Properties of Semiconductor Nanocrystals. *Physical Chemistry Chemical Physics* **2015**, *17*, 18882-18894.

10. Kambhampati, P., Hot Exciton Relaxation Dynamics in Semiconductor Quantum Dots: Radiationless Transitions on the Nanoscale. *The Journal of Physical Chemistry C* **2011**, *115*, 22089-22109.

11. Rumbles, G.; Selmarten, D. C.; Ellingson, R. J.; Blackburn, J. L.; Yu, P.; Smith, B. B.; Mićić, O. I.Nozik, A. J., Anomalies in the Linear Absorption, Transient Absorption, Photoluminescence and Photoluminescence Excitation Spectroscopies of Colloidal InP Quantum Dots. *Journal of Photochemistry and Photobiology A: Chemistry* **2001**, *142*, 187-195.

12. Tonti, D.; van Mourik, F.Chergui, M., On the Excitation Wavelength Dependence of the Luminescence Yield of Colloidal CdSe Quantum Dots. *Nano Letters* **2004**, *4*, 2483-2487.

13. Hoy, J.; Morrison, P. J.; Steinberg, L. K.; Buhro, W. E.Loomis, R. A., Excitation Energy Dependence of the Photoluminescence Quantum Yields of Core and Core/Shell Quantum Dots. *The Journal of Physical Chemistry Letters* **2013**, *4*, 2053-2060.

14. Dias, E. A.; Grimes, A. F.; English, D. S.Kambhampati, P., Single Dot Spectroscopy of Two-Color Quantum Dot/Quantum Shell Nanostructures. *The Journal of Physical Chemistry C* **2008**, *112*, 14229-14232.

15. Dabbousi, B. O.; Rodriguez-Viejo, J.; Mikulec, F. V.; Heine, J. R.; Mattoussi, H.; Ober, R.; Jensen, K. F.Bawendi, M. G., CdSe-ZnS Core–Shell Quantum Dots: Synthesis and Characterization of a Size Series of Highly Luminescent Nanocrystallites. *The Journal of Physical Chemistry B* **1997**, *101*, 9463-9475.

16. Xie, R.; Kolb, U.; Li, J.; Basché, T.Mews, A., Synthesis and Characterization of Highly Luminescent CdSe–Core CdS/Zn0.5cd0.5s/ZnS Multishell Nanocrystals. *Journal of the American Chemical Society* **2005**, *127*, 7480-7488.

17. van Embden, J.; Jasieniak, J.Mulvaney, P., Mapping the Optical Properties of CdSe/CdS Heterostructure Nanocrystals: The Effects of Core Size and Shell Thickness. *Journal of the American Chemical Society* **2009**, *131*, 14299-14309.

18. van Embden, J.Mulvaney, P., Nucleation and Growth of CdSe Nanocrystals in a Binary Ligand System. *Langmuir* **2005**, *21*, 10226-10233.

19. Fortunati, I.; Signorini, R.; Bozio, R.; Jasieniak, J. J.; Antonello, A.; Martucci, A.; Giustina, G. D.; Brusatin, G.Guglielmi, M., CdSe Core–Shell Nanoparticles as Active Materials for up-Converted Emission. *The Journal of Physical Chemistry C* **2011**, *115*, 3840-3846.

20. Todescato, F.; Minotto, A.; Signorini, R.; Jasieniak, J. J.Bozio, R., Investigation into the Heterostructure Interface of CdSe-Based Core-Shell Quantum Dots Using Surface-Enhanced Raman Spectroscopy. *ACS Nano* **2013**, *7*, 6649-6657.

21. Klimov, V. I., Spectral and Dynamical Properties of Multiexcitons in Semiconductor Nanocrystals. *Annual Review of Physical Chemistry* **2007**, *58*, 635-673.

22. Nirmal, M.; Norris, D. J.; Kuno, M.; Bawendi, M. G.; Efros, A. L.Rosen, M., Observation of the "Dark Exciton" in CdSe Quantum Dots. *Physical Review Letters* **1995**, *75*, 3728-3731.

23. Efros, A. L.; Rosen, M.; Kuno, M.; Nirmal, M.; Norris, D. J.Bawendi, M., Band-Edge Exciton in Quantum Dots of Semiconductors with a Degenerate Valence Band: Dark and Bright Exciton States. *Physical Review B* **1996**, *54*, 4843-4856.

24. Li, J.Wang, L.-W., First Principle Study of Core/Shell Structure Quantum Dots. *Applied Physics Letters* **2004**, *84*, 3648-3650.

25. Kossut, J., Quantum Dots: Squeeze or Stretch? *Nat Mater* **2009**, *8*, 8-9.

26. García-Santamaría, F.; Chen, Y.; Vela, J.; Schaller, R. D.; Hollingsworth, J. A.Klimov, V. I., Suppressed Auger Recombination in “Giant” Nanocrystals Boosts Optical Gain Performance. *Nano Letters* **2009**, *9*, 3482-3488.

27. Kambhampati, P., Unraveling the Structure and Dynamics of Excitons in Semiconductor Quantum Dots. *Accounts of Chemical Research* **2011**, *44*, 1-13.

28. Jones, M.; Lo, S. S.Scholes, G. D., Signatures of Exciton Dynamics and Carrier Trapping in the Time-Resolved Photoluminescence of Colloidal CdSe Nanocrystals. *The Journal of Physical Chemistry C* **2009**, *113*, 18632-18642.

29. McGuire, J. A.; Sykora, M.; Robel, I.; Padilha, L. A.; Joo, J.; Pietryga, J. M.Klimov, V. I., Spectroscopic Signatures of Photocharging Due to Hot-Carrier Transfer in Solutions of Semiconductor Nanocrystals under Low-Intensity Ultraviolet Excitation. *ACS Nano* **2010**, *4*, 6087-6097.

30. Gong, K.Kelley, D. F., Surface Charging and Trion Dynamics in CdSe-Based Core/Shell Quantum Dots. *The Journal of Physical Chemistry C* **2015**, *119*, 9637-9645.

31. Vaxenburg, R.; Rodina, A.; Shabaev, A.; Lifshitz, E.Efros, A. L., Nonradiative Auger Recombination in Semiconductor Nanocrystals. *Nano Letters* **2015**, *15*, 2092-2098.

32. Aruda, K. O.; Bohlmann Kunz, M.; Tagliazucchi, M.Weiss, E. A., Temperature-Dependent Permeability of the Ligand Shell of Pbs Quantum Dots Probed by Electron Transfer to Benzoquinone. *The Journal of Physical Chemistry Letters* **2015**, *6*, 2841-2846.

33. Rabouw, F. T.; Kamp, M.; van Dijk-Moes, R. J. A.; Gamelin, D. R.; Koenderink, A. F.; Meijerink, A.Vanmaekelbergh, D., Delayed Exciton Emission and Its Relation to Blinking in CdSe Quantum Dots. *Nano Letters* **2015**, *15*, 7718-7725.

34. Jortner, J., Temperature Dependent Activation Energy for Electron Transfer between Biological Molecules. *The Journal of Chemical Physics* **1976**, *64*, 4860-4867.

35. Cragg, G. E.Efros, A. L., Suppression of Auger Processes in Confined Structures. *Nano Letters* **2010**, *10*, 313-317.

CHAPTER 4

Surface and Interface Effects on Fast Recombinations

Part of this Chapter is based on:

Righetto et al. SPIE Optics & Photonics Proc. **2017**, 10348, 1034816
Righetto et al. SPIE Photonics Europe Proc. **2016**, 988421-988421-11

ABSTRACT- Understanding and controlling fast recombination in quantum dots (QDs) is prerequisite for most of QDs-based devices operations. As demonstrated in the previous Chapter, fast recombination may be triggered by charge accumulation at surfaces. Most of the fast recombination processes taking place in QDs rely on Auger mechanism. Hence, much of the current research in this field aims to achieve rationally tailored synthesis, through identification of factors lengthening recombinations, in the pursuit of better-performing nanostructures. Following this line, the effects of core/shell interface on fast recombination processes in CdSe/$Cd_xZn_{1-x}S$ QDs are investigated by means of ultrafast transient absorption (TA) spectroscopy.
In this work, the photophysical characterization of the core/shell QDs series, described in the first section of the previous Chapter, is brought to completion. A thorough data mining was carried on employing global and inversion methodologies on complex TA datasets. The disentangling of overlapping picosecond timescale dynamics unveiled both single and bi-exciton dynamics, and these results are discussed in relation to those obtained in the previous Chapter.
Specifically, the effect of the hetero-interface shape and defectivity on fast recombination dynamics was observed. Smoothing of interface potential, together with adequate surface passivation, appear to be crucial factors in slowing down both Auger-based and exciton trapping recombination. Either thick CdS shell or alloyed CdZnS shell efficiently suppress these processes. On the other hand, interfacial traps play a pivotal the recombination dynamics of CdSe/ZnS dots, providing additional relaxation channels. According to our results, alloyed CdZnS shell appears to be lucrative in view of the realization of QDs-based light emitting applications. Lastly, aiming to extend the validity of the kinetic model described in the previous Chapter, results from TA spectroscopy are compared with outcomes of kinetic modeling.

4.1 Introduction & State-of-the-Art

Although QDs based devices recently emerged as fast moving consumer goods, their potential in the optoelectronic field is yet to be fully disclosed. Indeed, beyond their current use as down-converters of blue light[1-2] in display devices, many more groundbreaking application promise to revolutionize the optoelectronic field, i.e., QD-light emitting devices (QD-LEDs) and wavelength tunable QD lasers.[3-5] Hurdles in the realization of these devices share a common origin: fast non-radiative recombination processes, severely impairing their performances.[6-7]

Since the inception of core/shell technology, many efforts have been spent on unraveling the effects of the inorganic shell on the QDs photophysics.[2, 8-11] Exciton and multi-exciton recombination processes are lively debated topics. The primary reason is that the coexistence of various and competitive photophysical effects (multi-exciton recombination, photo-charging and exciton trapping) hinders the unambiguous de-convolution of different recombination mechanisms.[12-14] Thus, the univocal determination of recombination rates is a challenging task and often leads to reported rates, differing by orders of magnitudes in identical conditions.

Klimov pioneered this field, employing ultrafast transient absorption (TA) and picosecond time-resolved photoluminescence (TRPL) techniques. In early 2000, he pointed out the role of Auger recombinations (AR) as the main hot-electron cooling mechanism in CdSe QDs (see Chapter 1).[15-16] Auger mediated energy transfer toward holes emerged as efficient relaxation channel, bypassing the phonon bottleneck effect caused by the absence of high-energy vibrations coupled with excitons. Indeed, the higher density of states for holes allows a rapid cooling of excitations. The exciton dynamics of core-only QDs systems was widely investigated, and Auger dimension scaling laws were formulated.[17-18] In the same years, kinetic analysis of TA data clarified the role of multi-exciton recombination. Multi-exciton Auger recombination (MER) is a detrimental process for laser applications. Indeed the optical gain lifetime is intrinsically limited by AR. Nevertheless, the possibility of multi-carrier generation raised interest in photovoltaic application of QDs.[19-20]

Recently, Kambhampati works shed new light on the impact of surfaces and interfaces on recombination processes. Indeed, he pointed out difficulties in disentangling surface-mediated and multi-exciton recombination.[21-22] Surface dangling bonds are localized sites that can act as charge acceptors, thereby generating non-emitting (dark) charged QDs.

As widely discussed in Chapter 1 and Chapter 3, long-lived surface charges enhance Coulomb interaction and promote Auger recombination of excitons and multi-excitons.[23] Therefore, a thorough understanding of surface and interface effects is of paramount importance, further emphasized by the wealth of available core/shell heterostructures. Indeed, the wide variety of inorganic heterostructures introduced during the last years (e.g., Type I, Quasi Type II, giant-QDs, alloyed shell, etc.) further complicated the picture.

For instance, the presence of an interface between core and shell alters the photophysics of core/shell systems and complicates the picture by adding a population of exciton traps.[24-25] Further studies identified the shape of the shell potential barrier as a parameter governing Auger recombination, singling out the role of shell chemical composition.[26-27] Although high-performing nanostructures were obtained, a deeper understanding of general principles governing these recombinations is still lacking. Thence, it would be highly desirable to carry on comparative studies, pointing out the role of different shell in either improving or hampering optical properties. This is precisely the line followed by much of the recent research in this field and underlies the philosophy of the work presented here.

As described in the previous Chapter, trapping in CdSe/$Cd_{1-x}Zn_xS$ core/shell QDs by nanosecond TRPL and steady-state emission spectroscopy.[28-29] Beyond the presence of thermodynamic trapping/detrapping equilibrium on the nanosecond timescale, hot exciton trapping and charged photoproduct creation was found to undermine emission efficiency.

Nevertheless, due to the complexity of the chain of events associated with charge trapping, which spans different timescales, a dynamical signature of these recombination processes has not been found yet. The following results and discussion aim to fill these gaps.

4.2 Transient Absorption Spectra of Core-Shell QDs

In this work, the three series of CdSe/$Cd_xZn_{1-x}S$ QDs (x = 0, 0.5, 1) presented in previous chapters were studied by means of TA technique. Measurements were carried on using the TA setup described in Materials&Method.1 Chapter, on QDs solutions in toluene.

Different measurements, under different excitation intensities, were carried on to probe different regimes of exciton dynamics. Quantitatively, the average number of excitons per dot ($\langle N \rangle = j \cdot \sigma$) was controlled by acting on pump fluence *j*, given the absorption cross section. In particular, for each sample fluence was set in order to achieve $\langle N \rangle = (0.8, 1.8, 3\ e-h)$, thereby giving access to both the mono and multi-excitonic regimes.

The quality of TA signals, i.e., ΔA values (differential absorption), depends on several parameters, such as the sample concentration, white light intensity, and stability. In this work, obtained spectra were post-processed to minimize noise (when necessary) and white light chirping effects, by using a homemade Matlab routine.

TA datasets consist of two-dimensional maps resolved both in wavelength and in time delay between pump and probe pulses, where the signal refers to pump-induced absorption changes (ΔA). In Figure 4.1**a**, an example of TA 2D map is reported. At first, a qualitative interpretation of these datasets can be obtained by sectioning 2D maps and pinpointing common features among different series.

Transient spectra (i.e., fixed time delay sections) observed for CdSe core QDs (Figure 4.1**b**) comprise five spectral features. Of these, two (A bands) are positive photo-induced absorptions (PIA), while three (B bands) are negative ground state bleaching signals (GSB). In Figure 4.1**b**, spectral structures for the first 6 ps of core CdSe QDs are shown.

In the literature, B1 is the most extensively investigated signal, representing the GSB of the band-edge 1S(e)-$1S_{3/2}$(h) exciton state. Other bleaching bands correspond to the 1S(e)-$2S_{3/2}$(h) (B2) and 1P(e)-$1P_{3/2}$(h) (B3) absorption transitions.[12]

As reported in the Figure, there is some degree of correspondence between the TA and linear absorption signals, especially for bleaching features. On the contrary, the nature of PIA signals is rather obscure at first sight. According to the discussion in Chapter 2, TA signals stems from three main contributions, i.e., GSB, PIA and stimulated emission (SE).

Hence, it is possible to express transient spectra as

$$\Delta A(\lambda) = -GSB(\lambda) - SE(\lambda) + PIA(\lambda) \qquad \textbf{(Eq. 4.1)}$$

where the spectral components of GSB and SE are usually taken to be the same as the linear absorption of the particular transition of interest.[30] On the other hand, the PIA signals depend on the systems considered. For QDs, PIA signals mainly concern transitions from a single exciton state to bi-excitonic states. The Coulomb potential of the two excitons squeezed into a dot confer to bi-excitonic states a bound character, associated with a bi-exciton binding energy Δ_{xx}.

According to Sewall [14] the transient spectra of QDs are then described as

$$\Delta A(\lambda) = -2A(\lambda) + A(\lambda + \frac{hc}{\Delta_{xx}}). \qquad \textbf{(Eq. 4.2)}$$

Recently, Tan demonstrated that A2 and B3 signals results as a "dispersive" lineshape originated from the different magnitude of the three contributions for biexcitonic states involving $|1P>$ excitons. This consideration explains the observed shift between linear absorption peak and B3 signal. Hence, observed features are induced by state filling.

However, in past years was postulated the presence of photo-generated local electric fields originated by photoexcited carries, acting on the spectral position and the oscillator strength of the probed transitions (quadratic Stark or bi-exciton effect). [21, 31] The bi-exciton effect is evident in Figure 4.1**b**. Observing the first recorded transient after t=0, the presence of two quantitatively smaller signals redshifted with respect to signals at longer time delays. These signals are generated by the presence of hot unrelaxed excitons in the dots, which shift the energy of the transitions with respect to the ground state.

Figure 4.1**c** shows qualitative evidence of the effect of the shell on transient spectra. In this figure, a representative comparison between QDs of the three different series with the same shell thickness (6ML) and at fixed time delay (Δt = 1ps), induced by the same pump fluence. The same signals observed in Figure 4.1**b** are present, reflecting that optical properties are mainly dictated by CdSe core.

Nevertheless, the ratio between the different signals varies with the shell composition. Some differences observed for the QDs with a CdS shell are likely related to the fact that also CdS absorbs at λ_{PUMP} = 400 nm. This leads to the bleaching of the CdS states, contributing to a fictitious decrease of the A2 band.

Such bleaching obscures the A2 band, and almost no positive ΔA signal is detected in CdS and CdZnS shells. Hence, a considerable fraction of the incident photons generates excitons in the shell material, which migrate to the lower band-gap CdSe core before recombining.[32]

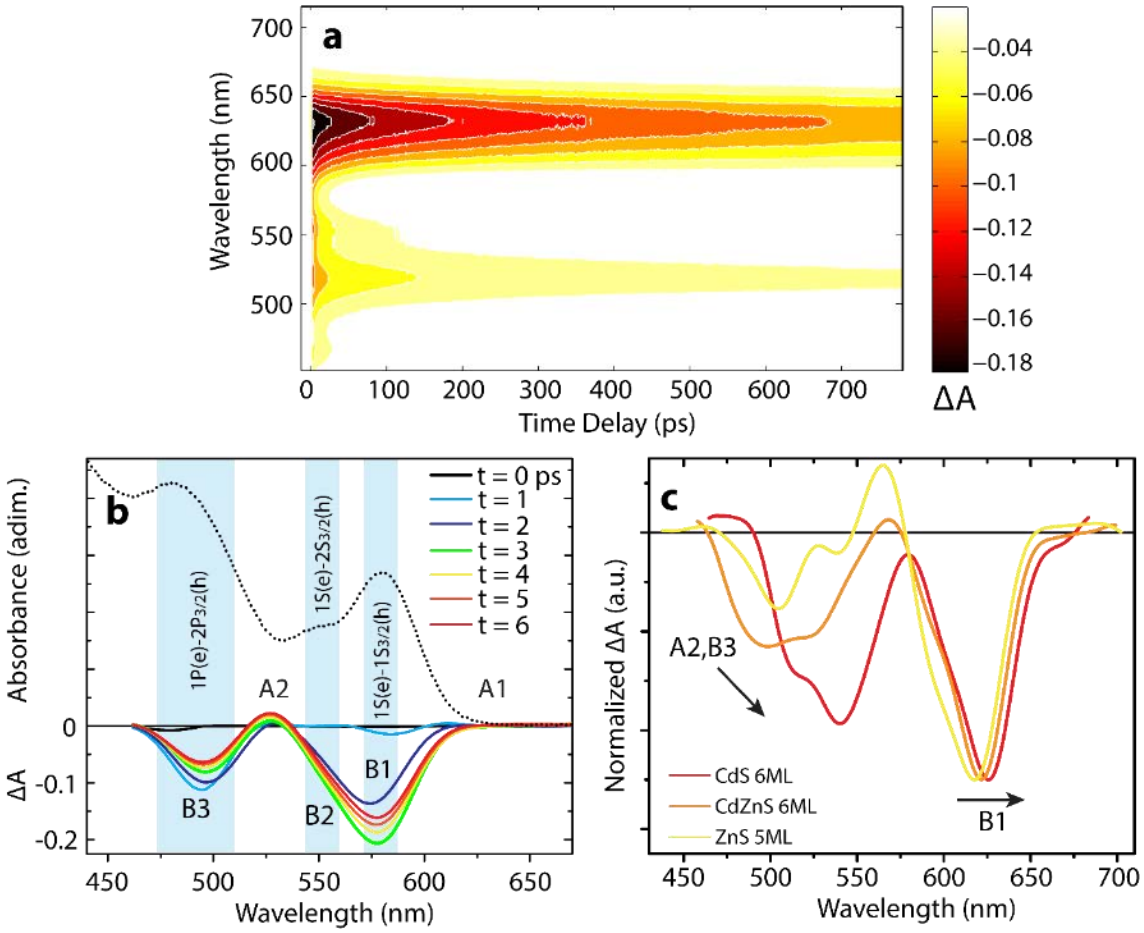

Figure 4.1 - (**a**) Complete multicolor TA dataset recorded for CdSe/ZnS QDs in toluene under <N>=1.8 excitation (**b**) Spectral structure (fixed delay time section) of TA 2D map recorded for small core CdSe at 3.0 average exciton occupancy. The dashed line shows the linear absorption spectrum; colored lines display the evolution of the differential absorption within the first 6 ps. Cyan shadowed regions assign each signal to a transition observable in the linear spectrum, in accordance with exciton transition defined in Chapter 1 (**c**) Comparison of transient spectra for different shell compositions at fixed shell thickness, fluence (3.0 e-h) and time delay (4 ps).

This transfer from CdS shell to CdSe core yields a shell dependent effective pumping rate of the core and consequently a modified relaxation dynamics. Considering that the CdS shell generated excitons can interact with surface trap states, the modification of the dynamics gets even more complicated.

4.3 Discussion on Absorption Cross Sections

Before discussing in detail the exciton dynamics of QDs and the shell effects on photophysics, it is crucial to address the question of absorption cross sections in QDs. As discussed in Chapter 2, the initial distribution of exciton occupancies in QDs ensembles, after a short laser pulse, follows Poissonian statistics. The average occupancy is then calculated as $\langle N \rangle = \sigma \cdot j$, where j [ph/cm^2] is the pump pulse fluence and σ [cm^2] is the absorption cross-section. Therefore, the probability distribution of having N excitons in a single quantum dot is given by:

$$P(N) = -\langle N \rangle^N e^{-(\langle N \rangle)}/N! \qquad \textbf{(Eq. 4.3)}$$

According to Klimov, it is possible to estimate maximum |ΔA/A| values, considering the exciton level multiplicity and assuming state filling as the source of the signal.[12]
For the B1 signal:

$$\left|\frac{\Delta A}{A}\right|_{max} = 0.5\,P(1) + \sum_{i=2}^{\infty} P(i) = 1 - e^{<N>}\left(1 + \frac{<N>}{2}\right) \qquad \textbf{(Eq. 4.4)}$$

Eq. 4.4 entails a universal relation between $|\Delta A/A|_{max}$ and the average number of e-h pairs generated in a QD assembly.

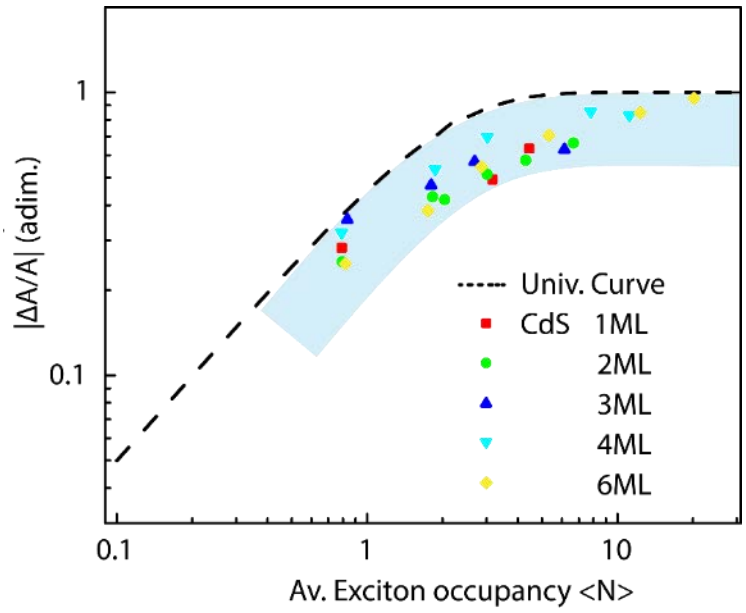

Figure 4.2-Comparison between Klimov's universal curve and measured data for CdSe/CdS series

As reported in Figure 4.2, our data show a substantial discrepancy from the calculated curve. Measured $|\Delta A/A|_{max}$ values systematically lay below the so-called "universal curve" (Eq. 4.4) in the cyan region.

A similar behavior was reported for other core/shell quantum dots and was ascribed to the presence of a PA component from charged QDs (i.e., trion PIA), which substantially overlaps the bleaching signal. [33] This contribution increases at high pump fluence, due to the *photocharging* effect, i.e., the accumulation of long living charges at QDs surfaces, among other detrimental for emission efficiency as discussed in the previous Chapter.[34]

Nevertheless, with the aim of delving deeper into this discrepancy, it would be more appropriate to consider this as a combination of several further contributions, among which the most important are: (i) the dependence of absorption cross section σ from the exciton occupancy; (ii) the shell effect during the exciton relaxation.

The first point to address is that the definitions of $|\Delta A/A|_{max}$ and ⟨N⟩ rely on the assumption of equal σ for exciton and multi-excitons. Recently, Pullerits and co-workers measured different σ for different average occupation numbers in CdSe QDs.[35] The decrease of σ with increasing ⟨N⟩ is compatible with the observed deviations. Howbeit, due to the high absorption coefficient at the excitation energy (400nm, 3.1eV) these deviations could arise from some inaccuracy in the estimation of the QDs concentration, as well. This is the most critical factor in determining a σ value independent from the e-h occupancy. Aiming to quantify these deviations, an effective value for σ was extracted from recorded data, through a manipulation of Equation 4.4 by expressing <N> as σ · j.

$$\left|\frac{\Delta A}{A}\right|_{max} = 0.5\,P(1) + \sum_{i=2}^{\infty} P(i) = 1 - e^{<N>}\left(1 + \frac{<N>}{2}\right) \qquad \textbf{(Eq. 4.5)}$$

As shown in Figure 4.3, 4.4, and 4.5, at higher fluence data strongly deviate from the predicted behavior, i.e., the universal curve is not a good model for such complex systems. Therefore, the presence of overlapping PIA components cannot be ruled out. The second crucial point is the effect of the CdS shell absorption cross-section, which influences the internal relaxation dynamics. Indeed, a non-unitary efficient shell-to-core exciton funneling process is a further possible source of deviation from the ideal behavior. Such a limited efficiency may arise from the higher probability of trapping of hot-excitons at the structural defects at interfaces (i.e., dislocations, stacking faults). [28, 36]

According to these preliminary considerations, it is evident that the source of TA signals is a complex mixture of differently populated QDs. Such a complex photophysical scenario requires an analytical method able to separate different contributions.

With this aim, the data analysis was carried on considering the entire set of data, exploiting two different and complementary methodologies: global analysis and inversion analysis.

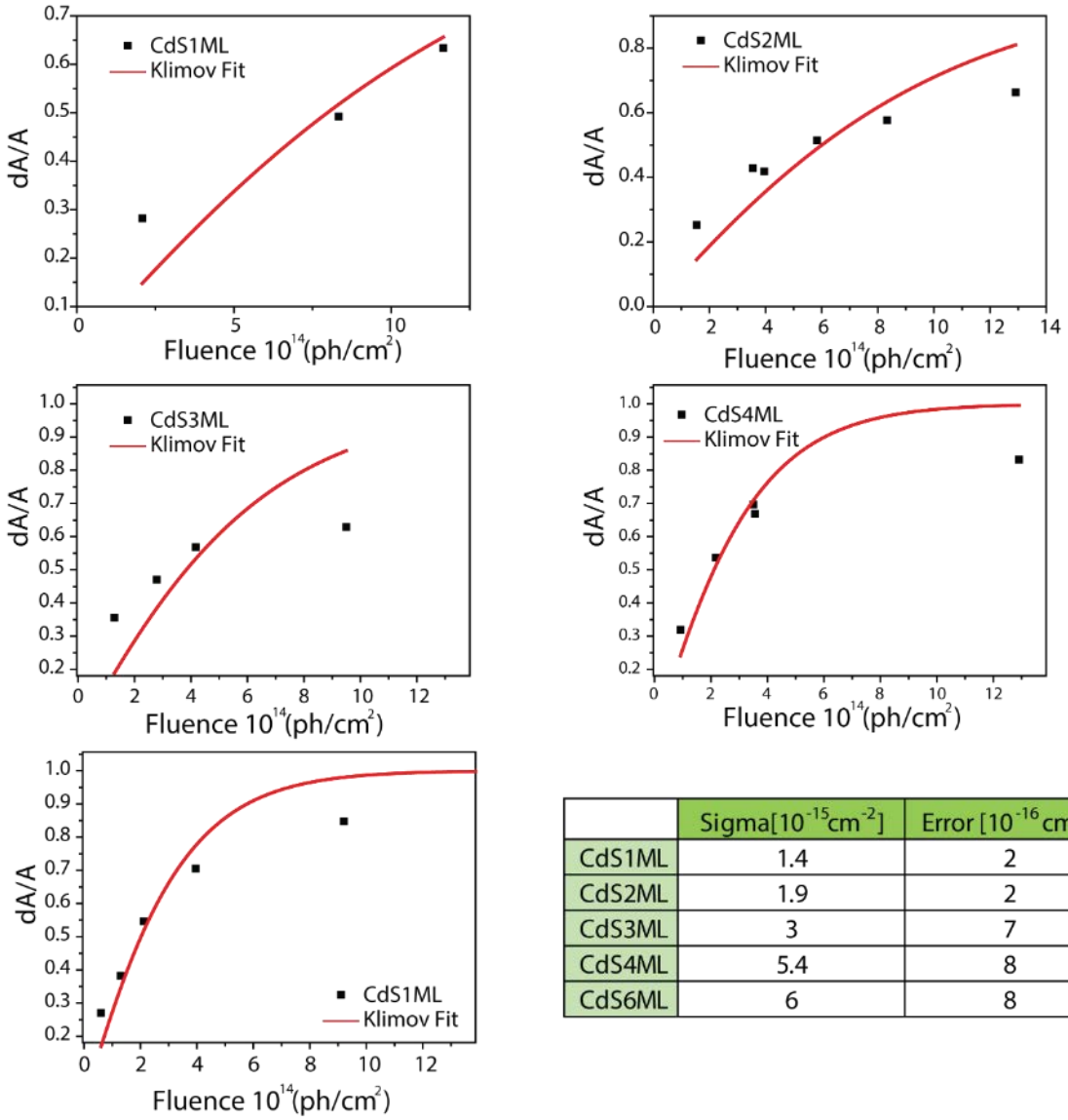

	Sigma[10^{-15}cm^{-2}]	Error [10^{-16} cm^{-2}]
CdS1ML	1.4	2
CdS2ML	1.9	2
CdS3ML	3	7
CdS4ML	5.4	8
CdS6ML	6	8

Figure 4.3- Nonlinear fitting curves of normalized B1 bleaching values as a function of the pump fluence for CdS series. Experimental points were fitted to the Klimov universal curve equation (Eq. 4.5), where absorption cross section σ is the only fitting parameter. In Table fitted values and fitting errors, these are inherently averaged values.

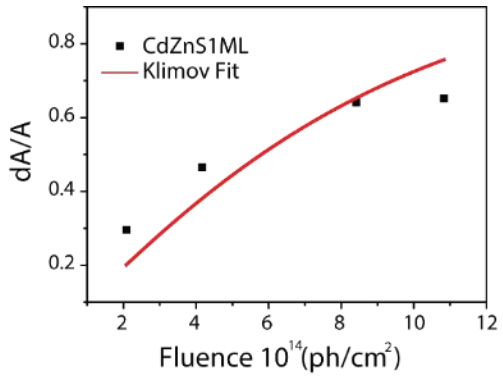

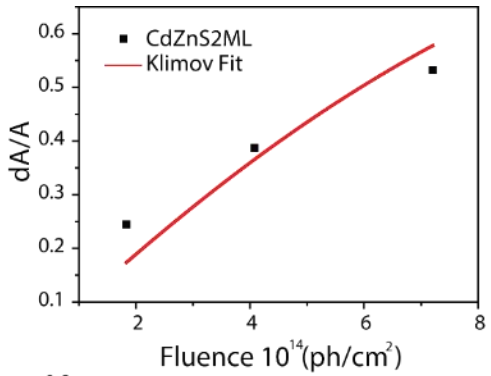

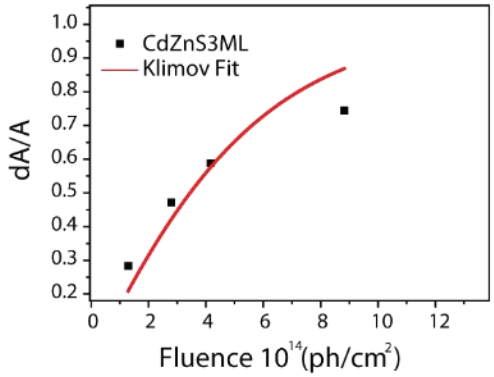

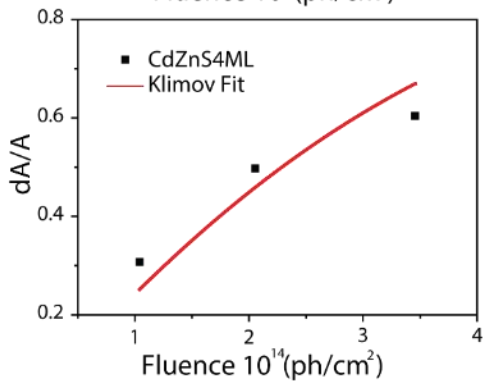

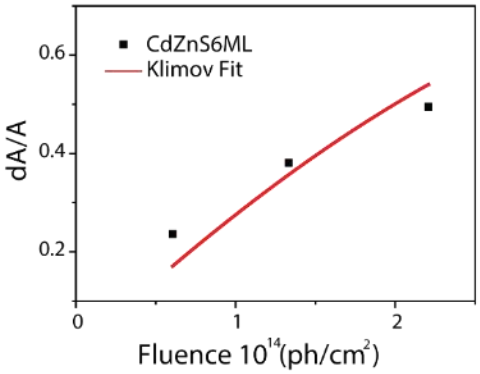

	Sigma[10^{15} cm^{-2}]	Error [10^{-16} cm^{-2}]
CdZnS1ML	1.9	3
CdZnS2ML	2	3
CdZnS3ML	3.3	5
CdZnS4ML	5	6
CdZnS6ML	5.7	7

Figure 4.4- Nonlinear fitting curves of normalized B1 bleaching values as a function of the pump fluence for CdZnS series. Experimental points were fitted to the Klimov universal curve equation (Eq. 4.5), where absorption cross section σ is the only fitting parameter. In Table fitted values and fitting errors, these are inherently averaged values.

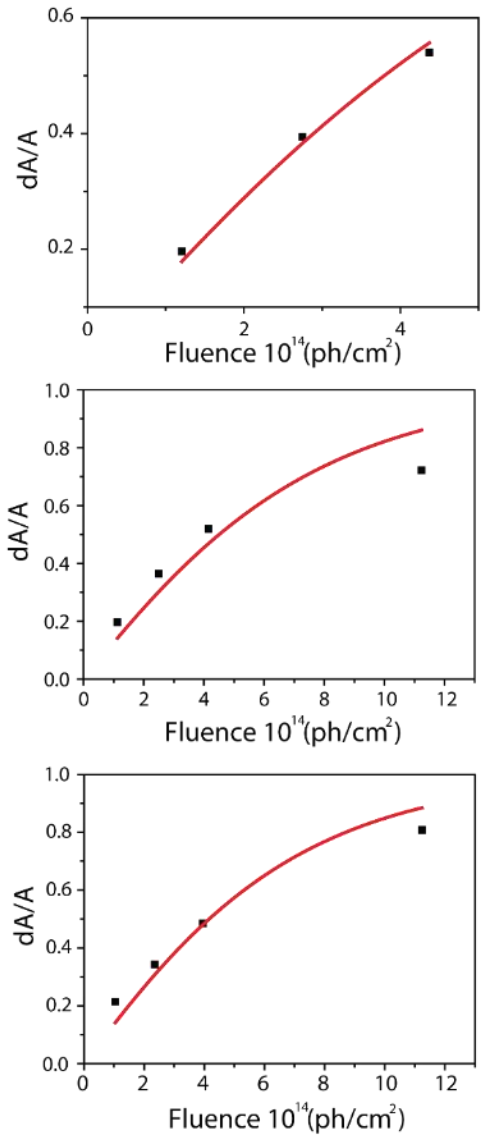

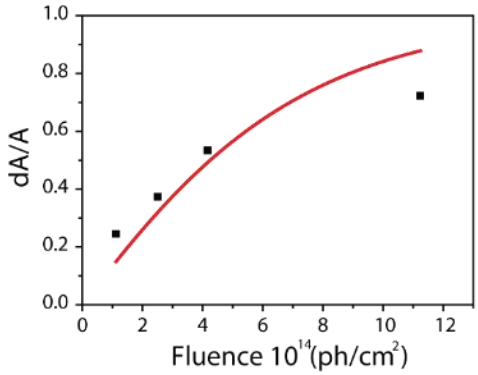

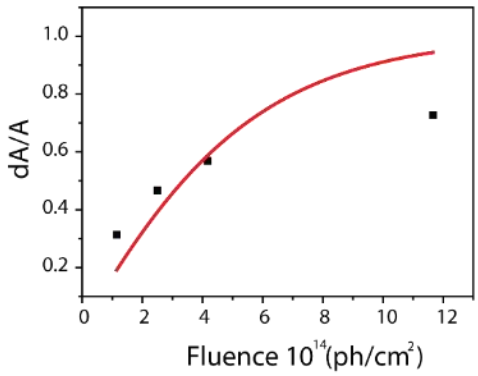

	Sigma[10^{15} cm^{-2}]	Error [10^{-16} cm^{-2}]
ZnS1ML	3	1
ZnS2ML	2.7	5
ZnS3ML	2.6	4
ZnS4ML	5	6
ZnS6ML	3	4

Figure 4.5- Nonlinear fitting curves of normalized B1 bleaching values as a function of the pump fluence for ZnS series. Experimental points were fitted to the Klimov universal curve equation (Eq. 4.5), where absorption cross section σ is the only fitting parameter. In Table fitted values and fitting errors, these are inherently averaged values.

4.4 Global Analysis of TA datasets

TA datasets were analyzed in a global fashion, in order to disentangle contributions from different photophysical species, as discussed above. In order to achieve a more stable and reproducible analysis, avoiding the occurrence of local minima due to parameter correlation, data were inspected by SVD analysis. SVD is one of the most employed mathematical techniques in solving nonlinear least squares problem.[37] This technique allows avoiding the fit of the whole wavelength set, therefore reducing the number of computational efforts. SVD is used to determine the set of signal components that can reconstruct the data via linear combination. It is widely accepted that fitting SVD traces provide the number and values of time constants with high accuracy, limiting the risk of mathematical artifacts.

Mathematically, SVD analysis looks for a collection of principal spectra $S_i(\lambda)$ and time decays $I_i(t)$ such that the observed TA dataset is reproduced by $\Delta A(\lambda, t) = \sum_i S_i(\lambda) \otimes I_i(t)$. In case only n distinct time behaviors in a data set are present, SVD analysis will return significant values of $S_i(\lambda)$ for only the first n spectra. Thus, SVD is particularly suitable for the identification of the number of independently evolving features. Notably, SVD analysis does not uniquely determine the components, allowing for orthogonal rotations that mix them, so that linear combinations need to be chosen on physical grounds.

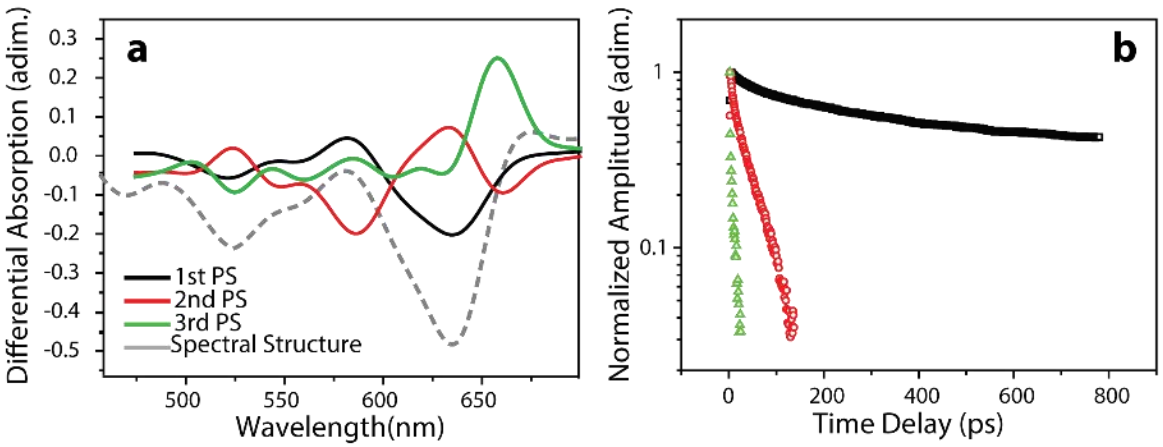

Figure 4.6- (**a**) First three principal spectra obtained by SVD global fit of CdSe/ZnS 3ML under <N>=3e-h excitation (solid lines) and normalized spectral structure at 2ps time delay (dashed line). **(b)** Corresponding normalized decay profiles, related to the temporal behavior of the three PS (note color correspondence).

This analysis was carried out using both an integrated Matlab routine by van Wilderen [38] and a homemade Matlab Routine. Then, the interpretation of SVD eigenvectors on the inspection of the spectral structures followed the approach proposed by Turk [39] .

Though this method, recurring pattering along the datasets recorded for the whole CdSe/$Cd_xZn_{1-x}S$ QDs series. The interpretation of SVD results was extended to three distinct temporal behaviors, considering up to the third significant singular vector.

Analogously to results by Turk, on different systems [39]. In Figure 4.6 are shown the outcomes of the SVD analysis for CdSe/ZnS 3ML QDs under a pump pulse fluence that generates an average number of electron-hole pairs (e-h) per dot <N> = 3. These outcomes consist of a set of right- and left-singular vectors (RSV, Figure 4.6**a,** and LSV, Figure 4.6**b**) and right singular values (RSVs) or *principal spectra* (PS).

PS represent the decomposition in constituting species of the spectral structures. Their amplitudes were found to be significant only for the first three RSV; thus, the whole 2D dataset is well described using these three components. Left singular values (LSVs), or *decay profiles* (DP), represent the temporal behavior of the corresponding PS. Despite being, in a strict sense, mathematical entities where signals related to physically relevant species are mixed to some degree; it is still possible to assign physical significance to singular values.[39-40]

The first principal spectrum corresponds precisely to the spectral structure recorded at long time delay (> 600ps, see Fig. 4.7) at which all species related to bi-exciton or multi-exciton species have decayed; therefore, it can be safely assigned to singly excited QDs species.

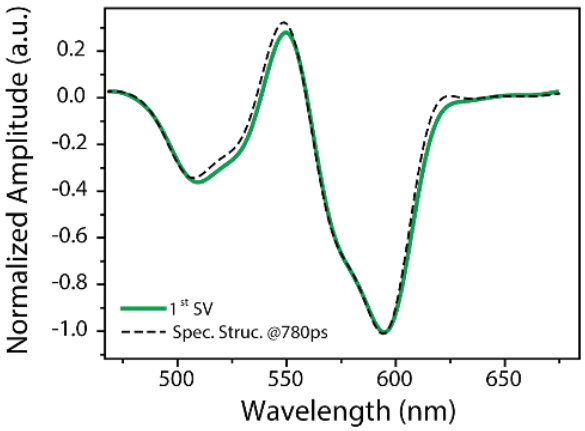

Figure 4.7- Comparison between the first RSV and the spectral structure, measured at 780ps time delay between pump and probe pulse., for CdSe/CdZnS 1ML sample. Other samples display the same recurrent behavior, i.e., the first RSV coincides with TA signals at long time delays.

A further inspection of principal spectra in Figure 4.6**a** reveals that the most significant feature of the second PS is a bleaching signal, red-shifted (660 nm) with respect to the B1 signal (around 635 nm). The magnitude of this redshift is consistent with reported values for bi-exciton binding energies Δ_{xx}.[12, 41-42] Moreover, the amplitude of this species increases with pump fluence.

Therefore, it can be safely assigned to doubly excited QDs (i.e., bi-excitons). The third PS exhibits a peculiar time behavior, indicating a combination of species rather than a pure one. According to Turk, this component mostly accounts for the first picoseconds of the spectrum, when hot-exciton relaxation occurs.[39] In addition, it is worth to note that at long time delays (i.e., t > 300 ps) the 2nd and 3rd decay profiles invert their sign and the negative amplitude reaches 10% of their initial (positive) value. This effect is probably a mathematical artifact, caused by mixing of different species, which could not be entirely eliminated by eigenvector rotations.

In Figure 4.8**a** are shown the DPs for the singly excited QDs species (first DP in Fig. 4.6**b**) for the three series of core/shell QDs. The recombination ratio is obtained out of these curves, by calculating the ratio between early time (t= 1 ps) and late time (t=780ps) amplitudes (Fig. 4.8**b**). The recombination ratio $R_x = \frac{\Delta A(t=780ps)}{\Delta A(t=1ps)}$ (also called B/A ratio) is widely used to calculate multi-exciton generation efficiencies (MEG).[12]

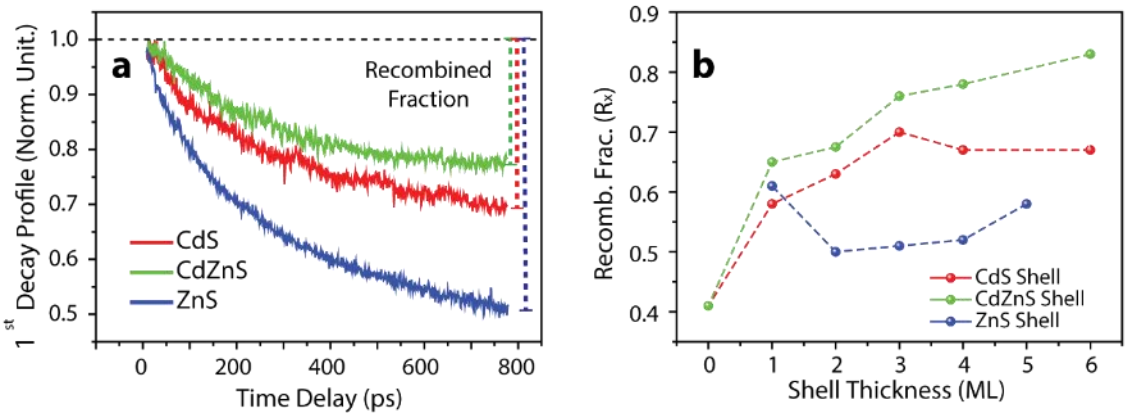

Figure 4.8- (**a**) Shell effect on first DP obtained by SVD analysis. Reported curves for CdSe/CdS 3ML (red) CdSe/CdZnS 3ML (green) CdSe/ZnS 3ML (blue) under fixed 0.8 average exciton occupancy. (**b**) Recombined fraction (R_x) values for different shell thickness and composition (lines are guide for the eyes) at fixed 0.8 average exciton occupancy

Yet in presented experiments, MEG effects can be ruled out by energetic considerations, i.e., the excitation energy of the pump is far lower than the energy of two relaxed excitons. According to the presented interpretation of SVD outputs, R_x describes the magnitude of recombination for singly excited QDs. Noteworthy, shell type and thickness profoundly influence R_x value. For the CdS and CdZnS shell series, a general increasing trend of R_x with increasing shell thickness is observed.

Table 4-I - Ratio between short and long time amplitudes for first DP, calculated by SVD

CdSe/CdS				CdSe/CdZnS				CdSe/ZnS			
ML	0,8 eh	1,8 eh	3 eh	ML	0,8 eh	1,8 eh	3 eh	ML	0,8 eh	1,8 eh	3 eh
0	0,41	0,31	0,26	0	0,41	0,31	0,26	--	--	--	--
1	0,58	0,55	0,45	1	0,65	0,6	0,56	1	0,61	0,51	0,47
2	0,63	0,55	0,46	2	0,675	0,63	0,59	2	0,5	0,48	0,46
3	0,7	0,63	0,5	3	0,76	0,63	0,6	3	0,51	0,475	0,43
4	0,67	0,61	0,5	4	0,78	0,64	0,63	4	0,52	0,47	0,43
6	0,67	0,62	0,53	6	0,83	0,67	0,63	5	0,58	0,5	0,46

Quantitatively, R_x increases from 0.41 in bare CdSe cores to 0.67 in CdSe/CdS 6ML and 0.83 in CdSe/CdZnS 6ML, under the same excitation condition (<N>=0.8). Conversely, the R_x trend for CdSe/ZnS series reveals an enhanced recombination, beyond the first shell ML growth. The dynamics of these fast recombinations can be ascribed to trap-mediated Auger or "*trion*" recombinations. Indeed, ultrafast trapping processes can produce long-lived charged states enhancing Auger recombination.[28, 43]

In the previous Chapter, these fast recombinations were hypothesized to account for non-unitary PLQY values. Here, is presented the direct observation of their dynamics. An increase of R_x is to be attributed to reduced trapping and enhanced surface passivation. Nevertheless, also the smoothness of hetero-interface confining potential plays a role in inhibiting Auger recombinations. These factors explain observed shell trends, where the smooth CdS hetero-interface provides a sufficient confinement, but better performances are obtained with alloyed CdZnS shell. CdZnS merges the good confinement provided by ZnS and the smoothness of the interface. ZnS shell behavior is due to dislocated and defective epitaxial growth. Indeed, CdSe/ZnS hetero-interface is known to exceed the elastic energy limit for coherent epitaxial growth, as shown by Raman measurements.[25, 44] Resulting interface traps contribute to the degradation of optical properties, thereby reducing shelling advantages.

In order to confirm the role of trapped charges accumulation in determining R_x values, fluence resolved experiments were performed and R_x values were evaluated at increasing average exciton population <N> = 0.8, 1.8 and 3, as reported in Table 4-I As a general trend, increasing in <N> results in a decrease of R_x values. Furthermore, this effect is more pronounced for thin CdS and CdZnS shell, suggesting that accumulation of long-lived charge states takes place at surfaces. This dynamical effect is consistent with the results first reported by Brus et al.[45] The accumulation of long-living charges due to hot-exciton trapping deeply affects exciton dynamics, especially under intense excitation.

The analysis of the 2nd DP allowed extracting information on the bi-exciton recombinations (Figure 4.9). Bi-exciton recombination times (τ_{xx}) are expected to be dependent on: (1) QDs volume (2) interface potential shape and height.[46-47]

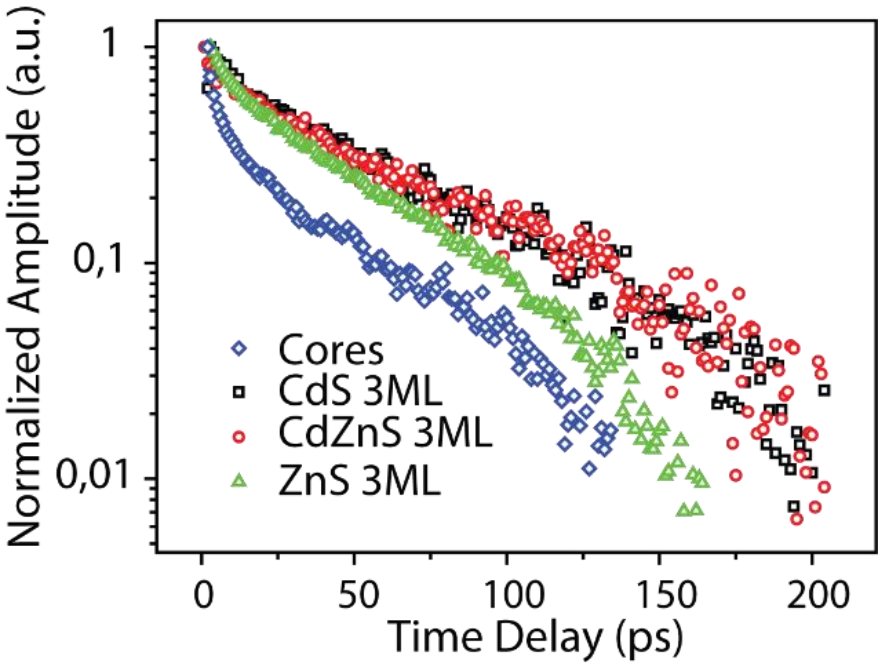

Figure 4.9- Amplitude of 2nd decay profiles of CdSe core (blue), CdSe/CdS 3ML (black), CdSe/CdZnS 1ML (red), CdSe/ZnS 3ML (green) from TA measurements in multi-excitonic regime (average exciton occupancy 1.8)

Multi-exponential fitting of curves in Figure 4.9 reveals two exponential decay components. Recently, Kelley observed a bi-exponential behavior of bi-excitons in CdSe/ZnSe; trapping and Auger recombination were assessed as recombination mechanisms. In particular, fast decay was associated with interface traps, while slow component was assigned to bi-exciton Auger recombination.[48] This view is enforced by recent work from Kambhampati, reporting the occurrence of a bi-excitonic trapping effect at surfaces.[21] Briefly, the two types of bi-exciton Auger recombinations can be explained in terms of considerations regarding momentum conservation. As discussed in Chapter 1, Auger recombination process is associated with considerable momentum variation. Indeed, starting from three or four carriers at zone center, this process results in highly excited particles, carrying high momentum. The translational symmetry breaking in QDs introduces high momentum components in the carriers' wavefunctions, thereby increasing the overlap between initial and final state. The rate of the biexciton Auger process is therefore dependent on momentum considerations. Trapped carriers at surfaces or interfaces are associated with high momentum component, due to their spatial localization. Thence, the Auger recombination dynamics involving these carriers are expected to be faster than those of conventional biexcitons.

Table 4-II Biexponential fitting results for decay profiles reported in Figure 4.9

QDs	α_1	t_1 (ps)	α_2	t_2 (ps)
Core CdSe	0,75	6±1	0,25	128±11
CdSe/CdS 3ML	0,52	39±5	0,48	196±20
CdSe/CdZnS 3ML	0,5	27±3	0,5	180±17
CdSe/ZnS 3ML	0,61	17±1	0,39	127±8

As reported in Table 4-II, shell type modulates both decay components. For CdS and CdZnS series, shell thickness growth has a double effect: a reduction of the magnitude of the short decay component and a lengthening of the longer one. Thus, the shell composition effect on bi-exciton recombination is evident, highlighting surface/interface defectivity and smoothness of interface potential as essential parameters. This effect is in agreement with that reported for giant CdS shell QDs [49-50]. On the contrary, ZnS exhibits a non-monotonous trend: the slowest recombination is obtained for 2ML thickness. Once more, the interface defectivity plays a fundamental role also in multi-excitations dynamics.[28-29] A quantitative analysis of the 3rd PS is challenging. As pointed out by Turk, this eigenvector contains residuals of different species and mixes them [39]. The position of the main PA (red-shifted with respect to B1) and the early fast decay of this signal are signatures of hot-exciton QDs species. As discussed in Chapter 1, hot exciton cooling mechanism is based on Auger processes, as well. In Figure 4.10 it is possible to observe how shell thickness and composition modulate these recombinations. Hence, through global analysis we confirmed the presence of early PA signal (3rd PS), affecting B1 normalized amplitude immediately after relaxation. This contributes to explain deviations from the universal curve calculated by Klimov.

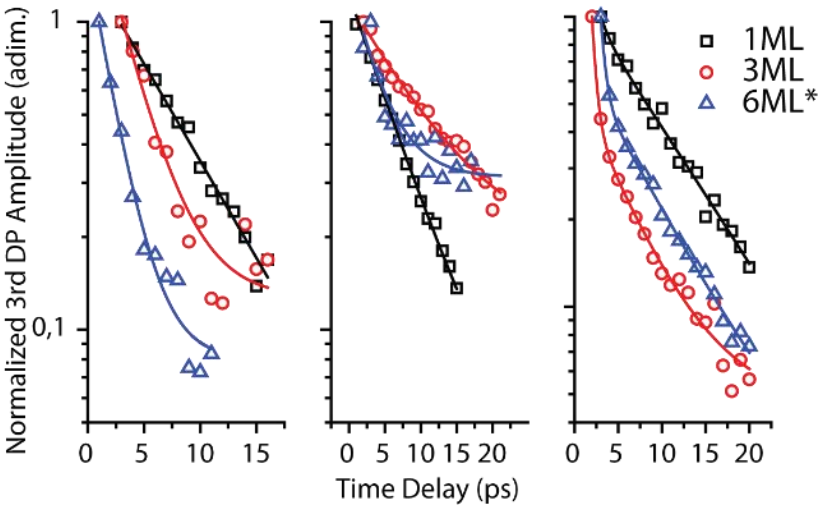

Figure 4.10 - Shell dependence of 3rd DPs, representing hot exciton relaxation in QDs. Dots are the experimental points, and solid lines are exponential fit. Data are reported for the three series.

4.5 Inversion Analysis of P&P transients

Despite being highly efficient in separating different contribution, SVD based global analysis is a semi-quantitative analysis technique. In order to obtain quantitative rates and get an insight into photo-physical processes involved, rather than on the different species, inversion analysis was applied to B1 transients. Such analysis was introduced for QDs by Bristow [51] and relies on the conversion of differential absorption signals in recombination curves, plotted as a function of excited carrier density. This method is widely used for bulk semiconductor characterization.[52] The underlying assumption is the direct and univocal relation between the differential absorption signal ΔA and the excited carrier density (n) within the material. The relation used to derive the number of excited carriers/cm^3 needed to apply the inversion analysis was slightly modified with respect to that used by Bristow.

Indeed, in a number of papers [51, 53], Bristow proposed a revised version of inversion method, initially introduced by Linnros. [52, 54-55]

The inversion equation proposed was

$$\boldsymbol{n} = -\frac{1}{\sigma d} ln\left(1 - \frac{\Delta A}{A}\right) \qquad \textbf{(Eq. 4.6)}$$

where the excited carrier density n is related to the measured signal ΔA, via absorption cross section σ and optical path.

This equation can be restated in a correct form, by starting from the very definition of the measured quantities in TA spectroscopy. The differential absorption signal in terms of transmittance $T = I/I_0$ can be expressed as

$$\frac{\Delta T}{T} = \frac{T_{on} - T_{off}}{T_{off}} = \frac{I_{on} - I_{off}}{I_{off}} \qquad \textbf{(Eq. 4.7)}$$

where subscript on/off indicates the presence/absence of optical pumping. According to Beer-Lambert law, the light intensity can be expressed as

$$I_{off} = I_0 e^{-\sigma_0 N d}$$
$$I_{on} = I_0 e^{-[\sigma_0 (N-n)+\sigma n]d} \sim I_0 e^{-[\sigma_0 N+\sigma n]d} \qquad \textbf{(Eq. 4.8)}$$

respectively for unpumped and pumped, where N is the number of QDs and n is the number of QDs excited by the pump. Last equivalence is obtained within weak pumping approximation, i.e., ground state depletion is neglected. Therefore, by substitution of Eq. 4.7 in Eq. 4.8

$$\frac{I_{on} - I_{off}}{I_{off}} = e^{-\sigma n d} - 1 = \frac{\Delta T}{T} \qquad \textbf{(Eq. 4.9)}$$

Solving for n, the obtained equation is

$$n = -\frac{1}{\sigma d} ln\left(1 - \frac{\Delta T}{T}\right) \qquad \textbf{(Eq. 4.10)}$$

which resemble Eq. 4.6, with absorbance replaced by transmittance. Notably, equation 4.10 is correct and cannot be transformed into equation (proposed by Bristow) without invoking some approximations.

Yet all experiments and reported data are presented in terms of absorbance $A = -\ln T$, then it is possible to recast the correct Eq. 4.10. Once more, starting from the very definition of absorbance

$$\frac{\Delta A}{A} = \frac{A_{on} - A_{off}}{A_{off}} \qquad \textbf{(Eq. 4.11)}$$

which, according to Beer-Lambert law can be restated as

$$\begin{gathered} A_{off} = \sigma_0 N d \\ A_{on} = [\sigma_0 (N - n) + \sigma n] d \sim [\sigma_0 N + \sigma n] d \end{gathered} \qquad \textbf{(Eq. 4.12)}$$

Then, the substitution of Eq. 4.12 into Eq. 4.11 yields

$$\frac{\Delta A}{A} = \frac{\sigma n d}{\sigma_0 N d} \qquad \textbf{(Eq. 4.13)}$$

Lastly, akin to equation 4.10 , when solving for n, it is possible to obtain the correct equation for inverting transient absorption data, expressed in absorbance

$$n = \frac{\Delta A}{\sigma d} \qquad \textbf{(Eq. 4.14)}$$

For practical purposes (e.g., the study of QDs) Eq. 4.14 can be recast as following

$$n(t) = \frac{\Delta A(t)}{\sigma_{1S}\, d} \qquad \textbf{(Eq. 4.15)}$$

where σ_{1S}, i.e., the absorption cross section (CS) for the $|1S\rangle$ exciton, d is the sample thickness.

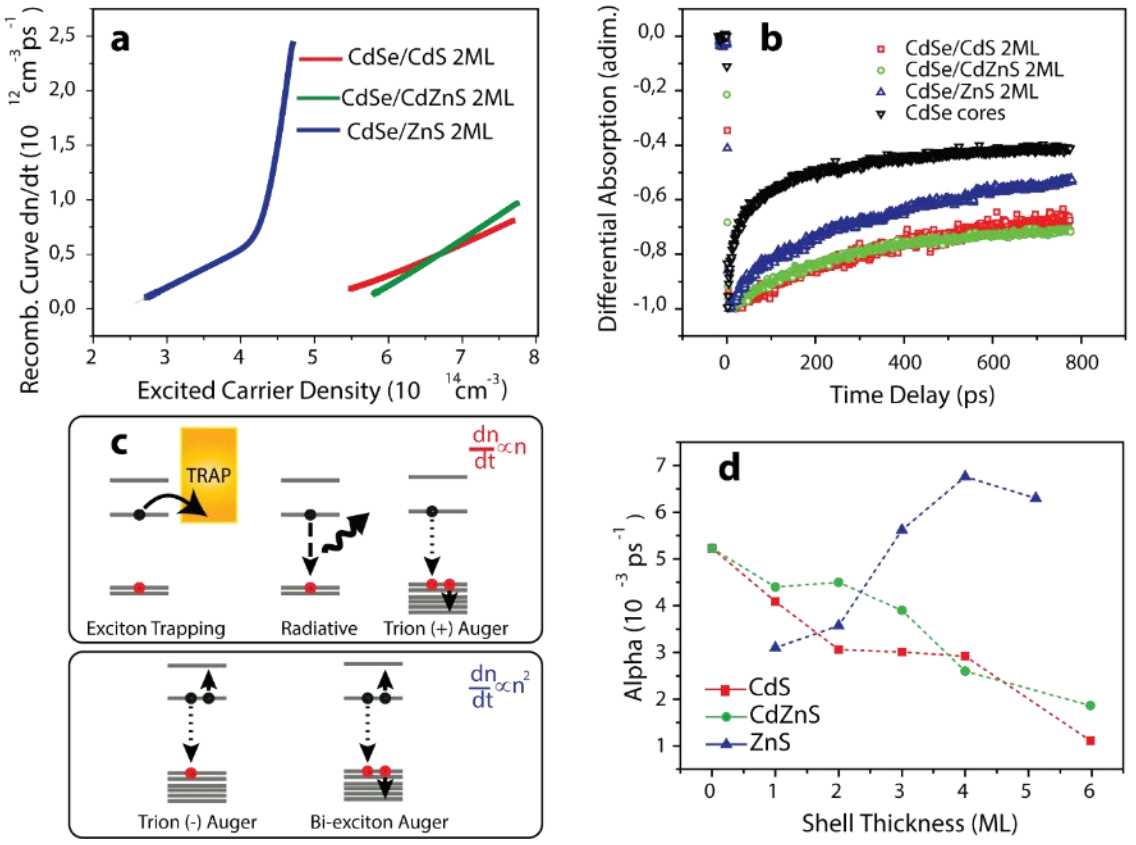

Figure 4.11 – Effect of shell composition on the recombination curves (**a**) and B1 transients (**b**). Data extracted from uTA measured under low fluence <N> = 0.8 and identical shell thickness (2ML). Differences in recombination dynamics are emphasized in the recombination curves with enlarged scales. (**c**) Microscopic recombination mechanisms classified by their excited carrier power dependence. In the upper part of the scheme mechanisms displaying a linear dependence on carrier density are collected, whereas in the lower part mechanism with a quadratic dependence are shown. (**d**) Linear recombination coefficient α, extracted from the recombination curves, as a function of shell composition and thickness. Data are extracted by linear fitting of the linear part of recombination curves for B1 transient, measured at low pump fluence <N> = 0.8 e-h

In Figure 4.11**a** and 4.11**b** are report the inverted and original transients for the different shell at a fixed thickness (2ML). Recombination curves are modeled according to the equation:

$$\frac{dn}{dt} = \alpha n + \beta n^2 + \gamma n^3 + \delta n^4 + \cdots \qquad \textbf{(Eq. 4.16)}$$

Albeit some differences are noticeable in the comparison of B1 transients (Figure 4.11**b**), inversion method amplifies them (Figure 4.11**a**). However, most importantly, different recombination mechanisms are separated according to power scaling with carrier density. The proposed interpretation deviates from that initially proposed in the definition of n^m dependence of various recombination processes (Figure 4.11**c**). The nature of B1 non-linear signal lies beneath this deviation. It is well established that, due to the asymmetry in the conduction and valence band density of states, B1 signal is proportional to the electron rather than exciton level occupancy,[12, 15, 21, 23] i.e. we have $\Delta A_{1S} \propto \langle n_{1S_e} \rangle$.

Therefore, linear dependence is assigned to single exciton trapping process, positive trion Auger recombination and radiative recombination. On the other hand, the quadratic dependence is ascribed to bi-exciton and negative trion Auger recombination. Figure 4.11**c** briefly sketches the different recombination processes and summarizes proposed assignments.

In Figure 4.11**d**, the quantitative behaviors of the linear coefficient α (Eq. 4.16) are reported. According to the assignment in Figure 4.**11c**, the linear part of recombination curves stems from Read-Hall-Shockley trapping processes, radiative recombination, and positively charged trions. Since electron trapping is not expected to be a dominant process in amine-capped QDs, due to passivation of Lewis acid Cd^{2+} sites,[21, 56] this recombination is mainly assigned to positively charged QDs. Linear coefficient α markedly decrease with increasing shell thickness, for both CdS and CdZnS series. On the other hand, within ZnS shell series the linear coefficient grows (Figure 4.11**d**). Noteworthy, these trends are consistent with those observed in the inspection of the first DP. The resemblance with the inverse of R_x (Figure 4.8) enforces our assignation to positively charged QDs recombination.

In this work were considered recombination curves calculated from the B1 transients for the entire set of data. Although different species concur with a considerable amplitude to the B1 signal, reported results on inversion focus on the sole single exciton dynamics.

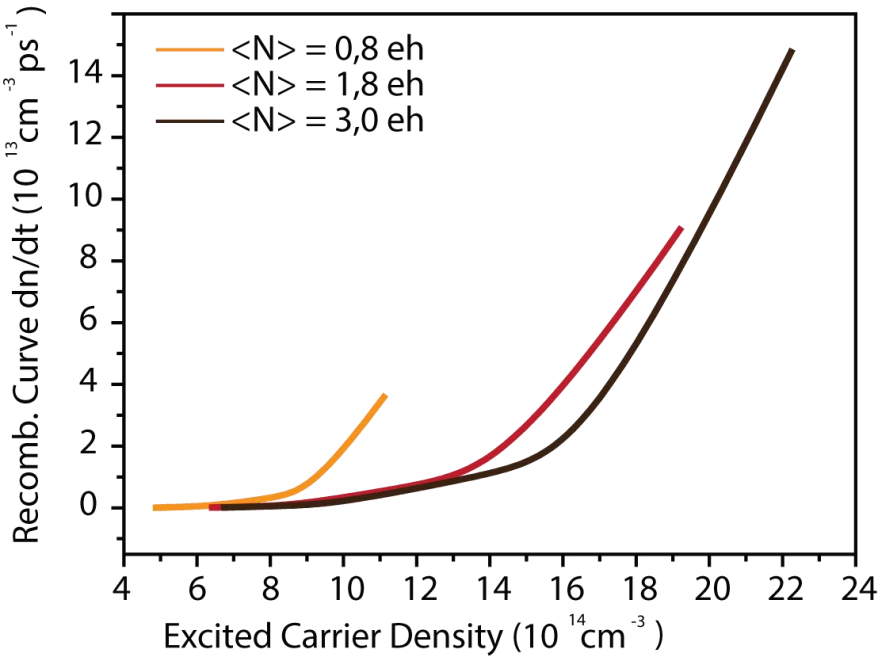

Figure 4.12- Recombination curves calculated for CdSe core B1 transient at increasing pump fluence. Increasing average exciton occupancy different dynamics appears in terms of different branches of recombination curves.

As shown in Figure 4.12, when increasing the pump fluence, it is possible to observe distinct regions in recombination curves. These are ascribed to different dominant recombination mechanisms, as already reported for core CdSe QDs.[51] Fluence plays a significant role in determining the shape of recombination curve. At increasing pump fluence (curves for <N> = 0.8, 1.8 and 3.0 in Fig. 4.12), branches with a different excited carrier power scaling appear. This indicates the presence of new species (multi-excitons, etc), leading to different recombination mechanisms. Beyond this, a fluence effect is observed on the slope at high carrier density (Fig. 4.12). A simple explanation relies on the dependence of quadratic and higher power rates on the excited carrier density. Nevertheless, it has to be stressed that these branches are only semi-quantitative in nature. Unfortunately, in this case, the application of inversion analysis to obtain multi-exciton recombination rates is inherently troublesome. This is a controversial point in the application of this method to QDs. The use of σ_{1S} (Eq. 4.15) implicitly assumes that the TA non-linear signal is generated by single excitons and forcedly assign to the wealth of other photo-physical species populating QDs ensemble the same absorption cross-section. However, multi-exciton cross sections were found to be substantially different from the single exciton one. [35] This would result in inherently biased and erroneous recombination rates.

4.6 A Comprehensive Photophysical Picture of the $CdSe/Cd_xZn_{1-x}S$ QDs series.

The TA data analysis provides information on fast recombination processes, occurring within the first hundreds of picoseconds after photo-excitation. As discussed above, prof. Bozio's group recently presented a thorough characterization of structures and fluorescence dynamics of $CdSe/Cd_xZn_{1-x}S$ QDs. [25, 29] A phenomenological kinetic model lays at the heart of the proposed analysis. As widely described in Chapter 3, the key to this model is the exciton trapping/detrapping equilibrium, operating on a nanosecond timescale. [29] Nevertheless, in Chapter 3, it is demonstrated that the phenomenological model can account for finite quantum yield (PLQY) values only by admitting processes operating on faster timescales, such as hot-exciton trapping and charged QDs Auger recombination.[28] The first PS, untangled by SVD from complex TA datasets, as well as the linear part of the recombination curves, obtained by inversion analysis, are the dynamical signatures of these fast recombination processes. In order to test further the consistency of the kinetic model, it is possible to predict these fast recombination rates for the studied samples.

Non-unitary PLQY values stem from the presence of non-radiative recombination pathways. However, it is necessary to define the relation between trapping (v_t) and de-trapping (v_{dt}) velocities and non-radiative recombination rate (k_{nr}). As discussed in Chapters 1 and 3, PLQY can be calculated by solving kinetic equations, in steady state approximation,

$$\begin{cases} 0 = \sum_i \left(v_{dt,i}\rho_i(t) - (v_{t,i} + k_{NR} + k_R)\rho_X(t) \right) \\ 0 = v_{t,i}\rho_X(t) - v_{dt,i}\rho_i(t) \end{cases} \qquad \textbf{(Eq. 4.17)}$$

where the second equation yields the equivalence $\rho_i = \frac{v_{t,i}}{v_{dt,i}}\rho_X$. Assuming that non-radiative recombinations are dominated by trapping and de-trapping the relation

$$k_{NR} = \sum_i \left(v_{t,i} - v_{dt,i} \right) \qquad \textbf{(Eq. 4.18)}$$

appears to be reasonable, i.e., non-radiative recombinations are dominated by the equilibrium between trapping and de-trapping velocities.

Substitution of Eq. 4.18 into the first equation in the systems Eq 4.17 yields

$$\left[\sum_i (v_{t,i} - v_{dt,i}) + k_R\right]\rho_X = 0 \qquad \textbf{(Eq. 4.19)}$$

and by manipulation, it is possible to obtain the definition

$$k_R = \sum_i (v_{dt,i} - v_{t,i}) = -k_{NR} \qquad \textbf{(Eq. 4.20)}$$

Using the very definition of PLQY, and substituting Eq. 4.20 yields to the unpromising and unphysical result

$$PLQY = \frac{k_R}{k_R + k_{NR}} \quad \Rightarrow \quad PLQY \to \infty$$

independently from k_t and k_{dt} rates, and from their definition. This fundamental inconsistency stems from the possibility of having detrapping from empty sites. Nevertheless, a re-definition of PLQYcould be useful in solving this basic inconsistency. Indeed, QDs are, at least, non-equilibrium three-level systems, whereas the definition $PLQY = \frac{k_r}{\sum_i k_i}$ is obtained for two-level systems.

To solve this, the phenomenological definition of PLQY as the ratio between emitted and absorbed photons must be used. According to the kinetic equations for bound excitons ρ_X and trapped excitons ρ_i :

$$\begin{bmatrix}\dot{\rho}_x \\ \dot{\rho}_t\end{bmatrix} = \begin{bmatrix}-(k_r + k_{nr} + v_t) & v_{dt} \\ v_t & -v_{dt}\end{bmatrix} \qquad \textbf{(Eq. 4.21)}$$

The resulting PLQY definition for three-level systems is

$$PLQY = \frac{k_r \int_0^\infty \rho_x(t)dt}{\rho_x(0)} \qquad \textbf{(Eq. 4.22)}$$

where the number of emitted photons is the product of radiative rate (k_r) and the time-integrated bound exciton population. On the other hand, the initial exciton population quantifies the number of absorbed photons.

Thus, using data from References 31 and 32, k_{nr} values were fitted to the measured PLQY values, presented in the previous Chapter.

Results, shown in Figure 4.13, show that calculated k_{nr} values are systematically lower (two to six times lower) with respect to linear recombination coefficient α, obtained by TA measurements.

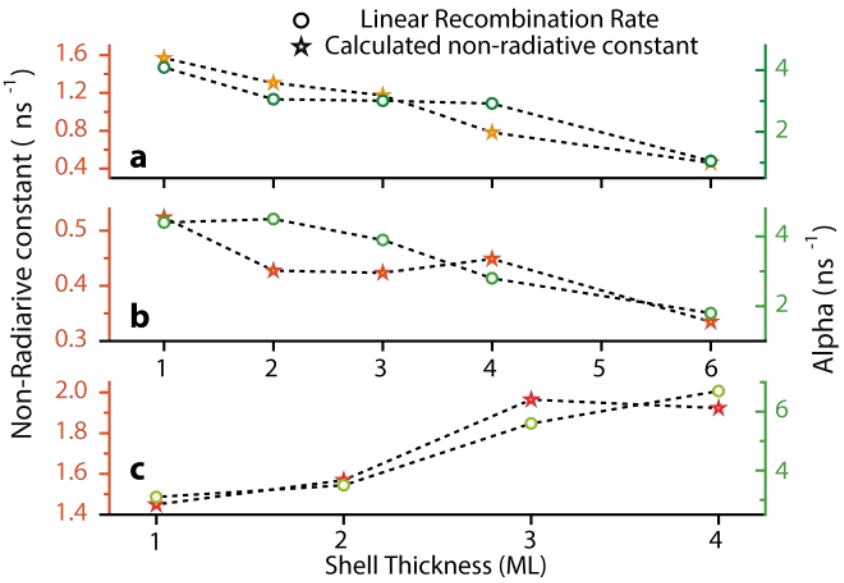

Figure 4.13- Comparison between non-radiative recombination constant (k_{nr}), estimated by kinetic model, and linear recombination coefficient (α), obtained by inversion analysis. Values are compared for CdSe/CdS (**a**) CdSe/CdZnS (**b**) and CdSe/ZnS (**c**) quantum dots.

From a physical point of view, higher recombination rates are consistent with the photophysics of QDs systems presented throughout these chapters. Indeed, TA measurements employ higher excitation fluences with respect to those commonly used in fluorescence spectroscopy. Therefore, the accumulation of surface charges is enhanced, and Auger recombinations are promoted.

Nevertheless, k_{nr} and α values behave in a similar way with respect to shell thickness. Namely, independently from the surface charging magnitude, the shell effect is similar. For CdS and CdZnS shell, thicker shell protects excitons from surface mediated Auger recombination. On the other hand, recombination rates increase with increasing ZnS shell thickness, because of interface defects.

4.7 Conclusions

The wealth of information contained in TA spectra was successfully disclosed, combining two different data analysis methods. The comparison between different shells evidenced the role of different factors in influencing fast recombination. Moreover, through the kinetic model description, these data allowed completing the photophysical picture of CdSe/$Cd_xZn_{1-x}S$ species.

The global analysis allowed identifying different species giving rise to the rich core-shell QDs photo-physics. Through inspection of the PS and fitting of their decay profile, single and bi-exciton species were assigned, and their dynamics were inspected. Their dynamics revealed the importance of surface passivation and the observed differences between shell composition pointed out the importance of hetero-interface defectivity and potential barriers. On the other hand, the revisited inversion analysis offered a disentangled point of view on TA transients. Consistently with global analysis outcomes, main processes governing single excitation dynamics within these timescales were found to be either exciton trapping or charge-mediated Auger recombination. The observed mounting surface passivation for CdS and CdZnS shells with increasing thickness highlights the importance of a complete surface passivation, i.e., shifting surface traps away from bound excitons, in smaller gap shells. On the other hand, despite higher passivation granted by a larger gap, ZnS fast recombinations are driven by interfacial defect sites. Thence, the interplay between surface and interface traps, surface passivation and strain-induced defects, stems as a fundamental character of core-shell QDs heterostructures. Moreover, through kinetic model-based analysis, these same photophysical processes were demonstrated to play a pivotal role in determining QY values. In summary, completed the characterization of CdSe/$Cd_xZn_{1-x}S$ QDs was taken to completion, providing both the characterization of their properties and the explanation for such behavior.

These findings, together with those reported in Chapter 2 are supposed to result in application directed suggestions.

Application concerning light emission, possibly involving bi-exciton emission (i.e. QD-LED and QD-Lasers), would preferably employ CdZnS o analogous shell determining a smoothed but confining potential barrier. Nonetheless, shell thickness plays a pivotal role in the optimization of CdS and CdZnS optical properties, mostly by mere displacement of surface traps away from surfaces.

Photo-chemical experiments and photo-voltaic application could look to CdSe/CdS or similar quasi-Type II core/shell systems. The intriguing combination of surface accessibility and long exciton and bi-exciton lifetimes offers attractive opportunities for QD solar and for the new field of QDs photochemistry.

References

1. Caruge, J. M.; Halpert, J. E.; Wood, V.; Bulovic, V.Bawendi, M. G., Colloidal Quantum-Dot Light-Emitting Diodes with Metal-Oxide Charge Transport Layers. *Nat Photon* **2008**, *2*, 247-250.

2. Yang, Y.; Zheng, Y.; Cao, W.; Titov, A.; Hyvonen, J.; MandersJesse, R.; Xue, J.; Holloway, P. H.Qian, L., High-Efficiency Light-Emitting Devices Based on Quantum Dots with Tailored Nanostructures. *Nat Photon* **2015**, *9*, 259-266.

3. Klimov, V. I.; Mikhailovsky, A. A.; Xu, S.; Malko, A.; Hollingsworth, J. A.; Leatherdale, C. A.; Eisler, H. J.Bawendi, M. G., Optical Gain and Stimulated Emission in Nanocrystal Quantum Dots. *Science* **2000**, *290*, 314-317.

4. Guzelturk, B.; Kelestemur, Y.; Akgul, M. Z.; Sharma, V. K.Demir, H. V., Ultralow Threshold One-Photon- and Two-Photon-Pumped Optical Gain Media of Blue-Emitting Colloidal Quantum Dot Films. *The Journal of Physical Chemistry Letters* **2014**, *5*, 2214-2218.

5. Todescato, F., et al., Soft-Lithographed up-Converted Distributed Feedback Visible Lasers Based on CdSe–CdZnS–ZnS Quantum Dots. *Advanced Functional Materials* **2012**, *22*, 337-344.

6. Klimov, V. I.; Ivanov, S. A.; Nanda, J.; Achermann, M.; Bezel, I.; McGuire, J. A.Piryatinski, A., Single-Exciton Optical Gain in Semiconductor Nanocrystals. *Nature* **2007**, *447*, 441-446.

7. Dang, C.; Lee, J.; Breen, C.; Steckel, J. S.; Coe-Sullivan, S.Nurmikko, A., Red, Green and Blue Lasing Enabled by Single-Exciton Gain in Colloidal Quantum Dot Films. *Nat Nano* **2012**, *7*, 335-339.

8. Reiss, P.; Protière, M.Li, L., Core/Shell Semiconductor Nanocrystals. *Small* **2009**, *5*, 154-168.

9. Dabbousi, B. O.; Rodriguez-Viejo, J.; Mikulec, F. V.; Heine, J. R.; Mattoussi, H.; Ober, R.; Jensen, K. F.Bawendi, M. G., CdSe-ZnS Core–Shell Quantum Dots: Synthesis and Characterization of a Size Series of Highly Luminescent Nanocrystallites. *The Journal of Physical Chemistry B* **1997**, *101*, 9463-9475.

10. Kim, H. H.; Park, S.; Yi, Y.; Son, D. I.; Park, C.; Hwang, D. K.Choi, W. K., Inverted Quantum Dot Light Emitting Diodes Using Polyethylenimine Ethoxylated Modified ZnO. *Scientific Reports* **2015**, *5*, 8968.

11. Kamat, P. V.Scholes, G. D., Quantum Dots Continue to Shine Brightly. *The Journal of Physical Chemistry Letters* **2016**, *7*, 584-585.

12. Klimov, V. I., Spectral and Dynamical Properties of Multiexcitons in Semiconductor Nanocrystals. *Annual Review of Physical Chemistry* **2007**, *58*, 635-673.

13. Kambhampati, P., Multiexcitons in Semiconductor Nanocrystals: A Platform for Optoelectronics at High Carrier Concentration. *The Journal of Physical Chemistry Letters* **2012**, *3*, 1182-1190.

14. Sewall, S. L.; Cooney, R. R.; Dias, E. A.; Tyagi, P.Kambhampati, P., State-Resolved Observation in Real Time of the Structural Dynamics of Multiexcitons in Semiconductor Nanocrystals. *Physical Review B* **2011**, *84*, 235304.

15. Klimov, V. I.; Mikhailovsky, A. A.; McBranch, D. W.; Leatherdale, C. A.Bawendi, M. G., Mechanisms for Intraband Energy Relaxation in Semiconductor Quantum Dots: The Role of Electron-Hole Interactions. *Physical Review B* **2000**, *61*, R13349-R13352.

16. Klimov, V. I.; Mikhailovsky, A. A.; McBranch, D. W.; Leatherdale, C. A.Bawendi, M. G., Quantization of Multiparticle Auger Rates in Semiconductor Quantum Dots. *Science* **2000**, *287*, 1011-1013.

17. Sampat, S.; Karan, N. S.; Guo, T.; Htoon, H.; Hollingsworth, J. A.Malko, A. V., Multistate Blinking and Scaling of Recombination Rates in Individual Silica-Coated CdSe/CdS Nanocrystals. *ACS Photonics* **2015**, *2*, 1505-1512.

18. Klimov, V. I.; McGuire, J. A.; Schaller, R. D.Rupasov, V. I., Scaling of Multiexciton Lifetimes in Semiconductor Nanocrystals. *Physical Review B* **2008**, *77*, 195324.

19. Klimov, V. I., Mechanisms for Photogeneration and Recombination of Multiexcitons in Semiconductor Nanocrystals: Implications for Lasing and Solar Energy Conversion. *The Journal of Physical Chemistry B* **2006**, *110*, 16827-16845.

20. Zhao, K.; Pan, Z.Zhong, X., Charge Recombination Control for High Efficiency Quantum Dot Sensitized Solar Cells. *The Journal of Physical Chemistry Letters* **2016**, *7*, 406-417.

21. Kambhampati, P., Hot Exciton Relaxation Dynamics in Semiconductor Quantum Dots: Radiationless Transitions on the Nanoscale. *The Journal of Physical Chemistry C* **2011**, *115*, 22089-22109.

22. Walsh, B. R.; Saari, J. I.; Krause, M. M.; Nick, R.; Coe-Sullivan, S.Kambhampati, P., Controlling the Surface of Semiconductor Nanocrystals for Efficient Light Emission from Single Excitons to Multiexcitons. *The Journal of Physical Chemistry C* **2015**, *119*, 16383-16389.

23. Tyagi, P.Kambhampati, P., False Multiple Exciton Recombination and Multiple Exciton Generation Signals in Semiconductor Quantum Dots Arise from Surface Charge Trapping. *The Journal of Chemical Physics* **2011**, *134*, 094706.

24. Jones, M.; Lo, S. S.Scholes, G. D., Quantitative Modeling of the Role of Surface Traps in CdSe/CdS/ZnS Nanocrystal Photoluminescence Decay Dynamics. *Proceedings of the National Academy of Sciences* **2009**, *106*, 3011-3016.

25. Todescato, F.; Minotto, A.; Signorini, R.; Jasieniak, J. J.Bozio, R., Investigation into the Heterostructure Interface of CdSe-Based Core-Shell Quantum Dots Using Surface-Enhanced Raman Spectroscopy. *ACS Nano* **2013**, *7*, 6649-6657.

26. Wang, X., et al., Non-Blinking Semiconductor Nanocrystals. *Nature* **2009**, *459*, 686-689.

27. Climente, J. I.; Movilla, J. L.Planelles, J., Auger Recombination Suppression in Nanocrystals with Asymmetric Electron-Hole Confinement. *Small* **2012**, *8*, 754-759.

28. Righetto, M.; Minotto, A.Bozio, R., Bridging Energetics and Dynamics of Exciton Trapping in Core-Shell Quantum Dots. *The Journal of Physical Chemistry C* **2016**.

29. Minotto, A.; Todescato, F.; Fortunati, I.; Signorini, R.; Jasieniak, J. J.Bozio, R., Role of Core-Shell Interfaces on Exciton Recombination in CdSe–Cdxzn1–Xs Quantum Dots. *The Journal of Physical Chemistry C* **2014**, *118*, 24117-24126.

30. Zhang, C.; Do, T. N.; Ong, X.; Chan, Y.Tan, H.-S., Understanding the Features in the Ultrafast Transient Absorption Spectra of CdSe Quantum Dots. *Chemical Physics* **2016**, *481*, 157-164.

31. Wen, G. W.; Lin, J. Y.; Jiang, H. X.Chen, Z., Quantum-Confined Stark Effects in Semiconductor Quantum Dots. *Physical Review B* **1995**, *52*, 5913-5922.

32. Bae, W. K.; Padilha, L. A.; Park, Y.-S.; McDaniel, H.; Robel, I.; Pietryga, J. M.Klimov, V. I., Controlled Alloying of the Core-Shell Interface in CdSe/CdS Quantum Dots for Suppression of Auger Recombination. *ACS Nano* **2013**, *7*, 3411-3419.

33. Nanda, J.; Ivanov, S. A.; Htoon, H.; Bezel, I.; Piryatinski, A.; Tretiak, S.Klimov, V. I., Absorption Cross Sections and Auger Recombination Lifetimes in Inverted Core-Shell Nanocrystals: Implications for Lasing Performance. *Journal of Applied Physics* **2006**, *99*, 034309.

34. Klimov, V. I.; Mikhailovsky, A. A.; Xu, S.; Malko, A.; Hollingsworth, J. A.; Leatherdale, C. A.; Eisler, H.-J.Bawendi, M. G., Optical Gain and Stimulated Emission in Nanocrystal Quantum Dots. *Science* **2000**, *290*, 314-317.

35. Lenngren, N.; Garting, T.; Zheng, K.; Abdellah, M.; Lascoux, N.; Ma, F.; Yartsev, A.; Žídek, K.Pullerits, T., Multiexciton Absorption Cross Sections of CdSe Quantum Dots Determined by Ultrafast Spectroscopy. *The Journal of Physical Chemistry Letters* **2013**, *4*, 3330-3336.

36. Xie, R.; Kolb, U.; Li, J.; Basché, T.Mews, A., Synthesis, and Characterization of Highly Luminescent CdSe−Core CdS/Zn0.5cd0.5s/ZnS Multishell Nanocrystals. *Journal of the American Chemical Society* **2005**, *127*, 7480-7488.

37. Golub, G. H.Van Loan, C. F., *Matrix Computations*; Johns Hopkins University Press, 2012.

38. van Wilderen, L. J. G. W.; Lincoln, C. N.van Thor, J. J., Modelling Multi-Pulse Population Dynamics from Ultrafast Spectroscopy. *PLoS ONE* **2011**, *6*, e17373.

39. Turk, M. E.; Vora, P. M.; Fafarman, A. T.; Diroll, B. T.; Murray, C. B.; Kagan, C. R.Kikkawa, J. M., Ultrafast Electron Trapping in Ligand-Exchanged Quantum Dot Assemblies. *ACS Nano* **2015**, *9*, 1440-1447.

40. Ruckebusch, C.; Sliwa, M.; Pernot, P.; de Juan, A.Tauler, R., Comprehensive Data Analysis of Femtosecond Transient Absorption Spectra: A Review. *Journal of Photochemistry and Photobiology C: Photochemistry Reviews* **2012**, *13*, 1-27.

41. Sewall, S. L.; Cooney, R. R.; Anderson, K. E. H.; Dias, E. A.; Sagar, D. M.Kambhampati, P., State-Resolved Studies of Biexcitons and Surface Trapping Dynamics in Semiconductor Quantum Dots. *The Journal of Chemical Physics* **2008**, *129*, 084701.

42. Choi, Y.; Sim, S.; Lim, S. C.; Lee, Y. H.Choi, H., Ultrafast Biexciton Spectroscopy in Semiconductor Quantum Dots: Evidence for Early Emergence of Multiple-Exciton Generation. *Scientific Reports* **2013**, *3*, 3206.

43. Klimov, V. I., *Nanocrystal Quantum Dots, Second Edition*; Taylor & Francis, 2010.

44. Gong, K.; Beane, G.Kelley, D. F., Strain Release in Metastable CdSe/CdS Quantum Dots. *Chemical Physics* **2016**, *471*, 18-23.

45. Li, S.; Steigerwald, M. L.Brus, L. E., Surface States in the Photoionization of High-Quality CdSe Core/Shell Nanocrystals. *ACS Nano* **2009**, *3*, 1267-1273.

46. Mangum, B. D.; Sampat, S.; Ghosh, Y.; Hollingsworth, J. A.; Htoon, H.Malko, A. V., Influence of the Core Size on Biexciton Quantum Yield of Giant CdSe/CdS Nanocrystals. *Nanoscale* **2014**, *6*, 3712-3720.

47. Zhao, J.; Chen, O.; Strasfeld, D. B.Bawendi, M. G., Biexciton Quantum Yield Heterogeneities in Single CdSe (CdS) Core (Shell) Nanocrystals and Its Correlation to Exciton Blinking. *Nano Letters* **2012**, *12*, 4477-4483.

48. Beane, G. A.; Gong, K.Kelley, D. F., Auger and Carrier Trapping Dynamics in Core/Shell Quantum Dots Having Sharp and Alloyed Interfaces. *ACS Nano* **2016**, *10*, 3755-3765.

49. García-Santamaría, F.; Brovelli, S.; Viswanathan, R.; Hollingsworth, J. A.; Htoon, H.; Crooker, S. A.Klimov, V. I., Breakdown of Volume Scaling in Auger Recombination in CdSe/CdS Heteronanocrystals: The Role of the Core–Shell Interface. *Nano Letters* **2011**, *11*, 687-693.

50. Rabouw, F. T., et al., Dynamics of Intraband and Interband Auger Processes in Colloidal Core-Shell Quantum Dots. *ACS Nano* **2015**, *9*, 10366-10376.

51. Senty, T. R.; Cushing, S. K.; Wang, C.; Matranga, C.Bristow, A. D., Inverting Transient Absorption Data to Determine Transfer Rates in Quantum Dot–Tio2 Heterostructures. *The Journal of Physical Chemistry C* **2015**, *119*, 6337-6343.

52. Linnros, J.Grivickas, V., Carrier Lifetime: Free Carrier Absorption, Photoconductivity, and Photoluminescence. In *Characterization of Materials*, John Wiley & Sons, Inc.: 2002.

53. Li, J.; Cushing, S. K.; Zheng, P.; Senty, T.; Meng, F.; Bristow, A. D.; Manivannan, A.Wu, N., Solar Hydrogen Generation by a CdS-Au-Tio2 Sandwich Nanorod Array Enhanced with Au Nanoparticle as Electron Relay and Plasmonic Photosensitizer. *Journal of the American Chemical Society* **2014**, *136*, 8438-8449.

54. Linnros, J., Carrier Lifetime Measurements Using Free Carrier Absorption Transients. I. Principle and Injection Dependence. *Journal of Applied Physics* **1998**, *84*, 275-283.

55. Linnros, J., Carrier Lifetime Measurements Using Free Carrier Absorption Transients. Ii. Lifetime Mapping and Effects of Surface Recombination. *Journal of Applied Physics* **1998**, *84*, 284-291.

56. Lifshitz, E., Evidence in Support of Exciton to Ligand Vibrational Coupling in Colloidal Quantum Dots. *The Journal of Physical Chemistry Letters* **2015**, *6*, 4336-4347.

CHAPTER 5

Engineering Interactions in QDs-PCBM Blends: A Surface Chemistry Approach

Part of this Chapter is based on:

Righetto et al. SPIE Optics & Photonics Proc. **2017**, 10363, 103632D

ABSTRACT- In this chapter, the photophysics of engineered QDs-fullerene blends is investigated and modeled. The aim of this work is to delve deeper into the role played by ligands in tailoring and addressing interaction. In particular, the role of three different ligands (oleylamine, octadecanethiol and propanethiol) in influencing the dynamics of charge generation, separation and recombination in blends made up by CdSe/CdS QDs and PCBM was investigated. A thorough photo-physical characterization was achieved by combining optical and magnetic spectroscopy. The magnetic spectroscopies were performed by Dr. A Privitera and their main results are only briefly summarized. Transient absorption measurements revealed a different and faster interaction dynamics in thiol-capped ligands.
Through phenomenological modeling of interaction processes, i.e. energy transfer and electron transfer, it was possible to estimate the suppression of exciton migration and enhancement of electron transfer processes when alkyl-thiols are employed as ligands. Moreover, short alkyl chain ligands resulted in bolstered interactions with PCBM acceptors. Quantitatively, a 10-fold increase in the electron transfer rate is measured when oleylamine is exchanged with propanethiol. Besides further demonstrating enhanced charge generation, EPR techniques disclosed the fate of photogenerated charges, i.e. charge recombination and separation processes. Therefore, the reported characterization evidences the importance of ligands in determining QDs interaction. These discoveries will contribute to the efficient incorporation of QDs in traditional organic photovoltaic technologies.

5.1 Introduction

In the burgeoning field of quantum dots based solar cells (QDSCs), the unconventional photo-physics of quantum dots (QDs) is exploited to achieve higher solar conversion efficiencies. The intriguing concurrence of broadband visible absorptions, high extinction coefficients and energy level tunability through size control offers unprecedented tools for harnessing sunlight.[1-3]

On top of that, the possibility to create multiple excitons by single high-energy photon absorption, through carrier multiplication, and the role of Auger recombination processes in promoting non-Marcus charge transfer behavior, hold promises to boost solar cell device efficiency.[4-8] Prospects are even brighter, since nanostructured hybrid perovskite materials are expected to be a game-changer.[9-10] These shiny expectancies on QDs motivate the interest in integrating these materials in photovoltaic technologies.

Main impairments, dictating current research directions, stem from QDs photo-physics, as well. Due to their excitonic nature, low charge mobility and exciton migration issues affect QDSCs.[11-12] Namely, the separation of excitons, considered as un-separated quanta of energy, in free carriers is hindered by the quantum confinement itself, resulting in high exciton binding energies.

Thus, many research efforts were spent in the quest for an exciton separating interface. Among different configurations of QDSC, Schottky heterojunction solar cells (SHJSC) and QD sensitized solar cells (QDSSC) attained impressively fast-growing efficiencies.[13-14, 15-16]

In SHJSC and QDSSC, charge separation is generally obtained at oxide-QDs interfaces, whereas hand, bulk heterojunction (BHJ) configuration exploits interfaces with organics. First pioneering reports by Alivisatos in early 2000, focused on the role of polymer-QDs charge transfer interaction. The devices based on polymer:QDs blends were capable reaching up to 2% power conversion efficiency, as first report.[17] Nonetheless, the dynamics of interactions within these blends have been explained only recently by transient optical measurements for PbS QDs. [18] The introduction of ternary hybrid solar cells (polymer: QDs: fullerene) further raised the interest in incorporating QDs in BHJ solar cells.[19-22] In recent years, the role of fullerene derivatives in promoting photo-induced electron transfer (eT) gained increasing attention. The eT interaction between QDs and fullerenes was investigated realizing covalently bound dyads by Kamat.[23] The charge generation in C_{60}-QDs blends was also observed by electrochemical and photocurrent measurements and by steady-state light-induced electron paramagnetic resonance (LEPR).[20, 24-25] Nevertheless, at this time, only a single work reported the photophysical characterization of hybrid films embedding QDs, prototypical to QDs-based BHJ devices, appealing for further investigations on the role of surfaces and ligands.[26]

Hence, a gap in the tailoring and characterization of through-space QDs:PCBM interaction can be recognized. The presented work was developed with a twofold aim: to track the dynamics of charge generation, separation, and recombination in QDs:PCBM blends and to engineer interactions exploiting the surface chemistry of QDs. In particular, the interaction dynamics of thin shell quasi-type II QDs (CdSe/CdS), described in the previous chapters, with fullerene derivatives (PCBM) in a prototypical BHJ active layer. Taking advantage of QDs' surface chemistry, their interaction was targeted towards the desired charge separation and minimized energy migration at QDs-PCBM interface.

5.2 Ligand Exchange Reaction and Isolate Dynamics

In this work, CdSe/CdS quantum dots in toluene solution were used as donor systems. Akin to the described in the previous chapters, the CdSe core radius is 2.1nm and the shell is 1ML thick. This QDs system was chosen as donor material, owing to the peculiarities of quasi-type II heterostructures. Indeed, the related band alignment (see Chapter 1) allows electron wavefunction reaching the surface, thereby prompting wavefunction overlap in interaction processes.[27] Namely, in order to envision possible electronic interactions, a quasi-Type II band alignment is expected to assist the wavefunction overlap allowing the accessibility of the electronic state.

On the other hand, the shell growth contributes to the passivation of surface dangling bonds, acting as traps.[28] Therefore, thin shell CdSe/CdS heterostructures provide a right balance between passivation and electronic state accessibility. Moreover, the shell growth is associated with hot carrier trapping, as widely discussed in Chapter 3. Although CdS thin shell is not outperforming thicker one in terms of emission efficiencies, the results discussed in previous chapters reveal how hot carrier trapping affect these systems to a lesser extent. Namely, in these systems, hot carriers are not more likely to be trapped than cold excitons. Considering that photovoltaic applications effectively take advantage of the entire absorption band of QDs, the hot carriers' dynamics play a pivotal role in determining the photon conversion efficiency.

Starting from as-synthesized CdSe/CdS quantum dots, ligand exchange allowed generating systems with different properties. As described in Materials & Methods.1 Chapter, the native ligands of as-synthesized QDs is 1-oleylamine ligand. According to HSAB theory for L-type ligand (see Chapter 1), amine ligands rapidly absorb and desorb from the surface, at room temperature.[29-30]

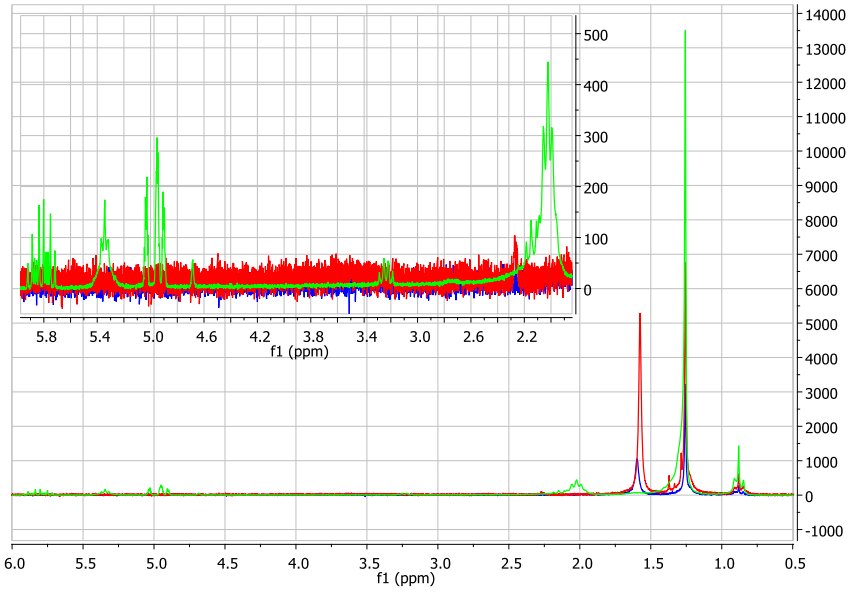

Figure 5.1 ^{1}H-NMR spectra of CdSe N-18 (green). S-3 (blue) and S-18 (red) in $CDCl_3$ acquired at room temperature in a 200 MHz spectrometer. A zoom in the 2-6 ppm region is shown in the inset. After ligand the exchange procedure, the disappearance of peaks at 5.35 ppm and 2.02 ppm ascribed respectively to alkenyl protons and protons attached to carbon atoms adjacent to the double bond of bound oleyl-amine are the signature that ligand exchange occurred. A further confirmation is the appearance of a strong peak at 1.60 ppm attributable to bound thiols. Other signals at 1.3ppm are related to aliphatic protons in the bound chain.

On the other hand, thiol ligands are X-type ligands and bind strongly to the CdSe surface. Hence, ligand exchange reaction was conducted adding an excess of thiol ligands in the starting QDs solution. In particular, both short chain 1-propanethiol (PT) and long chain 1-octadecanethiol (ODT) ligands were employed.

Resulting solutions were purified by anti-solvent precipitation them with a (1:1) acetone:methanol mixture and re-dispersing them in toluene.

The ligand exchange procedure was monitored by proton nuclear magnetic resonance (^{1}H-NMR) technique. Indeed, NMR is the principal tool in investigating molecules at QD surfaces. In this case, signals are characterized by broad linewidths associated with the reduced conformational motion of the bound ligands.[29] As shown in Figure 5.1, the oleylamine (OLA) signals are quantitatively replaced by those of PT and ODT, respectively. The diagnostic peaks are signals at 5.35 ppm and 2.02 ppm, related to alkenyl protons and protons bound to carbon atoms adjacent to double bonds. The disappearance of these peaks witnesses the quantitative substitution of OLA with other molecules.

Ligand exchange reaction was monitored and confirmed by optical techniques, as well.

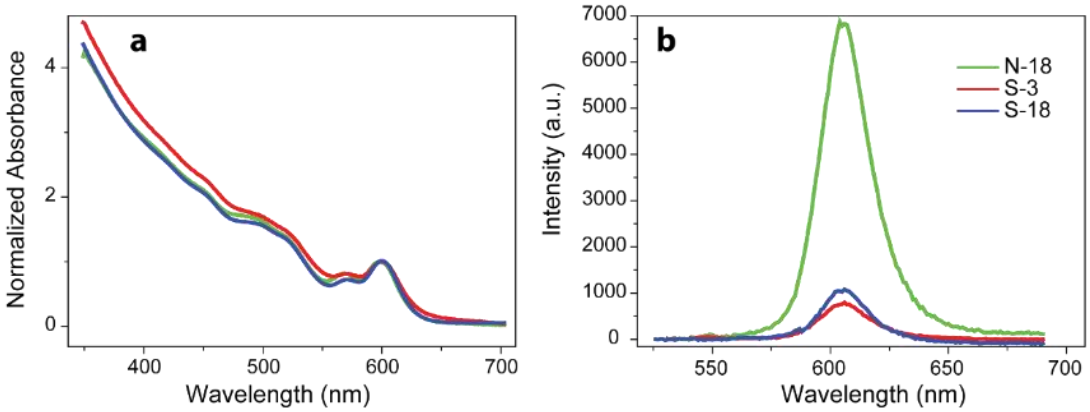

Figure 5.2 Normalized absorption (**a**) and emission (**b**) spectra of ligand-exchanged and bare QDs in toluene solution. The absorption lineshape is relatively unvaried for different ligands. On the other hand, the normalized emission is strongly quenched in thiol ligands. Color correspondence is preserved in two graphics: N-18 (green), S-3 (red), and S-18 (blue).

As shown in Figure 5.2, PL is extremely sensitive to thiol binding, due to thiol-mediated hole trapping process becoming dominant over radiative recombination. Indeed, the redox thiol levels lie above the valence band of CdSe-based QDs. Namely, in terms of solid state physics thiol ligands introduce shallow acceptor levels. According to Scholes and Minotto, this promotes the disruption of exciton bound state via band-edge charge transfer process (i.e., carrier trapping) and deeply affect emission properties.[31-32] The drastic changes of PL after ligand exchange concern emission efficiencies, whereas the band shape and, therefore, the nature of emissive states is unvaried. Quantitatively, the PL quantum yield (PLQY) drops from 10±1% to 1±0.2% and 1±0.1%, respectively for OLA-capped CdSe/CdS (N-18), PT-capped CdSe/CdS (S-3) and ODT-capped CdSe/CdS (S-18) ligands.

As suggested by PL spectroscopy, ligand exchange affects the excited carrier dynamics rather than modifying the nature of emissive species.

According to principles discussed in the previous chapters, the drastic decrease in PLQY generally originates from the opening of a fast recombination channel. Transient absorption (TA) spectroscopy is the fundamental tool in monitoring the excited state dynamics of QDs in the first hundreds of femtosecond after the photo-excitation. TA datasets are resolved in both time (0.2-800ps) and wavelength (450-700nm). The analysis of the 2D TA maps is based on the inspection of both spectral structures (i.e. fixed time section of 2D map) and transients (i.e. fixed wavelength section of 2D map). The rich QDs' excitonic structure gives rise to a number of TA signals in the spectral structures. In Figure 5.3 are reported the spectral structures of the studied samples (N-18, S-18, and S-3) in toluene solution, recorded 2ps after photo-excitation. Comparison of the normalized signals reveals similar spectral structures, except for the A2 and B3 signals. These signals result from the combination of bleaching and ESA associated with $|1P\rangle$ ($1P_e$-$1P_{3/2}$) exciton transition.[33] Unfortunately, bleaching band related to CdS absorption partially overlaps with A2 and B3 signals.[27] Ligand exchange process, by increasing the number of Cd-S couples results in enhanced CdS bleaching. Although its shape persists, A2 signal is shifted to negative values. Still, this effect is to be attributed to the enhanced B3 bleaching, which obscures and distorts A2 peak. The quantification of the different dynamics is generally obtained by focusing on B1 transients. In literature, the B1 signal (i.e. the ground state bleaching of the $|1S\rangle$ or $1S_e$-$1S_{3/2}$ exciton transition) is the most widely investigated signal.[34-35] Therefore, it is used as a doorway to access the QDs excited state dynamics. Due to asymmetry in electron and hole density of states, this signal was found to be sensitive to electron population only,[34] i.e. $\Delta A_{B1} \propto \langle n_e \rangle$.

Thence, B1 is a convenient probe for electron transfer processes and further consideration will be referred to this signal. As shown in Figure 5.3**a**, the comparison between normalized B1 transients in ligand-exchanged QDs evidences a different dynamics. Nevertheless, it is a rather counter-intuitive modification, i.e. a slower recombination dynamics is observed for low PLQY, thiol-capped QDs. Multi-exponential fitting allows extracting a quantitative estimation of this dynamics, results and average lifetimes are reported in Table 5-I. As confirmed by fitting, it is possible to distinguish a short time and a long time region in the QDs recombination dynamics in solution, fitted by a short (t_1) and a long (t_2) characteristic time. During TA measurements multiple excitation effects cannot be neglected (see Methods), hence the short time region of bleaching recovery is mostly related to Auger recombinations and ultrafast carrier trapping. [35-36]

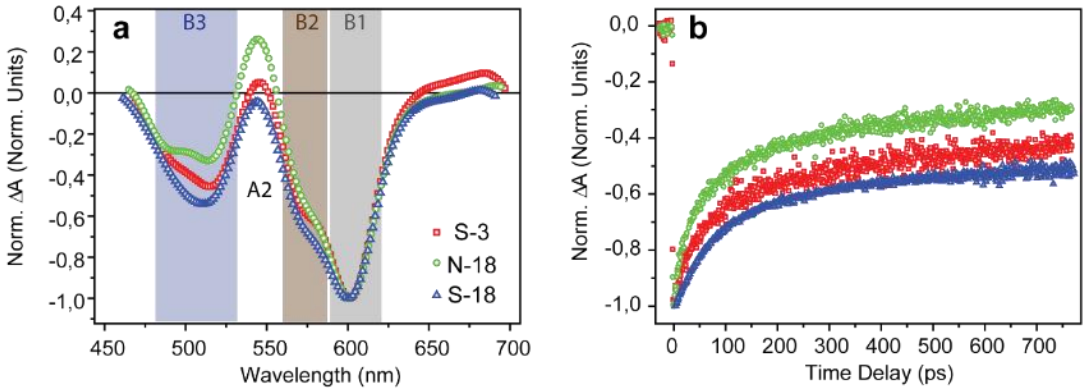

Figure 5.3- (**a**) TA spectral structures (taken at 2ps time delay) of pristine (N-18) and ligand-exchanged (S-18, S-3) CdSe/CdS QDs in toluene. Wavelength intervals associated with B1, B2, A2, B3 signals are colored. Data are normalized to B1 bleaching signal. (**b**) Normalized B1 transients (taken at 600 nm for N-18 (green circles), S-18 (blue triangle), S-3 (red square). Note color correspondence.

On the other hand, the long-time region is generally related to single exciton or trion species recombinations.[37] The sum of these processes will be referred as intrinsic recombinations. The B1 bleaching recovery is slowed down when QDs are capped with alkyl-thiol ligands, e.g., t_1 and t_2 values increase in S-18 and S-3 systems. According to PL data, a fast carrier trapping process underlies these changes. As mentioned earlier, thiols ligands result in hole trapping process. Recently, Pullerits group demonstrated the opening of a fast hole trapping channel (<250fs) in thiol-capped CdSe QDs.[38] Nevertheless, the present technique is highly sensitive to electron dynamics rather than hole dynamics. Hence, changes in the dynamics are an indirect effect of this fast hole trapping. Namely, the reduced electron-hole overlap when holes are trapped should abate Auger recombinations (requiring spatial overlap of the wavefunctions) and result in a slower bleaching recovery.[39]

5.3 The Dynamics of QDs:PCBM Blends

The excited state interaction between QDs and PCBM was investigated in solid-state random assemblies, namely in blends. Blended thin films were prepared using a spin coating technique on Mylar transparent thin substrates. Concentrated QD solutions in toluene (100μM) and PCBM solutions in ortho-dichloro-benzene (oDCB) at different concentration (20, 10, and 6 mg/mL) were mixed in equal amounts to obtain the mixed solution. Mixed solvent allowed a excellent solubility of both components and relatively slow evaporation time, assisting the spin coating process. 30μL of this solution was spin coated at 200rpm for 15s to obtain homogeneous coating and then 1500rpm for 30s to achieve complete solvent evaporation.

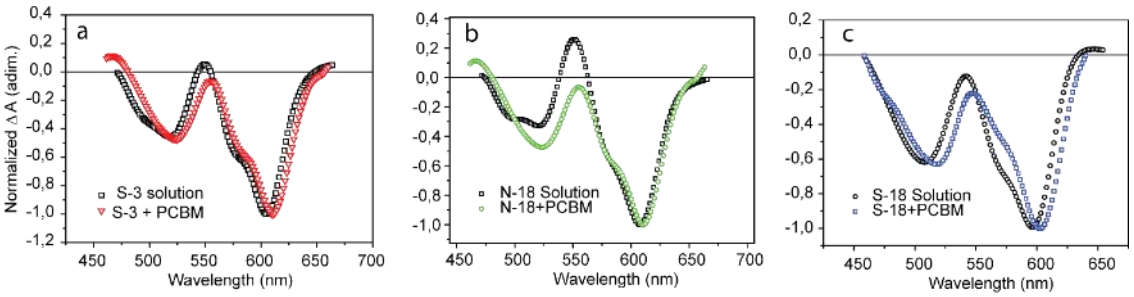

Figure 5.4- Comparison between spectral structures,taken at 2ps, for solutions (black) and blend with PCBM (10mg/mL): (**a**) S-3 (**b**) N-18 (**c**) S-18. A redshifting of the TA signals, and consequently of the entire excitonic structure is evident when considering B1 bleaching. Moreover, the normalization of the B1 signal at minimum reveals a different spectral distribution of TA signals. Most evident modifications concern the B3 and A2 signals.

Resulting high-quality films allowed investigating these samples through optical spectroscopies. The set of fabricated samples concerned both pristine (N-18) and ligand-exchanged QDs (S-18, S-3) blended with PCBM. In particular, for each sample, the blends spanned different relative concentrations of QDs (0.5, 1, 1.6% "molecular" ratio) and PCBM. QDs concentration was kept low, in order to avoid QDs segregation and obtain good quality thin-films. Due to a complete PL quenching, the excited state dynamics was monitored by TA measurements.

In Figure 5.4 is shown the comparison between spectral structures and B1 transients in solution and in blends, at 1% QDs concentration. The spectral structures for each ligand (Figure 5.4**a**,**b**,**c**) are red shifted by few nanometers. This is what generally expected for an electronic interaction. Namely, a possible spreading of the electron wavefunction would result in a lowering of the associated energy. Moreover, the relative amplitudes of A2 and B3 signals are modified, with respect to normalized B1 bleaching.

The observed modification is assigned to a different dynamics of the system, rather than to a modification of the energetic states. Indeed, A2 and B3 signals are related to $1P_e$ electron population, which generally relax to the $1S_e$ state, acting as a bottleneck due to its low (twofold) degeneracy. A faster depopulation of $1S_e$ state would then reverberate in a reduced B3 and A2 signal amplitude at a fixed time.

Such dynamics are readily observed through the inspection analyzing B1 transients, as shown in Figure 5.5**a**. The noticeable shortening of bleaching recovery time when QDs are blended together with PCBM is the spectroscopic signature of an excited state interaction, involving photoexcited electrons in the $1S_e$ state. Noteworthy, the long-living asymptote of B1 transients for QDs, as observed in solution (Fig. 5.3**b**), disappears in blends. The B1 bleaching signal almost wholly recovers during the timespan of TA experiments (Fig. 5.5**a**,**b**), demonstrating the opening of a novel fast recombination channel that leads to a fast and complete depopulation of QDs excited state.

Such effect is drastic for the S-3 sample, whereas remarkable changes in recombination dynamics are observed for N-18 and S-18 as well. Quantitatively, the fitting of N-18 bleaching recovery requires a bi-exponential decay function, while S-18 and S-3 display mono-exponential decay.

Sample	α1	t1(ps)	α2	t2(ps)	α3	t3(ps)	<τ> (ps)	Q
N-18 solution	0,21	16(2)	0,36	100(8)	0,43	2200(150)	2100	
N-18 0.5%	0,76	42(5)	0,23	280(20)			200	10
N-18 1%	0,15	10(3)	0,85	250(18)			250	8
N-18 1.6%	0,21	40(5)	0,79	400(40)			390	5
S-18 solution	0,21	55(7)	0,23	180(25)	0,56	6700(700)	6600	
S-18 0.5%			1	180(20)			180	36
S-18 1%			1	340(30)			340	19
S-18 1.6%	0,43	110(10)	0,57	800(80)			760	8
S-3 solution	0,24	18(2)	0,26	180(15)	0,54	3600(300)	3500	
S-3 0.5%	1	30(4)					30	116
S-3 1%	1	85(9)					85	41
S-3 1.6%	1	90(9)					90	38

Table 5-I- Multi-exponential fitting times and amplitudes for different QDs sample in solution and blends at different concentration (0.5%, 1%, and 1.6 %). S-3 and S-18 blends are fitted to a single exponential function, while N-18 requires at least a bi-exponential function. On the other hand, each solution transient is fitted to a triexponential function. The quenching factor Q is calculated as the ratio between the solution and blend average bleaching recovery time.

Noteworthy, B1 recoveries in blends outpace those observed in solution, as shown in Figure 5.5. This clearly indicates an interaction between QDs and PCBM is highly efficient. As discussed above, a fast B1 bleaching recovery identifies a rapid depopulation of 1Se electron state, thereby confirming the presence of a picosecond timescale interaction in our hybrid films. Moreover, the mono-exponential decay shown by S-3 and S-18 is indicative of the presence of a single photophysical process, driving energy relaxation in QDs. A qualitative comparison between S-3, S-18, and N-18 discloses the pivotal role played by alkyl chain length in modulating through-space interactions between QDs and PCBM.

Indeed, although the S-18 bleaching recovers on a timescale comparable to that of N-18, S-3 shows a faster recovery, thereby indicating an enhanced interaction. Moreover, the competition between internal recombination and interaction rates plays a pivotal role in defining interaction efficiency.

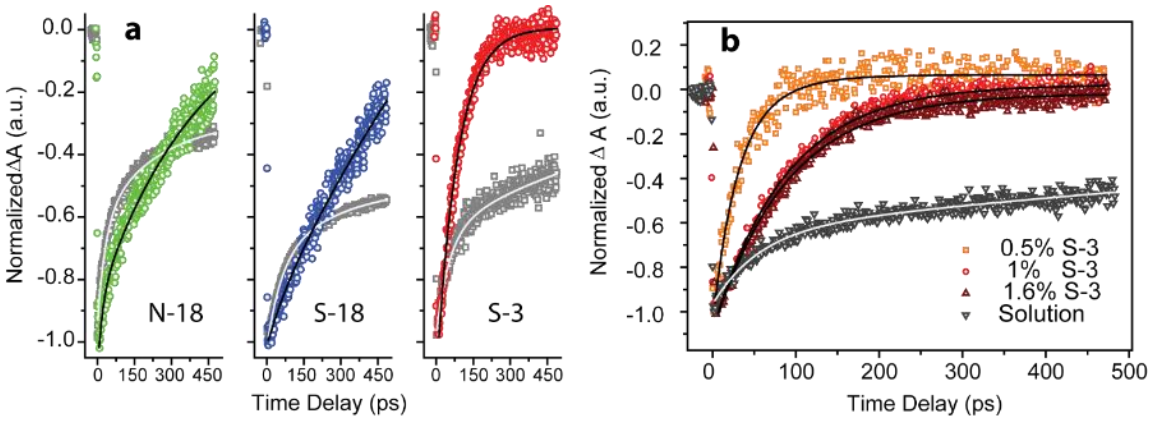

Figure 5.5- (**a**) Comparison between B1 transients of QDs in toluene solution and blend (1% QDs). Each solution transient is represented by grey squares. Transients N-18 (green), S-18 (blue) and S-3 (red) are fitted by multi-exponential function (solid line). (**b**) Concentration dependence of B1 transients for S-3 blends. The difference between 0.5% QDs (orange) and 1% QDs (red) is more marked than those between 1% QDs and 1.6% QDs (brown).

The presence of a single exponential in S-3 and S-18 suggests that all internal recombinations are replaced by a single, hence very efficient, interaction process, whose time scale is determined by alkyl ligand length. The concentration-dependent behavior of B1 transient for S-3 blends is shown in Figure5.5**b**. Bleaching recovery is observed to slow down when QDs concentration is increased. The same behavior is observed for other blends (Table 5-I). A possible rationalization invokes the number of acceptors for interaction processes.

Indeed, the [PCBM]/[QDs] molar concentration ratio establishes an averaged number of acceptors for each QDs, decreasing this ratio is expected to result in a reduction of overall interaction time. Qualitatively, the Q parameter is calculated as the ratio between bleaching recovery average time in solution and in blend and measures the magnitude of the excited state interaction. Although the reduction from 0.5% to 1% is noticeable, that from 1% to 1.6% is smaller. This indicates the presence of a threshold, above which inter-QDs interactions in blend induced by aggregation cannot be neglected. Similar behavior is observed for N-18 and S-18 blends, as reported in Table 5-I.

Recently, the coexistence of electronic energy transfer (EET) and electron transfer (eT) was studied in covalent QDs-PCBM dyads.[40] Unfortunately, TA measurements alone do not allow discriminating between these interaction processes. Indeed, both energy and electron transfer cause depopulation of $1S_e$ electron state probed by the B1 transient.

The above-presented photophysical characterization of QDs:PCBM blends is part of a comprehensive study of these systems, conducted in collaboration with EPR group at the University of Padova. Further characterization exploited electron paramagnetic resonance (EPR) techniques to study the fate of paramagnetic photoproducts (radicals and triplets) in these blends. Dr. A. Privitera and Prof. L. Franco obtained this characterization and related conclusions briefly resumed here.

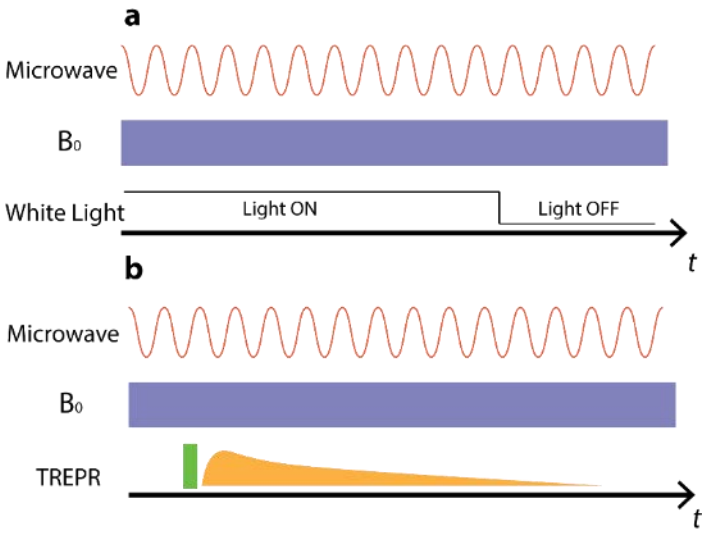

Figure 5.6-EPR techniques are based on monitoring the intensity of microwave (MW) signals in a high Q-factor resonant cavity. The application of a magnetic field induces Zeeman level splitting and microwaves induces absorptive and emissive transitions among those levels. Light can be used to generate paramagnetic species, susceptible to Zeeman splitting in magnetic fields. (**a**) LEPR scheme in which white light is shone on the sample, and contextually the MW intensity is measured. Light ON spectra is recorded during illumination, whereas Light OFF spectra monitor long-living species that persist after switching the light off. (**b**) TREPR scheme introduces time resolution though pulsed 532nm excitation (6ns pulses). The laser light pulse generates a bunch of paramagnetic species, whose time evolution is recorded immediately after the pulse.

Light-induced EPR (LEPR) detects long-living paramagnetic species generated after UV-vis light absorption. (Figure 5.6**a**) The species of interest is the radical anion localized on PCBM, generating a signal with typical anisotropic lineshape. This photophysical species is a suitable probe for monitoring the charge transfer interaction, as it is generated via electron transfer process from QDs to neutral PCBM. Notably, an accurate analysis established an increase in the LEPR signal for ligand-exchanged samples, i.e., signal intensity scaled as S-3 >> S-18 > N-18. The increase in this signal is consistent with the increased interaction, observed by TA spectroscopy.

Time-resolved EPR (TREPR) takes advantage of short laser pulses (few ns) to implement time-resolved detection (Figure 5.6**b**). By means of this technique, further information on the fate of charge transfer (CT) states was investigated. Beside charge separation, i.e., the overcoming of the Coulomb barrier in a CT state, many processes can occur, such as charge recombination following many roads, such as direct transition or back electron transfer to the donor (or acceptor) triplet excited state.

In this case, the evolution of the PCBM photoexcited triplet states was monitored, being highly informative on back-electron transfer processes.

Indeed, this signal contained different contributions, e.g., intersystem crossing and recombination. A best-fit simulation was used to disentangle such fundamental processes. Results evidenced a reduced recombination contribution in blends with respect to bare PCBM film (where the radical pair are generated due to inhomogeneity within the ensemble).

5.4 Tailoring Charge and Energy Transfer Processes

Hitherto, only a few studies reported electron transfer between covalently linked CdSe and C_{60} derivatives.[23, 40] The high electron affinity of PCBM (-3.9eV) [41] is compatible with eT process at the interface with CdSe QDs (-3.1eV, estimated for 2.1nm radius from Ref. 42). A peculiar eT mechanism was recently proposed for QDs. Auger-assisted electron transfer allows circumventing the typical Marcus inverted region, thanks to the assistance of Auger processes in storing energy exceeding the reorganization energy. Consistently with estimated energy levels, the studied QDs-PCBM couple was found to lay within an Auger-assisted regime,[23, 40] being $(-\Delta G\ [\sim 800\ meV] > \lambda[\sim 400\ meV])$. Alongside with eT, the energetics of the systems supports the possibility of having EET between QDs and PCBM. As shown in Figure 5.7, the spectral overlap between QDs emission and PCBM broad absorption bands is non-negligible.

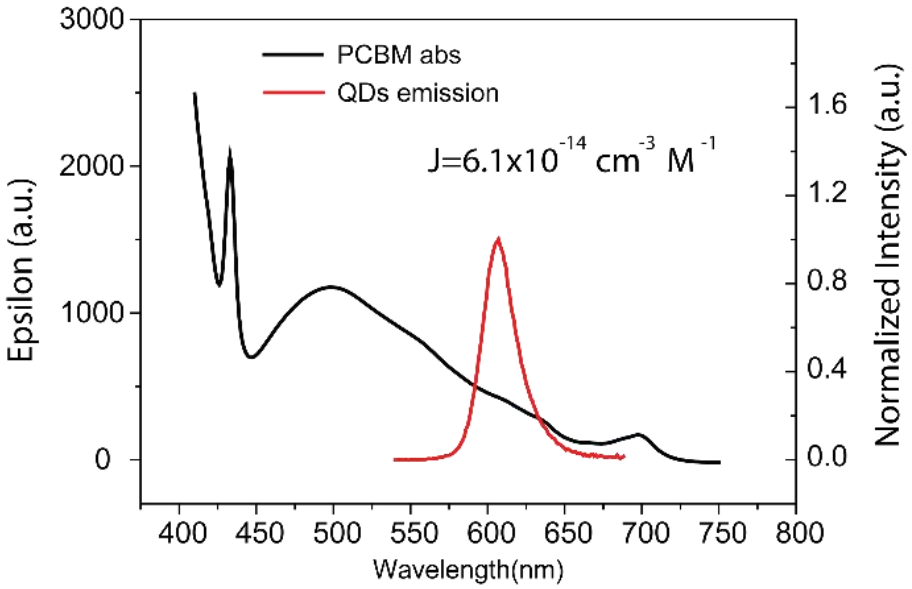

Figure 5.7- Spectral overlap between PCBM extinction coefficient (black line) and QD emission (red line). The extinction coefficient was estimated by applying the Lambert-Beer law to absorption measurements. This spectral overlap suggests that energy can flow from donor (QDs) to acceptor (PCBM) by coupling of their transition dipole moment. This process results in exciton migration at the heterointerface and is competitive to charge separation.

The use of surface chemistry was aimed at tuning the interaction between CdSe/CdS QDs and PBCM and direct it toward eT, thereby suppressing EET contributions. Ligand exchange procedure acts on two essential factors determining charge generation: (1) the distance between QDs electron-donor and PCBM electron-acceptor, (2) the nature of excitons in QDs. The length of ligand alkyl chain determines the minimum donor-acceptor distance within blends. This effect on eT rate is expected to overcome that on EET rate, due to different distance dependences.[43] Close packing distances for PT and ODT/OLA ligands were estimated from literature as 0.4 nm and 2.2 nm, respectively.[44] Qualitatively, considering the damping factor (0.35Å^{-1}) measured for CdSe/ZnS QDs with distance, eT rates should increase by one order of magnitude.[45] Moreover, the optical characterization of ligand-exchanged QDs suggests a different nature of exciton in thiol-capped QDs as compared to amine capped ones. The presence of redox levels above valence band gives rise to a Type-II hetero-interface. The drastic decrease of PL efficiency, according to literature,[28, 46-47] suggests a hole trapping quenching mechanism. This is further confirmed by TA data: the modification in B1 transients is indicative of hot-hole trapping.[38.] Therefore, thiol ligands should reduce the energetic barrier arising from Coulomb exciton binding and therefore promote charge generation.

Experimental results on charge generation reveal that the here presented surface chemistry approach successfully targeted the interaction between QDs and PCBM toward eT. Indeed, B1 bleaching recovery is faster for S-3 with respect to S-18 and N-18.

Moreover, S-3 and S-18 exhibit mono-exponential decay indicating the presence of a single contribution driving the interaction.

The suppression of EET is demonstrated by calculation of the theoretical EET rate, based on independent measurements of spectral overlap and QDs fluorescence lifetimes. EET is an interaction process, mediated by intermolecular forces, in which a photo-excited donor relaxes transferring excitation to nearby acceptor system.[48] In weak-coupling regime for QDs systems, EET is described by Förster model, in which EET rate is governed by distance, transition dipole moment and spectral overlap. The common expression for Förster rate is

$$k_{EET} = \frac{9000\ (ln\,10)\ \kappa^2\ QY}{128\ \pi^5 n^4\ N_a\ \tau_d r^6} \int_0^\infty F_D(\lambda)\epsilon_A(\lambda)\ \lambda^4\ d\lambda \qquad \textbf{(Eq. 5.1)}$$

where most important terms are the quantum yield (QY) and the donor lifetime (τ_D), the typical r^{-6} distance dependence and the overlap integral between normalized donor fluorescence and acceptor absorption. According to this analysis, the intrinsic EET rate for the minimum packing distance is calculated to be $k_{EET}\ (N-18) = 1 \cdot 10^{-5}\ ps^{-1}$, $k_{EET}\ (S-3) = 3 \cdot 10^{-5}\ ps^{-1}$, $k_{EET}\ (S-18) = 3 \cdot 10^{-6}\ ps^{-1}$.

This intrinsic EET rate should be multiplied by the number of acceptors in blends. Even though the considered blend is a disordered system, it is worth to consider an extreme case, such as the maximum number of PCBM acceptors allowed by QD surface area.

	N-18	S-18	S-3
Est. Forster Radius (Å)	31	19	19
Min. Close Contact Distance (Å)	44	44	29
QY	10±2	1±0.2	1±0.1
PL lifetime (ns)	12	2	2
EET intrinsic rate (10^{-6} ps^{-1})	10	33	3
Maximum EET rate (10^{-3} ps^{-1})	2.7	4	0,27

Table 5-II – Data and results from theoretical EET rate estimation by Forster model. Forster radius is defined as the distance at which EET efficiency is 50%, and measures the magnitude of Forster interactions.

A simple geometrical consideration allows estimating the maximum number of PCBM acceptors for each QD in a close-packed system (considering nearest neighbors). Considering a single QD surrounded by PCBM, as shown in Figure 5.8, it is sufficient to calculate the QD external surface are and divide it on the PCBM projected area.

Assuming a QD radius ($r_{QD} = 2.1nm$), a ligand length ($l_{OLA} = 1.5nm, l_{PT} = 0.4nm$) and a PCBM diameter ($d_{PCBM} = 1nm$), the resulting outer sphere radius is $r_{out} = r_{QD} + l_{OLA} + \frac{d_{PCBM}}{2} = 4.1nm$ for OLA/ODT ligands and $r_{out} = r_{QD} + l_{PT} + \frac{d_{PCBM}}{2} = 3nm$. Calculating the outer sphere diameter $S_{out} = 4\pi\, r_{out}^2$ and dividing it for the cross sectional PCBM area $S_{PCBM} = \pi \left(\frac{d}{2}\right)^2$, the resulting maximum number of PCBM acceptor allowed by geometry is $N_{max,OLA} = 270$ and $N_{max,PT} = 144$

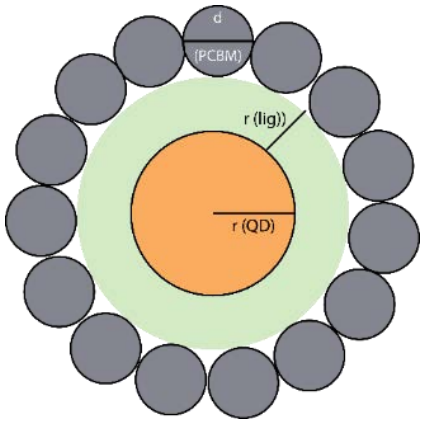

Figure 5.8- Scheme for calculation of the maximum number of PCBM acceptor around a single QD

According to these qualitative considerations, the calculated rates are compatible with observed B1 transients only in the case of N-18 blends (Table 5-II), whereas calculated maximum global EET rates for S-3 and S-18 are much slower with respect to experimental ones. This suggests that EET is efficiently suppressed by thiol ligand exchange, in favor of more efficient eT.

The quantitative extraction of EET and eT rates would require an accurate determination of the average number of acceptors, which would hinge on a number of assumption on the blend structure affecting the overall accuracy of the result. Notably, the suppression of EET in favor of eT is proved by the intensity of LEPR signals. Indeed, LEPR reveals different charge generation efficiency for different blends, i.e. LEPR signal intensity scales as S-3 >> S-18 > N-18. Thence, both the nature of ligand and the length of the alkyl chain influence electron transfer process, though to different extents. A possible speculation involves the observed exciton pre-dissociation, though thiol hole scavenging. This process in QDs would promote electron transfer and contextually decrease energy transfer. Nevertheless, it is the ligand alkyl chain length that mainly drives the increase in charge generation. Consequently, surface chemistry stems as a fundamental tool in manipulating and tailoring the interactions of QDs in blends.

5.5 Conclusions

The presented investigation delves deeper into the primary photophysical processes occurring in QDs:PCBM blends. In particular, the possibility of finely tuning QDs interactions with PCBM by acting on their surface chemistry is demonstrated.

Transient absorption (TA) investigation showed an increase in the electron transfer rate from QDs functionalized with shorter ligands to PCBM, due to exponential distance dependence. Contextually, thiol anchoring groups efficiently switch off the competitive EET interaction, thanks to the ultrafast hole scavenging. Moreover, EPR analysis further corroborated these results and extended them providing more profound insights into recombination mechanisms.

In conclusion, the incorporation of QDs into photovoltaic technology appears to be extremely lucrative, as long as QDs' surface chemistry is sufficiently engineered. The tailoring of QDs interactions (namely, eT and EET) in photovoltaic blends is the fundamental step toward their effective integration. Their prospect use in ternary solar cells (polymer:QDs:fullerene) will potentially enhance charge generation, charge separation and ultimately conversion efficiencies in BHJ architectures. Nevertheless, some open questions, such as that regarding morphology and solubility/aggregation issues will require further investigation

References

1. Semonin, O. E.; Luther, J. M.Beard, M. C., Quantum Dots for Next-Generation Photovoltaics. *Materials Today* **2012**, *15*, 508-515.

2. Kim, J. Y.; Voznyy, O.; Zhitomirsky, D.Sargent, E. H., 25th Anniversary Article: Colloidal Quantum Dot Materials and Devices: A Quarter-Century of Advances. *Advanced Materials* **2013**, *25*, 4986-5010.

3. Kamat, P. V., Quantum Dot Solar Cells. Semiconductor Nanocrystals as Light Harvesters. *The Journal of Physical Chemistry C* **2008**, *112*, 18737-18753.

4. Kamat, P. V., Quantum Dot Solar Cells. The Next Big Thing in Photovoltaics. *The Journal of Physical Chemistry Letters* **2013**, *4*, 908-918.

5. Carey, G. H.; Abdelhady, A. L.; Ning, Z.; Thon, S. M.; Bakr, O. M.Sargent, E. H., Colloidal Quantum Dot Solar Cells. *Chemical Reviews* **2015**, *115*, 12732-12763.

6. Kagan, C. R.; Lifshitz, E.; Sargent, E. H.Talapin, D. V., Building Devices from Colloidal Quantum Dots. *Science* **2016**, *353*.

7. Nozik, A. J.; Beard, M. C.; Luther, J. M.; Law, M.; Ellingson, R. J.Johnson, J. C., Semiconductor Quantum Dots and Quantum Dot Arrays and Applications of Multiple Exciton Generation to Third-Generation Photovoltaic Solar Cells. *Chemical Reviews* **2010**, *110*, 6873-6890.

8. Nozik, A. J., Nanoscience and Nanostructures for Photovoltaics and Solar Fuels. *Nano Letters* **2010**, *10*, 2735-2741.

9. Privitera, A.; Righetto, M.; Bozio, R.Franco, L., The Central Role of Ligands in Electron Transfer from Perovskite Nanocrystals. *MRS Advances* **2017**, 1-9.

10. Lamberti, F.; Litti, L.; De Bastiani, M.; Sorrentino, R.; Gandini, M.; Meneghetti, M.Petrozza, A., High-Quality, Ligands-Free, Mixed-Halide Perovskite Nanocrystals Inks for Optoelectronic Applications. *Advanced Energy Materials* **2017**, *7*, 1601703-n/a.

11. Meulenberg, R. W.; Lee, J. R. I.; Wolcott, A.; Zhang, J. Z.; Terminello, L. J.van Buuren, T., Determination of the Exciton Binding Energy in CdSe Quantum Dots. *ACS Nano* **2009**, *3*, 325-330.

12. Straus, D. B.; Goodwin, E. D.; Gaulding, E. A.; Muramoto, S.; Murray, C. B.Kagan, C. R., Increased Carrier Mobility and Lifetime in CdSe Quantum Dot Thin Films through Surface Trap Passivation and Doping. *The Journal of Physical Chemistry Letters* **2015**, *6*, 4605-4609.

13. Lan, X., et al., Passivation Using Molecular Halides Increases Quantum Dot Solar Cell Performance. *Advanced Materials* **2016**, *28*, 299-304.

14. Lan, X., et al., 10.6% Certified Colloidal Quantum Dot Solar Cells Via Solvent-Polarity-Engineered Halide Passivation. *Nano Letters* **2016**, *16*, 4630-4634.

15. Yang, J.; Wang, J.; Zhao, K.; Izuishi, T.; Li, Y.; Shen, Q.Zhong, X., CdSeTe/CdS Type-I Core/Shell Quantum Dot Sensitized Solar Cells with Efficiency over 9%. *The Journal of Physical Chemistry C* **2015**, *119*, 28800-28808.

16. Kamat, P. V., Boosting the Efficiency of Quantum Dot Sensitized Solar Cells through Modulation of Interfacial Charge Transfer. *Accounts of Chemical Research* **2012**, *45*, 1906-1915.

17. Huynh, W. U.; Dittmer, J. J.Alivisatos, A. P., Hybrid Nanorod-Polymer Solar Cells. *Science* **2002**, *295*, 2425.

18. Colbert, A. E.; Jedlicka, E.; Wu, W.Ginger, D. S., Subpicosecond Photon-Energy-Dependent Hole Transfer from PbS Quantum Dots to Conjugated Polymers. *The Journal of Physical Chemistry Letters* **2016**, *7*, 5150-5155.

19. Lu, L.; Kelly, M. A.; You, W.Yu, L., Status and Prospects for Ternary Organic Photovoltaics. *Nat Photon* **2015**, *9*, 491-500.

20. Lefrançois, A., et al., Enhanced Charge Separation in Ternary P3HT/PCBM/CuInS2 Nanocrystals Hybrid Solar Cells. *Scientific Reports* **2015**, *5*, 7768.

21. Liao, H.-C., et al., Nanoparticle-Tuned Self-Organization of a Bulk Heterojunction Hybrid Solar Cell with Enhanced Performance. *ACS Nano* **2012**, *6*, 1657-1666.

22. Martínez-Ferrero, E.; Albero, J.Palomares, E., Materials, Nanomorphology, and Interfacial Charge Transfer Reactions in Quantum Dot/Polymer Solar Cell Devices. *The Journal of Physical Chemistry Letters* **2010**, *1*, 3039-3045.

23. Bang, J. H.Kamat, P. V., CdSe Quantum Dot–Fullerene Hybrid Nanocomposite for Solar Energy Conversion: Electron Transfer and Photoelectrochemistry. *ACS Nano* **2011**, *5*, 9421-9427.

24. Brown, P.Kamat, P. V., Quantum Dot Solar Cells. Electrophoretic Deposition of CdSe–C60 Composite Films and Capture of Photogenerated Electrons with Nc60 Cluster Shell. *Journal of the American Chemical Society* **2008**, *130*, 8890-8891.

25. Chaban, V. V.; Prezhdo, V. V.Prezhdo, O. V., Covalent Linking Greatly Enhances Photoinduced Electron Transfer in Fullerene-Quantum Dot Nanocomposites: Time-Domain Ab Initio Study. *The Journal of Physical Chemistry Letters* **2013**, *4*, 1-6.

26. Itskos, G.; Othonos, A.; Rauch, T.; Tedde, S. F.; Hayden, O.; Kovalenko, M. V.; Heiss, W.Choulis, S. A., Optical Properties of Organic Semiconductor Blends with near-Infrared Quantum-Dot Sensitizers for Light Harvesting Applications. *Advanced Energy Materials* **2011**, *1*, 802-812.

27. Bae, W. K.; Padilha, L. A.; Park, Y.-S.; McDaniel, H.; Robel, I.; Pietryga, J. M.Klimov, V. I., Controlled Alloying of the Core–Shell Interface in CdSe/CdS Quantum Dots for Suppression of Auger Recombination. *ACS Nano* **2013**, *7*, 3411-3419.

28. Righetto, M.; Minotto, A.Bozio, R., Bridging Energetics and Dynamics of Exciton Trapping in Core-Shell Quantum Dots. *The Journal of Physical Chemistry C* **2016**.

29. Boles, M. A.; Ling, D.; Hyeon, T.Talapin, D. V., The Surface Science of Nanocrystals. *Nat Mater* **2016**, *15*, 141-153.

30. Green, M., The Nature of Quantum Dot Capping Ligands. *Journal of Materials Chemistry* **2010**, *20*, 5797-5809.

31. Jones, M.; Lo, S. S.Scholes, G. D., Quantitative Modeling of the Role of Surface Traps in CdSe/CdS/ZnS Nanocrystal Photoluminescence Decay Dynamics. *Proceedings of the National Academy of Sciences* **2009**, *106*, 3011-3016.

32. Minotto, A.; Todescato, F.; Fortunati, I.; Signorini, R.; Jasieniak, J. J.Bozio, R., Role of Core–Shell Interfaces on Exciton Recombination in CdSe–CdxZn1–xS Quantum Dots. *The Journal of Physical Chemistry C* **2014**, *118*, 24117-24126.

33. Zhang, C.; Do, T. N.; Ong, X.; Chan, Y.Tan, H.-S., Understanding the Features in the Ultrafast Transient Absorption Spectra of CdSe Quantum Dots. *Chemical Physics* **2016**, *481*, 157-164.

34. Klimov, V. I., Spectral and Dynamical Properties of Multiexcitons in Semiconductor Nanocrystals. *Annual Review of Physical Chemistry* **2007**, *58*, 635-673.

35. Kambhampati, P., Hot Exciton Relaxation Dynamics in Semiconductor Quantum Dots: Radiationless Transitions on the Nanoscale. *The Journal of Physical Chemistry C* **2011**, *115*, 22089-22109.

36. Kambhampati, P., Multiexcitons in Semiconductor Nanocrystals: A Platform for Optoelectronics at High Carrier Concentration. *The Journal of Physical Chemistry Letters* **2012**, *3*, 1182-1190.

37. Gong, K.Kelley, D. F., Surface Charging and Trion Dynamics in CdSe-Based Core/Shell Quantum Dots. *The Journal of Physical Chemistry C* **2015**, *119*, 9637-9645.

38. Lenngren, N.; Abdellah, M. A.; Zheng, K.; Al-Marri, M. J.; Zigmantas, D.; Zidek, K.Pullerits, T., Hot Electron and Hole Dynamics in Thiol-Capped CdSe Quantum Dots Revealed by 2d Electronic Spectroscopy. *Physical Chemistry Chemical Physics* **2016**, *18*, 26199-26204.

39. Pandey, A.Guyot-Sionnest, P., Slow Electron Cooling in Colloidal Quantum Dots. *Science* **2008**, *322*, 929-932.

40. Stewart, M. H., et al., Competition between Förster Resonance Energy Transfer and Electron Transfer in Stoichiometrically Assembled Semiconductor Quantum Dot–Fullerene Conjugates. *ACS Nano* **2013**, *7*, 9489-9505.

41. Larson, B. W.; Whitaker, J. B.; Wang, X.-B.; Popov, A. A.; Rumbles, G.; Kopidakis, N.; Strauss, S. H.Boltalina, O. V., Electron Affinity of Phenyl–C61–Butyric Acid Methyl Ester (Pcbm). *The Journal of Physical Chemistry C* **2013**, *117*, 14958-14964.

42. Jasieniak, J.; Califano, M.Watkins, S. E., Size-Dependent Valence and Conduction Band-Edge Energies of Semiconductor Nanocrystals. *ACS Nano* **2011**, *5*, 5888-5902.

43. Jortner, J., Temperature Dependent Activation Energy for Electron Transfer between Biological Molecules. *The Journal of Chemical Physics* **1976**, *64*, 4860-4867.

44. Weidman, M. C.; Yager, K. G.Tisdale, W. A., Interparticle Spacing and Structural Ordering in Superlattice Pbs Nanocrystal Solids Undergoing Ligand Exchange. *Chemistry of Materials* **2015**, *27*, 474-482.

45. Zhu, H.; Song, N.Lian, T., Controlling Charge Separation and Recombination Rates in CdSe/ZnS Type I Core–Shell Quantum Dots by Shell Thicknesses. *Journal of the American Chemical Society* **2010**, *132*, 15038-15045.

46. Chakrapani, V.; Baker, D.Kamat, P. V., Understanding the Role of the Sulfide Redox Couple (S2–/Sn2–) in Quantum Dot-Sensitized Solar Cells. *Journal of the American Chemical Society* **2011**, *133*, 9607-9615.

47. Wuister, S. F.; de Mello Donegá, C.Meijerink, A., Influence of Thiol Capping on the Exciton Luminescence and Decay Kinetics of CdTe and CdSe Quantum Dots. *The Journal of Physical Chemistry B* **2004**, *108*, 17393-17397.

48. Beane, G.; Boldt, K.; Kirkwood, N.Mulvaney, P., Energy Transfer between Quantum Dots and Conjugated Dye Molecules. *The Journal of Physical Chemistry C* **2014**, *118*, 18079-18086.

PART II:
Emerging Nanomaterials

CHAPTER 6

The Physics and Chemistry of Novel Nanomaterials

ABSTRACT- The previous Part of this thesis dealt with highly engineered and performing nanostructures, capable of reaching almost unitary emission efficiencies and a complete energy level tunability throughout the visible range. These fancy features are the hard-earned achievement of more than two decades of scrupulous research. The research on CdSe-based QDs is now almost entirely developed, and much of the underlying physics has been disclosed. Nevertheless, these materials present some inherent drawbacks, among others: toxicity issues, scalability issues, relatively large emission lines. Hence, the quest for solving these issues led scientist to investigate novel materials in QDs form. The resulting research fields focused on either obtaining cheap, biocompatible materials with comparable properties to that of CdSe QDs or obtaining materials largely outperforming conventional QDs.
This Part of the thesis deals with both of these research lines. First steps in the characterization of carbon-based and hybrid lead perovskites based nanostructures are here presented.

6.1 Carbon Nanostructures

Carbon has always occupied a prominent position in the development of modern science and technology, owing to its pervasive presence in the organisms, industries, and societies. [1] Besides the most famous carbon allotropes, i.e., graphite, diamond, carbon nanotubes [2] and fullerenes, [3] the carbon family recently ushered in two new members: graphene [4] and luminescent carbon/graphene dots.[5] Graphene revealed to be an extraordinary material, opening a novel research field, i.e., that of 2D materials, and earning a Nobel prize. Hence, high expectations are holding for graphene dots and carbon dots (CDs). After the first experimental evidence of fluorescence in carbon soot, the introduction of large-scale synthesis methodologies resulted in a meteoric rise of the research on these materials. Indeed, luminescent carbon materials answered to the global quest for cheap, earth-abundant, highly processable, non-toxic, eco-friendly, as well as biocompatible alternatives to conventional QDs.[5]

Although some confusing terminologies are often used in literature, here carbon dots (CDs) are referred as carbon-based nanoparticles or nano-dots, with an average size of roughly 1-10 nm, which display fluorescent properties to some appreciable extent.[6]
Owing to their high solubility in water, chemical inertness, facile modification and high resistance to photobleaching, CDs became rising stars and earned the name of carbon nanolights.[5]

According to this definition, different classes of materials can be considered as CDs, i.e. graphene quantum dots (GQDs) and polymer dots. Nevertheless, henceforth only CDs intended as spherically shaped carbon nano-cores, made up of sp^2 and sp^3 carbon atoms will be considerate.

6.1.1 Inception and Synthesis of CDs

First experimental evidence of CDs were reported in 2004, during the purification of carbon nanotubes and in 2006 as a by-product of laser ablation of graphite powder.[7] Nowadays, synthetic strategies have evolved to achieve large-scale production from cheap precursors. Akin to a wealth of other nanostructures, these methods can be roughly classified into "bottom-up" and "top-down" approaches. Among top-down methods, laser ablation can be enlisted electrochemical carbonization. On the other hand, microwave-assisted pyrolysis and hydro/solvothermal synthesis are the most used bottom-up methods.

First works applying laser ablation on graphite and cement powder reported non-fluorescent by-products. Only after extreme reflux in nitric acid and passivation by N-PEG, Sun and co-workers were able to observe CDs distinctive emission.[7] A single step route to create highly emissive CDs by laser irradiation of graphite powder in organic solvents was proposed by Hu.[8] This technique is analogue to the laser ablation synthesis in solution (LASiS) proposed by Amendola for noble metal nanostructures.[9]

The dispersion of graphite powder and N-PEG in different solvent allowed obtaining CDs directly by Nd:YAG pulsed laser irradiation. In this procedure, the combination of high temperatures and pressures induced by intense laser pulses result in a carbon plasma state. The cooling down process results in the formation of CDs. Moreover, the presence of oxygen contributes to forming surface functional groups.

Albeit many electrochemical methods were proposed to fabricate GQDs, only a few reports of electrochemical CDs synthesis are found in the literature.[10] GQDs production mostly relies on the electrochemical cutting of different carbon sources, e.g., graphite powder, graphene oxide, carbon black and carbon nanotubes. Resulting carbon materials feature a perfect sp^2 carbon structure, lacking the bandgap necessary for an efficient visible fluorescence. In this case, emission of obtained dots is obtained by careful modulation of their surface chemistry.[11] On the other hand, the few reports on CDs electrochemical production are based on small molecules carbonization. Hence, this should be considered a bottom-up synthesis technique. Deng reported electrochemical carbonization of low-molecular-weight alcohols under basic conditions. [10] Notably, sizes and graphitization of cores could be controlled with the applied potential. These electrochemically synthesized CDs exhibited excellent photophysical properties without further purification and passivation techniques.

Bottom-up approaches present many advantages for the synthesis of CDs. Namely, these methodologies result in facile, rapid, one-pot and generally single-precursors syntheses of high-quality CDs. The basic process underlying these techniques is the pyrolysis of small organic molecules in solution (generally water). In microwave-assisted methods, a water solution containing precursors is overheated, up to complete evaporation. [12-13]

The resulting black powder is re-dissolved in either water or other solvents. Locally, up to 170°C can be reached during synthesis. On the other hand, in hydro/solvothermal technique, the pyrolysis of precursors is induced by high pressures and temperatures achieved in an autoclave.[14] Both these approaches result in the generation of either carbon or carbogenic cores, with different surface moieties mimicking those of the selected precursors. The main challenges faced when synthesizing CDs are: [6] (i) preventing carbonaceous aggregation during carbonization (ii) controlling size and uniformity of the samples (iii) fine tuning of the surface properties, as a critical factor for solubility and selected applications.

Nevertheless, during bottom-up synthesis, precursors undergo pyrolysis in a somewhat uncontrolled fashion, i.e., there are no definitive mechanistic studies in the formation of CDs. The generally accepted formation mechanism encompasses dehydration, polymerization, and carbonization steps, as recently shown by Hou. [15] Hence, due to the poor exerted control, the above-mentioned challenged are generally addressed with purifications and post-treatments.[16]

Concerning precursors, a significant number of molecules were used to generate CDs. In particular, the introduction of N- and S-heteroatoms resulted in highly performing CDs.[17] Among them, citric acid, phenylenediamine, cysteine are most commonly used molecules. Nevertheless, numerous methods were devised to prepare CDs from natural sources.[18] Among them, glucose, honey, shrimp egg, lignin and others.[19] Furthermore, also waste materials such as waste frying oil,[20] urine [21] and animal excrements were observed to generate good quality CDs. The leap towards inexpensive and sustainable precursors for carbon dot synthesis is the hallmark of mass production and commercialization of these nanostructures. [19] Nevertheless, the burgeoning of countless different CDs, with different sizes and surface properties somehow hampered any photophysical considerations, depriving them of a general significance and outreach.

6.1.2 Photophysical properties of CDs

Despite the above-mentioned spreading of the properties of CDs, owing to the variety of different CDs synthesized, most of them present some recurring photophysical property. The absorption spectra of CDs present their most interesting features in the UV range. Generally, two main peaks are observed. For carbon cores, a maximum peak lying below 250 nm is ascribed to π-π*transition of aromatic C-C bonds. The second peak generally ranging from 300nm to the visible is attributed to the n-π* transition of C=O bonds or other connected moieties.[14] Nonetheless, even more redshifted absorbance peaks can be obtained using particular precursors or upon functionalization.[22] Although in some cases a quantum size effect is claimed, a general theory relating the sizes and the optical properties of CDs is still lacking.

The photoluminescence (PL) properties are perhaps the most exciting features of CDs. Generally, the PL spectra of the CDs are symmetrical, and very largely Stokes shifted, with respect to conventional organic dyes. Nevertheless, the most striking feature of these systems is their excitation-wavelength dependence of the PL.[23] The emission peak position is found to be tightly related to the selected excitation wavelength. Namely, a redshift of the emission peak is observed when increasing excitation wavelength. behaviors. Although this effect was observed for a number of different systems, the underlying mechanism is still an unresolved issue.[24] This problem will be addressed for some specifical CDs systems in the next Chapter.

Many efforts have been spent on the investigation of CDs excitation wavelength dependent PL. Hitherto many explanations were found to account for this phenomenon:[16] (i) joint effect of quantum size effect and size dispersion, i.e. presence of different sized CDs, defects and surface states, surface groups, presence of different fluorophores; (ii) the recombination of excitons within confined graphenic clusters embedded within a sp^3 matrix; (iii) the presence of molecules in solution.

From a general point of view, before discussing the excitation-dependent properties of CDs, a general consensus of the origin of PL itself should be established. Two main way of thinking can be found in the literature. A considerable part of the scientific community considers PL as a radiative recombination of excitons taking place either in cores or at surface sites.[25] These scientists portray CDs analogously to inorganic QDs, i.e., nanocrystalline entities with defined absorption and conduction band. On the contrary, an as much considerable part of the scientific community sustains the fundamental role played by molecular states in the luminescence of CDs.[14, 26] For instance, the role of carbon cores as a multi-chromophoric scaffold, i.e., a carbonaceous scaffold in which a wide variety of molecular fluorophores are embedded.[27]

The difference in these two approaches stems from differences in physics and chemistry schools, which should (be fused together in solving nanoscience and materials science problems.

Indeed, at the current stage of development, neither the physical nor the chemical approach were able to unravel the nature of these complicated systems. Nevertheless, much of the difficulty in solving these issues is originated in the ill-definiteness and diversity of the studies samples.

6.2 Hybrid Organic-Inorganic Perovskites

The discovery and rise of lead halide perovskites materials took the scientific community by storm.[28] Since 2012 these materials emerged as the new front-runner in the next-generation photovoltaic field. The effective bridging of two often-separated worlds, i.e., those of low-cost fabrication and exceptional device performance, has propelled interest among scientist from different disciplines.[29] Hence, this material was thrust to the forefront of research in various optoelectronic related fields. A concerted global effort allowed achieving a deeper level of understanding of their photophysics in less than five years.

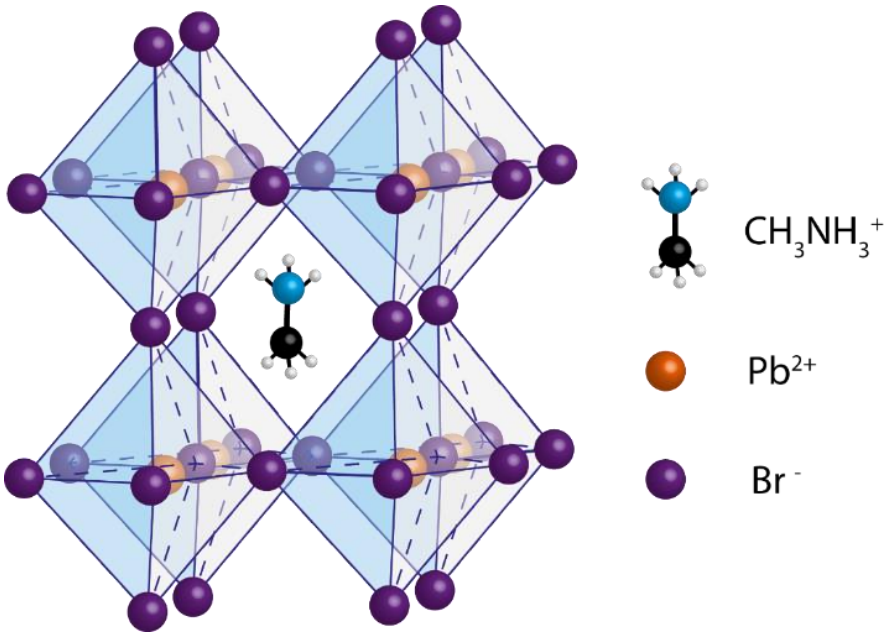

Figure 6.1-Shaded polyhedra representation of the structure and of three-dimensional (3-D) structural framework for cubic ABX_3 perovskite. In the case of organic–inorganic hybrid perovskites, at least one of the "A", "B", or "X" ions are organic; in this case, methylammonium cation $CH_3NH_3^+$ occupies the A site, whereas the B-site is occupied by Pb^{2+} cations. The structure is built upon corner-sharing BX_6 octahedra, formed my lead and bromide. A cations fill the 12-fold cuboctahedral voids among the octahedra.

The organic–inorganic hybrid lead halide perovskites (HPs) can be considered as an extension of oxide perovskites, with general stoichiometry ABO_3. In particular, HPs with general stoichiometry ABX_3 can be obtained by replacement of halide ions in place of oxygen anions in the X-site and embedding of organic cationic molecules into the A-sites.[30] Within these structures, B-site is occupied by an octahedrally coordinate cation (BX_6), which perhaps constitutes the heart of these structures (Figure 6.1).

Typically, B-sites are occupied by a divalent metal cation, e.g., Sn^{2+},Pb^{2+}, Ge^{2+}. On the other hand, A-sites are cubo-octahedral cavities formed by twelve X anions. The A component presents a high degree of flexibility, ranging from a single atom to small molecular cations. The choice of A-site cation is regulated by the Goldschmidt tolerance factor, which can predict the stability of perovskites structure given the ionic radii of the components. For most diffuse lead and tin-based perovskites, typical A-cations are Cs^+, $CH_3NH_3^+$ (MA) and $HC(NH_2)_2^+$ (FA).

The electronic structure of these systems was a lively debated topic throughout these years. Initially, quite unsuccessful theoretical predictions were based on semi-empirical LCAO methods.[29] Further refinements, with the introduction of relativistic and spin-orbit correction in self-consistent calculations, lead to an adequate description of the electronic states for these materials. [31] According to these calculations, many of the most relevant HPs are direct gap semiconductors. Nevertheless, in the first month of 2017, more subtle effects such as Rasbha/Dresselhaus splitting were reported for non-centrosymmetric phases.[32]

A substantial part of the electronic structure is dictated by the $[BX_6]^{4-}$ octahedral building blocks.[33] In the resulting band structure, the band extrema can be approximated by parabolic dispersion and similar dispersion of valence and conduction band results in comparable electron and hole effective masses. Although B-cations and X-anions effectively shape valence and conduction band, A-cation exerts an indirect effect on the band structure. Besides templating effects, A-cations introduce dynamic disorder through the rotational degree of freedom. This has significant consequences on the dielectric behavior of HPs and on Coulombic screening effects.[29]

The perceived effectiveness of thin film and non-sensitized perovskites solar cells raised interest in the role of excitons and free carriers in dictating the photophysics of HPs. Indeed, in the photovoltaic field excitons are considered as non-fully separated energy quanta. Therefore, exciton ionization or separation is the fundamental mechanism for carrier extraction. Excitons in bulk systems are described in terms of envelope function formalism. Namely, single particle Bloch functions are the product between two functions, i.e., a plane wave (stemming from translational symmetry) and a function with the periodicity of the crystal lattice (stemming from unitary cell potential).

When a carrier is excited through an interband transition, the presence of the hole Coulomb potential disrupts the translational symmetry and a hydrogenic interaction model becomes more adequate, with respect to the plane wave description. Hence, so-called Mott-Wannier excitons are excited electronic states comprising coulombically interacting electron-hole pairs, delocalized across different unitary cells, which wander freely across the bulk crystal.

This perturbative description of excitons is made possible by the scarce interaction between photoexcited carriers and contrasts with Frenkel description, adequate for strongly interacting carriers. The above-mentioned reduced interaction originates from the high dielectric screening and low effective masses, which counteract Coulomb localizing interaction. Indeed, the Wannier exciton binding energy (E_b) scales as

$$E_b \propto \frac{\mu}{\varepsilon^2} \qquad \textbf{(Eq. 6.1)}$$

where μ is the exciton reduced mass and ε is the dielectric constant. Combination of high dielectric constant and low effective masses is expected to result in loosely bound excitons in HPs. Measurements though magneto-absorption, temperature resolved PL and absorption spectroscopies reported a wide range of E_b, e.g., for $MAPbI_3$ (2-60meV) and for $MAPbBr_3$ (25-150meV).[29]

HPs display exciton binding energies which are relatively low, compared to thermal energy quanta (k_bT_{298K}~$26meV$). Therefore, similarly to GaAs free carriers play an important role in excited state dynamics of HPs. The semiconductor mass action law, in terms of the Saha equation, regulates the thermal equilibrium between free carriers and exciton within these materials. In particular in triiodide family $E_b \leq k_bT_{298K}$, whereas in tribromide and trichloride $E_b \geq k_bT_{298K}$. The ratio of free carriers with respect to excitons increases with increasing temperature due to phonon scattering induced ionization. Furthermore, the excitation density regulates the probability of electron-hole Coulomb capturing and therefore is proportional to the exciton density.[34]

6.2.1 Perovskite Dots

Determining whether either free carriers or excitons dominate the photophysics of HPs is a crucial step in envisaging their possible applications. Possible applications in light emitting devices would profit far more from excitons than from free carriers. Indeed, in free carrier semiconductors (e.g. GaAs) the radiative recombination is a quadratic process ($\propto n^2$) and must outpace Shockley-Read-Hall trap-mediated processes ($\propto n$) to achieve high quantum yields. Therefore, these materials are not suitable for low injection light emitting devices, such as LEDs.

Apparently, these essential features of HPs hamper their use in applications such as light emitting diodes and single photon emitters. Nevertheless, the reduction of dimensionality has proven to be a profitable strategy in coupling the electronic states of a material with the radiation field. As profusely explained in Chapter 1, the squeezing of excitons inside volume comparable with their spatial extension profoundly affects the excited state wavefunction.[28]

In particular, the enhanced Coulomb interaction between electron and holes (Eq. 1.8, Chapter 1) increases the exciton binding energy and confers superior optical properties to the nanostructures.

During last three years, much effort has been spent in developing HPs nanostructures. Perez-Prieto et al. first reported the synthesis of colloidal HPs nanocrystals, based on methylammonium lead bromide perovskite ($MAPbBr_3$).[35] This synthesis involved the reaction of MABr and $PbBr_2$ in a DMF solution and precipitation in acetone solution in the presence of long chain alkyl ammonium bromide, oleic acid (OLA) and octadecene (ODE). The proposed growth mechanism focused the attention on the long alkyl cations, unfitting to the voids of the corner-sharing PbX_6 octahedra. While the MA^+ cations can participate in the perovskites motive in A-sites, these molecules bind to the periphery of the octahedra acting as ligand groups.

To overcome poor solubility issues of perovskite precursors in ODE, Zhang and co-workers [36] developed ligand-assisted reprecipitation (LARP) strategy. This technique was based on the dropwise addition of the precursor/DMF solution to an antisolvent, such as toluene. Hence, by using toluene instead of acetone and by tuning the ratio of precursors in DMF (MABr, $PbBr_2$, octylammonium bromide (OABr)), analogous nanoparticles were obtained. In particular, resulting perovskites quantum dots (PDs) with a particle size of 5.5 nm reported up to 83% photoluminescence quantum yield (PLQY).

Rogach further extended this synthetic strategy and reported the synthesis of $MAPbBr_3$ PDs at various temperatures of the toluene (ranging between 0–60°C).[37]

This allowed controlling PDs size, and average diameters between 1.8 and 3.6nm were obtained. Accordingly, this resulted in spectral tuning of PL from 470 nm to 520 nm, with PLQY as high as 93%.

The structural instability of PDs and HPs is considered a significant hurdle in their applications.[38] Hence, the quest for mitigation strategies became increasingly important. This instability mostly stems from the excellent solubility of perovskites in polar solvents. This, together with the highly dynamic binding of ligands to the surface of PDs, threaten PDs and leads to their dissolution upon exposition to ambient. Among adopted strategies, the embedding of PDs in silica microbeads and the use of Cs^+ as A-site cations revealed to improve the PDs stability efficiently. [39-40] The reduction of HPs dimensionality led to the production of 1D and 2D nanostructures, as well. 1D nanorods and 2D nanoplatelets syntheses were reported, using both chemical and physical methods. Although different papers reported the synthesis of these nanostructures, many open questions on the formation mechanism stand still. This niche is expected to develop rapidly in view of lasing applications. [41-42]

Akin to traditional semiconductor QDs, PDs show superior PLQY over their bulk counterparts. As discussed above, the enhanced PLQY originates from increased exciton binding energy. The exciton Bohr radius was reported to range from 2 to 4nm in $MAPbBr_3$. Thus, quantum confinement effect is expected to play a role in the optical properties of PDs.[43] Unfortunately, only a few works reporting PDs electronic energy levels calculation have been published.

At the current stage of development, almost daily novel synthetic routes and applications (e.g., assembly or matrix embedding) are reported. In parallel with applications, a handful of research groups are focusing on PDs exciton dynamics. Current understanding and some advances within this field will be discussed in Chapter 9.

References

1. D'Souza, F., *Fullerenes, Nanotubes, and Carbon Nanostructures 2*; Electrochemical Society, 2007.

2. Guldi, D. M.Martín, N., *Carbon Nanotubes and Related Structures: Synthesis, Characterization, Functionalization, and Applications*; Wiley, 2010.

3. Guldi, D. M.Martin, N., *Fullerenes: From Synthesis to Optoelectronic Properties*; Springer Netherlands, 2002.

4. Geim, A. K.Novoselov, K. S., The Rise of Graphene. *Nat Mater* **2007**, *6*, 183-191.

5. Baker, S. N.Baker, G. A., Luminescent Carbon Nanodots: Emergent Nanolights. *Angewandte Chemie International Edition* **2010**, *49*, 6726-6744.

6. Li, X.; Rui, M.; Song, J.; Shen, Z.Zeng, H., Carbon and Graphene Quantum Dots for Optoelectronic and Energy Devices: A Review. *Advanced Functional Materials* **2015**, *25*, 4929-4947.

7. Sun, Y.-P., et al., Quantum-Sized Carbon Dots for Bright and Colorful Photoluminescence. *Journal of the American Chemical Society* **2006**, *128*, 7756-7757.

8. Hu, S.-L.; Niu, K.-Y.; Sun, J.; Yang, J.; Zhao, N.-Q.Du, X.-W., One-Step Synthesis of Fluorescent Carbon Nanoparticles by Laser Irradiation. *Journal of Materials Chemistry* **2009**, *19*, 484-488.

9. Amendola, V.Meneghetti, M., Laser Ablation Synthesis in Solution and Size Manipulation of Noble Metal Nanoparticles. *Physical Chemistry Chemical Physics* **2009**, *11*, 3805-3821.

10. Deng, J., et al., Electrochemical Synthesis of Carbon Nanodots Directly from Alcohols. *Chemistry – A European Journal* **2014**, *20*, 4993-4999.

11. Li, L.; Wu, G.; Yang, G.; Peng, J.; Zhao, J.Zhu, J.-J., Focusing on Luminescent Graphene Quantum Dots: Current Status and Future Perspectives. *Nanoscale* **2013**, *5*, 4015-4039.

12. Qu, D.; Zheng, M.; Zhang, L.; Zhao, H.; Xie, Z.; Jing, X.; Haddad, R. E.; Fan, H.Sun, Z., Formation Mechanism and Optimization of Highly Luminescent N-Doped Graphene Quantum Dots. *Sci. Rep.* **2014**, *4*.

13. Mosconi, D.; Mazzier, D.; Silvestrini, S.; Privitera, A.; Marega, C.; Franco, L.Moretto, A., Synthesis and Photochemical Applications of Processable Polymers Enclosing Photoluminescent Carbon Quantum Dots. *ACS Nano* **2015**, *9*, 4156-4164.

14. Strauss, V., et al., Carbon Nanodots: Toward a Comprehensive Understanding of Their Photoluminescence. *Journal of the American Chemical Society* **2014**, *136*, 17308-17316.

15. Hou, J.; Wang, W.; Zhou, T.; Wang, B.; Li, H.Ding, L., Synthesis and Formation Mechanistic Investigation of Nitrogen-Doped Carbon Dots with High Quantum Yields and Yellowish-Green Fluorescence. *Nanoscale* **2016**, *8*, 11185-11193.

16. Zhu, S.; Song, Y.; Zhao, X.; Shao, J.; Zhang, J.Yang, B., The Photoluminescence Mechanism in Carbon Dots (Graphene Quantum Dots, Carbon Nanodots, and Polymer Dots): Current State and Future Perspective. *Nano Res.* **2015**, *8*, 355-381.

17. Xu, Q.; Kuang, T.; Liu, Y.; Cai, L.; Peng, X.; Sreenivasan Sreeprasad, T.; Zhao, P.; Yu, Z.Li, N., Heteroatom-Doped Carbon Dots: Synthesis, Characterization, Properties, Photoluminescence Mechanism and Biological Applications. *Journal of Materials Chemistry B* **2016**, *4*, 7204-7219.

18. Alam, A.-M.; Park, B.-Y.; Ghouri, Z. K.; Park, M.Kim, H.-Y., Synthesis of Carbon Quantum Dots from Cabbage with Down- and up-Conversion Photoluminescence Properties: Excellent Imaging Agent for Biomedical Applications. *Green Chemistry* **2015**, *17*, 3791-3797.

19. Lin, P.-Y., et al., Eco-Friendly Synthesis of Shrimp Egg-Derived Carbon Dots for Fluorescent Bioimaging. *Journal of Biotechnology* **2014**, *189*, 114-119.

20. Hu, Y.; Yang, J.; Tian, J.; Jia, L.Yu, J.-S., Waste Frying Oil as a Precursor for One-Step Synthesis of Sulfur-Doped Carbon Dots with Ph-Sensitive Photoluminescence. *Carbon* **2014**, *77*, 775-782.

21. Essner, J. B.; Laber, C. H.; Ravula, S.; Polo-Parada, L.Baker, G. A., Pee-Dots: Biocompatible Fluorescent Carbon Dots Derived from the Upcycling of Urine. *Green Chemistry* **2016**, *18*, 243-250.

22. Dekaliuk, M. O.; Viagin, O.; Malyukin, Y. V.Demchenko, A. P., Fluorescent Carbon Nanomaterials: "Quantum Dots" or Nanoclusters? *Physical Chemistry Chemical Physics* **2014**, *16*, 16075-16084.

23. Pan, D.; Zhang, J.; Li, Z.; Wu, C.; Yan, X.Wu, M., Observation of Ph-, Solvent-, Spin-, and Excitation-Dependent Blue Photoluminescence from Carbon Nanoparticles. *Chemical Communications* **2010**, *46*, 3681-3683.

24. Cushing, S. K.; Li, M.; Huang, F.Wu, N., Origin of Strong Excitation Wavelength Dependent Fluorescence of Graphene Oxide. *ACS Nano* **2014**, *8*, 1002-1013.

25. Sciortino, A.; Marino, E.; Dam, B. v.; Schall, P.; Cannas, M.Messina, F., Solvatochromism Unravels the Emission Mechanism of Carbon Nanodots. *The Journal of Physical Chemistry Letters* **2016**, *7*, 3419-3423.

26. Galande, C., et al., Quasi-Molecular Fluorescence from Graphene Oxide. *Scientific Reports* **2011**, *1*, 85.

27. Fu, M.; Ehrat, F.; Wang, Y.; Milowska, K. Z.; Reckmeier, C.; Rogach, A. L.; Stolarczyk, J. K.; Urban, A. S.Feldmann, J., Carbon Dots: A Unique Fluorescent Cocktail of Polycyclic Aromatic Hydrocarbons. *Nano Letters* **2015**, *15*, 6030-6035.

28. Ha, S.-T.; Su, R.; Xing, J.; Zhang, Q.Xiong, Q., Metal Halide Perovskite Nanomaterials: Synthesis and Applications. *Chemical Science* **2017**, *8*, 2522-2536.

29. Manser, J. S.; Christians, J. A.Kamat, P. V., Intriguing Optoelectronic Properties of Metal Halide Perovskites. *Chemical Reviews* **2016**, *116*, 12956-13008.

30. Saparov, B.Mitzi, D. B., Organic-Inorganic Perovskites: Structural Versatility for Functional Materials Design. *Chemical Reviews* **2016**, *116*, 4558-4596.

31. Umari, P.; Mosconi, E.De Angelis, F., Relativistic Gw Calculations on Ch3nh3pbi3 and Ch3nh3sni3 Perovskites for Solar Cell Applications. **2014**, *4*, 4467.

32. Kepenekian, M.; Robles, R.; Katan, C.; Sapori, D.; Pedesseau, L.Even, J., Rashba and Dresselhaus Effects in Hybrid Organic-Inorganic Perovskites: From Basics to Devices. *ACS Nano* **2015**, *9*, 11557-11567.

33. Vincent, B. R.; Robertson, K. N.; Cameron, T. S.Knop, O., Alkylammonium Lead Halides. Part 1. Isolated Pbi64− Ions in (Ch3nh3)4pbi6•2h2o. *Canadian Journal of Chemistry* **1987**, *65*, 1042-1046.

34. D'Innocenzo, V.; Grancini, G.; Alcocer, M. J. P.; Kandada, A. R. S.; Stranks, S. D.; Lee, M. M.; Lanzani, G.; Snaith, H. J.Petrozza, A., Excitons Versus Free Charges in Organo-Lead Tri-Halide Perovskites. **2014**, *5*, 3586.

35. Gonzalez-Carrero, S.; Galian, R. E.Perez-Prieto, J., Maximizing the Emissive Properties of Ch3nh3pbbr3 Perovskite Nanoparticles. *Journal of Materials Chemistry A* **2015**, *3*, 9187-9193.

36. Zhang, F.; Zhong, H.; Chen, C.; Wu, X.-g.; Hu, X.; Huang, H.; Han, J.; Zou, B.Dong, Y., Brightly Luminescent and Color-Tunable Colloidal Ch3nh3pbx3 (X = Br, I, Cl) Quantum Dots: Potential Alternatives for Display Technology. *ACS Nano* **2015**, *9*, 4533-4542.

37. Huang, H.; Susha, A. S.; Kershaw, S. V.; Hung, T. F.Rogach, A. L., Control of Emission Color of High Quantum Yield Ch3nh3pbbr3 Perovskite Quantum Dots by Precipitation Temperature. *Advanced Science* **2015**, *2*, 1500194-n/a.

38. Manser, J. S.; Saidaminov, M. I.; Christians, J. A.; Bakr, O. M.Kamat, P. V., Making and Breaking of Lead Halide Perovskites. *Accounts of Chemical Research* **2016**, *49*, 330-338.

39. Huang, S.; Li, Z.; Kong, L.; Zhu, N.; Shan, A.Li, L., Enhancing the Stability of Ch3nh3pbbr3 Quantum Dots by Embedding in Silica Spheres Derived from Tetramethyl Orthosilicate in "Waterless" Toluene. *Journal of the American Chemical Society* **2016**, *138*, 5749-5752.

40. Fu, P.; Shan, Q.; Shang, Y.; Song, J.; Zeng, H.; Ning, Z.Gong, J., Perovskite Nanocrystals: Synthesis, Properties and Applications. *Science Bulletin* **2017**, *62*, 369-380.

41. Zhang, D.; Yu, Y.; Bekenstein, Y.; Wong, A. B.; Alivisatos, A. P.Yang, P., Ultrathin Colloidal Cesium Lead Halide Perovskite Nanowires. *Journal of the American Chemical Society* **2016**, *138*, 13155-13158.

42. Weidman, M. C.; Seitz, M.; Stranks, S. D.Tisdale, W. A., Highly Tunable Colloidal Perovskite Nanoplatelets through Variable Cation, Metal, and Halide Composition. *ACS Nano* **2016**, *10*, 7830-7839.

43. Tyagi, P.; Arveson, S. M.Tisdale, W. A., Colloidal Organohalide Perovskite Nanoplatelets Exhibiting Quantum Confinement. *The Journal of Physical Chemistry Letters* **2015**, *6*, 1911-1916.

CHAPTER 7

Materials and Methods.2

ABSTRACT- This short Chapter introduces both the materials studied and the methods employed in this Part of the thesis. Specifically, this Chapter completes the overview of experimental techniques of Chapter 2 and provides theoretical bases and experimental setups necessary for the understanding of upcoming Chapters. The discussion for each technique is marked out precisely in view of their application to systems studied. Concerning experimental techniques, the reviewing of fundamental principles and experimental expedients of fluorescence correlation spectroscopy and time-resolved photoluminescence spectroscopies is given. In addition, this chapter briefly reviews the synthesis of studied samples, which were provided in collaboration with other research groups.

7.1 Time-Resolved Photoluminescence (TRPL) spectroscopy

Photoluminescence (PL) lifetime, i.e., the parameter quantifying the persistence of the PL signal following photoexcitation, can shed light on the interplay between radiative and non-radiative recombination processes in nanostructures.[1] Hence, the accurate determination of this parameter is the doorway to access subtle aspects of the exciton dynamics of studied samples. Recording PL decay curves present some practical problem. Albeit in principle, it could be possible to record PL decays in single-shot measurements, real working conditions prevent from this. Namely, PL decays of nanostructures are usually too fast with respect to electronic dead times, typically in the pico-to-nanoseconds timescale. Moreover, the shape of this decay is complicated (e.g., multi-exponential or stretched exponential behavior).[2]

Time-correlated single photon counting (TCSPC) is the principal technique employed in nanoscience for the measurement of PL decays. Through TCSPC, the required time resolution and signal-to-noise ratio can be achieved. This technique relies on single photon detection of the PL signal produced by a pulsed excitation, and on the contextual measurement of the arrival times of each individual photon. The fundamental concept underlying TCSPC is the fact that, for low level and high repetition rate signals, the light intensity is usually low enough to consider the probability to detect one photon in one signal cycle much less than one. As shown in Figure 7.1, when recording an optical signal pumped by a low intensity and a high rep. rate excitation, many cycles (or excitation-detection periods) without emitted photons are observed, whereas in other periods one photon pulse is detected.[3]

Thanks to the high repetition rate of the source, a statistical analysis is conducted on a considerable number (typically billions) of cycles. This allows building a histogram of the photon detection events with respect to the arrival time. Provided a sufficient number of events, the resulting histogram statistically reconstructs the temporal profile of the PL signal.

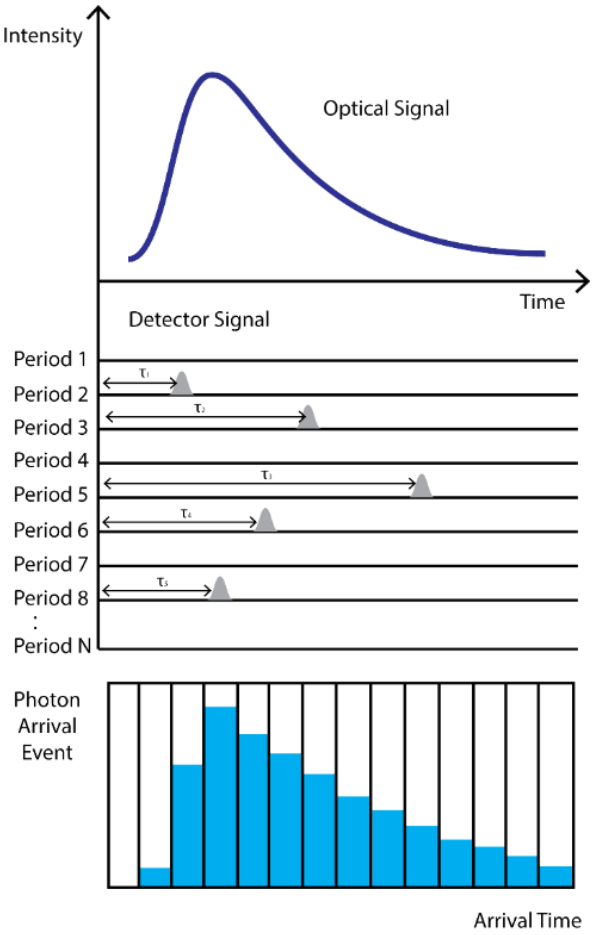

Figure 7.1- Working principle of TCSPC technique. The PL signal is repeatedly generated for a considerable number N of times. Each period consists of an excitation-detection cycle, during which a single photon event is measured, and its arrival time τ_n is recorded. If the excitation intensity is low and its repetition rate is high, then only single photon detection event will occur. Provided these conditions and an adequately high number of periods, the histogram of single photon arrival times ($N(\tau_n)$ vs. τ) statistically reconstructs the form of the optical signal. Adapted from Ref. 3.

Thus, TCSPC technique allows overcoming electronic dead times and time-gating related issues. Indeed, the time resolution is only limited by the source pulse width and by the transit time spread in the detector. In the best-case scenario, a width of the instrument response function (IRF) of about 25 ps can be achieved.[4]

7.1.1 TRPL Experimental Apparatus

The experimental apparatus was based on Fluoromax-P detection unit (grating monochromator and photomultiplier tube), powered by FluoroHub Single Photon Counting unit. The excitation source was a pulsed Horiba NanoLED, generating 1ns long pulses with a tunable repetition rate (1MHz-1kHz) and therefore time-windows. NanoLED with different emission wavelengths (370 and 455nm) were used for spectrally resolved studies. In addition, the low fluence of these sources allowed neglecting multi-

exciton effects in studied nanomaterials. The instrument response function (IRF) of ~1.2ns for the whole apparatus was determined by means of scattered light detection. Experimentally, the LED excitation was focused on the sample holder by means of a spherical lens, and the PL was collected with 90° geometry to minimize scattering interferences.

7.2 Fluorescence Correlation Spectroscopy (FCS)

Fluorescence Correlation Spectroscopy (FCS) is a powerful spectroscopic technique, initially developed for bio-physical investigation. Yet it can be harnessed to extract valuable information on the fluorescent species or nanoparticles in a studied solution.[5] Hence, FCS can be used as an analytical technique, providing direct access to structure-property correlation for molecules and nanoparticles.[6]

An alternative - and probably more appropriate - name for this technique is Fluctuations Correlation Spectroscopy. Indeed, the parameter of interest in FCS is not the fluorescence signal itself, but rather the intensity fluctuations of that signal. By means of a physical model, the microscopic fluctuations, produced by either nanoparticles or molecules while randomly wandering across the observation volume, are associated with diffusion coefficient and concentration of emitting species. The possibility of obtaining information on particles and molecules, without removing them from the solution/colloidal dispersion made FCS lucrative for nano-medicine and biochemistry. Nevertheless, in last year FCS emerged as a useful technique to size nanoparticles as well as monitor their interaction with the environment.

From a mathematical point of view, fluctuations are quantified by temporal autocorrelation analysis of the fluorescence signal. This operation measures the self-similarity of the intensity time-trace, thereby describing the persistence of the information carried by it, and provides characteristic time constants for physical processes governing the dynamics of the system. [7]

Seemingly, FCS is a counter-intuitive technique because the significance of the signal is inversely proportional to concentration or observed volume (e.g., in concentrated solutions/bulk observation volumes, the FCS signal tends to zero). Indeed, the consideration of a small number of observed molecules makes each one of them contributing significantly to the recorded signal. Therefore, substantial non-correlated fluctuations are observed only when concentration and observation volumes are reduced enough.

According to statistical mechanics, the number density fluctuations are quantified as

$$\frac{\Delta N}{N} \sim \frac{1}{\sqrt{N}} \qquad \textbf{(Eq. 7.1)}$$

where N is number density. Accordingly, fluctuations tend to zero when the number of observed particles increases. The most straightforward implementation of FCS is based on confocal detection methods, which allow shrinking the observed volumes down to femtoliter $(1fl = 1\mu m^3)$. In order to have an FCS signal, stemming out of the background, the average number of molecules in the observation volume should range between 1 and 1000. This limits the concentrations of interest, for FCS, to the $nM - \mu M$ range. [7]

When a fluorophore diffuses inside the observation volume is excited and consequently emits a photon. Under the above-mentioned conditions, the diffusion process cause a considerable intensity fluctuation $\delta I(t)$ over the average fluorescence intensity $\langle I(t)\rangle$.

Mathematically, the fluctuation is defined as $\delta I(t) = I(t) - \langle I(t)\rangle$. As discussed above the temporal autocorrelation of this signal, defined as

$$G(\tau) = \frac{\langle \delta I(t) \cdot \delta I(t+\tau)\rangle}{\langle I(t)\rangle^2} \qquad \textbf{(Eq. 7.2)}$$

physically represents the self-similarity of the signal at a lag time τ and allows gaining information on the fluorescent species. Considering that fluctuation originates from single fluorophore dynamics, it is possible to define

$$\delta I(t) = \beta \int_V F(r) \cdot S(r) \cdot \delta\big(\sigma \cdot PLQY \cdot C(r,t)\big) dr \qquad \textbf{(Eq. 7.3)}$$

where β is the detection efficiency, $\boldsymbol{F(r)}$ is the excitation profile, $\boldsymbol{S(r)}$ is the confocal microscope transfer function and $\delta(\sigma \cdot QY \cdot C(\boldsymbol{r},t))$ is the dynamics of the fluorophore on the single particle level. Specifically, this is caused by fluctuations in absorption cross section (σ), concentration (C) and quantum yield (PLQY). [5]

In order to obtain a useful definition, two approximations are necessary:

1. The convolution of exciting and detection transfer functions is approximated as a 3D Gaussian function

$$\frac{F(r)}{F_0} \cdot S(r) \sim W(r) = e^{-2\frac{x^2+y^2}{r_0^2}} e^{-2\frac{z^2}{z_0^2}} \qquad \textbf{(Eq. 7.4)}$$

2. The photon count rate per detected molecule per second is defined as constant $\eta_0 = F_0 \cdot \beta \cdot PLQY \cdot \sigma$. This implies that fluorophore properties are not changing within observation time and that excitation intensity and detection efficiency are constant throughout the measurement, as well. Therefore, the derivative term is approximated as $\delta\big(\eta \cdot C(\boldsymbol{r},t)\big) = C\delta\eta + \eta\delta C \sim \eta\delta C$.

Substitution in Eq. 7.2 yields

$$G(\tau) = \frac{\iint W(r)W(r')\langle\delta C(r,0)\delta C(r',\tau)\rangle\, drdr'}{(\langle C\rangle \int W(r)dr)^2} \qquad \textbf{(Eq. 7.5)}$$

where the number density autocorrelation function was calculated, for a particle diffusing in three dimensions, with diffusion coefficient D as

$$\langle\delta C(r,0)\ \delta C(r',\tau)\rangle = \langle C\rangle \frac{1}{(4\pi D\tau)^{-3/2}} \cdot e^{-\frac{(r-r\prime)^2}{4D\tau}} \qquad \textbf{(Eq. 7.6)}$$

Moreover, the effective volume V_{eff} is calculated using Gaussian integrals

$$V_{eff} = \frac{(\int W(\boldsymbol{r})d\boldsymbol{r})^2}{\int W^2(\boldsymbol{r})d\boldsymbol{r}} = \pi^{\frac{3}{2}} \cdot r_0^2 \cdot z_0\,. \qquad \textbf{(Eq. 7.7)}$$

The resulting autocorrelation function for freely diffusing molecules is

$$G(\tau) = \frac{1}{V_{eff}\langle C\rangle} \cdot \frac{1}{1+\frac{\tau}{\tau_d}} \cdot \frac{1}{\sqrt{1+\left(\frac{r_0}{z_0}\right)^2 \frac{\tau}{\tau_d}}}. \qquad \textbf{(Eq. 7.8)}$$

where τ_d is the lateral diffusion time and is related to the diffusion coefficient via the equation $\tau_d = \frac{r_0^2}{4D}$ and the term $V_{eff}\langle C\rangle = \langle N\rangle$ is the average number of particles in the observation volume.

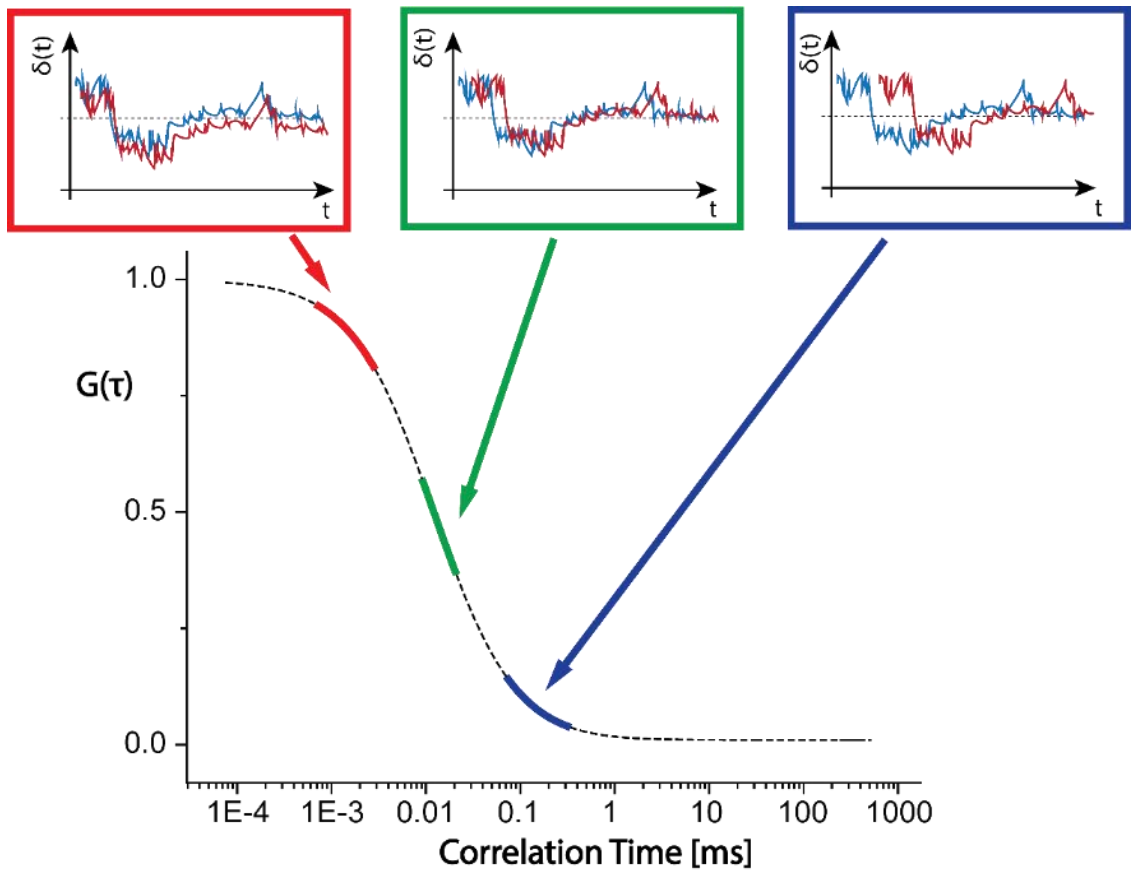

Figure 7.2 - Working principle of FCS technique. FCS technique analyzes intensity fluctuations of the fluorescence signal, originated by a small focal volume. When a small number of the molecules is involved, the fluctuations become statistically relevant with respect to the average value. The disclosure of quantitative information on the emitting species is achieved by autocorrelation analysis. This mathematical operation measures the persistence of the information carried by fluorescence signal, quantifying the self-similarity of the intensity trace at different correlation times. Operatively, the curve is translated by a correlation time τ_{corr} and multiplied by itself. The resulting correlation curve reaches its maximum at very short correlation times and progressively decreases with a characteristic time related to the physical process studied. Generally, when more than one processes cause fluctuations, more than one kink will be observed in the autocorrelation curve. Adapted from Ref 5.

Equation 7.7 gives rise to the typical decay profile depicted in Figure 7.2. Therefore, by fitting autocorrelation curves, it is possible to extract information on the translational diffusion coefficient of the particle. For unconstrained Brownian diffusion of a particle in three dimensions, this allows estimating its hydrodynamic radius R_H, using the Stokes-Einstein relation

$$R_H = \frac{k_b T}{6\pi\eta_D D} \qquad \textbf{(Eq. 7.9)}$$

if the dynamic viscosity η_D of the solvent at temperature T is known. Combining this equations, a linear proportionality relation between τ_d and R_H is established.

Physically, this translates to smaller particles travelling rapidly across the observation volume and causing a faster decay of the correlation curve, with respect to bulkier ones. Although FCS relies on the approximation of spherical particle, it proved to be a valuable and precise technique for measuring the size of nanoparticles. Obviously, an accurate determination of observation volume's dimensions is essential to estimate the hydrodynamic radius correctly.

The beam parameters of Equation 7.8 (r_0 and z_0) are usually obtained using a calibration standard (e.g. Alexa 488/Coumarine, whose diffusion coefficient is either known or calculated). According to this physical model, fluctuations are caused by translational diffusion. Nevertheless, many other photophysical processes can induce fluorescence intensity variations at single fluorophore level (e.g., intersystem crossing, blinking, photo-bleaching). Considering that these processes act on the emission efficiency of the fluorophore, a comprehensive description would request the relaxation of the $\delta\eta = 0$ approximation. Howbeit, instead of recalculating the correlation function, it is used to take advantage of timescale separation of the different processes. This allows recasting $G(\tau)$ as a product of autocorrelation functions

$$G(\tau) = G_{diff}(\tau) \cdot G_{phen}(\tau) \qquad \textbf{(Eq. 7.10)}$$

where the $G_{phen}(\tau)$ is usually related to intersystem crossing when dealing with molecules and to blinking when dealing with quantum dots.

7.2.1 Coumarin 503 as FCS Standard

Aiming to estimate of hydrodynamic radii of Carbon dots in Chapter 8, Coumarin 503 (C503) was used as a standard at 370-400-440nm excitation. (Figure 7.3)

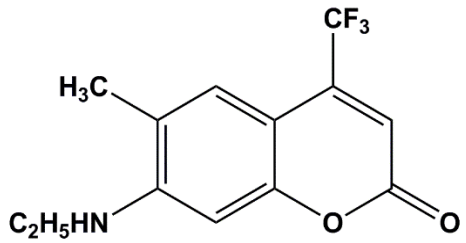

Figure 7.3 : Chemical formula of Coumarine 503 (C503) used as a standard in FCS measurements.

Even though this is a well-known standard for fluorescence measurements, an accurate determination/ knowledge of its structural parameters underlies it use as FCS standard. Hence, the diffusion coefficient of C503 standard was calculated, in collaboration with Dr. M. Zerbetto and Dr. I. Fortunati, starting from literature data on its dimensions.[8]

Since FCS measurements performed without polarization selection are insensitive to spatial anisotropy, an averaged diffusion coefficient over the three dimensions was calculated.[9] C503 molecules were considered as ellipsoids, of which the principal components of the diffusion tensor were estimated as

$$D_i^{rot} = \frac{k_B T}{f_i} \qquad (i = x, y, z) \qquad \textbf{(Eq. 7.11)}$$

where the frictional coefficients were calculated as

$$f_x = \frac{16\pi\eta(a_y^2 + a_z^2)}{3(a_y^2 Q + a_z^2 R)} \quad f_y = \frac{16\pi\eta(a_x^2 + a_z^2)}{3(a_x^2 P + a_z^2 R)} \quad f_z = \frac{16\pi\eta(a_x^2 + a_y^2)}{3(a_x^2 P + a_y^2 Q)} \qquad \textbf{(Eq. 7.12)}$$

where η is the viscosity, a_i are ellipsoid dimensions and parameters P,Q,R are integral expressed as

$$P = \int_0^\infty \frac{ds}{\sqrt{(a_x^2 + s)^3 (a_y^2 + s)(a_z^2 + s)}}$$
$$Q = \int_0^\infty \frac{ds}{\sqrt{(a_y^2 + s)^3 (a_x^2 + s)(a_z^2 + s)}} \qquad \textbf{(Eq. 7.13)}$$
$$R = \int_0^\infty \frac{ds}{\sqrt{(a_z^2 + s)^3 (a_y^2 + s)(a_x^2 + s)}}$$

The combination of resulting components as $D_0^{rot} = 1/3 \sum_{i=1}^{3} D_i^{rot}$ and the used of rotational diffusion coefficient definition yielded an average radius

$$R = \sqrt[3]{\frac{3k_B T}{4c\ \eta\pi D_0^{rot}}} \qquad \textbf{(Eq. 7.14)}$$

where *c* =4 or 6, depending on stick or slip conditions. *R* is the radius of the equivalent sphere obtained by the averaged rotational diffusion coefficient. This value was used to calculate the averaged translational diffusion coefficient by Stokes-Einstein formula

$$D^{trasl} = \frac{k_B T}{6\ \pi\eta R} \qquad \textbf{(Eq. 7.15)}$$

Resulting values for C503 were

$$D_{slip}^{trasl} = 672\ \mu m^2 s^{-1} \quad D_{stick}^{trasl} = 513\ \mu m^2 s^{-1}$$

Since C503 is a hydrophilic molecule, stick conditions were used in order to calculate the diffusion coefficient. From this value of the diffusion coefficient D_{stick}^{trasl} and from the fitting diffusion time τ_D of C503 used as standard, the radius of the focal volume was estimated by Brownian motion formula:

$$w_0 = \sqrt{4D_{stick}^{trasl}\tau_D}$$

Lastly, this value was in the calculation of the hydrodynamic radius of Cit-CDs and Arg-CDs from Stokes-Einstein formula.

7.2.2 Experimental Apparatus

The experimental apparatus used for FCS measurements was based on a confocal microscope (Olympus IX-71) coupled with a TimeHarp 200 TCSPC unit (PicoQuant) and two single-photon counting avalanche photodiodes (SPAD, MPD, Italy). Wavelength tunable excitation was provided by a frequency doubled Ti:sapphire femtosecond laser system (Coherent, model Mira Optima 900-F, 76 MHz, 100 fs) in the 370-440nm range. On the other hand, fixed 488nm excitation was provided by an Ar-Kr laser (Melles-Griot, 100mW). The excitation beam was focused on the particle solution through a water-immersion 100× objective. The fluorescence signal, collected through the same microscope objective, was focused into an optical fiber ($100\mu m$). A beam splitter divided the signal and sent it to two SPAD. A combination of band-pass filters and neutral density filter were used to reduce backscattered light signal.

7.3 Carbon Dots (CDs) synthesis

In this Part of the thesis were investigated the optical properties of two different CDs systems: Arg-CDs and Cit-CDs. The synthesis and the purification of these samples were performed by Dr. D. Mosconi in the lab of Prof. A. Moretto. These syntheses followed a protocol developed by professor Moretto and previously published on several papers.[10-12] For the sake of completeness, the basic procedure of the synthesis of these samples is here briefly reported and commented. From a general point of view, the reported syntheses are based on a bottom-up approach described in the previous Chapter, i.e., pyrolysis of small molecule precursors. Respectively, citric acid and arginine were used as carbon precursors, whereas the nitrogen doping was achieved by ethylenediamine. Being the pitfalls in characterization step themselves, the focus of the study carried on in the following Chapter, for the structural and optical characterization of as-synthesized samples the reader is referred to Chapter 8.

7.3.1 Citric Acid Based CDs (Cit-CDs)

Citric acid (1.05 g, 5.46 mmol) was dissolved in 25 ml of milliQ water (18.2 MΩ) and subsequently ethylenediamine (EDA; 1.00 ml, 14.98 mmol) was added as a nitrogen source. The solution was stirred in a 250 ml beaker until it became clear. The beaker was then placed into a domestic microwave oven, and it was irradiated for 4 minutes at 700 W. At the end of this time, the beaker was placed immediately into a water-ice bath to quench any further condensation. A brownish material was obtained, which was washed on a gooch filter with 3x20 ml of acetonitrile and 3x20 ml of diethyl ether. The product was redispersed in milliQ water, filtered through a cellulose syringe filter (0.45 μm cut-off) and put in dialysis (1 kDa cut-off) against water for 1 day. The suspension was frozen in an acetone/dry ice bath and dried through lyophilization.

7.3.2 Arginine Based CDs (Cit-CDs)

Chlorohydrated arginine (10.2 g, 48.4 mmol) and ethylenediamine (3.56 mL,53.3 mmol) are introduced in a 250 mL beaker containing 26.6 mL of ultrapure water. The solution was stirred at r.t. until complete dissolution of reactants, and then it was irradiated in a domestic microwave oven for 4 min at 1000 W. During this lapse of time, white-gray aqueous vapor came out from the vents of the oven. A porous black-reddish solid was obtained, and it was washed in a Gooch filter with 4x20 mL aliquots of acetonitrile and 4x20 mL of diethyl ether. The solid was dried for several minutes in air and dissolved in the minimum volume of ultrapure water to obtain a dark and turbid solution, which is filtered through a cellulose syringe filter (0.45μm cutoff) and put in a dialysis bag, analogous to that used for Cit-CDs. The purified solution was then frozen using a bath of acetone and solid carbon dioxide and then dried under vacuum through a lyophilization process, yielding the final brownish compound, ultimately dissolved in water.

7.4 Perovskite Dots (PDs) Synthesis

Perovskite Dots (PDs) samples were synthesized by Dr. A. Privitera, following the ligand assisted re-precipitation (LARP) synthesis originally proposed by Zhang.[13] Specifically, the synthesis followed a slight modification of LARP protocol, proposed by Rogach and co-workers.[14]

The synthesis was performed under ambient laboratory conditions. A solution of methylammonium bromide $MAPbBr_3$ (8.7 mg, 0.16 mmol) and PbBr2 (14.7 mg, 0.2 mmol) in 1mL of DMF was mixed with 4 μL of n-octylamine and 0.1 mL of oleic acid to form the precursor solution. The preparation of methylammonium bromide followed from a previously published procedure. A single-neck round bottom flask with methylamine in absolute ethanol was placed in a water bath thermostated at 0°C. Under stirring, hydrobromic acid was dropped into the flask, and the reaction was allowed to proceed for 2 hours. Subsequently, the solvent was evaporated by rotavapor at 50°C, and the precipitate was washed thoroughly with diethyl ether and dried.

DMF was chosen as a suitable solvent for both inorganic salts and small organic molecules. Hence, the precursor solution contained both perovskites building block, n-octylamine, and oleic acid. These small molecules were chosen to act co-ligands in the formation of PDs. The facile synthesis was performed by dropping 100μL of precursor solution into 5 mL of toluene, under finely controlled temperature. Toluene is an anti-solvent for inorganic salt, leading to the formation of PDs capped with organic ligand (ensuing a good solubility). Immediately after dropping the precursor solution, the transparent solution turned into a yellow-green turbid solution. The final solution was centrifuged at 10000 rpm for 5 min, and the supernatant was kept as a bright and clear yellow solution.

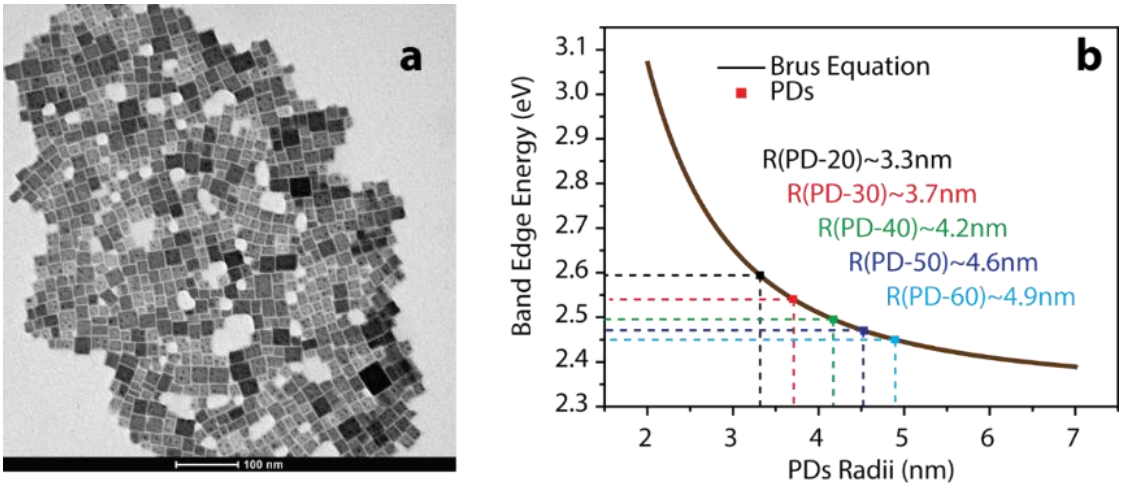

Figure 7.4 - (**a**) TEM micrograph of PD-60 sample deposited from toluene solution (**b**) Brus equation calculated for $MAPbBr_3$ quantum dots (using μ=0.12 m_0 and ε_{MAPbBr}=25.5 from literature). Radii for different PDs synthesized are roughly estimated by comparison of Brus curve and experimentally measured band-edge energy. Results are in accordance with reference 14

This synthesis was repeated for five different temperatures of the toluene (i.e., 20, 30, 40, 50 and 60°C) and five different samples (i.e., PD-20, PD-30, PD-40, PD-50, and PD-60) were obtained. Even though the strong PL of the resulting solution is an indirect proof of the synthesis of quantum-confined perovskite nanostructures, Dr. A. Privitera obtained a direct evidence of the successful synthesis, using the pXRD technique. Furthermore, a direct characterization of the dimensions of different PDs would require the analysis of electron micrographs obtained by transmission electron microscopy (TEM). An indicative micrograph of those resulting by TEM characterization for PD-60 is shown in Figure 7.4**a**.

Albeit similar TEM micrographs were reported by Sun et al.,[15] both the shape and the dimensions of the observed particles appear to be in contradiction with measured optical properties. Indeed the statistical analysis on micrograph provides a plausible value only for PD-20 ($L = 3.1 \pm 0.4nm$), whereas the average dimensions for other samples are well-beyond 15nm diameters

Considering that, the exciton Bohr radius of $MAPbBr_3$ perovskite was reported to be in the range $a_B = (2.1 - 2.5\ nm)$ and that in a similar synthetic procedure Rogach reported spherical PDs, it is possible to speculate that the evaporation procedure adopted in TEM measurements induces instability and coalescence of the PDs under the e-beam irradiation.

Instead, the average dimensions of PDs were estimated by measured optical properties. Specifically, in Chapter 1 was discussed the possibility of predicting the energy of excitons in a spherical dot using the effective mass approximation. Accordingly, the Brus model allows calculating the excess energy provided by confinement with respect to the bulk band gap, given the effective reduced mass μ and the dielectric constant ε_{PSK} .[16]

Hence, the average radii of the different PDs were estimated through their measured band edge absorption energy, using the Equation:

$$E_{band\ edge} = E_{bulk} + \frac{h^2}{8R^2} \cdot \frac{1}{\mu} - \frac{1.8e^2}{4\pi\epsilon_{PSK}R} \qquad \textbf{(Eq. 7.15)}$$

The resulting curve and extrapolated radii are shown in Figure 7.4**b**. Noteworthy, these values span the interval between 3 and 5 nm and are in good agreement with reports by Rogach. Yet this rough estimate cannot be considered quantitative because various approximations (e.g., spherical shape, two single and parabolic bands) underlies the Brus equation.

References

1. Lakowicz, J. R., *Principles of Fluorescence Spectroscopy*; Springer, **2007**.

2. Wahl, M., Time-Correlated Single Photon Counting. *PicoQuant TechNotes* **2010**.

3. Becker, W.; Bergmann, A.; Biscotti, G. L.Rueck, A., Advanced Time-Correlated Single Photon Counting Techniques for Spectroscopy and Imaging in Biomedical Systems. *Proceedings of SPIE* **2004**, *5340*.

4. Becker, W., *Advanced Time-Correlated Single Photon Counting Techniques*; Springer Berlin Heidelberg, 2005.

5. Schwille, P., Fluorescence Correlation Spectroscopy: An Introduction to Its Concepts and Applications

6. Dominguez-Medina, S.; Chen, S.; Blankenburg, J.; Swanglap, P.; Landes, C. F.Link, S., Measuring the Hydrodynamic Size of Nanoparticles Using Fluctuation Correlation Spectroscopy. *Annual Review of Physical Chemistry* **2016**, *67*, 489-514.

7. Ries, J.Schwille, P., Fluorescence Correlation Spectroscopy. *BioEssays* **2012**, *34*, 361-368.

8. Mannekutla, J. R.; Inamdar, S. R.; Mulimani, B. G.Savadatti, M. I., Rotational Diffusion of Coumarins: A Dielectric Friction Study. *J Fluoresc* **2010**, *20*, 797-808.

9. Ryabov, Y. E.; Geraghty, C.; Varshney, A.Fushman, D., An Efficient Computational Method for Predicting Rotational Diffusion Tensors of Globular Proteins Using an Ellipsoid Representation. *Journal of the American Chemical Society* **2006**, *128*, 15432-15444.

10. Mosconi, D.; Mazzier, D.; Silvestrini, S.; Privitera, A.; Marega, C.; Franco, L.Moretto, A., Synthesis and Photochemical Applications of Processable Polymers Enclosing Photoluminescent Carbon Quantum Dots. *ACS Nano* **2015**, *9*, 4156-4164.

11. Righetto, M., et al., Spectroscopic Insights into Carbon Dot Systems. *The Journal of Physical Chemistry Letters* **2017**, 2236-2242.

12. Privitera, A.; Righetto, M.; Mosconi, D.; Lorandi, F.; Isse, A. A.; Moretto, A.; Bozio, R.; Ferrante, C.Franco, L., Boosting Carbon Quantum Dots/Fullerene Electron Transfer Via Surface Group Engineering. *Physical Chemistry Chemical Physics* **2016**, *18*, 31286-31295.

13. Luo, B.; Pu, Y.-C.; Yang, Y.; Lindley, S. A.; Abdelmageed, G.; Ashry, H.; Li, Y.; Li, X.Zhang, J. Z., Synthesis, Optical Properties, and Exciton Dynamics of Organolead Bromide Perovskite Nanocrystals. *The Journal of Physical Chemistry C* **2015**, *119*, 26672-26682.

14. Huang, H.; Susha, A. S.; Kershaw, S. V.; Hung, T. F.Rogach, A. L., Control of Emission Color of High Quantum Yield CH3NH3PbBr3 Perovskite Quantum Dots by Precipitation Temperature. *Advanced Science* **2015**, *2*, 1500194-n/a.

15. Zhang, Z.-Y.; Wang, H.-Y.; Zhang, Y.-X.; Hao, Y.-W.; Sun, C.; Zhang, Y.; Gao, B.-R.; Chen, Q.-D.Sun, H.-B., The Role of Trap-Assisted Recombination in Luminescent Properties of Organometal Halide CH3NH3PbBr3 Perovskite Films and Quantum Dots. **2016**, *6*, 27286.

16. Brus, L. E., Electron-Electron and Electron-Hole Interactions in Small Semiconductor Crystallites: The Size Dependence of the Lowest Excited Electronic State. *The Journal of Chemical Physics* **1984**, *80*, 4403-4409.

CHAPTER 8

All that Glisters is not Carbon Dot

Part of this Chapter is based on:

Righetto et al. The Journal of Physical Chemistry Letters **2017**, 8, 2236-2242

ABSTRACT- The controversial nature of Carbon Dots (CDs) fluorescent properties, either ascribed to surface states or to small molecules adsorbed onto the carbon nanostructures, is a withstanding issue. To date, an accurate picture of CDs and an exhaustive structure-property correlation are still lacking. Namely, the nature of CDs themselves is still unknown and understanding what CDs are and how they work is a fundamental step toward sustainable and biocompatible nanotechnologies.
In this Chapter, this severe gap is filled by taking advantage an unconventional spectroscopic technique: fluorescence correlation spectroscopy (FCS). Albeit electron micrographs evidence the presence of carbon cores in every sample studied, FCS reveals that the emission properties of CDs are based neither on those cores nor on molecular species linked to them, but rather on free molecules. Hence, much of the previous studies on CDs were based on a deceptive inference, linking TEM observations directly with optical experiments. FCS proved to be a powerful technique, characterizing CDs as inherently heterogeneous systems, providing insights into the nature of such systems and paving the way to standardization of these nanomaterials.

8.1 On the origin of Emission in CDs

The opportunity to obtain environmental-friendly and biocompatible substitutes for high-performance inorganic nanostructures lies at the heart of the more recent and ever-increasing interest in carbon nano-materials. The last five years have witnessed an exponential growth in the research related to the synthesis and characterization of graphene and carbon quantum dots.[1-2] In analogy with their inorganic counterparts, different applications are being envisaged and tested for these materials ranging from two-photon tissue imaging [3-4] to metal ion sensing [5-6] and catalysis.[7-8] Furthermore, the possibility to tune the bandgap of these materials by quantum size effect [9-11] is exceptionally appealing for photovoltaic applications.

Looking at the inorganic counterpart, semiconductor colloidal quantum dots (QDs) offer superior and tunable optoelectronic properties.[12] However, toxicity issues hamper their use in biomedical applications and cast doubts on their large-scale production.[13]

It is essential to bear in mind that the successful evolution of QDs, since their inception some 25 years ago, was fueled by a fruitful synergy between a thorough characterization of their properties and the consequent development of tailored nano-structures.[14-15] A lack of such synergy is still present in the development of carbon nano-materials and in particular of the very promising nitrogen-doped carbon dots (N-CDs). The possible underlying cause is the variable and poly-disperse nature of these nanostructures,[10, 16-17,] i.e., the vast variability of structure, composition, and size of the reported systems. This ill-defined nature deprives photo-physical considerations on these materials of general significance, necessary for a rational development of their design. Many bottom-up syntheses of CDs have been proposed without reaching a complete characterization of their structural and chemical properties,[18-19] further complicating this picture.

The ongoing debate on the origin of their photoluminescence is just an example of how a thorough picture of these systems is still missing.[20-26] The "multi-chromophoric scaffold" (MCS) architecture is widely used as a model to account for the optical properties of many different CDs systems.[22-23, 25-27] The MCS model describes CDs as carbonaceous cores, which either embed or are decorated by emissive molecular species. Therefore, the absorption features are associated with a core state, whereas emission is ascribed to the presence of many molecular states. Within this model, the excitation-dependent emission is attributed to exciton self-trapping in an aromatic network or to surface chemical moieties. However, other models explain CDs properties by considering that the synthesis generates CDs with a broad dimensional distribution of CDs.[28] To a general extent, a unanimous agreement in the scientific community is still lacking.

This gap is worsened by the burgeoning field of CDs synthesis, reporting novel precursors and synthetic routes every month. Hence, a model system is needed to delve deeper into this field.

Citric acid based N-CDs proposed first by Sun et al.,[29] were obtained through a reaction between citric acid and ethylenediamine in an autoclave. Resulting N-CDs displayed a high quantum yield, up to 94%. These well-performing materials, generally considered to be carbonaceous nanoparticles, were employed in a number of applications ranging from bio-imaging [30] to light-emitting devices.[31-32] Moreover, this system display rather uniform optical properties and are widely regarded as flagship CDs systems. During the last two years, few works demonstrated the molecular nature of the emitting species in citric-acid based N-CDs.[33-34] Namely, albeit carbonaceous cores were actually synthesized and observed by electron micrographs, the photoluminescence (PL) origin was univocally ascribed to organic small molecules and in particular to imidazo[1,2-a]pyridine-7-carboxylic acid, 1,2,3,5-tetrahydro-5-oxo, (IPCA). This discovery cast doubts both on the MCS model and on the relation between PL and carbon cores. Thence, the question to solve became focused on the role of carbon cores, given that the optical properties of these CDs resemble those of IPCA. However, the hypothesis of IPCA molecules embedded in- or connected to- the carbonaceous scaffold (i.e., multi-chromophoric scaffold model) encompassed the formation of IPCA and the presence of highly luminescent CDs. The presence of IPCA grafted to the surface of or embedded within carbonaceous cores is currently accepted as the answer. This hypothesis portrays CDs are mere scaffolds, hence a further question arises: can this model be extended to the wealth of other CDs, synthesized from different precursors?

According to these advances in the field of CDs, it is of paramount importance to understand whether free small molecules effectively drive CDs samples fluorescence, because every bottom-up synthesized CDs potentially can present the same issue.

Unfortunately, the identification and separation of fluorescent molecules from carbonaceous cores via chemical methods is a tough hurdle to overcome due to the similar solubility of molecules and carbon cores [35, 42, 44, 45, 24, 33, 35-36]

The aim of this Chapter is to provide a spectroscopic approach to this point and to suggest the use of less-conventional techniques, beyond basic characterization, to shed light on some missing information concerning CDs characterization. By combining optical and magnetic spectroscopies with electron micrographs, a better description of these materials is obtained, and possible pitfalls of conventional characterization are highlighted. In the reported work two CDs systems were analyzed: citric acid based CDs (Cit-CDs) and arginine-based CDs (Arg-CDs). The study of Cit-CDs allowed testing the accepted hypothesis on model systems. On the other hand, the study of Arg-CDs allowed extending the outreach of the finding to other conventional CDs systems.

8.2 Conventional Characterization of CDs

Citric acid-based N-CDs (Cit-CDs) and Arginine-based N-CDs (Arg-CDs) were synthesized by Dr. Mosconi and Prof. Moretto, using a conventional microwave-assisted modification of previously reported synthesis.[29, 37] The as-synthesized samples were purified by dialysis, following standard published procedures. Transmission electron microscopy (TEM) micrographs for Cit-CDs (Fig.1**a**) uncover a distribution of rather uniform and spherical shaped particles. The particle size distribution was obtained by statistical analysis over 180 nanoparticles and reported an average diameter 2.6±0.6 nm. Similarly, the diameter of Arg-CDs was found to be 2.4±0.5 nm, as reported in a previous paper by Prof. Moretto.[38]

Standard structural characterization of Cit-CDs (Figure 8.1) is in agreement with many literature reports on N-CDs. Raman spectrum (Fig.8.1**b**) reveals the presence of graphitic carbon (G bands) as well as oxidized carbon (D*,D',D'').[39] Photoemission spectroscopy (XPS) further confirms this result (Fig.8.1**c**). Furthermore, the analysis of N*1s* peak allowed identifying the presence of pyrrolic and pyridinic nitrogen, as well as graphitic nitrogen (further discussion in SI), confirming results on Arg-CDs, reported in previous papers.[38]

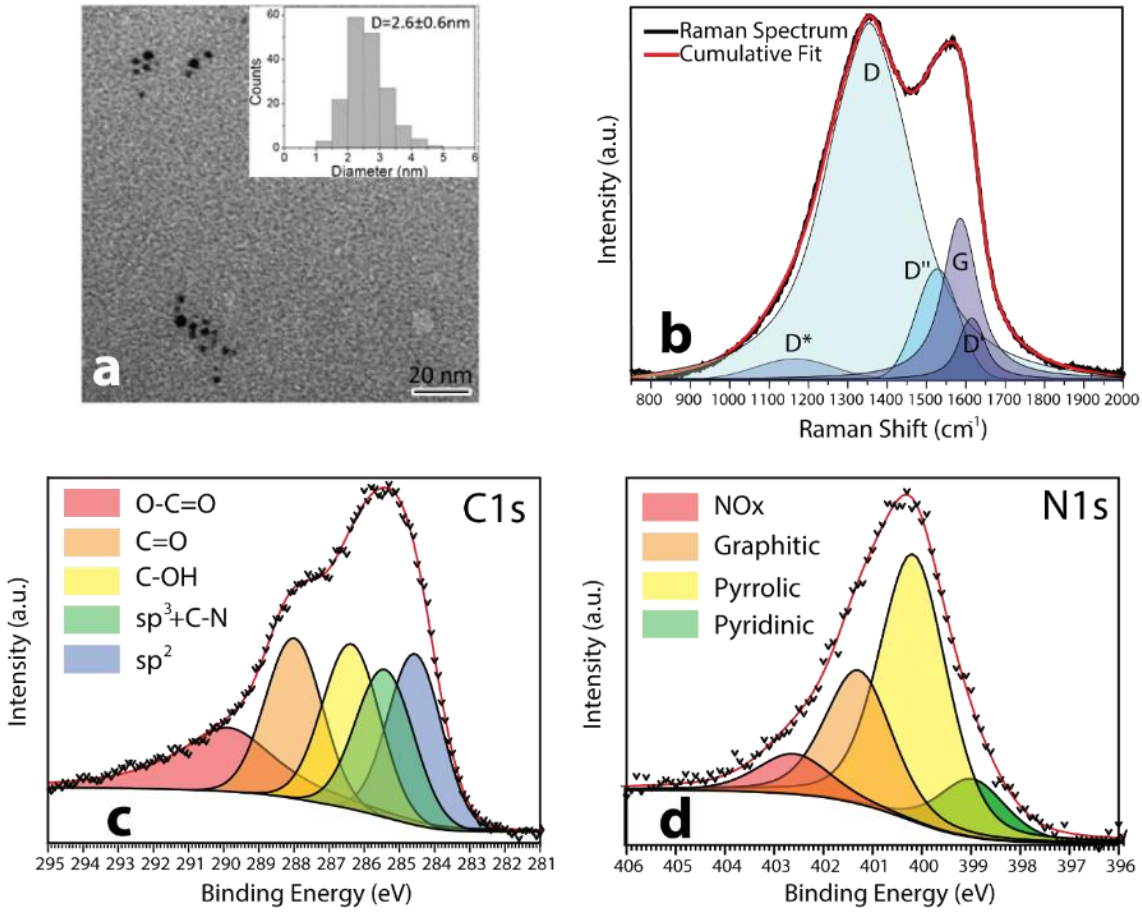

Figure 8.1- (**a**) TEM micrograph of Cit-CDs. Size distribution bar chart is shown in the inset. (**b**) Raman spectrum of Cit-CDs (black) and multi-peak fit (red), according to Ref.39 (**c**),(**d**) Carbon peak and nitrogen peak of the XPS spectrum of Cit-CDs.

Thus, standard characterization outlines two typical carbon dot systems, but a direct structure-property correlation can be misleading since it does not adequately uncover the possible heterogeneous nature of the sample, meaning the possibility to have both nanometer size carbonaceous nanoparticles as well as small organic molecules.

Optical properties as well are consistent with those reported in the literature [21, 24, 29] for both Cit-CDs and Arg-CDs (Fig. 8.2). Cit-CDs display a well-defined (30nm FWHM) absorption peak at 355nm (Fig. 8.2**a**), while Arg-CDs show a broad absorption spectrum (Fig. 8.2**a**).

The absorption spectra are different: Cit-CDs display a well-resolved peak, whereas Arg-CDs display a broader absorption tail. These differences reflect in the PL spectra, by differences in the excitation wavelength dependence of the PL band, i.e., the wavelength dependence is more markedly observed for Arg-CDs. Excitation wavelength dependence is reported in Fig. 8.2**b** and Fig. 8.2**d** for both studied samples. As discussed in Chapter 3, excitation energy/wavelength dependent PL is a puzzling phenomenon related to the broader topic of CDs photoluminescence mechanism.

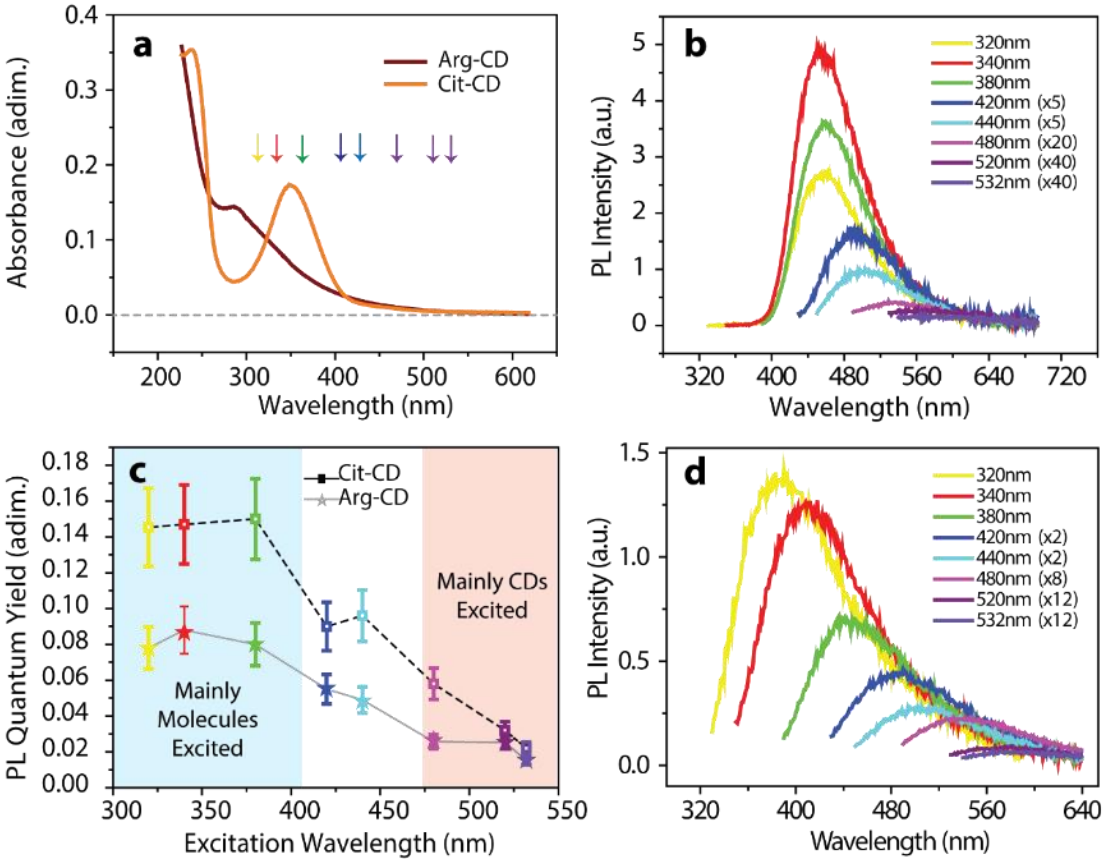

Figure 8.2- (**a**) Absorption spectrum of Cit-CDs (orange) and Arg-CDs (dark red) in water solution. Colored arrows indicate excitation wavelengths, color coding is respected and is related to excitation wavelength used for emission measurements. (**b**) Excitation wavelength dependence of Cit-CDs emission. (**c**) Excitation wavelength dependence of PL QY for Cit-CDs and Arg-CDs. Blue and red shadowed regions identify the leading contribution of different species (molecular species and CDs). (**d**) Excitation wavelength dependence of Arg-CDs emission.

Albeit complete agreement on the origin of this phenomenon is still lacking, the excitation-energy dependent emission is considered distinctive of CDs systems. This phenomenon is entirely different from EED phenomenon discussed in Chapter 3. Indeed, EED for QDs involves different emission efficiencies due to modified interaction with traps. Albeit in a few lines the effect on PLQY will be demonstrated, for CDs excitation wavelength dependence is generally referred to PL band shift.

Possible explanations of this phenomenon range from heterogeneity in sample composition to slow solvent relaxation properties. Recent work employing single molecule and anisotropy measurements revealed the presence of different emitters within CDs emission band.[23, 25] According to these papers, the progressive redshift of the emission band as the excitation wavelength is also tuned towards the red (Fig. 8.2**b** and 8.2**d**) originates from the presence of different moieties/entities (for example aggregates of specific moieties) characterized by an overlapping spectral distribution.

When the excitation wavelength is changed, different moieties/entities are excited to a different extent. In these works, the authors still maintain that these entities are either embedded within the sp^3 carbon core of the CDs or attached to its surface.

On the other hand, Yang demonstrated that a citrazinic acid derivative called IPCA plays a fundamental role in the central optical properties of citric-acid based N-CDs.[33-34] Within this framework, optical properties of Cit-CDs should combine those of IPCA with the one of carbon cores. Photoluminescence quantum yield (PLQY) is the ratio between the number of emitted and absorbed photons and is usually constant for a single emitting state/moiety. Instead, a marked excitation energy dependence of PLQY was observed for both studied samples. Notably, PLQY is observed to be almost stationary, when sweeping the excitation wavelength from 320nm to 380nm (Fig. 8.2**c**). Yet PLQY rapidly decreases above 440nm excitation. Albeit in Chapter 3 EED for QDs was explained in terms of hot-carrier trapping, in this case the PLQY trend is inverse.[40] Therefore, in this case, the utterly different explanation relies on the heterogeneity of emitters in CDs solutions (i.e., in as-synthesized CDs both molecules and nanometric sized carbon particles are present and contribute to emission). This would imply that the absorption of photons is shared between molecular and carbon core species, whereas their emission efficiencies are different. For instance, in Cit-CDs 520nm photons are not expected to excite IPCA molecules and the resulting emission is assigned to carbon cores.[33-34] Being the reported PLQY for IPCA about 80%, this model suggests that highly emitting molecular species and poorly emitting carbon cores compose CDs systems.

Similar results were recently reported by Rogach, for Cit-CDs.[26] Noteworthy, the PLQY behavior of Arg-CDs is akin to that of Cit-CDs. In order to delve deeper into the nature of emissive species the conventional characterization was extended, including pH resolved measurements and chromatographic separation.

8.2.1 pH resolved measurements on Cit-CDs

A pH resolved characterization was carried on for Cit-CDs, in order to confirm the presence of IPCA and test its importance in driving optical properties of these systems. The analysis was based on both stationary and transient optical spectroscopies. In particular, pH values were conditioned to five fixed values in the 3 to 13 interval. Precise pH values were obtained by small amounts of NaOH and HCl and controlled by means of a pH-meter. The ζ-potential technique was used to verify the colloidal stability at different pHs. For pH values above 3, the ζ-potential is in the range +8mV and dispersions were stable, at lower pH the ζ-potential became negligible, and aggregation was observed.

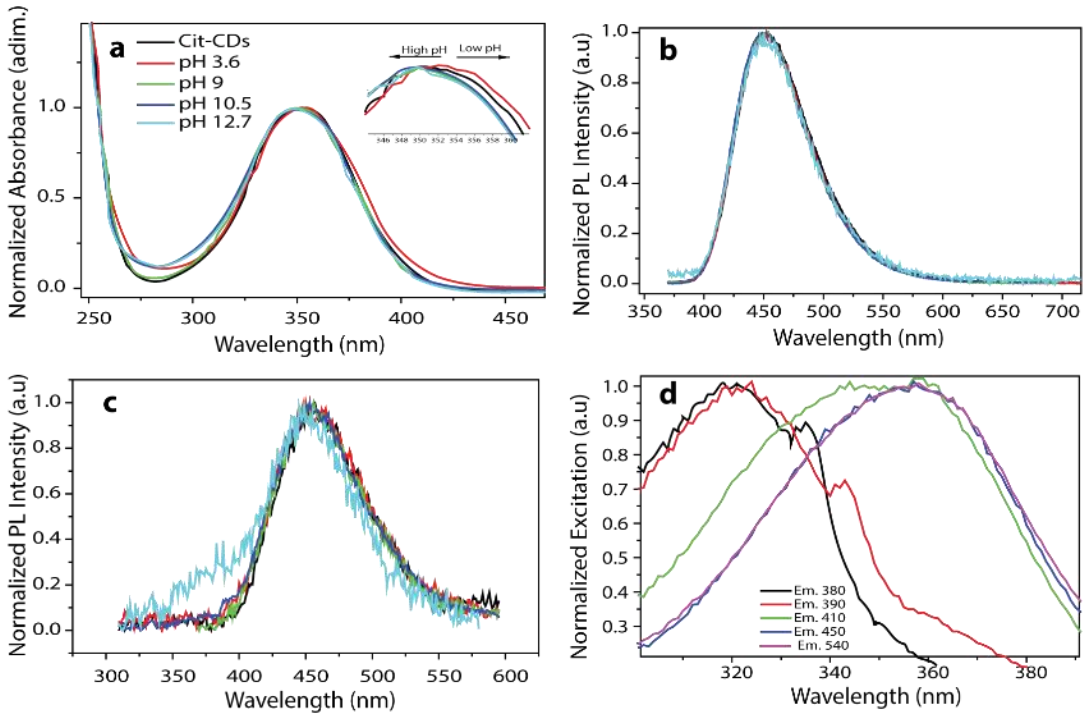

Figure 8.3-(**a**) Comparison of normalized absorption at different pH values of Cit-CDs water solutions. (**b**) Comparison of normalized PL spectra measured in different pH conditions under 370nm excitation. (**c**) Comparison of normalized PL spectra measured in different pH conditions under 330nm excitation. (**d**) Normalized excitation spectra for different emission wavelength at pH=12.7 (side peaks of 380nm and 390nm curves are water Raman signals).

Notably, these relatively low potential values suggest the dominance of molecular species, being low with respect to conventional potential observed for nanoparticles. The outcomes of pH resolved characterization point out an inhomogeneity in the emission properties when extremely basic conditions are applied.

As reported in Figure 8.3, a slight redshift (2nm) for the main absorption band is observed in basic aqueous media. On the contrary, the behavior of PL is more complicated, involving changes of both line shape and efficiency.

Regarding PL line shape it is observed (Figure 8.3**b**) that when the sample is excited at 370nm the spectral position of the band results to be both pH- and excitation-wavelength independent. On the contrary, when 330 nm excitation is applied, a second band grows on the blue edge at pH higher than 9 (Figure 8.3**c**). Interestingly, the presence of this band is observed only for excitation below 330 nm. Excitation spectra supply a more unobstructed view of this phenomenon. Their evolution, measured for 390 nm and 450 nm emission, shows that PL line shape originates from two well-separated absorption features. This effect is hidden at acid pH value but is disclosed when the dispersion is basified at pH 10.5 and 12. PLQY measurements reveal a decrease in emission efficiency at high pH, as shown in Fig. 7.4**c**.

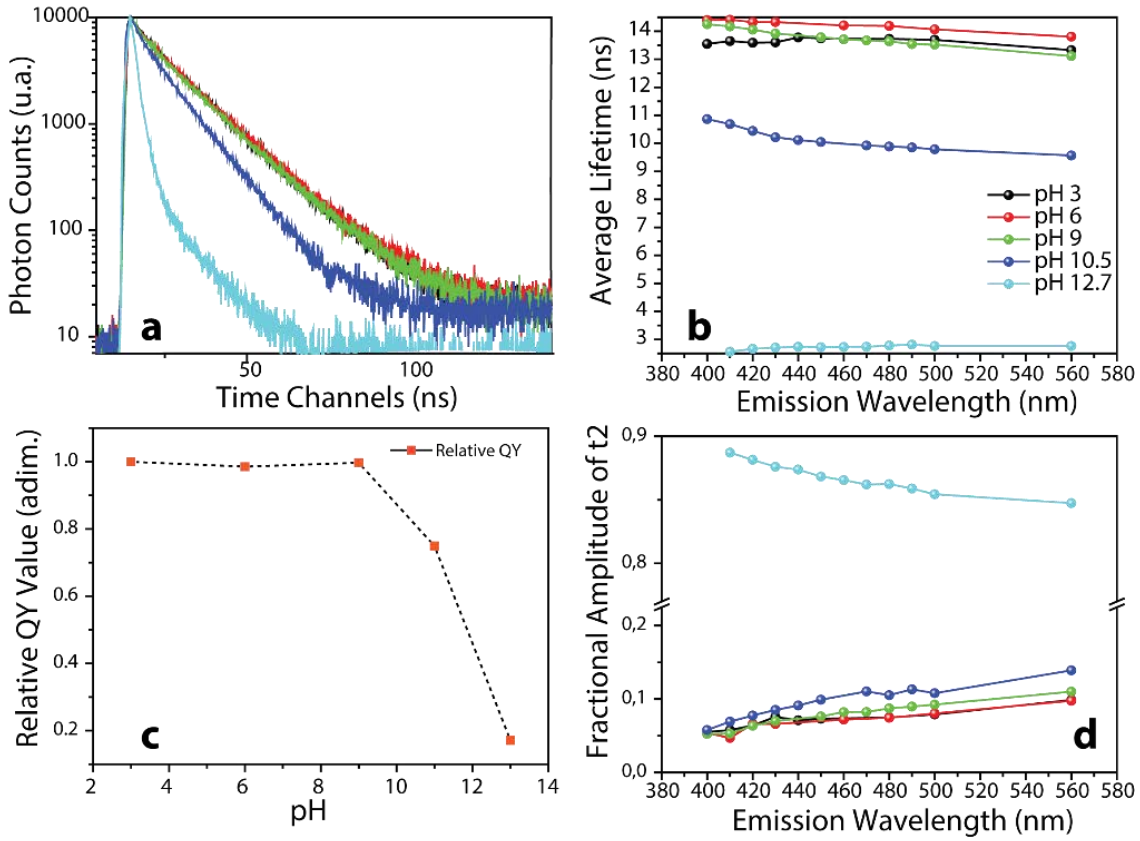

Figure 8.4- Comparison between (**a**) TRPL decay curves measured for Cit-CDs as a function of pH and (**b**) relative average lifetimes for different emission wavelength. (**c**) Quantum yield quenching with respect to pH (**d**) Fractional Amplitude of the second time component t_2=2ns at different emission wavelength and pH values. Color coding is respected for **a**,**b**,**d** graphs.

According to stationary characterization outcomes, the effects of pH on TRPL are primarily expressed by a steep decrease of the average PL lifetime. The inspection of lifetime component, obtained by bi-exponential fitting, reveals a substantial exchange in the role of long (15ns) and short (2ns) components. The predominance of the extended lifetime component in the 3-9 pH range, with amplitudes around 94%, is flipped over to 6% when pH is set at 12. (Figure 8.4**d**). Furthermore, the emission wavelength dependence on TRPL decay curves is emphasized up to pH 10.5, while disappearing at pH 12.

pH resolved characterization reveals a PL quenching under strongly basic conditions, as well as a drastic change in the spectral position of the emission and in the average excited state lifetime of the fluorescent state. These experimental findings can be related to IPCA pH-active groups: carboxylic acid and amines. Indeed benzoic acid was found to be fluorescent only in its protonated form 4. Therefore, the acid-base equilibrium of carboxylic acid functionality drives this pH dependence. As observed in Figure 7.4, at pH=12 the PL spectrum reveals an additional peak, blue-shifted with respect to the main one. Allowing for an acid-base equilibrium for IPCA molecule, this peak can be assigned to the anion form of IPCA.

8.2.2 Chromatographic separation of Arg-CDs

In 2015 Yang and co-worker managed to separate Cit-CDs in their components by chromatographic separation techniques.[3] They were able to isolate the very stable citrazinic acid derivative called IPCA. As shown above, this plays a prominent role in the emission of Cit-CDs.

With the aim of testing the hypothesis for this recurring scheme in CDs (i.e., small molecules dominate emission properties), column chromatography was applied to purify Arg-CDs and isolate highly emissive molecules. Flash column chromatography was performed using silica gel and chloroform:methanol (7:3) as eluent. Different fractions, reflecting different chemical functionalization and molecular weight, were separated.

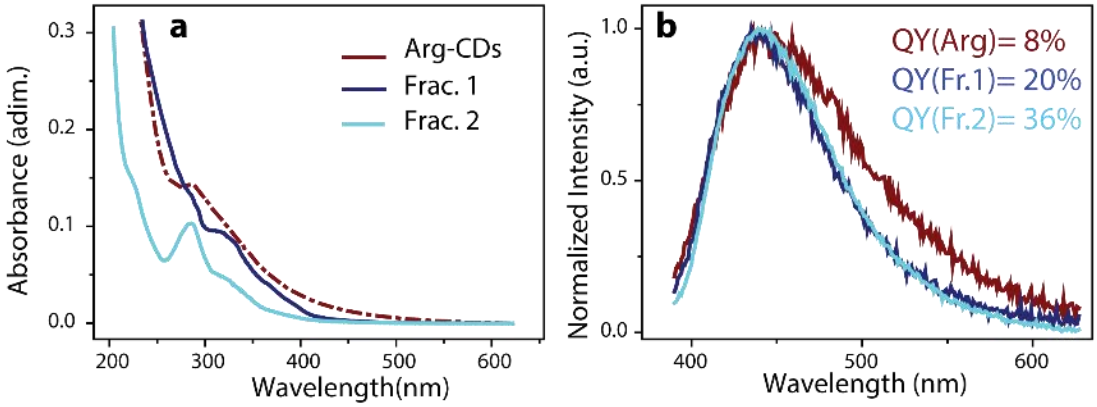

Figure 8.5-(**a**) Absorption spectrum of Arg-CDs in water and Fr.1 and Fr.2 in water. (**b**) Fluorescence spectrum of Arg-CDs, Fr.1, and Fr.2 in water.

Figure 8.5 shows the comparisons between optical properties of the as-prepared sample of Arg-CDs and the first two fractions collected from the column. Noteworthy, Fr.1 and Fr.2 display well-resolved absorption peaks at 290nm and 320nm, respectively. Moreover, their absorption spectrum drops off above 400nm, whereas that of Arg-CDs persists up to 600nm. Analogously, emission band of Fr.1 and Fr.2 are narrower than Arg-CDs ones, suggesting that the longer wavelength emission tail is not present in the first fractions. Finally Fr.1 and Fr.2 display higher emission efficiencies in comparison to the pristine Arg-CD sample. Indeed, the PLQY of Fr.2 is 4 times higher than that of the pristine Arg-CDs solution when excited at 380nm. To identify the composition of various fractions, ^{1}H-NMR, ^{13}C-NMR, and ESI-MS techniques were employed.

These analyses were performed under the supervision of Prof. A. Moretto, and their outcomes are only briefly reviewed here.

The ESI-MR spectrum revealed the presence of a statistical distribution of small molecules. According to mass and NMR characterization, a possible structure of the most abundant molecular structure is reported in Figure 8.6.

Nevertheless, these data stress out that decomposition of arginine does not result in a well-defined molecular structure, but instead in the generation of molecules with a statistical distribution of molecular weights, reflecting different molecular structures. Hence, the univocal identification of a single fluorescent molecule, driving Arg-CDs fluorescence would be inherently incorrect. This different behavior, with respect to Cit-CDs, where Yang identified IPCA as a source of fluorescence, [3] stems from chemical aspects of the synthesis. Indeed, Cit-CDs are synthesized via carbonization of a mixed solution of citric acid and ethylenediamine, whereas Arg-CDs are obtained by carbonization of a mixture of arginine and ethylenediamine. While the reaction of citric acid with ethylenediamine yields IPCA as the dominant product, there is no such single outcome for the other mixture. Therefore, a statistical mixture of small molecules is expected.

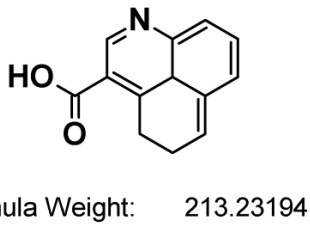

Figure 8.6- Structure of the most abundant and recurrent molecule observed in MS and NMR spectra of first and most fluorescent fractions obtained by column chromatography separation of Arg-CDs.

8.3 FCS on Arg-CDs and Cit-CDs

Whilst conventional characterization techniques cast doubts on the prominence of the role played by small molecules in CDs emission, fluorescence correlation spectroscopy (FCS) effectively unravels the nature of the emission in CDs. According to the above discussion, the assignment of good emissive properties to CDs is based on a -at this time, questionable- inference: the observed PL spectra are ascribed to carbonaceous core observed by TEM. FCS dissects this inferential process by providing information on the size of emitters.

As explained in Chapter 7, FCS records fluorescence intensity fluctuations in femtoliter volumes. [49] The autocorrelation of these curves provides information on the different processes determining noticeable fluorescence variation. A wide variety of processes concur to these fluctuations and potentially give rise to structured autocorrelation curves at different time scale.

Among these, a pivotal role is played by translational diffusion of the luminescent species inside the investigated volume: this is the most critical process determining intensity fluctuations for small (molecular and nanometer-sized) fluorescence systems and operates on the micro-to-milliseconds timescale.
Hence, the CDs fluorescence autocorrelation curve were analyzed to estimate the diffusion coefficient of the emitting species and, from this, its average hydrodynamic size. FCS curves for Arg-CDs and Cit-CDs, reported in Figure 8.7, are typical of molecular entities and very similar to the curve collected for the reference standard Coumarin 503 (curves are normalized to allow direct comparison).
FCS curves of Arg-CDs and Cit-CDs are fitted to the equation

$$G(\tau) = \frac{1}{N}\left(1+\frac{\tau}{\tau_D}\right)^{-1}\left(1+\frac{\tau}{S^2\tau_D}\right)^{-1/2} \qquad \textbf{(Eq. 8.1)}$$

where N is the number of molecules in focal volume and the characteristic time τ_D is associated with the diffusion coefficient D via relation $\tau_D = \omega_0^2/4D$. S is the confocal shape factor, i.e., the ratio between axial (z_0) and lateral (ω_0) radius at which intensity is reduced by an e^{-2} factor. In normalized FCS curves, N is set equal to 1. This model accounts for fluorescence intensity fluctuation caused by translational diffusion of fluorophores and well fits recorded curves (Fig.7.7). Coumarin 503 is used as standard to determine the parameters ω_0 and z_0, which in turn are used to obtain the hydrodynamic radius of CDs via Stokes-Einstein relation

$$R_H = \frac{4k_B T\tau_D}{6\pi\eta\omega_0^2} \qquad \textbf{(Eq. 8.2)}$$

Where k_B is the Boltzmann constant, T is the absolute laboratory temperature, τ_D is the CD diffusion time gained from fitting, and η is the solution viscosity.

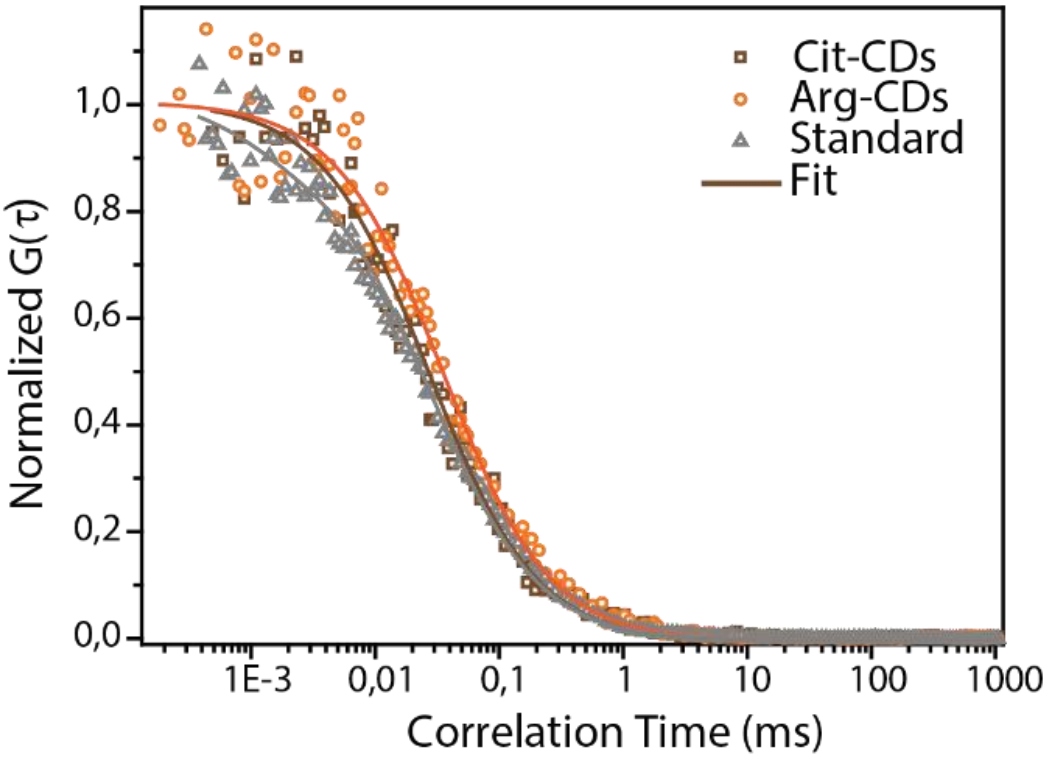

Figure 8.7- Normalized FCS curves for Cit-CDs (brown dots), Arg-CDs (orange dots), and Coumarin 153 (grey dots). Normalization allows direct comparison between diffusional times, fitting was performed before normalization operation. FCS curves are fitted (solid lines) to the translational diffusion model in Eq.1

FCS fitting outcomes revealed an average hydrodynamic radius of $R_H = 4.9 \pm 0.8$ Å for Cit-CDs and $R_H = 5.4 \pm 0.7$ Å for Arg-CDs. These dimensions are typical of common organic dyes. Notably, these estimates are also in agreement with the one of the IPCA molecule found by Yang in Cit-CDs [42]. Consequently, it can be stated unequivocally that Arg-CDs and Cit-CDs emission properties when excited in the 370-440 nm range are dominated by a "molecular" entity with below-nm hydrodynamic radius.

Notably, FCS measurements performed at different excitation wavelengths (370nm, 400nm, 440nm, throughout the red region in Fig. 8.2**c**) are very similar. It should be emphasized that FCS results refer to translational diffusion of emitting species. Therefore, emission under reported excitation wavelengths is originated by free molecular species, having comparable diffusion coefficients. The carbonaceous cores do not seem to concur to generate this emission signal. Nevertheless, they could be playing a role in the emission in different spectral intervals.

FCS curves measured under 488nm excitation bolstered this interpretation of CDs heterogeneity. Indeed, wavelength resolved PLQY experiments, and chromatographic separation of Arg-CDs clearly show that above 440nm excitation, the emission efficiency strongly decreases.

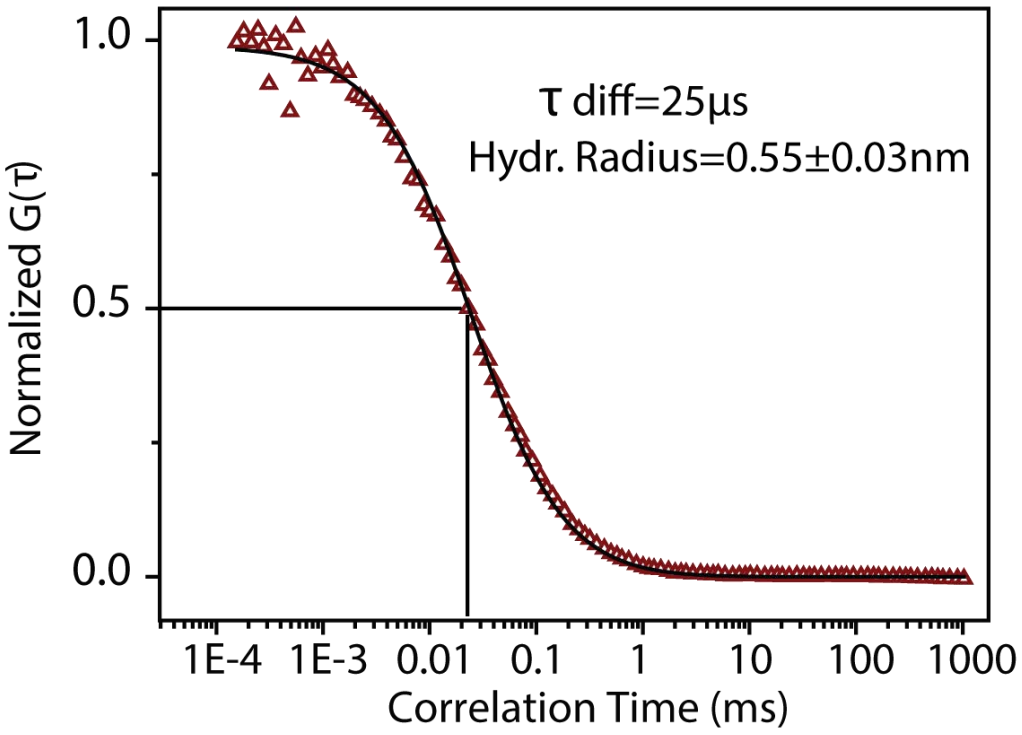

Figure 8.8-FCS correlation curve of Alexa488 dye in water, under 488 nm excitation. This fluorophore is used as a standard in hydrodynamics radii calculations, with reported R_H=0.58nm.

In order to demonstrate that such poor emission originates from bulkier carbon cores, FCS experiments were performed exciting the samples, Cit-CD and Arg.CD, at 488nm (CW Ar^+ laser), using Alexa488 dye as standard, with reported hydrodynamics radius of 0.58nm[41] (Fig. 8.8). Indeed, small molecules absorption in Arg-CDs drops off above 400nm (Fig. 7.5), and IPCA in Cit-CDs presents only an absorption tail at these wavelengths.[33]

In Figure 8.9 the FCS spectra of both Arg-CDs and Cit-CDs are reported. The autocorrelation curve of Arg-CDs (Fig. 8.9**a**) is shifted towards longer correlation times, with respect to that measured under 370nm excitation. Hydrodynamics radius calculation yield R_H=1.1±0.15nm. This increase in hydrodynamics radius confirms that excitation at 488 nm promotes emission from bulkier entities. The observed value is within the diameter range found with TEM analysis.

Fitting the autocorrelation curve of Cit-CDs (Fig. 8.9**b**) extending model in Eq. 8.1, a diffusional time in agreement with that obtained under 370nm excitation is obtained. Nevertheless, as shown in Fig. 8.9**b**, a secondary component is present. Through two-component fitting it is possible to obtain confirmation that fluorescence under 488nm excitation originates from two species. Indeed, a small fraction (about 15%) of fluorophores display an even bulkier hydrodynamics radius, estimated to be R_H=1.9±0.3nm.

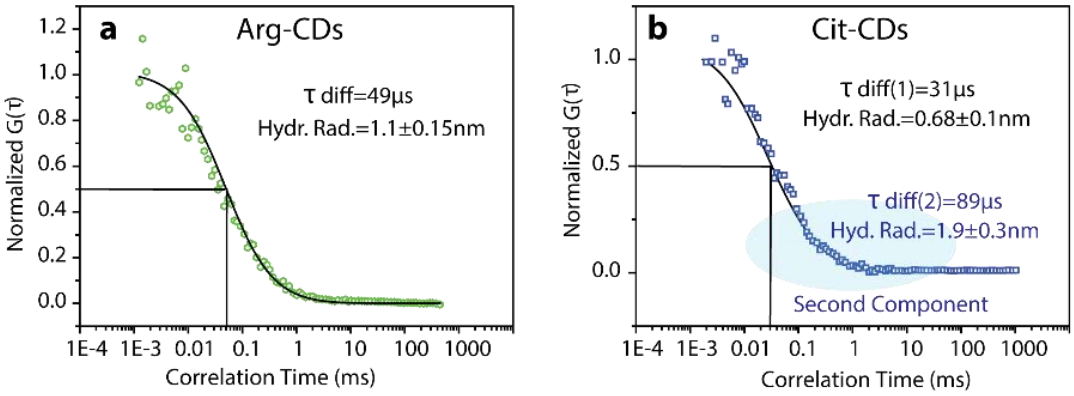

Figure 8.9 – Averaged FCS correlation curve spectra of (**a**) Arg-CDs and (**b**) Cit-CDs in water, under 488 nm excitation. Solutions were concentrated in order to obtain sufficient emission intensity at this wavelength. Graphically, diffusional time is identified as the correlation time at which G(0) is halved.

These results bolster the present interpretation of heterogeneity in CDs emission: the low-intensity emission band observed at longer wavelength excitation is likely to originate from moieties embedded in the carbon cores.

A final consideration concerns the emission of CDs. By choosing 488nm excitation, it was possible to minimize free molecular species contribution (i.e., as reported by chromatographic separation and previously by Yang,[33] the absorption tail of identified small molecules is negligible). Yet molecular contributions are still observed, albeit bulkier emissive object being observed. This can be considered as further proof of the inherently weak emitting properties of carbon cores, overtaken by those of small molecules in solution.

8.4 Envisioning the Future of Carbon Dots

Considering the complete picture emerging from our observations, small photo-luminescent molecules free in solution are mainly responsible for the emissive properties of CDs systems, in 320-450nm excitation range. On the other hand, excitation above 480nm allows observing almost selectively carbon cores. These photophysical entities display lower QYs and bulkier hydrodynamics radii, consistently with TEM micrographs results.

These results reveal the complex nature of the system, made up of different species, presenting non-homogeneous photo-physics. In agreement with recently reported PL anisotropy measurements,[23] different emitters concur to the puzzling and unusual emission of CDs.

In conclusion, this photophysical characterization portrays CDs systems behave as multiple facet entities, often switching through the borders separating single molecules and nanomaterials. According to this picture, for our CDs, we could devise applications in catalysis or photodynamic therapy. Their use as fluorescent tracers must take into account that luminescence mainly originates from free small molecules dispersed in solution: consequently, those molecules, rather than carbon cores, will label biological substrates. Such outcome could result underwhelming for a scientist working with CDs. Indeed, many previous papers reported applications of the same systems studied here, considering the emission to be originated from carbonaceous cores. Nevertheless, the outreach of these results is inherently limited to the samples investigated in this work, i.e. microwave assisted one-pot CDs synthesis. Although the resemblance of optical and structural properties suggests a potential extension of these results to CDs from different synthetic routes, it is not excluded that highly emitting carbon dots can be obtained with other synthetic techniques. Further experimental work is currently underway to test this hypothesis. Dealing with this complexity, FCS can lend a precious hand to investigate the properties of pristine and chemically functionalized CDs.

References

1. Ritter, K. A.Lyding, J. W., The Influence of Edge Structure on the Electronic Properties of Graphene Quantum Dots and Nanoribbons. *Nat Mater* **2009**, *8*, 235-242.

2. Li, H.; Kang, Z.; Liu, Y.Lee, S.-T., Carbon Nanodots: Synthesis, Properties and Applications. *Journal of Materials Chemistry* **2012**, *22*, 24230-24253.

3. Liu, Q.; Guo, B.; Rao, Z.; Zhang, B.Gong, J. R., Strong Two-Photon-Induced Fluorescence from Photostable, Biocompatible Nitrogen-Doped Graphene Quantum Dots for Cellular and Deep-Tissue Imaging. *Nano Letters* **2013**, *13*, 2436-2441.

4. Zhu, S., et al., Strongly Green-Photoluminescent Graphene Quantum Dots for Bioimaging Applications. *Chemical Communications* **2011**, *47*, 6858-6860.

5. Dong, Y.; Shao, J.; Chen, C.; Li, H.; Wang, R.; Chi, Y.; Lin, X.Chen, G., Blue Luminescent Graphene Quantum Dots and Graphene Oxide Prepared by Tuning the Carbonization Degree of Citric Acid. *Carbon* **2012**, *50*, 4738-4743.

6. Wang, Y.Hu, A., Carbon Quantum Dots: Synthesis, Properties and Applications. *Journal of Materials Chemistry C* **2014**, *2*, 6921-6939.

7. Favaro, M., et al., Single and Multiple Doping in Graphene Quantum Dots: Unraveling the Origin of Selectivity in the Oxygen Reduction Reaction. *ACS Catalysis* **2015**, *5*, 129-144.

8. Fei, H.; Ye, R.; Ye, G.; Gong, Y.; Peng, Z.; Fan, X.; Samuel, E. L. G.; Ajayan, P. M.Tour, J. M., Boron- and Nitrogen-Doped Graphene Quantum Dots/Graphene Hybrid Nanoplatelets as Efficient Electrocatalysts for Oxygen Reduction. *ACS Nano* **2014**, *8*, 10837-10843.

9. Kim, S., et al., Anomalous Behaviors of Visible Luminescence from Graphene Quantum Dots: Interplay between Size and Shape. *ACS Nano* **2012**, *6*, 8203-8208.

10. Cao, L.; Meziani, M. J.; Sahu, S.Sun, Y.-P., Photoluminescence Properties of Graphene Versus Other Carbon Nanomaterials. *Accounts of Chemical Research* **2013**, *46*, 171-180.

11. Fuyuno, N.; Kozawa, D.; Miyauchi, Y.; Mouri, S.; Kitaura, R.; Shinohara, H.; Yasuda, T.; Komatsu, N.Matsuda, K., Drastic Change in Photoluminescence Properties of Graphene Quantum Dots by Chromatographic Separation. *Advanced Optical Materials* **2014**, *2*, 983-989.

12. Saha, A.; Chellappan, K. V.; Narayan, K. S.; Ghatak, J.; Datta, R.Viswanatha, R., Near-Unity Quantum Yield in Semiconducting Nanostructures: Structural Understanding Leading to Energy Efficient Applications. *The Journal of Physical Chemistry Letters* **2013**, *4*, 3544-3549.

13. Winnik, F. M.Maysinger, D., Quantum Dot Cytotoxicity and Ways to Reduce It. *Accounts of Chemical Research* **2013**, *46*, 672-680.

14. Kim, J. Y.; Voznyy, O.; Zhitomirsky, D.Sargent, E. H., 25th Anniversary Article: Colloidal Quantum Dot Materials and Devices: A Quarter-Century of Advances. *Advanced Materials* **2013**, *25*, 4986-5010.

15. Klimov, V. I., Spectral and Dynamical Properties of Multiexcitons in Semiconductor Nanocrystals. *Annual Review of Physical Chemistry* **2007**, *58*, 635-673.

16. Baker, S. N.Baker, G. A., Luminescent Carbon Nanodots: Emergent Nanolights. *Angewandte Chemie International Edition* **2010**, *49*, 6726-6744.

17. Zhang, Z.; Zhang, J.; Chen, N.Qu, L., Graphene Quantum Dots: An Emerging Material for Energy-Related Applications and Beyond. *Energy & Environmental Science* **2012**, *5*, 8869-8890.

18. Zhang, Z.; Sun, W.Wu, P., Highly Photoluminescent Carbon Dots Derived from Egg White: Facile and Green Synthesis, Photoluminescence Properties, and Multiple Applications. *ACS Sustainable Chemistry & Engineering* **2015**, *3*, 1412-1418.

19. Zhang, J.Yu, S.-H., Carbon Dots: Large-Scale Synthesis, Sensing and Bioimaging. *Materials Today* **2016**, *19*, 382-393.

20. Dekaliuk, M. O.; Viagin, O.; Malyukin, Y. V.Demchenko, A. P., Fluorescent Carbon Nanomaterials: "Quantum Dots" or Nanoclusters? *Physical Chemistry Chemical Physics* **2014**, *16*, 16075-16084.

21. Strauss, V., et al., Carbon Nanodots: Toward a Comprehensive Understanding of Their Photoluminescence. *Journal of the American Chemical Society* **2014**, *136*, 17308-17316.

22. Fu, M.; Ehrat, F.; Wang, Y.; Milowska, K. Z.; Reckmeier, C.; Rogach, A. L.; Stolarczyk, J. K.; Urban, A. S.Feldmann, J., Carbon Dots: A Unique Fluorescent Cocktail of Polycyclic Aromatic Hydrocarbons. *Nano Letters* **2015**, *15*, 6030-6035.

23. Demchenko, A. P.Dekaliuk, M. O., The Origin of Emissive States of Carbon Nanoparticles Derived from Ensemble-Averaged and Single-Molecular Studies. *Nanoscale* **2016**, *8*, 14057-14069.

24. Zhu, S.; Song, Y.; Zhao, X.; Shao, J.; Zhang, J.Yang, B., The Photoluminescence Mechanism in Carbon Dots (Graphene Quantum Dots, Carbon Nanodots, and Polymer Dots): Current State and Future Perspective. *Nano Res.* **2015**, *8*, 355-381.

25. Sharma, A.; Gadly, T.; Gupta, A.; Ballal, A.; Ghosh, S. K.Kumbhakar, M., Origin of Excitation Dependent Fluorescence in Carbon Nanodots. *The Journal of Physical Chemistry Letters* **2016**, *7*, 3695-3702.

26. Schneider, J.; Reckmeier, C. J.; Xiong, Y.; von Seckendorff, M.; Susha, A. S.; Kasák, P.Rogach, A. L., Molecular Fluorescence in Citric Acid-Based Carbon Dots. *The Journal of Physical Chemistry C* **2017**, *121*, 2014-2022.

27. Sciortino, A.; Marino, E.; Dam, B. v.; Schall, P.; Cannas, M.Messina, F., Solvatochromism Unravels the Emission Mechanism of Carbon Nanodots. *The Journal of Physical Chemistry Letters* **2016**, *7*, 3419-3423.

28. Ghosh, S., et al., Photoluminescence of Carbon Nanodots: Dipole Emission Centers and Electron–Phonon Coupling. *Nano Letters* **2014**, *14*, 5656-5661.

29. Qu, D.; Zheng, M.; Zhang, L.; Zhao, H.; Xie, Z.; Jing, X.; Haddad, R. E.; Fan, H.Sun, Z., Formation Mechanism and Optimization of Highly Luminescent N-Doped Graphene Quantum Dots. *Sci. Rep.* **2014**, *4*.

30. Xu, G.; Zeng, S.; Zhang, B.; Swihart, M. T.; Yong, K.-T.Prasad, P. N., New Generation Cadmium-Free Quantum Dots for Biophotonics and Nanomedicine. *Chemical Reviews* **2016**, *116*, 12234-12327.

31. Zhang, X., et al., Color-Switchable Electroluminescence of Carbon Dot Light-Emitting Diodes. *ACS Nano* **2013**, *7*, 11234-11241.

32. Li, X.; Zhang, S.; Kulinich, S. A.; Liu, Y.Zeng, H., Engineering Surface States of Carbon Dots to Achieve Controllable Luminescence for Solid-Luminescent Composites and Sensitive Be2+ Detection. *Scientific Reports* **2014**, *4*, 4976.

33. Song, Y.; Zhu, S.; Zhang, S.; Fu, Y.; Wang, L.; Zhao, X.Yang, B., Investigation from Chemical Structure to Photoluminescent Mechanism: A Type of Carbon Dots from the Pyrolysis of Citric Acid and an Amine. *Journal of Materials Chemistry C* **2015**, *3*, 5976-5984.

34. Shi, L.; Yang, J. H.; Zeng, H. B.; Chen, Y. M.; Yang, S. C.; Wu, C.; Zeng, H.; Yoshihito, O.Zhang, Q., Carbon Dots with High Fluorescence Quantum Yield: The Fluorescence Originates from Organic Fluorophores. *Nanoscale* **2016**, *8*, 14374-14378.

35. Vinci, J. C.; Ferrer, I. M.; Seedhouse, S. J.; Bourdon, A. K.; Reynard, J. M.; Foster, B. A.; Bright, F. V.Colón, L. A., Hidden Properties of Carbon Dots Revealed after HPLC Fractionation. *The Journal of Physical Chemistry Letters* **2013**, *4*, 239-243.

36. Song, Y.; Zhu, S.; Xiang, S.; Zhao, X.; Zhang, J.; Zhang, H.; Fu, Y.Yang, B., Investigation into the Fluorescence Quenching Behaviors and Applications of Carbon Dots. *Nanoscale* **2014**, *6*, 4676-4682.

37. Karfa, P.; Roy, E.; Patra, S.; Kumar, S.; Tarafdar, A.; Madhuri, R.Sharma, P. K., Amino Acid Derived Highly Luminescent, Heteroatom-Doped Carbon Dots for Label-Free Detection of Cd2+/Fe3+, Cell Imaging and Enhanced Antibacterial Activity. *RSC Advances* **2015**, *5*, 58141-58153.

38. Mosconi, D.; Mazzier, D.; Silvestrini, S.; Privitera, A.; Marega, C.; Franco, L.Moretto, A., Synthesis and Photochemical Applications of Processable Polymers Enclosing Photoluminescent Carbon Quantum Dots. *ACS Nano* **2015**, *9*, 4156-4164.

39. Claramunt, S.; Varea, A.; López-Díaz, D.; Velázquez, M. M.; Cornet, A.Cirera, A., The Importance of Interbands on the Interpretation of the Raman Spectrum of Graphene Oxide. *The Journal of Physical Chemistry C* **2015**, *119*, 10123-10129.

40. Righetto, M.; Minotto, A.Bozio, R., Bridging Energetics and Dynamics of Exciton Trapping in Core-Shell Quantum Dots. *The Journal of Physical Chemistry C* **2016**.

41. Heyman, N. S.Burt, J. M., Hindered Diffusion through an Aqueous Pore Describes Invariant Dye Selectivity of Cx43 Junctions. *Biophysical Journal* **2008**, *94*, 840-854.

CHAPTER 9

Excited State Dynamics of Hybrid Perovskite Dots

ABSTRACT- Lead Halide Perovskites (HPs) display outstanding electronic properties, originated by an intriguing combination of many-body interactions and peculiar structural features. Throughout these years, the photovoltaic field was the leading recipient of such peculiar physics and chemistry, taking advantage of low exciton binding energies, long carrier diffusion length and reduced trapping. Yet the shrinkage of the size of these materials opened the way to different applications, inducing vast modifications of the nature of excited states. Hence, a thorough characterization of the energy relaxation processes is prerequisite to envision, engineer and ultimately tailor the possible application of HP-based nanomaterials. In this Chapter, the first steps of the photophysical characterization of hybrid lead halide perovskites quantum dots are presented. In particular, energy relaxation processes are investigated as a function of the magnitude of the quantum confinement through optical spectroscopic methods. The primary results are obtained by fluorescence spectroscopy, but preliminary results on transient absorption spectroscopy data are also presented. The performed analysis reveals a peculiar behavior of these materials in terms of trapping rates, cold and hot exciton relaxations. Possible hypotheses on both the nature and the causes for observed behaviors are presented. Yet much work is needed to decipher the exciton dynamics of HPs-based nanomaterials and to portray a comprehensive photophysical picture of these systems. Nevertheless, from these results, nanostructures based on HPs stem as promising candidates for light emitting applications, tracing a distinction from their bulk counterpart.

9.1 Introduction

In the last five years, HPs took by storm the scientific community of photovoltaics.[1] These materials allowed creating cheap and highly efficient optoelectronic devices, owing to their excellent absorption, rapid charge generation from loosely bound excitonic states, and contextual slow recombination rates.[2-4] Moreover, high carrier mobility and diffusivity are enormously advantageous for solar cells, resembling first generation solar cells rather than third-generation ones. Some of these properties are desirable for the application of such materials in light emitting devices such as light-emitting diodes (LED) and lasers. However, such an application is restricted by the low photon emission efficiency.[2] Some other features further hamper their efficient conversion to the light emitting field. A potential strategy to overcome these limitations is the reduction of dimensionality.[5-6]

Recently, the synthesis of HP-based nanocrystals was reported through colloidal methodologies by Rogach et al.[7,] and quantum confinement in other HP-based nanostructures was reported, as well.[8-10] The possibility of realizing quantum confined HP materials is a crucial step in the development of light emitting perovskites. As widely discussed in Chapter 1, quantum confinement profoundly modifies the nature of electronic excitations. Recent works reported the increase in exciton binding energies and consequent high emission efficiencies from colloidal nanocrystals of methylammonium lead bromide ($MAPbBr_3$) perovskite.[9, 11] Moreover, high-quality cesium lead bromide ($CsPbBr_3$) nanocrystals were produced by hot-injection techniques.[12]

The success of bromide-based HPs is circumstantial to their relatively weaker success in photovoltaics. Indeed, these materials display reasonably pronounced excitonic features in their bulk form and mid-visible band gap. The resulting nanostructures display among the narrowest photoluminescence (PL) bands and very high PL efficiency, holding promises in the replacement of more expensive Cd-based nanostructures. The stability of these nanostructures was initially a severe issue, hampering their characterization and causing degradation in few days.[13] Nevertheless, different strategies were developed in order to augment the stability, i.e., using sufficiently passivizing ligands, creating core-shell heterostructures or using non coordinating solvents.[14] State-of-the-art samples display increased stability and allow investigating the photophysics of these nanostructures.

As witnessed in the previous Part of this thesis, the relaxation dynamics of semiconductor materials experience abrupt changes upon nanoscale miniaturization. Thence, during the last two years, many groups spent much effort in a thorough characterization of these nanocrystals. Analogously to the case of Cd-based quantum dots (QDs), trapping processes were found to play a fundamental role in the relaxation of excitations.[15] Zhang first reported some results on the first photophysical characterization of $MAPbBr_3$ perovskites quantum dots (PDs).[16] Unfortunately, the investigated samples were of lower quality with respect to those available now. According to Zhang, the relaxation in these PDs is dominated by shallow or deep traps. In 2016, Pullerits suggested the dual origin and behavior of traps to stem from either volume or surface defects.[15] Volume traps were reported to result in an ultra-long lifetime and were mainly observed in bulk HPs. Conversely, surface traps mainly drive energy relaxation in PDs, being reported with up to 0.7 trap per nanocrystal densities. Other groups reported the presence of 1-4 traps per nanocrystals, related to the surface of PDs. [17]

In this Chapter, the exciton dynamics of $MAPbBr_3$ is investigated as a function of the crystal size reduction and of the magnitude of the quantum confinement. Specifically, the analysis spans not only essential aspects such as radiative and non-radiative relaxation time constant but also hot carrier relaxation efficiencies. The presented results add some piece to the PDs puzzle, thereby assisting to the portrayal of a whole photophysical scenario that can be helpful as a guideline for tailoring the synthetic routes towards the desired properties.

9.2 Optical Properties of $MAPbBr_3$ quantum dots

As explained in the previous Chapter, the studied PDs were synthesized in collaboration with Dr. A. Privitera, following the synthetic route developed by Rogach and coworkers.[7] The realization of a series of PDs, synthesized at different temperatures allowed delving deeper into the effect of sizes on various processes determining excited state relaxations.

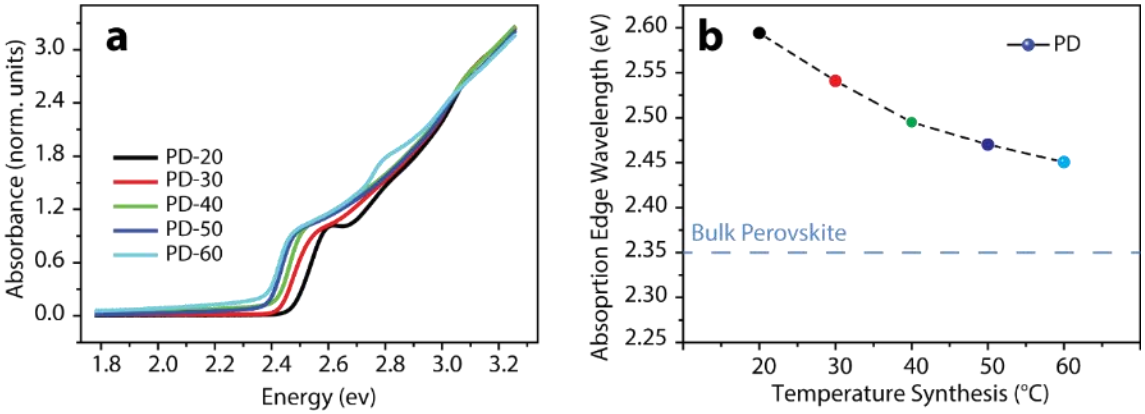

Figure 9.1- (**a**) Absorption spectra for the series of PDs, synthesized at different temperatures, in toluene dispersion. Reported spectra are normalized to the band edge peak. (**b**) Dependence of the band edge peak energy, obtained by inspection of the second derivative of the absorption spectrum, on the synthesis temperature (the dot color corresponds to that used in panel (**a**)).

Qualitatively, the absorption edges (Figure 9.1**a**) show a redshift with increasing synthesis temperature. According to Rogach and Zhang, this redshift is caused by the quantum confinement effect exerted by reduced crystallite size on the photogenerated carriers.[7, 16] Unfortunately, as reported in the previous Chapter it was not possible to obtain a direct determination of the nanocrystals sizes and size distribution. Yet according to Rogach calibration, we were able to estimate a radius ranging from 2.2 to 3.6nm for 20 and 60°C, respectively. The exciton Bohr radius for bulk $MAPbBr_3$ was reported to range from 2.0 to 2.5 nm, with some variability associated with the methods used to determine this value. Nevertheless, the photogenerated carriers are likely to experience quantum confinement effect, in between strong and weak confinement regimes. Quantitatively, the absorption edge was determined by inspection of the second derivative and resulting values are reported in Figure 9.1**b**. As expected for quantum confined systems, the band edge energy for PDs lies above that of bulk $MAPbBr_3$ (2.35eV, *Refs 2,10*). Moreover, the excess energy provided as an enhanced interaction between photogenerated carriers is a decreasing function of synthesis temperature. As shown by Rogach for perovskites, this effect is caused by the different size of crystallite, i.e., caused by the quantum size effect, discussed in Chapter 2.

Hence, the absorption spectra suggest a modified nature of the electronic states, with respect to bulk $MAPbBr_3$ perovskite. The excess energy, shown in Figure 9.1**b**, can be understood in terms of enhanced interaction between photogenerated electron and hole. According to this increase in the binding energy, excitonic states are expected to be stable at room temperature and therefore drive optical properties of PDs. Pullerits et al. demonstrated the role of excitons in PDs and reported up to 320 meV binding energies, using X-Ray absorption spectroscopies. [18]

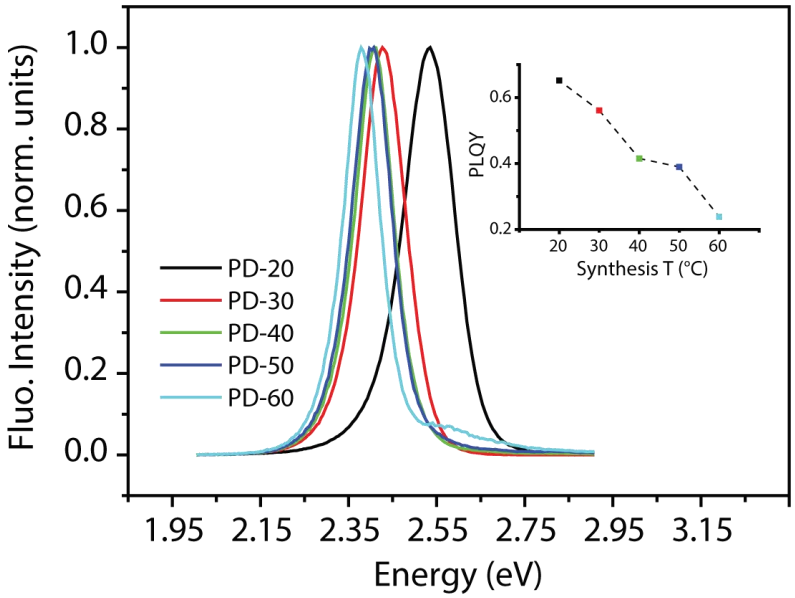

Figure 9.2- PL spectra for the series of PDs, synthesized at different temperatures, in toluene dispersion. Reported spectra are normalized on the PL peak. The PL bands redshift with increasing synthesis temperature, in analogy with absorption edges, reported in Figure 8.1. In the inset, PLQY values calculated with the relative method, using Coumarine 343 as fluorescent standard.

The observed strong photoluminescence is the most direct and revealing evidence of the excitonic character, which drives the PDs photophysics. As reported in Figure 9.2, PDs display a narrow emission band with FWHM as low as 90 meV, and small Stokes shifts (40-50 meV). Thanks to these features, the high color saturation of PDs widely outperforms that of CdSe based QDs, according to the Commission International de L'Eclarage (CIE) chromaticity diagram.[12] The emission efficiency is observed to be a decreasing function of the synthesis temperature. Indeed, the photoluminescence quantum yield (PLQY) behavior is reported in the inset of Figure 9.2. PLQY values are as high as 65% for PD-20 and fall down to 24% for PD-60. This quantifies the interplay between radiative and non-radiative relaxation mechanisms and is influenced by a number of factors, e.g., radiative constant, phonon coupling, and trapping velocities.[15] Such high PLQY values are remarkable, considering the low synthesis temperature and the absence of any inorganic shell over-coating the PDs, which is usually required in order to observe efficient emission from II-VI quantum dots (see Chapter 3).

This could stem from either a reduced defectivity or a reduced electronic interaction with trap sites. Furthermore, it is not possible to observe any signatures of intra-gap emission, which is often present in bare core CdSe quantum dots. These observations suggest a considerably lower abundance of intra-gap states in perovskite QDs compared to other studied QDs.

9.3 Cold Exciton Dynamics in $MAPbBr_3$ quantum dots

We investigated the exciton dynamics in PDs by means of time-resolved photoluminescence (TRPL) spectroscopy. This technique allows investigating the recombination dynamics of the band edge exciton, i.e., the cold exciton dynamics.[19]

Specifically, these measurements were carried on by time-correlated single photon counting (TCSPC) with nanosecond time resolution. The excitation fluence was kept low in order to avoid multiple excitations within nanocrystals.[20] The TRPL spectra were recorded under 2.72 eV excitation and collecting a 2 nm band centered on the peak of the PL signal. The series of TRPL spectra in reported in Figure 9.3**a**. Qualitatively, the PL decay appears slowed down with increasing synthesis temperature, i.e., the PL decay of PD-60 is slower than the PL decay of PD-20. The fitting by means of multi-exponential function provides more quantitative insights: PL decays are well fitted using multiple exponentials, suggesting either complex recombination mechanism or an inhomogeneous ensemble.[21] As reported in Table 9-I, the decays of PD-20 and PD-30 require a bi-exponential fitting function, whereas those synthesized at higher temperatures require a tri-exponential fitting function. The average lifetime $\langle\tau_X\rangle$ quantifies the slowing down of the PL dynamics. Indeed, $\langle\tau_X\rangle$ values, reported in Table 9-I, increase from 15 ns for PD-20 to 60 ns for PD-60. At first blush, this behavior could appear rather counterintuitive, given the inverse trend for the measured PLQY, reported in Figure 9.3**c**. Yet PLQY measures the fraction of radiative recombination with respect to the total recombination dynamics, comprising radiative and non-radiative recombinations, which is measured by TRPL decay.[22] Therefore, the independent variation of the radiative constant Γ_r and non-radiative constant Γ_{nr} can lead to different behavior of PLQY and $\langle\tau_x\rangle$, as observed in this case. The accurate extraction of the radiative and non-radiative constant requires combining the information, independently obtained by TRPL and PLQY measurements, according to a photophysical model. In this work, two different models were applied: the inhomogeneous PD ensemble, proposed by Klimov [20] for QDs, and the trapping\de-trapping model, proposed by Scholes.[23]

9.3.1 Inhomogeneous PD ensemble model

Considering the PL dynamics for an ensemble of PDs, it can be assumed that all PDs share a common Γ_r value, while the differences in the number and identity of non-radiative recombination centers give rise to various $\Gamma_{nr,i} (i = 1,..,n)$ values.

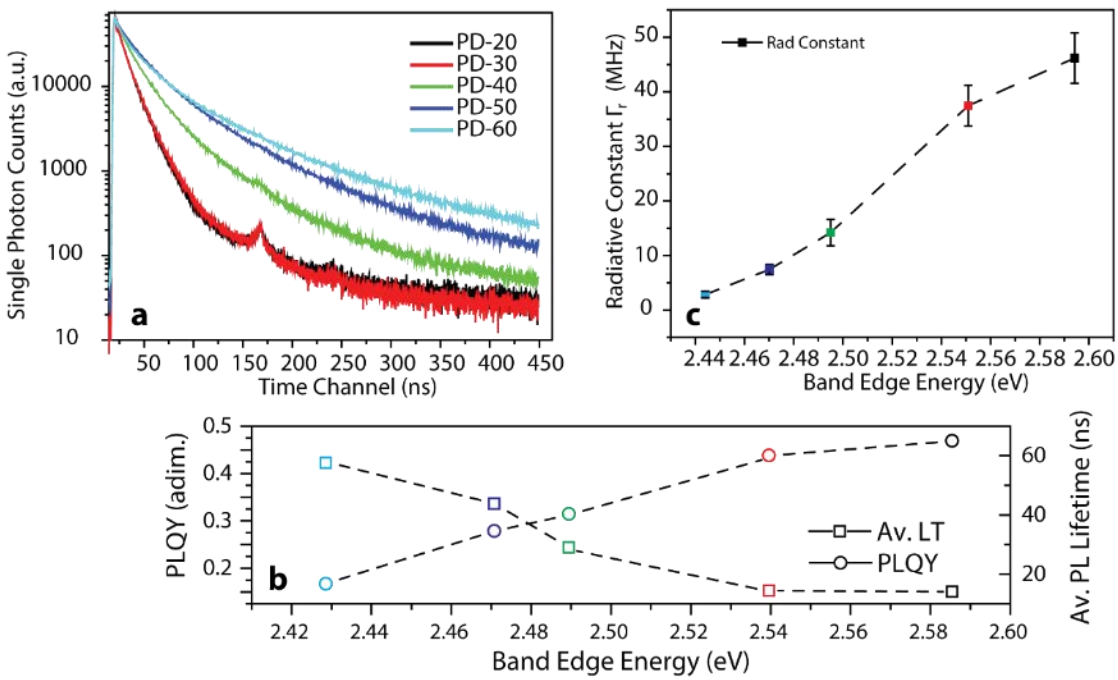

Figure 9.3-(**a**) Time-resolved photoluminescence decay curves measured for different PDs, under 2.7eV excitation and recording 2nm bandwidth on the PL maximum. (**b**) Comparison between PLQY values and average lifetimes extracted by multi-exponential fitting, measured under the same 2.7ev excitation energy. The opposite trend is rationalized in terms of independent variation of radiative and non-radiative recombination rate constants. (**c**) Radiative rate constant extracted by inhomogeneous PD ensemble model, considering PDs as an inhomogeneous ensemble in which different dots display different non-radiative rates. The increasing trend with increasing band-edge energy is explained by simple dipole emitter theory.

In the case of the n PDs sub-ensembles with distinct values of $\Gamma_{nr,i}$, it is possible to define an effective exciton lifetime τ_{x_i}, as $\tau_{x_i} = \frac{\tau_r \cdot \tau_{nr,i}}{(\tau_r + \tau_{nr,i})}$, where $\tau_r = \Gamma_r^{-1}$ is the radiative lifetime and $\tau_{nr_i} = \Gamma_{nr,i}^{-1}$ is the non-radiative lifetime of the i-th sub-ensemble.

Accordingly, the PL decay is described as $I_{PL}(t) = \sum_{i=1}^{n} A_i \cdot e^{-\frac{t}{\tau_{x,i}}}$, where $A_i$is the fraction of PDs populating the i-th sub-ensemble. The PLQY varies in different sub-ensembles, and the PLQY of the individual i-th sub ensemble is given by the relation $q_i = \frac{\tau_{x_i}}{\tau_r}$. Hence, the PLQY for the ensemble of PDs is defined as

$$PLQY = \sum_{i=1}^{n} k_i q_i = \frac{1}{\tau_r} \sum_{i=1}^{n} k_i \tau_{x_i} = \frac{\langle \tau_x \rangle}{\tau_r} \qquad \textbf{(Eq. 9.1)}$$

where holds the definition $k_i = (A_i)^{-1}$ Consequently, it is possible to extract the radiative lifetime and the radiative constant as

$$\tau_r = \frac{\langle \tau_x \rangle}{PLQY} = \frac{1}{\Gamma_r} \qquad \textbf{(Eq. 9.2)}$$

The values extracted for Γ_r are reported in Figure 9.3**c** and exhibit an increasing trend with respect to band edge energy. Thence, the independent variation of Γ_r accounts for the inverse trends of $\langle \tau_x \rangle$ and *PLQY*. The observed behavior of the radiative constant with emission energy can be rationalized by considering the emission from a point-dipole.[20] The radiative rate for a simple dipole emitter scales as $\Gamma_{r,dip} \propto E_{em}|\boldsymbol{\mu}|^2$, where E_{em} is the energy of the emitted radiation and $|\boldsymbol{\mu}|$ is the dipole moment. For a PD, the emission energy is the band gap energy E_g, whereas the dipole moment can be intended as interband transition dipole moment, expressed in terms of Kane energy parameter E_p as $|\boldsymbol{\mu}|^2 \propto \frac{m_o}{2} E_p$. [24] According to $\boldsymbol{k} \cdot \boldsymbol{p}$ method, this parameter is a constant for a given material. Although other factors influence the dipole moment, e.g. dielectric screening *f*, and thermal population of possible sublevels $\gamma(T)$, a linear dependence on E_g is expected for the radiative rate $\Gamma_{r,dip} \propto f\gamma(t)E_g E_p$.[20] From a physical point of view, this trend is related to the overlap between photoexcited carriers, i.e. in smaller (larger) PDs the emission is blueshifted (redshifted) and the overlap between photoexcited electron and hole is reduced (augmented), causing an increase (decrease) of the radiative rate. Nevertheless, the contextual decrease in PLQY value, suggest an increase in the non-radiative recombinations. As widely discussed in Chapters 1 and 3, carrier trapping is one of the most important mechanism driving non-radiative energy relaxation in QDs. Recently, the occurrence of trapping in PDs was addresses by few works, as well.[15-16] Thence, a more adequate and insightful model can be used to interpret PL dynamics of PDs, considering the dynamics of trapping and de-trapping.

9.3.2 Dynamical Trapping model

Recent investigations, delving deeper into the nature of carrier trapping in hybrid perovskites materials, reported the predominant role of shallow trap levels.[25] As proposed originally by Scholes for inorganic QDs,[23] these trap sites do not behave as static charge accumulators. Thence, being de-trapping possible and energetically advantageous for these traps, their dynamical nature need to be taken into account when modeling PL dynamics. Thus, the observations of relatively low PLQY values and long PL decays can be rationalized in terms of trapping/de-trapping equilibrium.

The de-trapping process results in a lucrative regeneration of either free carriers or excitons, contributing to PL in a delayed fashion, coherently with persistent tails in PL decay curves.[26] This difficult balance of processes profoundly affects the PL dynamics. Hence, the radiative rate combines with trapping and de-trapping rates, resulting in multi-exponential PL decays (Table 9-I). The inherently overlapping timescales made the conventional multi-exponential fitting analysis not reliable in separating these contributions. As explained in Chapter 3, Minotto et al. developed a phenomenological kinetic model, deciphering PL dynamics and disentangling this interplay of processes.[19] For further information on the kinetic model, the reader is referred to Chapter 3. Thus, this model was applied to describe the PL recombination dynamics of PDs, in order to extract relevant parameters regarding their dynamics, i.e., radiative, non-radiative and trapping/detrapping rates. Briefly, the dynamics of the PDs is described by the following system of coupled differential equations

$$\begin{cases} \dfrac{d\rho_X(t)}{dt} = \sum_i \left(v_{dt,i}\rho_i(t) - (v_{t,i} + \Gamma_{NR} + \Gamma_R)\rho_X(t) \right) \\ \dfrac{d\rho_i(t)}{dt} = v_{t,i}\rho_X(t) - v_{dt,i}\rho_i(t) \end{cases} \qquad \textbf{(Eq. 9.3)}$$

where $\rho_X(t)$ is the population of bound excitons, $\rho_i(t)$ is the population of the i-th trap state distribution, and $v_{t,i}(v_{dt,i})$ is the related trapping (de-trapping) velocity.

As discussed in Chapter 3, this is a simplified version of the kinetic model, comprising velocities rather than rate constants for the trapping process. The description of the trapping process as a molecular reaction unveils that trapping velocities contain an empty trap concentration term, i.e., trapping process necessitates of a bound exciton and an empty trap site. However, being the trapping mechanism (as well as the very nature of traps) in perovskites still under debate, the model proposed here is not specialized. To this level, the model in Eq. 8.3 describes the PL dynamics of excitons in PDs as shaped by the interaction of emissive states with some dark trap states, acting as reservoirs.

Notably, this model adequately describes the PL dynamics of different PDs. As reported in Table 9-I, although the PL decay PD-20 and PD-30 are well described by a single trap state distribution, PL decays of other samples require two trap distributions. This is contextual to the appearance of a third decay time constant (i.e.,$\tau_{x,3}$) in multi-exponential fitting for PD-40, PD-50 and PD-60. Thence, this second trap distribution describes this longer-lived decay component as a further (and slower) trapping/de-trapping equilibrium, involving a second trap state distribution. The substantial increase in fitting accuracy for PD-40 decay, when a second trap state distribution is introduced, can be appreciated in Figure 9.4**a**.

The dynamics of trap state populations is fundamental to achieve an insightful understanding of the PDs photophysics. The interplay between trapping and de-trapping drives the growth of trap state population up to a maximum, within the first hundreds of nanoseconds. The trap state population is depleted by de-trapping mechanism and acts as a bound exciton population reservoir, contributing to the PL decay curve afterwards. Hence, the net effect of this trapping/de-trapping equilibrium is a distortion of decay curves, i.e., the PL decay is accelerated at short times (due to trapping), and slowed down at longer times (thanks to de-trapping).

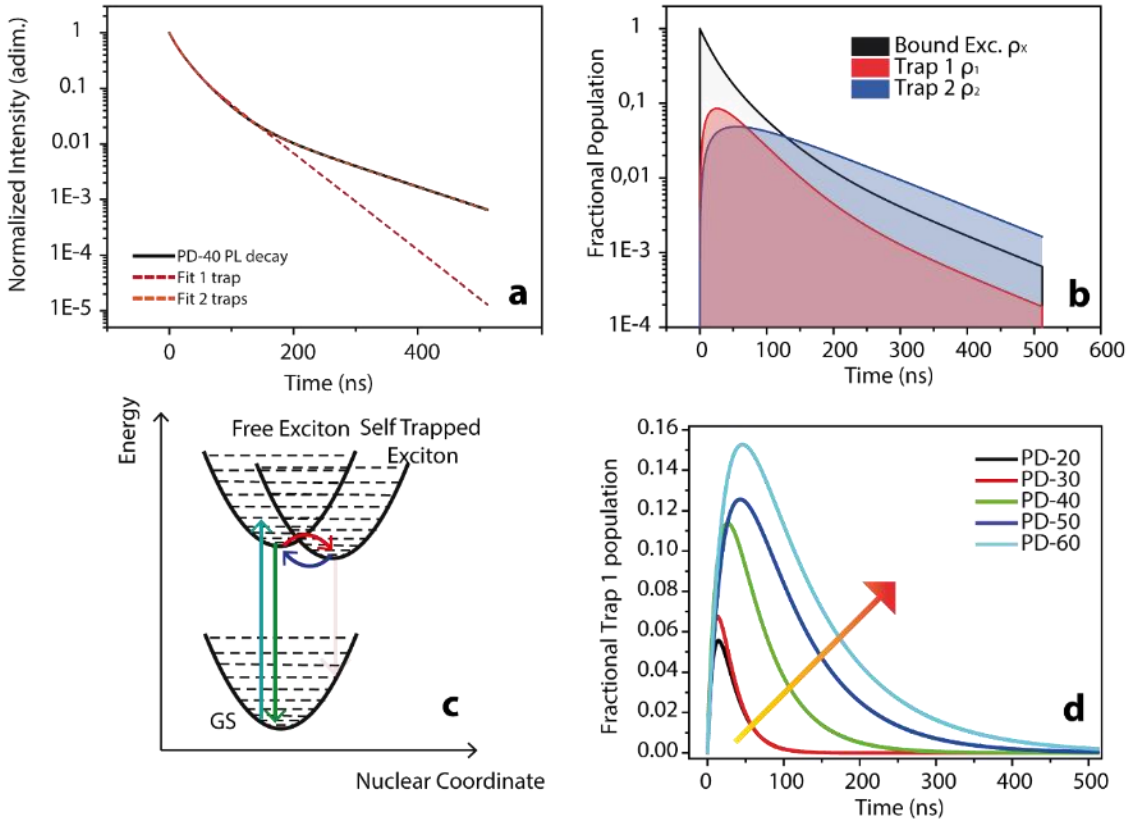

Figure 9.4 – (**a**) Results of the fitting procedure of PL decays for PD-40, carried out through the phenomenological kinetic modeling (Eq. 8.3) of exciton dynamics. An adequate fitting of PD-40 PL dynamics (as well as that of PD-50 and PD-60) requires at least two trap distributions. Black solid line represents experimental data, and dashed lines represent best-fit curves. (**b**) Populations of different states that describe the PL decay for PD-40 (orange dashed line, **a** panel). Black lines represent the bound exciton population, directly related to PL decay. Red and blue lines represent the fractional populations of two different trap distributions. (**c**) Scheme adapted from Ref . 31. Potential energy curves represent the ground state (GS), the free exciton and the self-trapped exciton states. Akin to the charge transfer model proposed by Scholes, self-trapped excitons generate a shallow potential minimum. This opens to possible equilibrium between these two states. (**d**) Fractional population of the first trap distribution ρ_1 (t) for different samples. With increasing synthesis temperature, the population of traps becomes more persistent. In accordance with data reported in Table I, this effect is caused by slower detrapping rates, rather than fast trapping rates.

The dynamics of different states $\rho_x(t), \rho_1(t), \rho_2(t)$ associated to the orange dashed curve in Figure 9.4**a** is shown in Figure 9.4**b**. Accordingly, the population of the second trap distribution reaches its maximum at a delayed time, with respect that of the first trap distribution.

A dual nature of trap distributions was originally reported by Scholes and Minotto for CdSe-based core/shell QDs.[19, 23] In the case of inorganic QDs, the appearance of a second trap distribution was univocally ascribed to interface defects, generated by interfacial strain and anion interdiffusion.[19, 23] Nevertheless, hybrid perovskite materials are sensibly different materials with respect to II-VI semiconductors. Consequently, an assignment of these trapping constant would require a discussion on the nature of both traps and trapping process.

As mentioned above, the nature of these trap state is still under debate within the scientific community. Two different processes were indicated as a possible origin of trap states: (i) carrier trapping at chemical defects, such as interstitial halide anions or undercoordinated lead sites at surfaces; (ii) exciton self-trapping, due to strong carrier-lattice interactions.

Kobori and co-workers pointed out the role of surface states.[17] They first reported luminescence blinking in PDs, and through chemical passivation analyses, they hypothesized the presence of Pb^{2+} acting as charge trapping sites. Other works on the photoconductivity of bulk lead halide perovskites revealed the presence of a broad trap distribution, associated with deep electron traps stemming from interstitial anions.[27-28] The presence of these defects in HPs is highly plausible, considering the extremely high anionic mobility values hitherto reported. In addition, the generation of Frenkel defects (F-H pairs) was reported for alkali halide compounds. [29]

Yet the "softness" of the lattice and the high electron-phonon coupling cannot be neglected when dealing with hybrid perovskite. Indeed, a number of previous work reported polaronic effects in perovskites. In particular, Zhu and co-workers proposed a direct role of vibrations in trapping excitons.[30] By a combination of valence band photoemission spectroscopy and temperature resolved PL spectroscopy, the exciton self-trapping was proposed as the central trapping mechanism.

The carrier self-trapping process was extensively studied in both molecular and ionic crystals in the '70s. Accordingly, strong electron-phonon interactions may induce a spatial localization of carriers within a lattice deformation potential, thereby yielding polaronic species formation.[31] The self-trapping of non-equilibrium quasi-particles, such as excitons, (Figure 9.4**c**) is expected to be a dynamical process resulting in a modification of their emissive properties. In particular, a low oscillator strength is generally associated with these states (non-Condon states), which should contribute to the absorption spectrum only by a broad and low-intensity absorption tail.

Taking a broader look, some similarities could be noticed in these two approaches for the description of trap states in a polarizable lattice such as that of HPs, i.e., the self-trapped exciton could be intended as a nascent F-H defect pair.

Whilst these two approaches in describing trapping in perovskites share some similarities, a recent work calculated the energy state for shallow traps and polaron formation in lead iodide perovskites.[25] Albeit it was found that shallow trap is more energetically favorable than polaron formation, it should be considered that self-trapping has both intrinsic and extrinsic origins, and the reduction of dimensionality, as well as disorder, would lower the deformation energy and favor this process. [29, 32]

The origin of trap states is still unclear and widely debated, yet the trapping rates reported in Table 9-I appear quantitatively different with respect to those reported for CdSe (Chapter 3). Indeed, reported rates are up to two orders of magnitude smaller than those reported for core CdSe. Slow exciton trapping in PDs was recently reported by Pullerits, as well.[33] If not a substantially different mechanism, such discrepancies could suggest a non-negligible role of phononic and polaronic effects. Moreover, for PDs synthesized at increasing temperatures, it is possible to observe decreasing de-trapping rates, contextually to the appearance of the second trap distribution. According to the proposed interpretations, such trends could be stemming from either a modified energetics or a size-dependent coupling with vibrations. Nevertheless, much work and further analyses are needed to disclose more details on the nature of traps.

Table 9-I Multi-exponential and phenomenological kinetic fitting results of different perovskites dots

	Γ_{rad} [MHz]	$\upsilon_{t,1}$ [MHz]	$\upsilon_{t,2}$ [MHz]	$\upsilon_{dt,1}$ [MHz]	$\upsilon_{dt,2}$ [MHz]	PLQY	R_{DT}
PD-20	46,3	15		85		65 ± 4	5,8
PD-30	37,6	15		81		56 ± 4	5,6
PD-40	14,2	12	7	36	10	41 ± 3	3,0
PD-50	7,4	9	3	26	37	38 ± 3	2,7
PD-60	4,0	10	5	24	10	23 ± 2	2,4
	k_1	k_2	k_3	$\tau_{x,1}$ (ns)	$\tau_{x,2}$ (ns)	$\tau_{x,3}$ (ns)	$\langle\tau_x\rangle$
PD-20	65	35		9,9	21,9		14
PD-30	50	50		8,7	21,3		15
PD-40	32	63	5	10,6	31,5	118,2	29
PD-50	54	41	5	16,0	42,3	120,0	52
PD-60	14	58	28	9,1	40,7	126,3	60

Lastly, the radiative rate obtained by the application of the phenomenological kinetic model is nearly coincident with that derived by the inhomogeneous PD ensemble method, shown in Figure 9.3c. This near coincidence may derive from resorting to the measured PLQY in both models. However, a more detailed analysis is needed to understand the similar results obtained by applying two physically different models. It is clear, however, that the dynamical trapping model is much more insightful.

9.4 Hot Carriers Dynamics in $MAPbBr_3$ quantum dots

The existence of a trapping/de-trapping equilibrium poses further questions on the role of hot-carriers trapping within these systems. A theory of hot-carrier trapping was developed for CdSe core/shell QDs in Chapter 3. Briefly, the equilibrium between trapping and de-trapping events was identified as the fundamental process determining the *PLQY* value. [22]

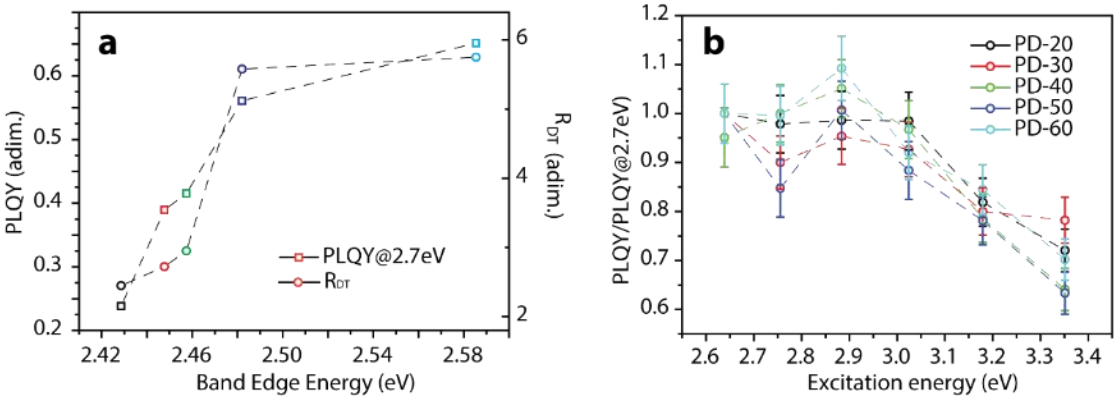

Figure 9.5 -(**a**) Correlation between PLQY values measured under 2.72eV excitation energy and phenomenological parameter R_{DT}, indicating the equilibrium between detrapping and trapping, obtained by kinetic modeling of TRPL decay curves. (**b**) Evolution of PLQY values measured under different excitation energies. PLQY values were normalized to maximum values reported in panel **a** and Table 9-I.

From a physical point of view, the accumulation of long living trapped states in inorganic QDs, ultimately lead to the creation of charged QD species and resulted in the lowering of PLQY values by the creation of dark QDs within the ensemble.[34] Within this framework, the (fast) trapping of hot-carriers is expected to unbalance the trapping/detrapping equilibrium and to favor surface charge accumulation, being this process under kinetic rather than thermodynamic control.[35] In summary, the developed model predicts a lowering of *PLQY* values, recorded under higher energy excitations.

Hence, the adequacy of trapping-de/trapping equilibrium in describing the photophysics of PDs opens to further investigations. Namely, an investigation on the interaction of hot carriers with trap states could reveal exciting details on the nature of these traps.

The correlation between the ratio of de-trapping and trapping velocities $R_{DT} = \frac{v_{dt_1}}{v_{t_1}}$ obtained by phenomenological kinetic modeling and the experimentally measured *PLQY* is shown in Figure 9.5**a**. Akin to CdSe-based QDs (Chapter 3), the agreement appears not to be fully accurate, yet a general trend can be established, i.e. higher R_{DT} values corresponds to higher *PLQY* values. The established correlation is somewhat intuitive and confirms that a more extended population residency in trap states is associated with lower *PLQY* values.

Therefore, it is possible to study the energetics of trapping process through the analysis of *PLQY* excitation profiles, or *photo-action* spectra.[34, 36] Namely, envisioning a mechanism resembling that formulated in Chapter 3, the generation of long-lived trap states is expected to influence the emission dynamics within the ensemble. Recent reports of giant blinking in PDs and blinking in bulk perovskites further confirm this hypothesis.[37] Indeed, Rosenthal et al. recently demonstrated the strong relation between blinking, non-unitary *PLQY* and trapping dynamics in inorganic QDs.[38]

The *PLQY* excitation profiles (Figure 9.5**b**) reveal a decreasing trend of *PLQY* with increasing excitation energy for each PD sample. In particular, the decrease of *PLQY* value is observed above 3eV, whereas below this excitation energy the PLQY value is constant. Albeit this effect is less pronounced with respect to the case of CdSe core/shell QDs, *PLQY* values recorded under 3.35eV are significantly reduced (up to 35%) with respect to band edge excited *PLQY* value. In addition, the absolute variation of *PLQY* value is different for each PDs, but the normalization with respect to the higher *PLQY* value measured results in comparable trends. Thence, the reduction of emission efficiency when higher excitation energies are employed appears to be a widespread phenomenon for emitting nanostructures. Following theories developed in Chapter 3, a possible explanation involves the distinct interaction of hot-carriers with trap sites.

However, also in this case, more detailed considerations would require a less partial knowledge of the nature of trap states. In fact, both theories mentioned in the previous section would share some common points for the explanation of these findings. When dealing with high energy excitations, vibrationally excited trap states (whether they are charged sites or self-trapped excitons) play a crucial role in understanding the effects of hot carrier trapping. Indeed, the high density of acceptor states results in a kinetically controlled process and an ultrafast trapping process.[22] Thus, this ultrafast trapping favors the accumulation of trapped carriers, thereby leading to the creation of either trions (charged trap hypothesis) or biexcitons (self-trapped excitons hypothesis) and affecting the recombination dynamics.

9.4.1 Preliminary Transient Absorption spectroscopy results

The importance of hot carrier trapping processes is further emphasized by recent reports on long-lived hot carriers in bulk and nanocrystalline lead iodide perovskites ($MAPbI_3$).[39] In particular, a strong bandgap renormalization effect, induced by hot carriers generation, was found for a wide range of carrier densities. Moreover, many works reported a phonon bottleneck effect in bulk perovskites.[2] Hitherto only a single work reported slow carrier relaxation in quantum confined perovkites.[40]

Here, the thermalization of hot carriers was directly studied by non-resonant pump and probe or transient absorption (TA) spectroscopy. This technique - extensively introduced in Chapter 2 – provides valuable insights into the electronic and optical properties of the studied systems, within fast and ultra-fast timescales.

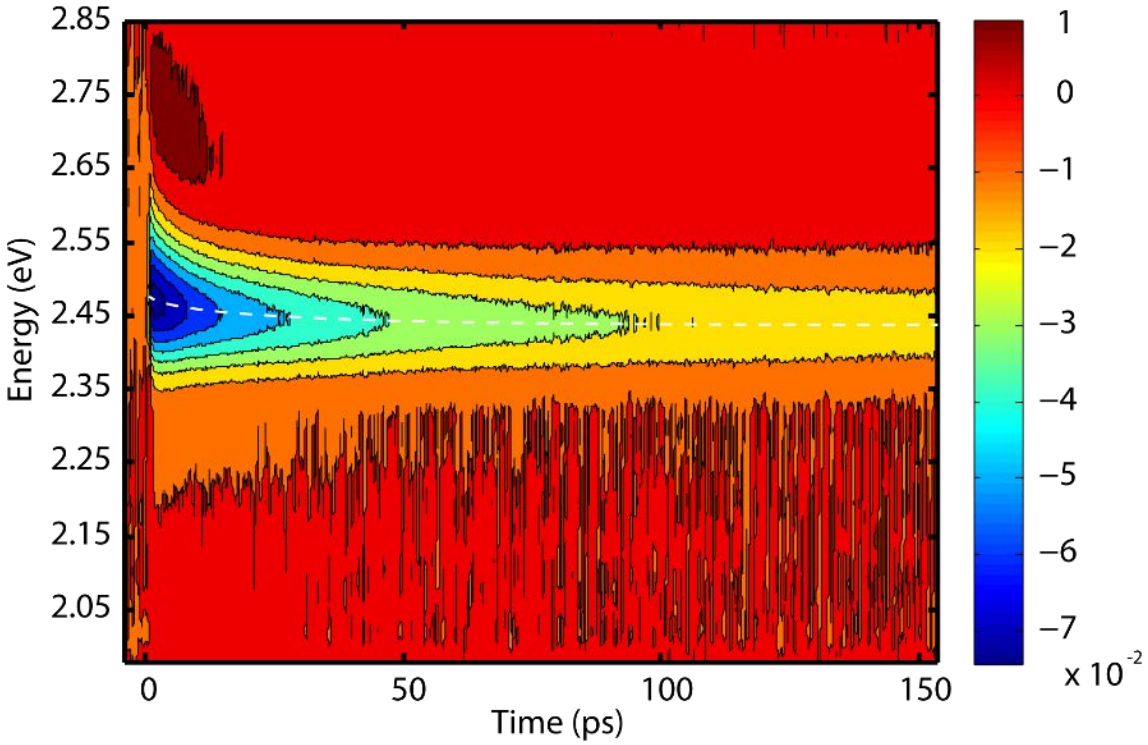

Figure 9.6 - Two-dimensional TA map for PD-50, measured under 3.1eV excitation at 80 μJ cm^{-2}. The white dashed line indicates the time-dependent redshift of the B_x bleaching signal.

Indeed, following an optical photoexcitation, which pumps the material up to an excited state of the continuum, the wealth of various photophysical processes is tracked by monitoring the absorption of a second pulse of light. The autocorrelation geometry allows achieving high temporal resolution of ~120*fs* and therefore opens to studies on carrier thermalization.

Generally, TA signals in semiconductors originates from a number of photophysical processes: (i) the attenuation of linear absorption from state filling, i.e., ground state bleaching (GSB); (ii) the opening of novel absorption pathways from the excited state to higher-lying energy levels, i.e. photoinduced absorption (PA); (iii) stimulated emission (SE); (iv) renormalization of the band edge or electric field effects, established by the excited state population (e.g., electroabsorption or quadratic Stark effect), and (v) photoinduced modulation of the refractive index. Interestingly, all of these mechanisms were invoked to explain the TA spectra of bulk HPs in recent years.[13] The signals usually observed in TA spectra of HPs are two: a prominent GSB near the optical bandgap and a broad PA at higher energy with respect to band gap.[39] Generally, the GSB signal coincides with the exciton peak determined from linear absorption and is interpreted as the bleach of excitonic absorption due to phase-space filling by free carriers and/or the presence of excitons. Conversely, the broad PA above the bandgap is attributed to many-body effects, e.g., bandgap renormalization and reduced Columbic screening.[41]

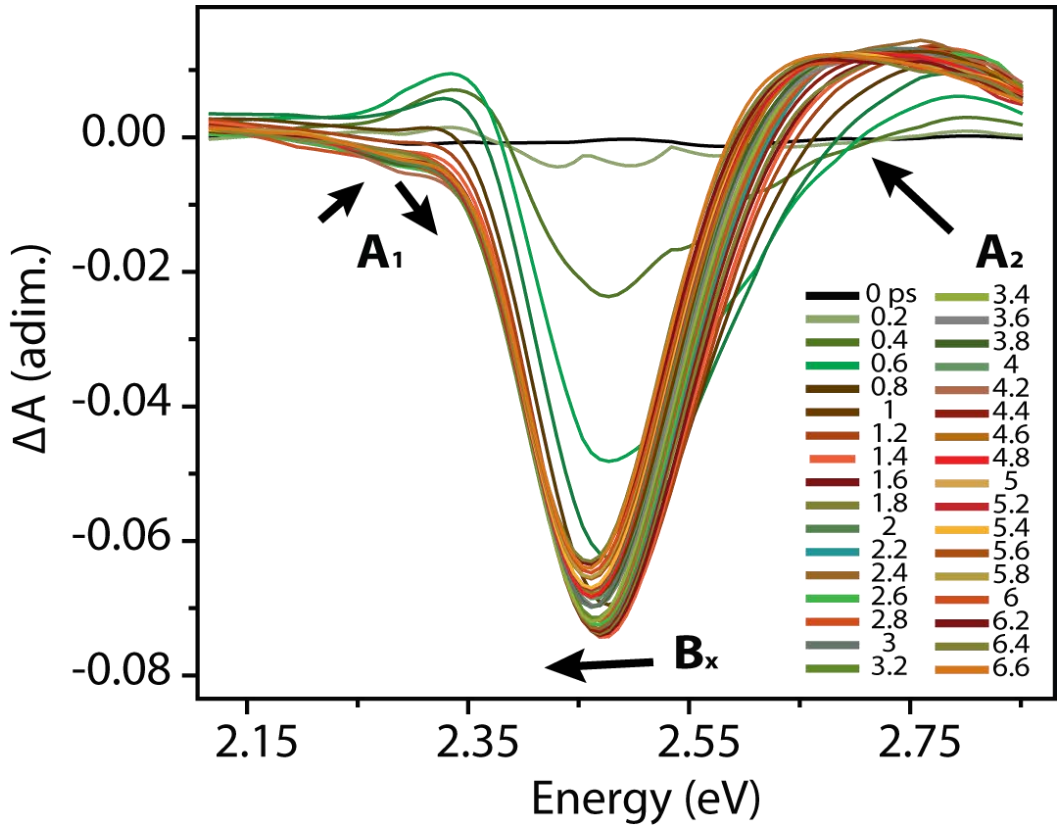

Figure 9.7- Temporal evolution of TA signals for PD-50 samples, obtained at slices at fixed time delays (every 200fs) of Figure 9.6. Three main signals can be observed: two PA (A_1 and A_2) and one GSB (B_x). The A_1 signal appears and vanishes within the first 1.2 ps and is related to hot carrier cooling. The B_x and A_2 signals grow contextually to the vanishing of A_1, and experience a time-dependent red-shift, in accordance with Figure 9.6.

The TA map recorded for PD-50, using $80\,\frac{\mu J}{cm^2}$ @ $3.1eV$ pump pulse and white light detection, is reported in Figure 9.6. Notably, the two main signal, typical for bulk HPs, can be observed in PDs, as well. The exciton transition bleaching (B_x) is found at 2.47eV, while the above band-gap PA (A_2) signal is observed at 2.65eV. Both B_x and A_2 signals experience a time dependent redshift of ~$30meV$, indicated by the white dashed line in Figure 8.6. Noteworthy, this effect was observed for each of the different PDs studied and was observed to be independent of the pump fluence.[40] Moreover, a secondary and short-lived PA (A_1) signal is observed on the low energy side of the main signal B_x. This signal grows and vanishes within the first picosecond and is peaked at 2.35eV.

In view of an accurate interpretation of the position and of the dynamics of these signals, a complete understanding of the energy levels and physical processes contributing to TA signals is mandatory. Since the initial observations, analogous optical nonlinearities in bulk HPs band edge have attracted significant attention. Specifically, the origins of A_1 and A_2 were widely disputed for bulk $MAPbI_3$.[2] Different authors proposed three possible mechanisms for the origin of A_1 signal: (i) electric field, quadratic Stark effect, [42-43] (ii) band gap renormalization[30, 44-45] and (iii) broadening of the excitonic transition through phase-space filling.[46] On the other hand, the proposed sources of the A_2 signal were: (i) Band Gap Renormalization[46] (ii) Burnstein-Moss effect[39] (iii) modulation in the refractive index of the medium.[39]

Yet the application of such hypothesis in explaining the origin of the signals for PDs needs to consider one significant difference between HPs and PDs: the confinement effects turn bound excitons into the leading actors of PDs photophysics, whereas both free carriers and exciton significantly contribute to the photophysics of bulk HPs.[18]

In analogy with CdSe-based QDs, the A_1 peak can be considered as the signature of hot carrier relaxation.[34] Namely, when hot carriers are created into the PD, the material quasi-instantaneously experiences a rapid band-gap renormalization or bi-exciton effect.[34, 47-48] Therefore, novel states are available for optical transition and the A_1 signal is observed. Contextually, photogenerated hot carriers undergo a cooling process, which reduces this signal ultimately leading to a bleaching signal at the same energy. According to Figures 9.7 and 9.8**a**, this entire dynamic run out within the first 1200fs after photoexcitation. Following a complementary dynamics to that of A_1, both the high energy PA signal A_2 and the band-edge bleaching B_x grow after 1ps and persist to times longer than 100ps. The rise time of B_x is quantified by exponential fitting with 490±20 fs time constant (Figure 9.8**a**).

Albeit additional work is needed, in order to verify the size and fluence dependency of observed processes, these are to be considered as spectroscopic signatures of an ultra-slow carrier cooling in PDs.

A slow hot carrier cooling would be of paramount importance not only in outpacing thermodynamic conversion limits in photovoltaic applications but also in designing highly efficient (and tunable) laser systems. Indeed, slow recombinations are fundamental in lowering lasing thresholds.

An in-depth analysis of B_x signal provides further insight into the hot carrier dynamics in PDs. As proposed by Price for $MAPbI_3$, this signal exhibits a fluence-dependent, high energy tail that persists at longer times >100ps.[39] This signal is characteristic of state filling by carriers with kinetic energies higher than the lattice temperature, i.e., hot carriers, and is evident in the region between 2.55 and 2.65 eV of Figure 9.8.

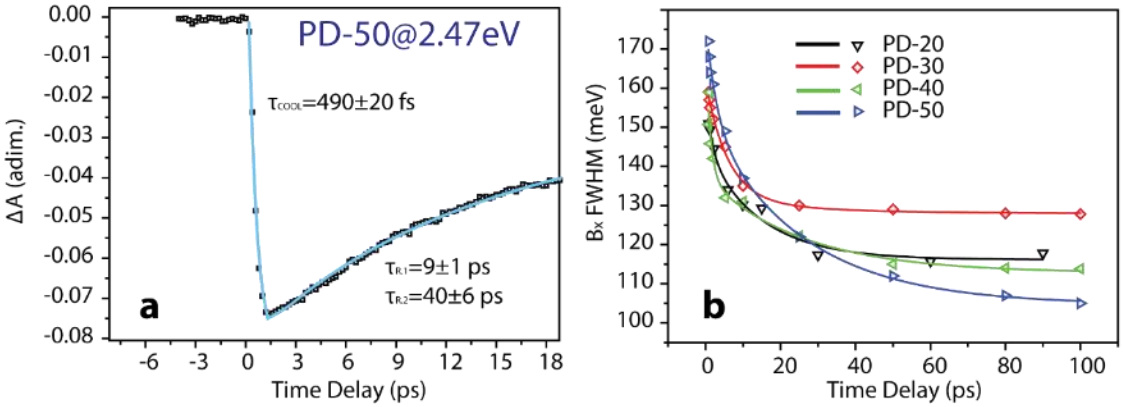

Figure 9.8- (**a**)Time trace for the B_x signal of Figure 9.7 (black dots) and exponential fitting curves (solid line) obtained by fitting of the rise and decay parts. A slow hot carrier cooling is observed as slow rise time (490fs) of the B_x signal. Conversely, the decay of this signal displays two time constants, associated with phonon scattering and Auger relaxation processes. (**b**) Temporal evolution of FWHM of the B_x signal for different PDs. The sharpening of B_x signal is associated with further hot carrier cooling and multi-exciton relaxations.

Here, the analysis of the peak broadening was performed under the assumption that, a quasi-equilibrium carrier distribution is established soon after the initial photoexcitation. This approximation is usually applied to extract the hot carrier temperatures in bulk semiconductors, such as GaAs. Recently, this ansatz was applied to formamidinium lead iodide ($FAPbI_3$) quantum-confined nanocrystals.[40] Explicitly, the validity of such an approach was justified by the relatively small energy level spacing compared to the thermal energy, as extensively discussed by Graetzel et al. for similar PDs.[49] The broadening of the B_x peak was quantified by a Gaussian fitting procedure, and results are reported in Figure 9.8**b**. Noteworthy, the FWHM parameter follows a similar trend in all different PDs studied and its temporal evolution for each of the different PD samples was fitted by bi-exponential decay function. The short time component was found to be $\tau_s = 2 \pm 0.5\ ps$ for PD-20 and PD-40, and longer $\tau_s = 3 \pm 0.5\ ps$ for PD-30 and PD-50. The long time components was found to be $\tau_l = 26 \pm 3\ ps$ for all samples.

The different amplitudes of these components concur in generating different decay curves, reported in Figure 9.8**b**.

Moreover, all curves tend to an asymptotic value of FWHM in the interval 110-130 meV, which is likely to depend on the quality of the synthesis, rather than on intrinsic factors. Similar results were recently reported by Itskos for $FAPbI_3$ nanostructures.[40] According to the interpretation provided in Refs. 32 and 39, these two time constants are associated with phonon coupling (fast) and Auger heating (slow) processes. Slow hot carrier relaxation is a lively debated topic. During this year, many works reported such an effect in bulk perovskites. A consensus is being of formed around the hypothesis of a substantial role played vibration, polarons and electron-phonon coupling,[32, 50-51] thereby supporting what initially proposed by Zhu, i.e., a "polaron protection" of carriers in hybrid perovskites.[52-53]

The observation of these effects in quantum-confined nanostructures, partially elucidate and address the discussion on cold carrier trapping, pinpointing the role of vibrations. Yet this opens for further questions: (i) what is the role of confinement-enhanced electronic interactions? (ii) is Auger recombination as crucial as for inorganic QDs?

In order to either confirm these hypotheses or/and provide additional mechanistic insights, extensive measurements, and data analysis are currently underway. Nonetheless, these preliminary insights into TA results evidence the enormously important role of hot carriers as principal actors in picoseconds timescale dynamics of PDs, thereby opening to future applications, such as hot carrier extractions for photovoltaics.

9.5 Conclusions

Summarizing, in this Chapter was presented a thorough analysis of the photophysics of quantum confined HP nanostructures. Both the hot carrier and cold exciton dynamics of five different PD samples was investigated by means of PL spectroscopies. Moreover, preliminary results of TA spectroscopy characterization were presented.

The fundamental analysis revealed an effective quantum confinement, leading to size-dependent emission and radiative rates. Nevertheless, the application of methodologies developed in the previous part for inorganic QDs revealed the different behavior of these materials.

Indeed, the reported analysis revealed that the PL decays of PDs are compatible with a delayed luminescence mechanisms, akin to inorganic QDs. However, some peculiarities suggested a slightly different scenario. Albeit a bright exciton- dark reservoir mechanism well describes the PL decay curves, the dynamics resulted in being one order of magnitude slower with respect to that observed for inorganic QDs.

Together with reduced hot carrier trapping, measured by PLQY excitation profiles, and slower carrier relaxation, observed in preliminary TA results, the presented results would support one of the currently most discussed suggestions about HPs, i.e., the role of polaronic effects, triggered by the lattice deformability.

Within this context, the knowledge gathered on inorganic QDs served as picklock and helped to disclose some peculiarities of PDs, such as slower trapping and carrier relaxation. Hence, the reported analysis calls for further studies, especially on the vibrational structure and on the electron-phonon coupling in PDs. Indeed, the scenario is still incomplete and many open questions persist. A complete picture would encompass a comprehensive description of the interaction between electronic and phononic subsystems, also consider the quantum confinement effects.

References

1. Grätzel, M., The Rise of Highly Efficient and Stable Perovskite Solar Cells. *Accounts of Chemical Research* **2017**, *50*, 487-491.

2. Manser, J. S.; Christians, J. A.Kamat, P. V., Intriguing Optoelectronic Properties of Metal Halide Perovskites. *Chemical Reviews* **2016**, *116*, 12956-13008.

3. Huang, J.; Yuan, Y.; Shao, Y.Yan, Y., Understanding the Physical Properties of Hybrid Perovskites for Photovoltaic Applications. **2017**, *2*, 17042.

4. Li, W.; Wang, Z.; Deschler, F.; Gao, S.; Friend, R. H.Cheetham, A. K., Chemically Diverse and Multifunctional Hybrid Organic-Inorganic Perovskites. **2017**, *2*, 16099.

5. Choi, J. J.Billinge, S. J. L., Perovskites at the Nanoscale: From Fundamentals to Applications. *Nanoscale* **2016**, *8*, 6206-6208.

6. Xing, J., et al., High-Efficiency Light-Emitting Diodes of Organometal Halide Perovskite Amorphous Nanoparticles. *ACS Nano* **2016**, *10*, 6623-6630.

7. Huang, H.; Susha, A. S.; Kershaw, S. V.; Hung, T. F.Rogach, A. L., Control of Emission Color of High Quantum Yield Ch3nh3pbbr3 Perovskite Quantum Dots by Precipitation Temperature. *Advanced Science* **2015**, *2*, 1500194-n/a.

8. Tyagi, P.; Arveson, S. M.Tisdale, W. A., Colloidal Organohalide Perovskite Nanoplatelets Exhibiting Quantum Confinement. *The Journal of Physical Chemistry Letters* **2015**, *6*, 1911-1916.

9. Gonzalez-Carrero, S.; Galian, R. E.Perez-Prieto, J., Maximizing the Emissive Properties of Ch3nh3pbbr3 Perovskite Nanoparticles. *Journal of Materials Chemistry A* **2015**, *3*, 9187-9193.

10. Weidman, M. C.; Seitz, M.; Stranks, S. D.Tisdale, W. A., Highly Tunable Colloidal Perovskite Nanoplatelets through Variable Cation, Metal, and Halide Composition. *ACS Nano* **2016**, *10*, 7830-7839.

11. Polavarapu, L.; Nickel, B.; Feldmann, J.Urban, A. S., Advances in Quantum-Confined Perovskite Nanocrystals for Optoelectronics. *Advanced Energy Materials* **2017**, *7*, 1700267-n/a.

12. Protesescu, L.; Yakunin, S.; Bodnarchuk, M. I.; Krieg, F.; Caputo, R.; Hendon, C. H.; Yang, R. X.; Walsh, A.Kovalenko, M. V., Nanocrystals of Cesium Lead Halide Perovskites (Cspbx3, X = Cl, Br, and I): Novel Optoelectronic Materials Showing Bright Emission with Wide Color Gamut. *Nano Letters* **2015**, *15*, 3692-3696.

13. Manser, J. S.; Saidaminov, M. I.; Christians, J. A.; Bakr, O. M.Kamat, P. V., Making and Breaking of Lead Halide Perovskites. *Accounts of Chemical Research* **2016**, *49*, 330-338.

14. Huang, S.; Li, Z.; Kong, L.; Zhu, N.; Shan, A.Li, L., Enhancing the Stability of Ch3nh3pbbr3 Quantum Dots by Embedding in Silica Spheres Derived from Tetramethyl Orthosilicate in "Waterless" Toluene. *Journal of the American Chemical Society* **2016**, *138*, 5749-5752.

15. Zheng, K.; Žídek, K.; Abdellah, M.; Messing, M. E.; Al-Marri, M. J.Pullerits, T., Trap States and Their Dynamics in Organometal Halide Perovskite Nanoparticles and Bulk Crystals. *The Journal of Physical Chemistry C* **2016**, *120*, 3077-3084.

16. Luo, B.; Pu, Y.-C.; Yang, Y.; Lindley, S. A.; Abdelmageed, G.; Ashry, H.; Li, Y.; Li, X.Zhang, J. Z., Synthesis, Optical Properties, and Exciton Dynamics of Organolead Bromide Perovskite Nanocrystals. *The Journal of Physical Chemistry C* **2015**, *119*, 26672-26682.

17. Tachikawa, T.; Karimata, I.Kobori, Y., Surface Charge Trapping in Organolead Halide Perovskites Explored by Single-Particle Photoluminescence Imaging. *The Journal of Physical Chemistry Letters* **2015**, *6*, 3195-3201.

18. Zheng, K., et al., Exciton Binding Energy and the Nature of Emissive States in Organometal Halide Perovskites. *The Journal of Physical Chemistry Letters* **2015**, *6*, 2969-2975.

19. Minotto, A.; Todescato, F.; Fortunati, I.; Signorini, R.; Jasieniak, J. J.Bozio, R., Role of Core–Shell Interfaces on Exciton Recombination in CdSe–Cdxzn1–Xs Quantum Dots. *The Journal of Physical Chemistry C* **2014**, *118*, 24117-24126.

20. Makarov, N. S.; Guo, S.; Isaienko, O.; Liu, W.; Robel, I.Klimov, V. I., Spectral and Dynamical Properties of Single Excitons, Biexcitons, and Trions in Cesium–Lead-Halide Perovskite Quantum Dots. *Nano Letters* **2016**, *16*, 2349-2362.

21. van Driel, A. F.; Nikolaev, I. S.; Vergeer, P.; Lodahl, P.; Vanmaekelbergh, D.Vos, W. L., Statistical Analysis of Time-Resolved Emission from Ensembles of Semiconductor Quantum Dots: Interpretation of Exponential Decay Models. *Physical Review B* **2007**, *75*, 035329.

22. Righetto, M.; Minotto, A.Bozio, R., Bridging Energetics and Dynamics of Exciton Trapping in Core-Shell Quantum Dots. *The Journal of Physical Chemistry C* **2016**.

23. Jones, M.; Lo, S. S.Scholes, G. D., Quantitative Modeling of the Role of Surface Traps in CdSe/CdS/ZnS Nanocrystal Photoluminescence Decay Dynamics. *Proceedings of the National Academy of Sciences* **2009**, *106*, 3011-3016.

24. Klimov, V. I., *Nanocrystal Quantum Dots, Second Edition*; Taylor & Francis, 2010.

25. Kang, B.Biswas, K., Shallow Trapping Vs. Deep Polarons in a Hybrid Lead Halide Perovskite, Ch3nh3pbi3. *Physical Chemistry Chemical Physics* **2017**.

26. Rabouw, F. T.; Kamp, M.; van Dijk-Moes, R. J. A.; Gamelin, D. R.; Koenderink, A. F.; Meijerink, A.Vanmaekelbergh, D., Delayed Exciton Emission and Its Relation to Blinking in CdSe Quantum Dots. *Nano Letters* **2015**, *15*, 7718-7725.

27. Leijtens, T.; Eperon, G. E.; Barker, A. J.; Grancini, G.; Zhang, W.; Ball, J. M.; Kandada, A. R. S.; Snaith, H. J.Petrozza, A., Carrier Trapping and Recombination: The Role of Defect Physics in Enhancing the Open Circuit Voltage of Metal Halide Perovskite Solar Cells. *Energy & Environmental Science* **2016**, *9*, 3472-3481.

28. Stranks, S. D.; Burlakov, V. M.; Leijtens, T.; Ball, J. M.; Goriely, A.Snaith, H. J., Recombination Kinetics in Organic-Inorganic Perovskites: Excitons, Free Charge, and Subgap States. *Physical Review Applied* **2014**, *2*, 034007.

29. Song, A. K. S.Williams, R. T., *Self-Trapped Excitons*; Springer, 1996.

30. Wu, X.; Trinh, M. T.; Niesner, D.; Zhu, H.; Norman, Z.; Owen, J. S.; Yaffe, O.; Kudisch, B. J.Zhu, X. Y., Trap States in Lead Iodide Perovskites. *Journal of the American Chemical Society* **2015**, *137*, 2089-2096.

31. Rashba, Ė. I.Sturge, M. D., *Excitons*; North-Holland Publishing Company, 1982.

32. Smith, M. D.; Jaffe, A.; Dohner, E. R.; Lindenberg, A. M.Karunadasa, H. I., Structural Origins of Broadband Emission from Layered Pb-Br Hybrid Perovskites. *Chemical Science* **2017**, *8*, 4497-4504.

33. Zheng, K.; Žídek, K.; Abdellah, M.; Chen, J.; Chábera, P.; Zhang, W.; Al-Marri, M. J.Pullerits, T., High Excitation Intensity Opens a New Trapping Channel in Organic-Inorganic Hybrid Perovskite Nanoparticles. *ACS Energy Letters* **2016**, *1*, 1154-1161.

34. Kambhampati, P., Hot Exciton Relaxation Dynamics in Semiconductor Quantum Dots: Radiationless Transitions on the Nanoscale. *The Journal of Physical Chemistry C* **2011**, *115*, 22089-22109.

35. Mooney, J.; Krause, M. M.Kambhampati, P., Connecting the Dots: The Kinetics and Thermodynamics of Hot, Cold, and Surface-Trapped Excitons in Semiconductor Nanocrystals. *The Journal of Physical Chemistry C* **2014**, *118*, 7730-7739.

36. Righetto, M.; Minotto, A.Bozio, R., Bridging Energetics and Dynamics of Exciton Trapping in Core-Shell Quantum Dots. *The Journal of Physical Chemistry C* **2017**, *121*, 896-902.

37. Tian, Y., et al., Giant Photoluminescence Blinking of Perovskite Nanocrystals Reveals Single-Trap Control of Luminescence. *Nano Letters* **2015**, *15*, 1603-1608.

38. Orfield, N. J.; McBride, J. R.; Wang, F.; Buck, M. R.; Keene, J. D.; Reid, K. R.; Htoon, H.; Hollingsworth, J. A.Rosenthal, S. J., Quantum Yield Heterogeneity among Single Nonblinking Quantum Dots Revealed by Atomic Structure-Quantum Optics Correlation. *ACS Nano* **2016**, *10*, 1960-1968.

39. Price, M. B., et al., Hot-Carrier Cooling and Photoinduced Refractive Index Changes in Organic-Inorganic Lead Halide Perovskites. **2015**, *6*, 8420.

40. Papagiorgis, P.; Protesescu, L.; Kovalenko, M. V.; Othonos, A.Itskos, G., Long-Lived Hot Carriers in Formamidinium Lead Iodide Nanocrystals. *The Journal of Physical Chemistry C* **2017**, *121*, 12434-12440.

41. Yang, Y.; Yang, M.; Li, Z.; Crisp, R.; Zhu, K.Beard, M. C., Comparison of Recombination Dynamics in Ch3nh3pbbr3 and Ch3nh3pbi3 Perovskite Films: Influence of Exciton Binding Energy. *The Journal of Physical Chemistry Letters* **2015**, *6*, 4688-4692.

42. Chen, K.; Barker, A. J.; Morgan, F. L. C.; Halpert, J. E.Hodgkiss, J. M., Effect of Carrier Thermalization Dynamics on Light Emission and Amplification in Organometal Halide Perovskites. *The Journal of Physical Chemistry Letters* **2015**, *6*, 153-158.

43. Trinh, M. T.; Wu, X.; Niesner, D.Zhu, X. Y., Many-Body Interactions in Photo-Excited Lead Iodide Perovskite. *Journal of Materials Chemistry A* **2015**, *3*, 9285-9290.

44. Deschler, F., et al., High Photoluminescence Efficiency and Optically Pumped Lasing in Solution-Processed Mixed Halide Perovskite Semiconductors. *The Journal of Physical Chemistry Letters* **2014**, *5*, 1421-1426.

45. Wehrenfennig, C.; Liu, M.; Snaith, H. J.; Johnston, M. B.Herz, L. M., Homogeneous Emission Line Broadening in the Organo Lead Halide Perovskite CH3NH3PbI3–XClx. *The Journal of Physical Chemistry Letters* **2014**, *5*, 1300-1306.

46. Yang, Y.; Ostrowski, D. P.; France, R. M.; Zhu, K.; van de Lagemaat, J.; Luther, J. M.Beard, M. C., Observation of a Hot-Phonon Bottleneck in Lead-Iodide Perovskites. **2015**, *10*, 53.

47. Kambhampati, P., Unraveling the Structure and Dynamics of Excitons in Semiconductor Quantum Dots. *Accounts of Chemical Research* **2011**, *44*, 1-13.

48. Kambhampati, P., Multiexcitons in Semiconductor Nanocrystals: A Platform for Optoelectronics at High Carrier Concentration. *The Journal of Physical Chemistry Letters* **2012**, *3*, 1182-1190.

49. Li, M.; Bhaumik, S.; Goh, T. W.; Kumar, M. S.; Yantara, N.; Grätzel, M.; Mhaisalkar, S.; Mathews, N.Sum, T. C., Slow Cooling and Highly Efficient Extraction of Hot Carriers in Colloidal Perovskite Nanocrystals. **2017**, *8*, 14350.

50. Frost, J. M.; Whalley, L. D.Walsh, A., Slow Cooling of Hot Polarons in Halide Perovskite Solar Cells. *ACS Energy Letters* **2017**, 2647-2652.

51. Straus, D. B.; Hurtado Parra, S.; Iotov, N.; Gebhardt, J.; Rappe, A. M.; Subotnik, J. E.; Kikkawa, J. M.Kagan, C. R., Direct Observation of Electron–Phonon Coupling and Slow Vibrational Relaxation in Organic-Inorganic Hybrid Perovskites. *Journal of the American Chemical Society* **2016**, *138*, 13798-13801.

52. Zhu, X. Y.Podzorov, V., Charge Carriers in Hybrid Organic-Inorganic Lead Halide Perovskites Might Be Protected as Large Polarons. *The Journal of Physical Chemistry Letters* **2015**, *6*, 4758-4761.

53. Miyata, K.; Meggiolaro, D.; Trinh, M. T.; Joshi, P. P.; Mosconi, E.; Jones, S. C.; De Angelis, F.Zhu, X.-Y., Large Polarons in Lead Halide Perovskites. *Science Advances* **2017**, *3*.

SUMMARY AND OUTLOOK

ABSTRACT- The combination of experiments and modeling carried on throughout this Ph.D. project allowed delving deeper into the photophysics of quantum dots. Albeit the thesis comprises two Parts, these are not to be intended as separated entities. On the contrary, the thesis is developed on a leitmotiv, concerning the excited state dynamics and the interaction with trap states of nanomaterials, thereby pursuing a better control on these systems. The first Part describes the investigation on CdSe-based core/shell quantum dots. Two primary goals were reached within this Part: (i) a deeper understanding of application-tailored passivation strategies, encompassing inorganic shelling and surface chemistry tailoring (ii) the portrayal of a comprehensive photophysical model, aiming to describe trapping and Auger recombination processes within a phenomenological approach. The expertise and the deeper level of understanding gathered in the first Part were harnessed and applied to novel materials studied in the second Part. Through this approach, trapping in hybrid perovskite-based quantum dots was successfully investigated. In addition, the peculiarities of these materials stemmed by contrast with inorganic QDs. On the other hand, a similar scheme could not be used in carbon-based dots, due to their inherently more complex and ill-defined nature. Yet some insights into the nature of their photoluminescence were provided, using unconventional spectroscopic techniques. Here, the primary results of the thesis are summarized, and some potential directions for future research are sketched.

Colloidal quantum dots (QDs) sparked the interest of the scientific community for more than two decades. The enticing prospects of their application in devices, harnessing their broad and strong absorption bands as well as their size- and shape-tunable emission underlie this interest. Howbeit, the fulfillment of these expectancies is ancillary to both a deeper understanding and a smart engineering of QDs. In practical terms, when envisioning bio-imaging or phosphor materials application, QDs must have highly efficient photoluminescence (PL). Nonetheless, the use of QDs as electricity-to-light (e.g., light-emitting diodes) or light-to-electricity (e.g., solar cells) converters requires an efficient outcoupling of QDs electronic states. Albeit different strategies must be used to address each specific challenge, they wholly rest on a broad and comprehensive understanding of the photophysics of these systems.

In the first Part of this thesis CdSe/$Cd_xZn_{1-x}S$ core/shell QDs were studied as archetypal systems, and both of the above-mentioned challenges were addressed. The detrimental effects of hot-carriers trapping and trion Auger recombinations of the photon conversion efficiency were investigated.

The analysis of PL quantum yield excitation profiles (Chapter 3) revealed the interactions of un-relaxed carriers with trap states. A refinement of the dynamical trap model (i.e., that assuming trap states involved in a trapping/de-trapping equilibrium) allowed investigating the hot-carrier trapping process and the related accumulation of long-lived trap state populations. As witnessed by transient absorption spectroscopy (Chapter 4), the resulting trion states suffer from fast Auger recombinations, which ultimately hamper the emission efficiencies. Inorganic shelling is the most promising approach to overcome these issues, providing an electronic decoupling between trap states and bound excitons. Among different shell compositions (i.e., CdS, CdZnS, and ZnS) and thicknesses (i.e., 1-6 ML) studied, alloyed CdZnS shells with intermediate thickness stemmed as the most lucrative compromise in view of light emitting applications. Indeed, as a resulting general criterion, an efficient shell should provide both an adequate decoupling from surface trap states and smooth interfaces, avoiding the nucleation of interfacial traps and inhibiting Auger recombinations. Much of the smart engineering on these nanomaterials could be summarized as the quest to find heterostructures providing the best compromise among these counteracting features.

Unfortunately, the decoupling from surface trap states inherently leads to a reduced coupling to acceptor molecules or nanostructures. Hence, inorganic shelling is not a profitable strategy, when envisioning applications that require the outcoupling of QDs electronic states. Conversely, a fine tuning of this coupling was achieved by tailoring the surface chemistry of QDs. The interaction between QDs and PCBM molecules was successfully addressed by ligand exchange reactions (Chapter 5). Indeed, CdSe and PCBM interaction generally comprises both charge and energy transfer, but capping with short thiols revealed to address this interaction toward charge transfer adequately. The resulting engineered hetero-interface QDs-PCBM stemmed as a suitable candidate for excitonic device applications (e.g., solar cells).

In the second Part of this thesis, the quest for novel materials, outpacing CdSe-based QDs, in terms of both performances and bio-compatibility, was addressed. Specifically, carbon-based dots (CDs) and hybrid perovskite-based dots (PDs) were studied, aiming to mine information on these novel systems by mimicking some of the methodologies developed in the first Part of the thesis.

Unfortunately, due to the multifaceted and ambiguous nature of novel quantum-confined nanostructures, the paradigm formulated for CdSe QDs served as a touchstone, rather than an effective study roadmap. Indeed, each of the novel material studied revealed its peculiar nature.

Perovskite dots (PDs) displayed very promising properties, potentially outpacing those of CdSe-based QDs. The size-resolved study, proposed in Chapter 9, revealed the combined effects of confinement strength and interaction with trap states. Specifically, more strongly confined dots reported enhanced radiative rates and higher quantum yields.

The PL decay dynamics outlined some peculiarities with respect to inorganic QDs. Even though the conventional analysis - based on the hypothesis of inhomogeneity of non-radiative centers- unveiled a size-dependent radiative rate, the phenomenological kinetic model provided different and more insightful results.

Specifically, the trapping /de-trapping equilibrium appeared to describe their dynamics well, but extracted velocities resulted up to one order of magnitude slower with respect to inorganic QDs. This suggested either different interactions with trap states or an entirely different nature of trap states. According to the recent literature on hybrid perovskites, phonons and the lattice deformability seemed to play a pivotal role in these systems. Hence, among different possible speculations, the self-trapping mechanism was proposed. Nevertheless, it is clear that much work will be needed in elucidating the nature of the trap states in nano perovskites.

Moreover, the size-resolved study revealed a size dependence in trapping rates, thereby calling into question the energetics of trapping. Akin to CdSe QDs, this lead to the study of hot-carrier trapping, observed as quasi-static quenching in PLQY excitation profiles. This effect appeared quantitatively less pronounced with respect to CdSe QDs. This is further confirmed by slow hot-carrier cooling processes evidenced in TA measurement. In fact, the persistence of hot-carriers related signals at t >40ps suggest and confirm the marginal role played by hot-carrier trapping processes. Though preliminary, these results outlined PDs as excitonic nanostructures with reduced interactions with trap states. Therefore, they are very promising in view of almost every possible optoelectronic application, i.e., phosphors, lasers, LEDs and solar cells.

Conversely, the elusive nature of carbon dots (CDs) required taking some steps back and questioning a paradigmatic approach in nanoscience. Specifically, the failure of the inferential process, ensuring the *a priori* link between TEM micrographs and optical properties measurements, was verified for widely employed CDs. Albeit carbon nanostructures were observed by TEM, fluorescence correlation spectroscopy (FCS) provided a direct link between the measured optical properties and fluorescent species, which were discovered to be small organic molecules free in solution.

The poor emitting properties of carbon cores, revealed by FCS, impose a reconsideration of the synthetic approaches producing CDs. Howbeit, FCS stems as a valuable tool to address the synthetists toward highly efficient CDs, as presented in Chapter 8.

In sums, this thesis bolstered the understanding of the photophysics of different quantum confined systems. The studies on core/shell CdSe/$Cd_xZn_{1-x}S$ QDs allowed both uncovering the role played by shells in the exciton dynamics and deciphering the complex interaction with trap states, leading to the portrayal of a complete photophysical scenario.

Future work will encompass the quest for better performing heterostructures, suppressing trapping and Auger recombinations, but also allowing for an efficient outcoupling of the electronic states. On the other hand, the reported investigations on CDs and PDs deepened the understanding of both their nature and photophysics, paving the way for their use in practical applications. Nevertheless, CDs are demanding much work in order to achieve highly luminescent carbon nanostructure and ruling out the contributions from free molecules. Lastly, the nature and the role of trap states in quantum confined perovskites, as well as the role of hot carriers, will undoubtedly generate a burgeoning interest in the years to come.